RIGOROUS SIMULATION MODEL OF KEROGEN PYROLYSIS FOR THE IN-SITU UPGRADING OF OIL SHALES

A Dissertation

by

KYUNG JAE LEE

Submitted to the Office of Graduate and Professional Studies of
Texas A&M University
in partial fulfillment of the requirements for the degree of

DOCTOR OF PHILOSOPHY

Chair of Committee,	Christine A. Ehlig-Economides
Co-Chair of Committee	George J. Moridis
Committee Members,	Maria A. Barrufet
	Thomas A. Blasingame
Head of Department,	A. Daniel Hill

December 2014

Major Subject: Petroleum Engineering

ABSTRACT

Oil shale is a vast, yet untapped energy source, and the pyrolysis of kerogen in the oil shales releases recoverable hydrocarbons. In this dissertation, we investigate how to increase process efficiency and decrease the costs of in-situ upgrading process for kerogen pyrolysis, which is applicable to the majority of the oil shales. In-situ upgrading processes include (a) Shell In-situ Conversion Process (ICP), (b) ExxonMobil Electrofrac, and (c) Texas A&M (TAMU) Steamfrac. We evaluate these three processes in realistic scenarios using our newly developed multi-phase, multi-component, non-isothermal simulator.

Kerogen pyrolysis is represented by 6 kinetic reactions resulting in 10 components and 4 phases. Expanding TAMU Flow and Transport Simulator (FTSim), we develop a fully functional capability that describes the kerogen pyrolysis and the accompanying system changes. The simulator describes the coupled process of mass transport and heat flow through porous and fractured media, and accurately accounts for phase equilibria and transitions. It provides a powerful tool to evaluate the efficiency and the productivity of the in-situ upgrading processes.

We validate our simulator by reproducing the field production data of the Shell ICP implemented in Green River Formation. We conduct the sensitivity analyses of the presence and absence of pre-existing fracture system, oil shale grade, permeability of the fracture network, and thermal conductivity of the formation. Validated model has the oil shale grade of 25 gal/ton, fracture domain permeability of 150 md, and formation thermal conductivity of 2.0 W/m-K.

In the application cases, we analyze the significant factors affecting each process. In the Shell ICP, the ExxonMobil Electrofrac, and the TAMU Steamfrac, we study the effects of heater temperature, electrical conductivities of injection material, and steam injection strategy, respectively. We find that the best case of the Shell ICP showed the highest energy efficiency of 144 %. The best cases of the ExxonMobil Electrofrac and the TAMU Steamfrac show the energy efficiency of 74.1 %, and 54.1 %, respectively.

We obtain positive Net Present Value (NPV) in the TAMU Steamfrac by much less number of wells than the Shell ICP and the ExxonMobil Electrofrac, though it has the lowest energy efficiency.

DEDICATION

To my beloved dad, Kanghoon Lee

ACKNOWLEDGEMENTS

I sincerely appreciate my advisors, Dr. Christine A. Ehlig-Economides and Dr. George J. Moridis, advising and supporting me with confidence. Dr. Maria A. Barrufet and Dr. Thomas A. Blasingame are gratefully acknowledged for their helpful idea and suggestions for fulfilling this dissertation.

Gratitude also goes to my former advisor in Korea, Dr. Jonggeun Choe, who has been giving me invaluable advice.

To my mom, Jong Ok Kim, I owe the greatest gratitude for her infinite love and encouragement. To my older brother, Dongjae Lee, and my sister-in-law, Sujeong Kim, I wholeheartedly appreciate your love and warmness. Finally, I appreciate my husband, HeonYong Kang, giving me brilliant ideas and being a best friend for my life.

NOMENCLATURE

A	Aqueous phase
A_k	Frequency factor of reaction *k*, 1/sec (1/day in Table 4)
A_{nm}	Contacting area between grid blocks *n* and *m*
C_κ	Concentration of component κ , kg/m^3
C_R	Rock heat capacity, J/kg/K
c_{chw}	Cost for completion of the horizontal well, $/ft
c_{cvw}	Cost for completion of the vertical well, $/ft
c_{dhw}	Cost for drilling of the horizontal well, $/ft
c_{dvw}	Cost for drilling of the vertical well, $/ft
c_{fr}	Cost for fracturing treatment, $/#
c_{ht}	Cost for heating the well, $/BOE
c_{icm}	Cost for injection of the conductive material, $/kg
c_{ist}	Cost for steam injection, $/kg
d_{cvw}	Distance of the completion in the vertical well
d_{vw}	Depth of the vertical well
E_k	Activation energy of reaction *k*, J/mole (KJ/mole in Table 4)
$\mathbf{F}^\kappa$	Flux term of component κ , kg/m^2/sec
$\mathbf{F}^\theta$	Heat flux term, J/m/sec
f_o	Operating cost, fraction
f_r	Royalty in NPV computation, fraction
f_t	Tax in NPV computation, fraction
G	Gaseous phase

h_β	Enthalpy of phase β , J/kg
I	Initial investment in NPV computation, $
K	Thermal conductivity, W/m-K
K_H	Thermal conductivity of the conductive material in the ExxonMobil Electrofrac process, W/m-K
K_k	Reaction rate constant,
k_f	Permeability of fracture network,
L	Lorenz number (= 2.44e-8 W-Ω/K^2)
L_{chw}	Length of the completion in the horizontal well
L_{hw}	Length of the horizontal well
M	Oil yield of oil shale, gal/ton
M^{κ}	Mass accumulation term for component κ , kg/m^3
M^{θ}	Heat accumulation term, J/m^3
m_{icm}	Mass of the injected conductive material in ExxonMobil Electrofrac, kg
NPV	Net Present Value, $
n_{hf}	Number of the hydraulic fractures
n_{hw}	Number of the horizontal wells
n_{pw}	Number of the production wells
n_{vw}	Number of the vertical wells
O	Liquid organic phase
P_G	Price of hydrocarbon gas, $/MSCF
P_o	Price of liquid hydrocarbon, $/STB
$\Delta Q_{G,n}$	Annual cumulative hydrocarbon gaseous phase production, MSCF
$\Delta Q_{o,n}$	Annual cumulative liquid organic phase production, STB
q^{κ}	Source/sink term of component κ , kg/m^3/sec

q^{θ}	Source/sink term of heat, J/m^3/sec
R	Residual
R_n	Annual revenue from the production, $
r_k	Reaction rate, kg/m^3/sec
S	Solid phase
S_{β}	Saturation of phase β
S_{ira}	Irreducible saturation of aqueous phase
S_{iro}	Irreducible saturation of liquid organic phase
S_{irg}	Irreducible saturation of gaseous phase
T	Temperature, K
T_H	Temperature of electric heaters in the Shell ICP process, K
U	Internal energy, J/kg
V_n	Volume of grid block n, m3
X	Primary variable
X_{β}^{κ}	Mass fraction of component κ in phase β
σ	The electrical conductivity, Ω^{-1}-m^{-1}

TABLE OF CONTENTS

LIST OF FIGURES

LIST OF TABLES

Page

CHAPTER I

INTRODUCTION

Oil shale occurs in 27 countries in worldwide, and the rich oil shale which has the commercial interest is believed to be around 2.6 trillion barrels, and 2.0 trillion barrels of them are located in United States (Braun and Burnham 1990; Crawford et al. 2008). The most concentrated oil shales are located in Colorado, Utah, and Wyoming (Biglarbigi et al. 2007). 1.2 trillion barrels of the highly favorable resources are located in Green River Formation of 11 million acres (Biglarbigi et al. 2010). Oil shale can be a promising energy resource in the US, considering the abundant amount of resource, accessibility, and the importance of the stable energy supply.

Oil shale was used as a source of fuel in Europe in 1600s, and Sweden produced oil from oil shale until 1966 (Crawford et al. 2008). As other hydrocarbon fuels are came into wide use, oil production from the oil shale became unfavorable resource, due to the necessity of heating. In order to produce hydrocarbon from oil shale successfully, we need to overcome the economic and technical challenges.

1.1 Motivation for the research

The heating technologies for oil shale development can be categorized into two groups. First is pyrolysis after mining, and the second is in-situ heating of the oil shale, which is called in-situ upgrading. Surface mining and following pyrolysis are only applicable for shallow formation, and the in-situ upgrading is applicable regardless of the formation depth. In this work, we focus on the in-situ upgrading which is suitable for the majority of the oil shale deposits.

There have been several approaches to develop an effective way of the in-situ upgrading. Shell has been seeking a process that could produce oil from Green River Oil Shale for more than 40 years, and has focused on the In-situ Conversion Process (ICP) from 1980 (Fowler and Vinegar 2009). It implements the in-situ upgrading by using vertical electric heaters as shown in Fig. 1. This approach utilizes multiple vertical wells.

ExxonMobil suggested the Electrofrac, which utilizes highly conductive material injected into vertical fractures, and constructs vertical heating plane as provided in Fig. 2. This approach necessitates the horizontal well for fracturing, multiple horizontal wells for the heat injection, and the vertical wells for the hydrocarbon production. Heat is injected in longitudinal direction from the horizontal wells to the vertical fractures.

There present necessity of the multiple vertical wells in the Shell ICP, and the multiple vertical wells and horizontal wells in the ExxonMobil Electrofrac. To reduce capital costs, Thoram and Economides (2011) suggested the in-situ upgrading by steam flowing through the hydraulic fractures in the Multistage Transverse Fractured Horizontal (MTFH) well system. We call this method Steamfrac. They analyzed the formation temperature while circulating the steam from one side to the other side. The configuration of this method is provided in Fig. 3. Hydraulic fracture provides sufficient heating area to the formation.

There have been a few studies on simulation of the in-situ upgrading process. The work of Shen (2009) reproduced the results of Mahogany Field Experiment (MFE) conducted at Shell’s Mahogany property in the Piceance Basin. He simulated the heating and production process following a 30 days of pre-dewatering by using STARS of Computer Modeling Group (CMG). In order to simplify the heat withdrawal resulted by fluid production, he used virtual negative heater for energy removal.

Fan et al. (2010) implemented the in-situ upgrading simulation by using Stanford’s General Purpose Research Simulator (GPRS). They presented the result of sensitivity analyses of heater temperature, pattern of heaters, and spacing of heaters on the energy efficiency by describing Shell’s Mahogany Demonstration Project-South (MDP-S). They used a simplified high-permeability reservoir model without solid phase and pre-existing fracture system.

Hazra et al. (2013) compared the energy efficiency of diverse in-situ upgrading methods by simulating each in-situ upgrading process using STARS of CMG. They showed the energy efficiencies of 170 %, 110 % and 80 % of Exxon's Electrofrac, Shell ICP, and Steamfrac, respectively. In their work, we can infer that the low energy efficiency of Steamfrac case resulted from the fact that they didn't account the flow of steam through the horizontal injection well, and only account the steam injection at the point on the hydraulic fracture.

In this work, we simulate each in-situ upgrading process by using diverse factors affecting productivity and process efficiency, and investigate how to increase them. This will be done by the sensitivity analyses on the temperature of heaters, electrical conductivity of the proppant, and the strategy of stem injection in the case of Shell ICP, ExxonMobil Electrofrac and TAMU Steamfrac, respectively. The energy efficiency and NPV of each process will be compared.

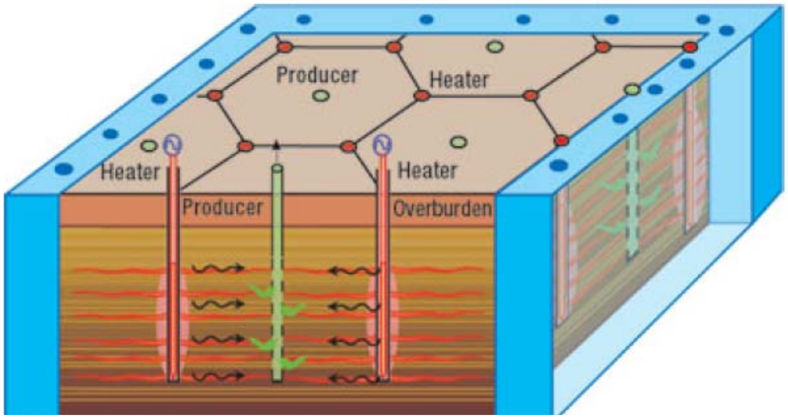

Fig. 1 Configuration of Shell ICP implemented in Green River Formation Adapted from Thoram and Economides (2011)

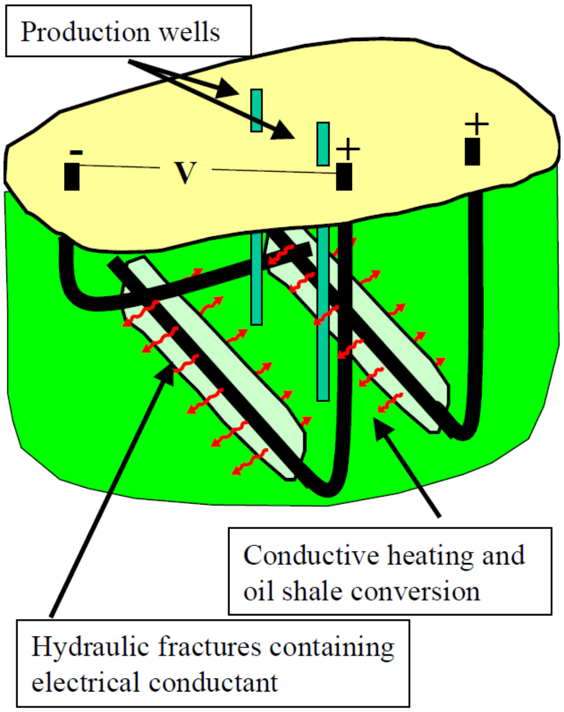

(a) Concept of Electrofrac process

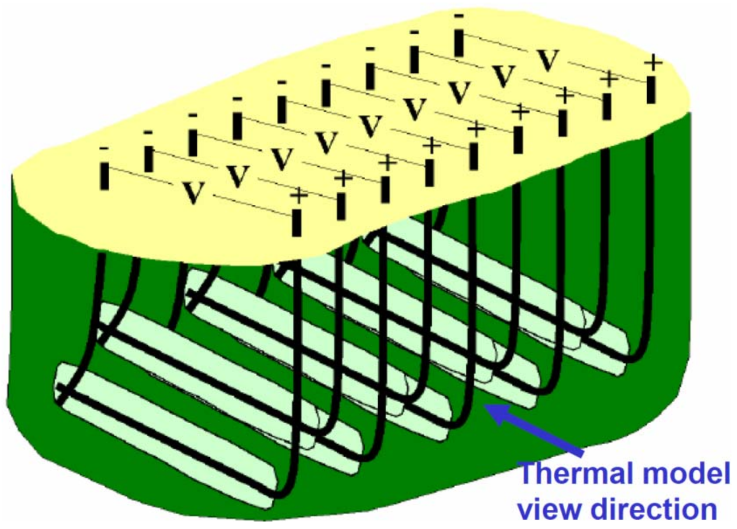

(b) Application of Electrofrac in multiple fracture system

Fig. 2 Configuration of ExxonMobil Electrofrac (Olgaard et al. 2009)

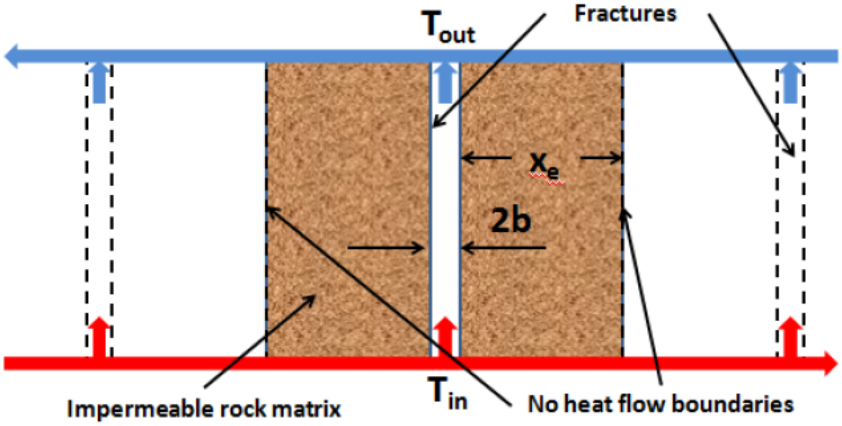

Fig. 3 Configuration of TAMU Steamfrac
(Thoram and Ehlig-Economides 2011)

1.2 Research objectives

The overall goals of this research are to develop fully functional simulator for the oil shale in-situ upgrading, to apply it to the diverse in-situ upgrading processes, and to evaluate the recoverable amount of hydrocarbons of each process. By these series of works, we estimate the energy efficiency and the process economics. The tasks for fulfilling these objectives are listed as below.

1. Database development
    a. Geological structure of the oil shale
    b. Physical properties of the oil shale rock
    c. Kinetic reactions of the in-situ upgrading process
2. Simulator development
    a. Mathematical description of the mass conservation, energy conservation and chemical reactions equations

    b. Interaction between fluids and porous medium
    c. Phases and components thermodynamics
    d. Equation of state
    e. Fully implicit solution
    f. Numerical description of the fractured medium
3. Validation of the simulator
    a. Analysis of the effect of pre-existing fracture network
    b. Sensitivity analyses of the oil shale grade (organic matter content)
    c. Sensitivity analyses of the fracture domain permeability
    d. Sensitivity analyses of the formation thermal conductivity
    e. Development of the realistic model for the oil shale formation by reproducing Shell ICP field production data
4. Application of the simulation cases
    a. Cases of Shell ICP in a pattern by using the several temperatures of the multiple electric heaters
    b. Cases ExxonMobil Electrofrac by using the several electrical conductivities of the proppant
    c. TAMU Steamfrac with huff-and-puff processes by using diverse number of wells, and continuous injection and production method
    d. Comparison of the energy efficiency and NPV among the three processes

CHAPTER II

DATABASE DEVELOPMENT

Before developing a simulator for oil shale in-situ upgrading, it is necessary to build a database in order to thoroughly understand the oil shale characteristics and the accurate description of the in-situ upgrading process and system changes. Composition and structure of the oil shale rock determine success likelihood of oil shale development. Oil shale rocks in the in-situ upgrading process are distinguished from other kind of shale reservoir rocks by the changing organic matter contents from solid kerogen to liquid and gaseous hydrocarbon phases plus a solid char phase. In this chapter, we cover the geological structure, physical properties of the oil shale, kinetic reactions of the kerogen, and the chemical properties of the products from kerogen decomposition.

2.1 Geological structure of the oil shale

The organic rich sedimentary rock, oil shale is composed of kerogen, fine mineral grains and void spaces of pores and fractures. The mineral content of some oil shales consists of carbonate, and in other oil shales consists of silicates (Dyni 2006). Kerogen, the organic matter, is a complex mixture which has large carbon number that can produces hydrocarbons when heated to a sufficiently high temperature. The grade of oil shale is defined by the oil yield by the retorting from the sample oil shale. The oil shale grade ranges from 10 to 60 or more gal/ton in the US (Biglarbigi et al. 2007).

The oil shale deposits are in a variety of geological environments, and are different in the physical and chemical properties. The Green River Formation, the largest oil shale formation in the US, has been researched for many years. The formation contains sodium carbonate minerals mixed with kerogen which yields at least 16.6 gal/ton (Dyni 2006). Natural fractures can occur in the calcareous shales as well as in sandstones.

In the work of Shell ICP, they found that the pre-existing fracture system helps the heating and fluid flow in some parts of Green River Formation (Fowler and Vinegar 2009). In the work of Lorenz (2003), he showed that the large parts of Green River have been extensively fractured, but the permeability of the fracture domain is not specified.

2.2 Physical properties of the oil shale rock

The content of the kerogen, which can be also called the organic matter content, affects the properties of oil shale rock such as bulk density, thermal conductivity, specific heat and absolute permeability. Organic matter content as a volumetric percent has the relationship with bulk rock density as shown in Eq. (2.1) (Eseme et al. 2007).

$$O_c = 164.8 - 60.6\rho_m \tag{2.1}$$

Here, the organic matter content, O_c is in %, and ρ_m is a bulk density in g/cm^3.

The thermophysical properties have the relationship between oil yield of oil shale and temperature. Thermal conductivity of oil shale bulk rock is computed by using Eq. (2.2) as follows (Lee et al. 2007).

$$K = 4.921/M + 0.06 + 0.003\left(T - 273.15\right) \tag{2.2}$$

Here, K is the thermal conductivity in W/m-K, M is the oil yield in gal/ton, and T is the temperature in Kelvin.

Specific heat of oil shale bulk rock is related to the oil yield and temperature as shown in Eq. (2.3) (Prats and O'Brien 1975).

$$C_p = \frac{1}{4{,}186.8}\left[0.172 + 10^{-3}\left(0.067 + 0.00162M\right)\left(\frac{T}{1.8}\right)\right] \tag{2.3}$$

Here, C_p is the specific heat of oil shale bulk rock in J/kg-K, M is the oil yield in gal/ton, and T is the temperature in Kelvin.

Oil yield and organic matter contents have the relationship in following Eq. (2.5) (Lee et al. 2007), and oil yield can be described by using O_c as provided in Table 2.

$$O_c = 164.9M/\left(M + 111.8\right) \tag{2.5}$$

Here, O_c is in volumetric %, and M is in gal/ton.

As well as thermophysical properties, the absolute permeability is related to the oil yield of oil shale as provided in Table 1. We summarize these properties of oil shale rock in Table 2.

Table 1 Oil yield and absolute permeability of the oil shale

Oil yield (gal/ton)	Absolute permeability (md) - horizontal and vertical directions	
1.0	0.56	0.36
6.5	0.65	0.21
13.5	8.02	4.53

Table 2 Formulae for the oil shale rock properties

Bulk properties	Formulae, f(O_c (%), M (gal/ton), T (K))
Density (g/cm^3)	$\rho_m = \frac{1}{60.6}(164.8 - O_c)$
Oil yield (gal/ton)	$M = 111.8 O_c / (164.9 - O_c)$
Thermal conductivity (W/m-K)	$K = 4.921/M + 0.06 + 0.003\,(T - 273.15)$
Specific heat (J/kg-K)	$C_p = \frac{1}{4186.8}\left[0.172 + 10^{-3}(0.067 + 0.00162M)\left(\frac{T}{1.8}\right)\right]$

2.3 Kinetic reactions of the in-situ upgrading process

The chemical formulae of the kerogen varies with environment, and one of them is defined as $CH_{1.5}N_{0.026}O_{0.02}$ (Braun and Burnham 1990). In-situ upgrading of the kerogen is very complex, and consists of successive reactions. There are numerous experimental studies on the retorting of the oil shale to find out constituents and the decomposition procedure. However, a majority of them have been focusing on the surface retorting rather than in-situ upgrading.

We investigated the experimental works conducted in the similar environment to real reservoir. The work done by Shell in Green River Formation showed that the in-situ upgrading process consists of 6 kinetic reactions as provided in Table 3 (Wellington et al. 2005). The reactions are kerogen decomposition, cracking of heavy oil in gaseous phase and liquid organic phase, cracking of light oil in gaseous phase and liquid organic phase, and coking of hydrocarbon gas. The components contained in the reactions are kerogen, water, heavy oil, light oil, hydrocarbon gas, hydrogen, carbon dioxide, prechar and char. The kerogen, prechar and char present in solid phase, and the others present in fluid phases.

The reactions shown in the Table 3 cover the pressure range of 1 bar to 20 bars, and they are applicable to the in-situ upgrading. The kinetic parameters of the reactions are provided in Table 4, and we can compute the starting temperature for each reaction from frequency factor and activation energy. Kerogen decomposition, cracking of oils, and coking of hydrocarbon gas processes start from 554 °F, 626 °F, and 680 °F, respectively.

The hydrocarbons in the kinetic reactions are indicated as heavy oil, light oil and hydrocarbon gas. In order to compute their thermophysical and transport properties, we should know their chemical formulae. In the work of Wellington et al. (2005), hydrocarbons produced from the formation contains typically include alkanes as the one of the major components. Thus, we consider docosane ($C_{22}H_{46}$), undecane ($C_{11}H_{24}$), and ethane (C_2H_6) for heavy oil, light oil, and hydrocarbon gas, respectively, by considering the molar weight provided in the work of Wellington et al(2005). In their work, heavy oil, light oil, and hydrocarbon gas have the molar weights of 317.96, 154.11, and 26.895 g/mole, respectively, while $C_{22}H_{46}$, $C_{11}H_{24}$, and C_2H_6 have the molar weights of 310.61, 156.31, and 37.07, respectively. The molar weights, critical properties and acentric factor of the fluid components included in the kinetic reactions are provided in Table 5 (Yaws, 2003). These will be used in the computation of fluid properties which we will cover the details in CHAPTER III.

Table 3 Kinetic reactions of the in-situ upgrading process

Reactions	Chemical formula
Kerogen decomposition	(1) KER → $0.0269H_2O$ + 0.009588heavy oil + 0.01780 light oil + 0.04475 HC gas + $0.01049H_2$ + $0.00541CO_2$ + 0.5827 PRCH
Cracking of heavy oil	(2) Heavy oil(G) → 1.8530light oil + 0.045HC gas+ 2.4515 PRCH (3) Heavy oil(O) →0.2063light oil + 2.365HC gas + 17.497 PRCH
Cracking of light oil	(4) Light oil(G) → 5.730HC gas (5) Light oil(O) → 0.5730HC gas+ 10.904PRCH
Coking of hydrocarbon gas	(6) HC gas(G) → $2.8H_2$ + 1.6706CHAR

Table 4 Parameters of the kinetic reactions

Reactions	Frequency factor (1/day)	Activation energy (KJ/mole)	Starting temperature (°F, °C)
Kerogen decomposition	(1) 3.74×10^{12}	161.6	554, 290
Cracking of heavy oil	(2) 6.25×10^{16}	206.034	626, 330
	(3) 2.647×10^{20}	206.034	626, 330
Cracking of light oil	(4) 9.85×10^{16}	219.328	626, 330
	(5) 3.82×10^{20}	219.328	626, 330
Coking of hydrocarbon gas	(6) 7.66×10^{20}	311.432	680, 360

Table 5 Molar weights, critical properties and acentric properties of the fluid components

Properties	$C_{22}H_{46}$	$C_{11}H_{22}$	C_2H_6	H_2	CO_2	N_2	H_2O
Molar weight (g/mol), MW	310.61	156.31	37.07	2.016	44.01	28.014	18.016
Critical pressure (psi), P_c	181	285	707	188	1,070	493	3,208
Critical temperature (°F), T_c	964.71	690.17	89.91	-398.82	87.75	-232.51	705.47
Critical volume (cm^3/mol), V_c	1,267.5	657.0	145.5	65.0	94.07	90.1	57.11
Critical density (g/cm^3), ρ_c	0.245	0.238	0.203	0.031	0.468	0.311	0.318
Critical compressibility, Z_c	0.174	0.243	0.279	0.305	0.274	0.289	0.229
Acentric factor, ω	0.751	0.536	0.099	-0.216	0.225	0.037	0.344

CHAPTER III

SIMULATOR DEVELOPMENT

We developed a simulator for the in-situ upgrading of the oil shale by accounting the mass transport and the heat flow in porous medium and phase equilibrium and transition thermodynamics. We modeled them by expanding TAMU FTSim which can be used as the basis to construct a reservoir simulator for complex problems. As we stated in the previous section, multiphase-multicomponent products occur from a series of chemical reactions in the in-situ upgrading process. The chemical reactions and the properties of the resulting products are very sensitive to the pressure and temperature. We implement the in-situ upgrading process in the simulator by coupling the chemical reactions with mass transport, heat flow and phase thermodynamics, while accurately accounting the properties of the phases and porous medium.

3.1 Mathematical description

We consider mass conservation equation, energy conservation equation and chemical reaction equations. These equations describe the physics and chemistry of the system.

3.1.1 Mass conservation equation

Mass of each component is conserved in the system. Mass conservation equation for each element is considered in the integral finite difference method as provided in Eq. (3.1) (Pruess et al. 1999).

$$\frac{d}{dt}\int_{V_n} M^{\kappa} dV_n = \int_{\Gamma_n} \mathbf{F}^{\kappa} \cdot \vec{\mathbf{n}} d\widetilde{A} + \int_{V_n} q^{\kappa} dV_n \tag{3.1}$$

Here, V_n is a volume of element *n*, and M^{κ}, $\mathbf{F}^{\kappa}$ and q^{κ} are the mass accumulation, flux vector, and source/sink terms of the component κ, respectively. Accumulation, flux terms are computed by Eq. (3.2) and Eq. (3.3).

$$M^{\kappa} = \sum_{\beta \equiv A,O,G,S} \phi S_{\beta} \rho_{\beta} X_{\beta}^{\kappa} \tag{3.2}$$

$$\mathbf{F}^{\kappa} = \sum_{\beta \equiv A,O,G} \mathbf{F}_{\beta}^{\kappa} \tag{3.3}$$

Here, ϕ is the medium porosity, S_{β} and ρ_{β} are the saturation and the density of phase β, respectively, and X_{β}^{κ} is the mass fraction of the component κ in the phase β. Subscript *A*, *O*, *G* and *S* indicate the aqueous phase, gaseous phase, liquid organic phase, and solid phase, respectively. $\mathbf{F}_{\beta}^{\kappa}$, the flux term of component κ in the phase β, is computed by Darcy's law.

In the mass conservation equation, we consider the chemical reaction as the accumulations for reactants and products. The abrupt change of mass accumulation makes mass conservation equation highly nonlinear, and this leads to the necessity of small grid size and short time interval in the computations.

3.1.2 Energy conservation equation

In the energy conservation equation, we consider heat flow occurred by conduction and convection. Energy conservation equation is described by the integral finite difference method as provided in Eq. (3.4) (Pruess et al. 1999).

$$\frac{d}{dt}\int_{V_n} M^{\theta} dV_n = \int_{\Gamma_n} \mathbf{F}^{\theta} \cdot \vec{\mathbf{n}} d\widetilde{A} + \int_{V_n} q^{\theta} dV_n \tag{3.4}$$

Here, M^{θ} is the heat accumulation term of the component κ, $\mathbf{F}^{\theta}$ is the heat flux vector, and q^{θ} is the heat source/sink terms. Heat accumulation and flux terms are computed by Eq. (3.5) and Eq. (3.6).

$$M^{\theta} = (1-\phi)\rho_R C_R T + \sum_{\beta \equiv A,O,G,S} \phi S_B \rho_{\beta} U_{\beta} \tag{3.5}$$

$$\mathbf{F}^{\theta} = -\lambda \nabla T + \sum_{\beta \equiv A,O,G} h_{\beta} \mathbf{F}_{\beta}^{\theta} \tag{3.6}$$

Here, ρ_R and C_R are the density and the heat capacity of the rock, respectively. ∇T is the temperature difference, and U_β is the internal energy of the phase β. λ is the composite thermal conductivity of phases and medium, and h_β is the specific enthalpy of the phase β. In the gaseous phase, we include the departure function of the specific enthalpy to account for the deviation from ideal gas behavior. From the Peng-Robinson equation, we have the enthalpy departure function for real gas as shown in Eq. (3.7) (Kyle 1999).

$$\frac{h_{ideal} - h_{real}}{RT_c} = 2.078(1+\kappa)\left[1+\kappa\left(1-T_r^{1/2}\right)\right]\ln\left[\frac{Z+\left(1+\sqrt{2}\right)B}{Z+\left(1-\sqrt{2}\right)B}\right] - T_r(Z-1) \tag{3.7}$$

Here, T_c is the critical temperature, T_r is the reduced temperature, and Z is the gas compressibility factor. The parameters A, B and κ are computed from Eq. (3.8) – (3.10) as follows.

$$A = 0.45724\frac{P_r}{T_r}\left[1+\kappa\left(1-T_r^{1/2}\right)\right]^2 \tag{3.8}$$

$$B = 0.07780\frac{P_r}{T_r} \tag{3.9}$$

$$\kappa = 0.37464 + 1.54226\,\omega - 0.26992\,\omega^2 \tag{3.10}$$

Here, P_r is the reduced pressure, and ω is the acentric factor.

3.1.3 Chemical reaction equations

To model the chemical reactions, we compute the reaction rate of the each fluid and solid component based on the first order rate law as shown in Eq. (3.11), because whole reactions of the in-situ upgrading consist of first order reactions.

$$r_k = K_k C_\kappa \tag{3.11}$$

Here, r_k and K_k are the reaction rate and the reaction rate constant of the reaction *k*, respectively, and C_κ is the concentration of the component κ. K_k and C_κ are defined by Eq. (3.12) and Eq. (3.13).

$$K_k = A_k \exp\left(-\frac{E_k}{RT}\right) \tag{3.12}$$

$$C_\kappa = \rho_\beta S_\beta \phi X_\beta^\kappa \tag{3.13}$$

Here, A_k and E_k are the frequency factor and activation energy of reaction *k*, respectively, and *R* is the gas constant.

3.2 Interaction between fluids and porous medium

The interaction between porous medium and fluids significantly affect the fluid flow in the multiphase-multicomponent system. The characteristics of the porous medium such as wettability and irreducible saturations of phases affect the interaction between the fluids and porous medium, and they define the relative permeability and the capillary pressure. Also, the concept of the porosity and permeability is very important in the systems with solid phase as well as fluid phases.

3.2.1 Concept of porosity and permeability

In the oil shale formation, solid kerogen presents in the pores initially. Kerogen decomposes into fluid products and solid products by absorbing heat in the in-situ upgrading process. Decomposition of the kerogen and occurrence of the prechar and char as reaction products affect the pore space for fluid to flow. There are two methods to describe the porosity and permeability for the medium containing solid phase. First is Original Porous Medium (OPM) model, and the second is Evolving Porous Medium (EPM) model (Moridis 2008). In our simulation, we use OPM model for defining medium porosity and absolute permeability.

In the OPM model, we treat solid as one of the phases in the pores, and we have the relationship of the phase saturations as provided in Eq. (3.14).

$$S_A + S_O + S_G + S_S = 1 \tag{3.14}$$

Here, S_A, S_O, S_G and S_S indicate the saturations of the aqueous phase, liquid organic phase, gaseous phase and the solid phase, respectively. We treat porosity as not affected by the amount of the solid phase, and absolute permeability as not changing due to the evolution or disappearance of the solid phase. The relative permeability of each phase is defined by its saturation as provided in Eq. (3.15) – Eq. (3.17), while capillary pressure is defined by the scaled saturation as provided in Eq. (3.18).

$$k_{rA} = k_{rA}(S_A) \tag{3.15}$$

$$k_{rO} = k_{rO}(S_O) \tag{3.16}$$

$$k_{rG} = k_{rG}(S_G) \tag{3.17}$$

$$P_{cap} = P_{cap}(S_A*, S_O*, S_G*) \tag{3.18}$$

Here, we define the scaled saturations by using Eq. (3.19) – Eq. (3.21) as follows.

$$S_A* = \frac{S_A}{S_A + S_O + S_G} \tag{3.19}$$

$$S_O* = \frac{S_O}{S_A + S_O + S_G} \tag{3.20}$$

$$S_G* = \frac{S_G}{S_A + S_O + S_G} \tag{3.21}$$

3.2.2 Relative permeability functions

We facilitate a number of functions for the computation of relative permeability in our simulator. The functions have different formulae, and require different input data for the computation. The sets of functions are categorized into two-phase relative permeability functions and three-phase relative permeability functions.

(1) Two-phase relative permeability functions

In our simulator, two options are available for the two-phase relative permeability functions of matrix block. They are Van Genuchten-Mualem and Corey model.

1) Van Genuchten-Mualem model

The relative permeability functions for the wetting phase and non-wetting phase are computed from Eq. (3.22) and Eq. (3.23), which are the modified version of Van Genuchten model (Moridis 2008; Mualem 1976; Parker et al. 1987; Van Genuchten 1980).

$$k_{rw} = \sqrt{S^*}\left\{1-\left[1-\left(S^*\right)^{1/\lambda}\right]^{\lambda}\right\}^2 \tag{3.22}$$

$$k_{rnw} = \sqrt{1-S^*}\left\{\left[1-\left(S^*\right)^{1/\lambda}\right]^{\lambda}\right\}^2 \tag{3.23}$$

Here, k_{rw} and k_{rnw} are the relative permeabilities of the wetting phase and non-wetting phase, respectively, and λ is the parameter defined based on the porous medium. S^* is computed by using Eq. (3.24) as follows.

$$S^* = \frac{S_w - S_{irw}}{S_{mxw} - S_{irw}} \tag{3.24}$$

Here, S_w, S_{irw}, and S_{mxw} are the wetting phase saturation, irreducible saturation of the wetting phase, and the maximum saturation of the wetting phase, respectively. The relative permeabilities satisfy the restrictions in Eq. (3.25).

$$0 \le k_{rw},\, k_{rnw} \le 1 \tag{3.25}$$

2) Corey model

The relative permeability functions for the wetting phase and non-wetting phase are computed from Eq. (3.26) and Eq. (3.27) (Corey 1954; Moridis 2008).

$$k_{rw} = \hat{S}^4 \tag{3.26}$$

$$k_{rnw} = \left(1-\hat{S}\right)^2\left(1-\hat{S}^2\right) \tag{3.27}$$

Here, $\hat{S}$ is defined as Eq. (3.28).

$$\hat{S} = \frac{S_w - S_{irw}}{1 - S_{irw} - S_{irnw}} \tag{3.28}$$

Here, S_w, S_{irw}, S_{irnw} are the wetting phase saturation, irreducible saturation of the wetting phase, and the irreducible saturation of the non-wetting phase, respectively.

(2) Three-phase relative permeability functions

We compute the three-phase relative permeability by the model provided by Parker et al (1987).The relative permeabilities of aqueous phase, liquid organic phase and gaseous phase are defined by Eq. (3.29) – Eq. (3.31).

$$k_{rA} = \sqrt{\overline{S}_A}\left\{1-\left[1-\left(\overline{S}_A\right)^{1/m}\right]^m\right\}^2 \tag{3.29}$$

$$k_{rO} = \sqrt{\overline{S}_t - \overline{S}_A}\left\{\left[1-\left(\overline{S}_A\right)^{1/m}\right]^m - \left[1-\left(\overline{S}_t\right)^{1/m}\right]^m\right\}^2 \tag{3.30}$$

$$k_{rG} = \sqrt{\overline{S}_G}\left\{\left[1-\left(\overline{S}_t\right)^{1/m}\right]^m\right\}^2 \tag{3.31}$$

Here, m is the parameter defined based on the porous medium in Parker's model. $\overline{S}_A$, $\overline{S}_t$ and $\overline{S}_G$ are defined as Eq. (3.32) – Eq. (3.34).

$$\overline{S}_A = \frac{S_A - S_m}{1 - S_m} \tag{3.32}$$

$$\overline{S}_t = \frac{S_A + S_o - S_m}{1 - S_m} \tag{3.33}$$

$$\overline{S}_G = \frac{S_G}{1 - S_m} \tag{3.34}$$

Here, S_m is the apparent irreducible saturation of the wetting phase. S_A, S_O, and S_G are the saturations of aqueous, liquid organic, and gaseous phases, respectively.

(3) Relative permeability functions for the fracture and wellbore

In the computation of the relative permeability functions for the fracture and wellbore, we use the linear relationship between the phase saturation and the relative permeability. These are computed by using Eq. (3.35) – Eq. (3.37), which are the modified model of Stone (Moridis 2008; Stone 1970).

$$k_{rA} = \frac{S_A - S_{irA}}{1 - S_{irA}} \tag{3.35}$$

$$k_{rO} = \frac{S_O - S_{irO}}{1 - S_{irA}} \tag{3.36}$$

$$k_{rG} = \frac{S_G - S_{irG}}{1 - S_{irA}} \tag{3.37}$$

Here, S_{irA} is the irreducible saturation of the aqueous phase, and S_{irO} and S_{irG} are the irreducible saturations of the liquid organic phase and gaseous phase, respectively. S_A, S_O, and S_G are the saturations of the aqueous, liquid organic, and gaseous phases, respectively.

3.2.3 Capillary pressure functions

We facilitate a number of functions for the computation of capillary pressure in our simulator. The functions have different formulae, and require different input data for the computation. The sets of functions are categorized into two-phase capillary pressure functions and three-phase capillary pressure functions.

(1) Two-phase capillary pressure functions

In our simulator, two options are available for the two-phase capillary pressure functions of matrix. They are Van Genuchten and Brooks-Corey model. We consider zero capillary pressure in the fracture and wellbore.

1) Van Genuchten model

Capillary pressure between the wetting phase and non-wetting phase are computed by Eq. (3.38) provided by Van Genuchten (1980).

$$P_c = -\frac{\rho_w g}{\alpha}\left[\left(S^*\right)^{-1/\lambda} - 1\right]^{1-\lambda} \tag{3.38}$$

Here, λ and S^* are defined as the same manner as the relative permeability computation of Van Genuchten-Mualem model. ρ_w is the density of the wetting phase, and α is the parameter defined based on the porous medium, and g is the acceleration of gravity.

2) Brooks-Corey model

In this model, capillary pressure between the wetting phase and non-wetting phase is computed by Eq. (3.39) provided by Brooks and Corey (1964).

$$P_c = -P_e\left(S_w^{\ *}\right)^{-\frac{1}{\lambda}} \tag{3.39}$$

Here, P_e is the capillary pressure at the maximum wetting phase saturation, and λ is the parameter defined based on the porous medium. $S_w^{\ *}$ is defined by Eq. (3.40).

$$S_w^{\ *} = \frac{S_w - S_{irw}}{1 - S_{irw} - S_{irnw}} \tag{3.40}$$

Here, S_w , S_{irw}, and S_{irnw} are the wetting phase saturation, irreducible saturation of the wetting phase, and irreducible saturation of the non-wetting phase, respectively.

(2) Three-phase capillary pressure functions

We compute the three-phase capillary pressure by the model provided by Parker et al (1987). The functions are defined as Eq. (3.41) – Eq. (3.43).

$$P_{cAO} = -\frac{\rho_A g}{\alpha_{AO}}\left(\overline{S}_A^{\,-m} - 1\right)^{\frac{1}{n}} \tag{3.41}$$

$$P_{cOG} = -\frac{\rho_O g}{\alpha_{OG}}\left(\overline{S}_t^{\,-m} - 1\right)^{\frac{1}{n}} \tag{3.42}$$

$$P_{cAG} = P_{cAO} + P_{cOG} \tag{3.43}$$

Here, P_{cAO}, P_{cOG}, and P_{cAG} are the capillary pressures between the aqueous phase and liquid organic phase, liquid organic phase and gaseous phase, and the aqueous phase and gaseous phase, respectively. $\overline{S}_A$, $\overline{S}_t$ and $\overline{S}_G$ are defined as the same way as the relative permeability computation of Parker's model. *m* and *n* are the parameters defined based on the porous medium.

3.3 Phases and components

Here, we cover the phases and components in the system and the thermophysical states. The thermophysical states and transition between them are defined by the phase equilibrium and the phase transition thermodynamics.

3.3.1 Multiphase-multicomponent system

Our simulator describes the system of 4 phases and 10 components, which are resulted from the chemical reactions of the in-situ upgrading process. There exist 7 components of fluid-species and 3 components of solid-species. Phases, which are composed of the multiple components, indicate the physical states of the materials. Components of the fluid-species exist in the fluid phases, while components of solid-species exist in the solid phase. The phases and the components of our system are provided in Table 6. Here, we consider the heavy oil, light oil, and hydrocarbon gas as the integrated components, with the numbers indicating the carbon numbers.

In the aqueous phase, heavy oil (IC_{22}), light oil (IC_{11}), hydrocarbon gas (IC_2), hydrogen (H_2), carbon dioxide(CO_2) and nitrogen (N_2) are dissolved in liquid water. In the liquid organic phase, hydrocarbon gas, water, hydrogen, carbon dioxide and nitrogen dissolved in the liquid mixture of heavy oil and light oil. In the gaseous phase, hydrocarbon gas, hydrogen, carbon dioxide and nitrogen present as free gas, and heavy oil, light oil and water present as vapor. In the solid phase, solid-species components, kerogen presents as solid hydrocarbon, and prechar and char present as solid carbon.

Table 6 Phases and components resulted from kerogen pyrolysis

Components, κ	Phases, β			
	Fluid phases			
	(1) Aqueous phase	(2) Liquid organic phase	(3) Gaseous	(4) Solid phase
1) Heavy oil (IC_{22})	Dissolved oil	Liquid oil	Oil vapor	-
2) Light oil (IC_{11})	Dissolved oil	Liquid oil	Oil vapor	-
3) HC gas (IC_2)	Dissolved gas	Dissolved gas	Free gas	-
4) Water (H_2O)	Liquid water	Dissolved water	Water vapor	-
5) Hydrogen (H_2)	Dissolved gas	Dissolved gas	Free gas	-
6) Carbon dioxide (CO_2)	Dissolved gas	Dissolved gas	Free gas	-
7) Nitrogen (N_2)	Dissolved gas	Dissolved gas	Free gas	-
8) Kerogen (KER)	-	-	-	Solid HC
9) Prechar (PRCH)	-	-	-	Solid carbon
10) Char (CHAR)	-	-	-	Solid carbon

3.3.2 Phase equilibrium and transition

Material in the reservoir can present in the states of the single phase or multiphase equilibrium. We call material rather than fluid, because there exists solid phase as well as the fluid phases in our system. The thermodynamic state of the material and the concentration of the components in each phase are determined by the equation of state, which includes the computation of the phase properties as the function of primary variables.

The phases are in equilibrium state, if multiple phases exist in the same space simultaneously. The phase states can change from one to another, and we call it phase transition. Phase transition is resulted from the mass transfer of the component by fluid flow, or the change of temperature and pressure. Phase transition includes the phase evolution and phase disappearance. Criteria of the phase evolution and phase disappearance are shown in Table 7.

The aqueous phase and liquid organic phase evolve, if the partial pressure of the liquid component is bigger than its vapor pressure. The vapor pressure of the aqueous phase as the function of the temperature is determined from the ASME steam table (Meyer et al. 1993). The vapor pressure of the oil component is estimated by using the method of Riedel (1954). The gaseous phase evolves, when one of the criteria is satisfied, and the criteria are that the dissolved gas mole fraction in the aqueous phase or liquid organic phase is bigger than the maximum dissolved mole fraction of them, and that the partial pressure of water component or oil component is bigger than its vapor pressure. The maximum mole fraction of the gas components in the aqueous phase is defined from the Henry's constant as shown in Eq. (3.44).

$$Y_A^g = P_g / H \tag{3.44}$$

Here, Y_A^g is the mole fraction of the gas component in the aqueous phase, P_g is the partial pressure of the gas component, and H is the Henry's constant as the function of the component and temperature. The mole fraction of the gas components in the liquid organic phase is computed by multiplying proper numbers to the mole fraction in the aqueous phase, by comparing the magnitude of the gas solubility in the aqueous phase and liquid organic phase (Ghosh et al. 2003; Logvinyuk et al. 1970; Riazi and Roomi 2007). The disappearance of phases is determined by obtaining negative phase saturation.

There present two domains in our system, matrix and fracture. The matrix domain describes the reservoir rock containing grains and pores, and the fracture domain describes the fluid-filled space of the natural fractures and hydraulic fractures. In the matrix, there exists solid phase with whole kerogen initially. Decomposition of the kerogen produces prechar and char, and the solid is immobile, so the solid phase always exists in the matrix. In the fracture, there exist only fluid phases. In our system, the fracture contains single phase aqueous initially, and the liquid organic and gaseous phases evolve by fluid flow from the matrix while in-situ upgrading proceeds.

The possible phase states of our system are listed in Table 8. We describe 15 states for matrix, fracture and heater block. In the matrix, we have two-phase, three-phase and four-phase equilibrium states. In the fracture, we have single-phase state, and two-phase and three-phase equilibrium states.

Table 7 Phase evolution and disappearance criteria

Phases	Phase evolution criteria	Phase disappearance criteria
Aqueous	$P_{water} > P_{vapor\_water}$	$S_{aqu} < 0$
Liquid organic	$P_{oil} > P_{vapor\_oil}$	$S_{liq\_org} < 0$
Gaseous	$Y_A^g > \max\ Y_A^g$, $Y_O^g > \max\ Y_O^g$ $P_{water} < P_{vapor\_water}$, $P_{oil} < P_{vapor\_oil}$	$S_{gas} < 0$
Solid	-	-

Table 8 Thermophysical states in the system

Domain	States	Existing phases
Matrix	1) Two-phase AquSol	Aqueous + Solid
	2) Two-phase OrgSol	Organic +Solid
	3) Two-phase GasSol	Gaseous + Solid
	4) Three-phase AqGSol	Aqueous + Gaseous + Solid
	5) Three-phase AqOSol	Aqueous + Organic + Solid
	6) Three-phase GsOSol	Gaseous + Organic + Solid
	7) Four-phase AOGS	Aqueous + Organic + Gaseous + Solid
Fracture	8) Single-phase Aqueous	Aqueous
	9) Single-phase Organic	Organic
	10) Single-phase Gaseous	Gaseous
	11) Two-phase AqG	Aqueous + Gaseous
	12) Two-phase AqO	Aqueous + Organic
	13) Two-phase GsO	Gaseous + Organic
	14) Three-phase AOG	Aqueous + Organic + Gaseous
Electric heater	15) Single-phase Solid	Solid

3.4 Equation of state

Here, we cover the equation of state in the system related to the selection of primary variables of the thermophysical states and the computation of the phase properties.

3.4.1 Primary variables

Primary variables are necessary and sufficient to determine the system (Pruess et al. 1999). They are independent to each other, and cannot be computed from any other parameters, and only can be obtained by the primary solution of the matrix equation. They consist of pressure, temperature, mass fractions or mole fractions of the components and saturations of the phases. The choice of the primary variables has a huge effect on computation speed, so they should be selected properly.

The primary variables in the states of our system are listed in Table 9. PX and TX indicate pressure and temperature, respectively, and X and Y indicate the mass fraction and mole fraction, respectively. Since we consider the material of 10 components, we have 11 equations to solve, including heat equation for each grid block. In the fracture, there only exist fluid components, so we use three dummy variables such as X_kA, X_pcA and X_cA, which are the mass fractions of solid components in the aqueous phase, and they are automatically set to zero. We assign single-phase solid state for the electric heater grid block, and we compute only pressure and temperature changes by using dummy variables except for PX and TX.

We can compute the mass fraction, mole fraction and saturation, which are not included in the primary variable set by using the constraints equations as provided in Eq. (3.45) – Eq. (3.47).

$$\sum_{\kappa} X_{\beta}^{\kappa} = 1, \quad \beta = A, O, S \tag{3.45}$$

$$\sum_{\kappa} Y_{\beta}^{\kappa} = 1, \quad \beta = G \tag{3.46}$$

$$\sum_{\beta} S_{\beta} = 1 \tag{3.47}$$

Table 9 Primary variables of the thermophysical states

States	Primary variables
1) Two-phase AquSol	PX, X_H$_2$A, X_CO$_2$A, X_IC$_{22}$A, X_IC$_{11}$A, X_IC$_2$A , X_N$_2$A, X_kS, X_pcS, S_aqu, TX
2) Two-phase OrgSol	PX, X_H$_2$O, X_CO$_2$O, X_IC$_{22}$O, X_IC$_{11}$O, X_wO, X_N$_2$O, X_kS, X_pcS, S_org, TX
3) Two-phase GasSol	PX, Y_H$_2$G, Y_CO$_2$G, Y_IC$_{22}$G, Y_IC$_{11}$G, Y_IC$_2$G, Y_N$_2$G, X_kS, X_pcS, S_gas, TX
4) Three-phase AqGSol	PX, Y_H$_2$G, Y_CO$_2$G, Y_IC$_{22}$G, Y_IC$_{11}$G, S_gas, Y_N$_2$G, X_Ks, X_pcS, S_aqu, TX
5) Three-phase AqOSol	PX, X_H$_2$A, X_CO$_2$A, S_org, X_IC$_{11}$O, X_IC$_2$A , X_N$_2$A, X_kS, X_pcS, S_aqu, TX
6) Three-phase GsOSol	PX, Y_H$_2$G, Y_CO$_2$G, S_org, X_IC$_{11}$O, Y_IC$_2$G, Y_N$_2$G, X_kS, X_pcS, S_gas, TX
7) Four-phase AOGS	PX, Y_H$_2$G, Y_CO$_2$G, S_org, X_IC$_{11}$O, S_gas, Y_N$_2$G, X_Ks, X_pcS, S_aqu, TX
8) Single-phase Aqu	PX, X_H$_2$A, X_CO$_2$A, X_IC$_{22}$A, X_IC$_{11}$A, X_IC$_2$A , X_N$_2$A, X_kA, X_pcA, X_cA, TX
9) Single-phase Org	PX, X_H$_2$O, X_CO$_2$O, X_IC$_{22}$O, X_IC$_{11}$O, X_wO, X_N$_2$O, X_kO, X_pcO, X_cO, TX
10) Single-phase Gas	PX, Y_H$_2$G, Y_CO$_2$G, Y_IC$_{22}$G, Y_IC$_{11}$G, Y_IC$_2$G, Y_N$_2$G, Y_kG, Y_pcG, Y_cG, TX
11) Two-phase AqG	PX, Y_H$_2$G, Y_CO$_2$G, Y_IC$_{22}$G, Y_IC$_{11}$G, S_gas, Y_N$_2$G, X_kA, X_pcA, X_cA, TX
12) Two-phase AqO	PX, X_H$_2$A, X_CO$_2$A, S_org, X_IC$_{11}$O, X_IC$_2$A , X_N$_2$A, X_kA, X_pcA, X_cA, TX
13) Two-phase GsO	PX, Y_H$_2$G, Y_CO$_2$G, S_org, X_IC$_{11}$O, Y_IC$_2$G, Y_N$_2$G, X_kO, X_pcO, X_cO, TX
14) Three-phase AOG	PX, Y_H$_2$G, Y_CO$_2$G, S_org, X_IC$_{11}$O, S_gas, Y_N$_2$G, X_kA, X_pcA, X_cA, TX
15) Single-phase Solid	PX, X_H$_2$ S, X_CO$_2$ S, X_IC$_{22}$ S, X_IC$_{11}$ S, X_w S , X_N$_2$ S, X_k S, X_pc S, X_ IC$_2$S, TX

3.4.2 Properties of the fluid phases

Estimation of the fluid properties is essential to the multiphase-multicomponent simulator development. The fluid properties are affected by the properties and the fractions of the individual components as well as pressure and temperature, because each fluid phase presents in the form of a mixture of components. Aqueous phase consists of water component, dissolved oil and gas components. Liquid organic phase consists of the mixture of heavy oil, light oil, and dissolved water and gas components. Gaseous phase consists of the free gas of the gas components and vapors of the oil and water components.

The methods of the properties computation are provided in the Table 10 for each phase. For the aqueous phase, we use the equations of ASME steam table (Meyer et al. 1993). The density, heat capacity and viscosity are computed as the functions of dimensionless variables such as reduced pressure, reduced temperature and reduced critical volume.

In the computation of the properties of liquid organic phase and gaseous phase, we consider the base method and mixing rule, and apply the effect of high pressure, because their thermodynamic and transport properties are strongly dependent on the system conditions as well as their composition.

In the computation of the density of liquid organic phase, we compute the density of oil components by substituting the critical properties of each component into Riedel correlation (1954) as a function of temperature. We evaluate the mixture density of the liquid organic phase by using the pseudo-critical properties computed from Kay’s rule (1936). We account for the effect of pressure higher than the saturation pressure of organic phase by using the equation suggested by Chang-Zhao (1990).

We estimate the density of the gaseous phase by using the cubic equation of state of Peng-Robinson method (1976). Mixture density of gaseous phase is determined by van der Waal’s mixing rule (Poling et al. 2001). Since the equation of state already covers the range of pressure from low value to high value, the effect of high pressure is not applied.

In the computation of the heat capacity of liquid organic phase, we apply the Yaws correlation (2003). They are described as a polynomial equation of the temperature as provided in following equation. Eq. (3.48) is applicable to the liquid components, and Eq. (3.49) is applicable to the gaseous components.

$$C_p = A + BT + CT^2 + DT^3 \tag{3.48}$$

$$C_p = A + BT + CT^2 + DT^3 + ET^4 \tag{3.49}$$

Here, C_p is the heat capacity in J/mol-K, *T* is temperature in Kelvin, and *A*, *B*, *C*, *D*, and *E* are the coefficients defined based on the components. In the computation of the heat capacity of gaseous phase, we use the data from Thermodynamic Research Center (TRC) data bank (Tables-Hydrocarbons 1996). Enthalpy of each component is computed by the integration of heat capacity, and we determine the phase enthalpy by using mass fraction average for the liquid phase, and mole fraction average for the gaseous phase, respectively.

For the liquid organic phase viscosity computation, we also use the Yaws correlation (2003) as a function of temperature. The formula is described by Eq. (3.50).

$$\log_{10} \mu = A + B/T + CT + DT^2 \tag{3.50}$$

Here, μ is the viscosity of liquid oil component in cp, and *T* is the temperature in Kelvin, and *A*, *B*, *C* and *D* are the regression coefficients of the each component. The viscosity of the liquid organic phase is estimated by using the mixing rule provided by Teja and Rice (1981). It computes the liquid mixture viscosity by the logarithmic linear relationship of the components. The high pressure effect for the viscosity of liquid organic phase is provided by Lucas (1981).

In the gaseous phase viscosity computation, we use the rule of Chung et al (1984; 1988). Since this method directly cover the viscosity of the mixture and high pressure effect, the additional application of the mixing rule and high pressure effect are not necessary.

Table 10 Computation methods of the thermodynamic and transport properties of the fluid phases

Properties	Base method	Mixing rule	High pressure effect
Aqueous phase density, specific heat and viscosity	ASME steam table (Meyer et al. 1993)		
Liquid organic phase density	Riedel's correlation (1954)	Kay's rule (1936)	Equation of Chang-Zhao (1990)
Gaseous phase density	Cubic EOS of Peng-Robinson (1976)	van der Waals mixing rule	Base method covers.
Liquid organic phase heat capacity	Yaws' correlation (2003)	Mass fraction average	No pressure effect
Gaseous phase heat capacity	TRC data bank (Pedley 1994)	Mole fraction average	No pressure effect
Liquid organic phase viscosity	Yaws' correlation (2003)	Method of Teja & Rice (1981)	Method of Lucas (1981)
Gaseous phase viscosity	Method of Chung et al. (1984, 1988)	Method of Chung et al. (1984, 1988)	Method of Chung et al. (1984, 1988)

3.4.3 Properties of the solid phase

Solid phase consists of kerogen, prechar and char. Solid phase is immobile, so the transport properties are not considered. We evaluate the density and heat capacity of each component, and determine the phase properties by using mass fraction average.

Density of the kerogen, prechar and char are computed from Eq. (3.51) (Kahl 1999; Vernik and Nur 1992).

$$\rho = \rho_0 \left[1 + c_f \left(P - P_0\right)\right] \tag{3.51}$$

Here, ρ, ρ_0, and c_f are the solid component density, and the density at the reference pressure, P_0, and the compressibility of the components, respectively.

Heat capacity of the kerogen, prechar and char are evaluated by using Eq. (3.52) (Braun 1981; Ragland et al. 1991).

$$C_p = A + BT \tag{3.52}$$

Here, C_p is the specific heat of the solid components, and T is the temperature. The coefficients, A and B, are defined based on the component.

3.5 Numerical description

This section covers the numerical description of the mathematical equations describing the physics and chemistry of the system. It includes the Jacobian matrix setup and solution of the matrix equation.

3.5.1 Jacobian matrix for the fully implicit solution

The continuum equations, Eq. (3.1) and Eq. (3.4) are discretized in the space and time using the integral finite difference method. Time is discretized with first order difference, and the flux and source/sink terms are evaluated at the new time level. In this regard, mass conservation and energy conservation equations become the residual equations as shown in Eq. (3.53) and Eq. (3.54) (Pruess et al. 1999).

$$R_n^{\kappa,k+1} = M_n^{\kappa,k+1} - M_n^{\kappa,k} - \frac{\Delta t}{V_n}\left(\sum_m A_{nm}F_{nm}^{\kappa,k+1} + V_n q_n^{\kappa,k+1}\right) = 0 \tag{3.53}$$

$$R_n^{\theta,k+1} = M_n^{\theta,k+1} - M_n^{\theta,k} - \frac{\Delta t}{V_n}\left(\sum_m A_{nm}F_{nm}^{\theta,k+1} + V_n q_n^{\theta,k+1}\right) = 0 \tag{3.54}$$

Here, $R_n^{\kappa,k+1}$ is a residual of component κ in element n at time level $k + 1$, A_{nm} is a contacting area between element m and n, and Δt is a time step between current time level k and next time level $k + 1$. Superscript θ indicates the terms of heat. This is the fully implicit method, and we can only get the accurate solution in this manner, since the problem we solve is highly nonlinear, because we account chemical reactions.

By differentiating the set of the residual equations in terms of the primary variable sets, X, we get Jacobian matrix as provided in Eq. (3.55). The matrix has the dimension of $(N_E \cdot n)\times(N_E \cdot n)$, where N_E is the number of equations for each element, and n is the number of elements.

$$J = \begin{bmatrix} \dfrac{\partial R_n^{\kappa,k+1}}{\partial X_n^{\kappa,k+1}} & \Lambda \\ \mathrm{M} & \mathrm{O} \end{bmatrix} \tag{3.55}$$

Here, the differential terms in the matrix are defined by using Eq. (3.56) and Eq. (3.57).

$$\frac{\partial R_n^{\kappa,k+1}}{\partial X_n^{\kappa,k+1}} = \frac{\partial M_n^{\kappa,k+1}}{\partial X_n^{\kappa,k+1}} - \frac{\Delta t}{V_n}\left(\sum_m A_{nm}\frac{\partial F_{nm}^{\kappa,k+1}}{\partial X_n^{\kappa,k+1}} + V_n\frac{\partial q_n^{\kappa,k+1}}{\partial X_n^{\kappa,k+1}}\right) \tag{3.56}$$

$$\frac{\partial R_n^{\theta,k+1}}{\partial X_n^{\theta,k+1}} = \frac{\partial M_n^{\theta,k+1}}{\partial X_n^{\theta,k+1}} - \frac{\Delta t}{V_n}\left(\sum_m A_{nm}\frac{\partial F_{nm}^{\theta,k+1}}{\partial X_n^{\theta,k+1}} + V_n\frac{\partial q_n^{\theta,k+1}}{\partial X_n^{\theta,k+1}}\right) \tag{3.57}$$

Here, each differential term is computed by using the numerical differentiation by perturbing the primary variables. We increase our computation efficiency by considering the order of primary variables and the order of equations.

3.5.2 Solution of the matrix equation and the convergence criteria

The Jacobian matrix is simply described by the following equation, Eq. (3.58). We get our primary variables by using Newton-Raphson iteration, which is described in the Eq. (3.59).

$$J = R'\left(X_n^{\kappa,k+1}\right) \tag{3.58}$$

$$X_n^{\kappa,k+1} = X_n^{\kappa,k} - \frac{R\left(X_n^{\kappa,k+1}\right)}{R'\left(X_n^{\kappa,k+1}\right)} \tag{3.59}$$

By arranging this equation and letting $\delta = X_n^{\kappa,k+1} - X_n^{\kappa,k}$, we have the Eq. (3.60). This matrix equation gives δ, and we get our fully implicit solution, *X*, by the Eq. (3.61).

$$J\delta = -R \Rightarrow \delta = -J \setminus R \tag{3.60}$$

$$X_n^{\kappa,k+1} = X_n^{\kappa,k} + \delta \tag{3.61}$$

We solve this matrix equation considering following relative convergence criteria and absolute convergence criteria as provided in Eq. (3.62) and (3.63), respectively.

$$\left|\frac{R_{n,p+1}^{\kappa,k+1}}{M_{n,p+1}^{\kappa,k+1}}\right| \le \varepsilon_1 \tag{3.62}$$

$$\left|R_{n,p+1}^{\kappa,k+1}\right| \le \varepsilon_1 \varepsilon_2 \tag{3.63}$$

Here, ε_1 and ε_2 are the relative and absolute convergence criteria, respectively. We use the criteria of Eq. (3.64) and Eq. (3.65).

$$1.0\times10^{-6} \le \varepsilon_1 \le 1.0\times10^{-5} \tag{3.64}$$

$$1 \le \varepsilon_2 \le 1{,}000 \tag{3.65}$$

The iteration is continued until the system satisfies these convergence criteria. The maximum number of Newton-Raphson iteration of 8 is used, and if it cannot compute the solution in the maximum number of iterations, we decrease the time step.

3.6 Description of the fractured media by using Multiple Interacting Continua (MINC)

We apply the Multiple Interacting Continua (MINC) method to describe the fractured media. As we stated in the CHAPTER II, there is the pre-existing fracture system in Green River Formation. We simulate the in-situ upgrading process in the fracture media for the realistic implementation. MINC method has been provided for the description of the fractured media by Pruess and Narasimhan (1985).

MINC method models the fractured media by dividing the primary grid block into fracture and matrix subgrid blocks as described in Fig. 4. A proximity function based on the volume fraction is used for generating the secondary grid blocks from primary grid blocks. In the MINC, thermodynamic conditions are accounted by the distance from the fracture, and flow occurs perpendicular to the fractures. In our simulation, we use two subgrid blocks, one for fracture, and the other one for matrix.

We assign the different properties and initial conditions for the matrix and fracture subdomains, such as phase states, porosity, permeability, and thermal conductivity. The matrix subdomain contains kerogen initially, and the effective permeability changes during the in-situ upgrading process. The fluid products including hydrocarbon flow from the matrix to the fracture subdomain, and global flow occurs in the fracture networks.

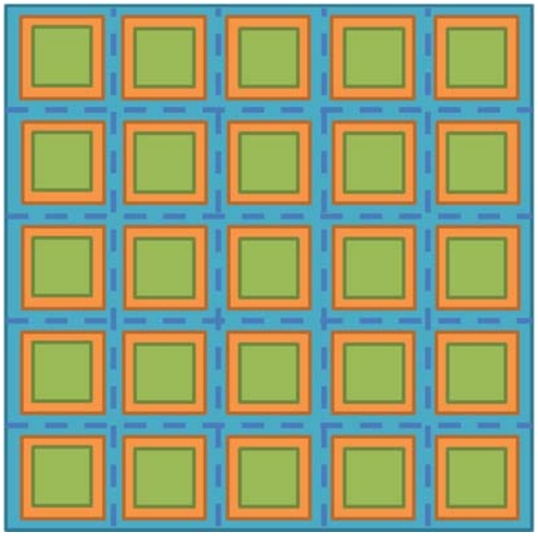

Fig. 4 Subgridding in MINC for fractured media description

CHAPTER IV

SIMULATOR VALIDATION

In this chapter, we validate the developed simulator by matching the field production data of Shell Mahogany Demonstrate Project South (MDP-S), which is implemented in Green River Formation from 2004 to 2005. We perform the sensitivity analyses of the reservoir parameters, and construct the realistic model of the Green River Formation through this work. We analyze the effects of the presence of pre-existing fracture network, oil shale grade (organic matter contents), permeability of pre-existing fracture network, and thermal conductivity of the formation on the hydrocarbon production.

4.1 Standard case: validated model

Shell has actively conducted a research to produce hydrocarbons from the oils shales in the Green River Formation. They implemented a Mahogany Demonstration Project South (MDP-S) from 2004 to 2005 in a naturally fractured zone of Mahogany field, in order to produce a significant volume of oil greater than 1,000 bbl (Fowler and Vinegar 2009). In this project, they used 16 vertical electric heaters to increase the average formation temperature to 650 °F, and 2 production wells in a hexagonal pattern as shown in Fig. 5 . We consider the formation with a square of 140 ft-length, in order to account heat loss to the surrounding formation. We simulate a quarter of the model by using 2D simulation geometry with 25*25 grid blocks as shown in Fig. 5. The model has 113 ft-height.

We have an input data for reservoir properties and initial condition as listed in Table 11. The initial reservoir pressure is 3,000 psi, and the initial temperature is 95 °F. Pore is initially filled with aqueous phase (30 %) and solid phase of whole kerogen (70 %). The irreducible saturations of the formation matrix and the pre-existing fracture network are shown in Table 12.

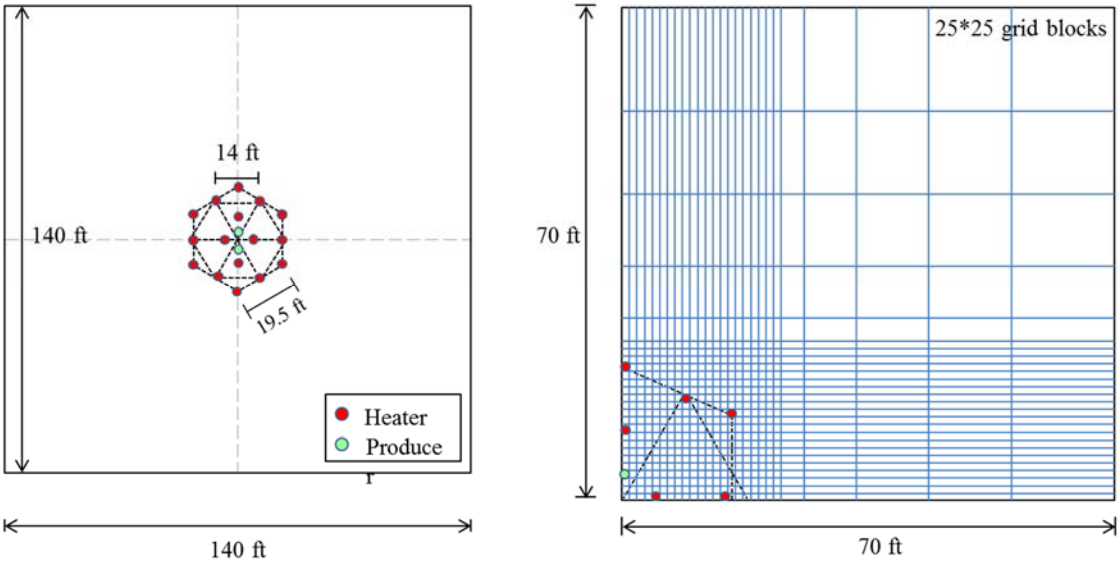

(a) Configuration of heaters and producers (b) Simulation geometry

Fig. 5 Configuration and simulation geometry of Shell ICP

Table 11 Reservoir properties and initial condition: standard case (Shell ICP)

Parameters	Values	Parameters	Values
Initial pressure (psi)	3,000	Initial aqueous phase saturation	0.3
Initial temperature (°F)	95	Initial solid phase saturation	0.7
Rock density(kg/m^3)	2,000	Kerogen mass fraction in solid phase	1

Table 12 Irreducible saturations in the formation matrix and fracture network: standard case (Shell ICP)

Formation matrix		Fracture network	
S_{ira}	0.30	S_{ira}	0.03
S_{iro}	0.12	S_{iro}	0.02
S_{irg}	0.03	S_{irg}	0.003

By conducting the various cases of oil shale grade (organic matter contents), fracture network permeability, and the formation thermal conductivity, we find that the validated model has the properties listed in Table 13. The organic matter content is computed by substituting the oil shale grade into the Eq. (2.5). The realistic model of the oil shale reservoir in Green River Formation is represented by these parameters. Formation porosity is computed from the organic matter contents and initial saturations by using the Eq. (2.5). Permeability of the rock is computed from the regression formula drawn from the Table 1.

We simulate 400 days of heating and production by using variable flowing bottomhole pressure as shown in Fig. 6. We only heat the formation by the multiple vertical heaters from 0 to 65 days, and produce fluid from 65 to 400 days while continuously heating the formation. We keep the bottomhole pressure constant from 65 to 200 days, and gradually decrease it from 200 days. In Fig. 6, the kerogen mass in place is plotted as the in-situ upgrading process proceeds. Here, we find that prechar and little amount of char are produced from the kerogen pyrolysis and cracking/coking reactions. At 400 days, the mass of remaining kerogen in the hexagon is 2.9 % of original mass in place.

Table 13 Reservoir properties of the validated model: standard case (Shell ICP)

Reservoir properties	Values
Oil shale grade (gal/ton)	25
Organic matter content (volume fraction)	0.301
Permeability of fracture network (md)	150
Formation thermal conductivity (W/m-K)	2.0
Porosity	0.43
Formation matrix permeability k_x and k_z (md)	128, 64

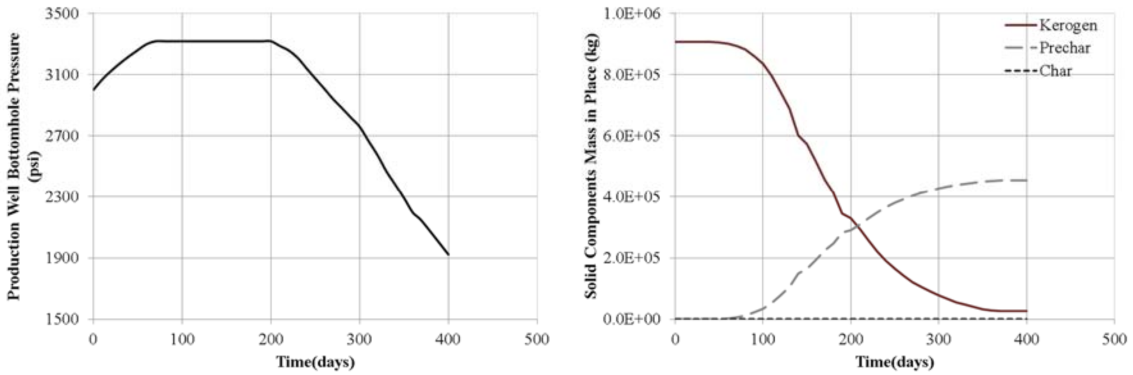

(a) Flowing bottomhole pressure (b) Kerogen mass in place

Fig. 6 Flowing bottomhole pressure and kerogen mass in place: standard case (Shell ICP)

The production rate and the cumulative production of the liquid organic phase in a hexagon are illustrated in Fig. 7. The simulation result in solid line shows good match with the filed data in dots (Vinegar 2006). The production of phases - aqueous phase, liquid organic phase and gaseous phase is plotted in Fig. 8. The cumulative productions of liquid organic phase, aqueous phase and gaseous phase are 1,680 STB, 6,100 STB, and 4,220 MSCF, respectively. The produced hydrocarbon gas (IC_2) is 841 MSCF, and we get total of 1,830 barrel of oil equivalent (BOE) by using the conversion factor of 0.1767 BOE/MSCF. Produced gas oil ratio (GOR) is 2.51 MSCF/STB. These results are listed in Table 14.

The fraction of the components in the produced liquid organic phase and the gaseous phase are shown in Fig. 9. In the liquid organic phase of the produced fluid, the major portion is composed with heavy oil (IC_{22}) and light oil (IC_{11}) components, so only the oil components are plotted. In the gaseous phase of the produced fluid, there exist vapor of water and oil components as well as free gas components. The hydrocarbon gas component (IC_2) shows the highest mole fraction at the beginning, but the water vapor component gradually increases, and reaches 50 % of mole fraction.

Table 14 Summary of the simulation results: standard case (Shell ICP)

Parameters	Values	Parameters	Values
Duration (days)	400	Aqueous production (STB)	6,100
Remaining kerogen (%)	2.90	GOR (MSCF/STB)	2.51
Liquid organic production (STB)	1,680	HC gas production (MSCF)	841
Gaseous production (MSCF)	4,218	Produced HC (BOE)	1,829

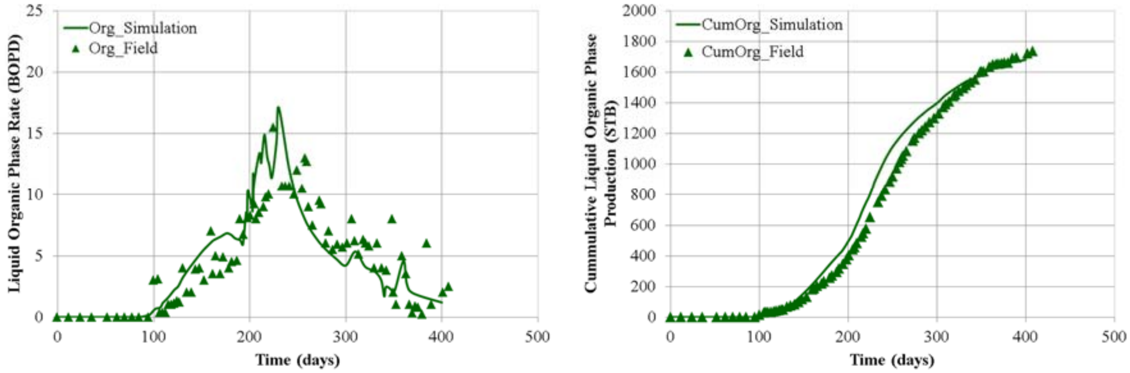

Fig. 7 Production rate and cumulative production of liquid organic phase: standard case (Shell ICP)

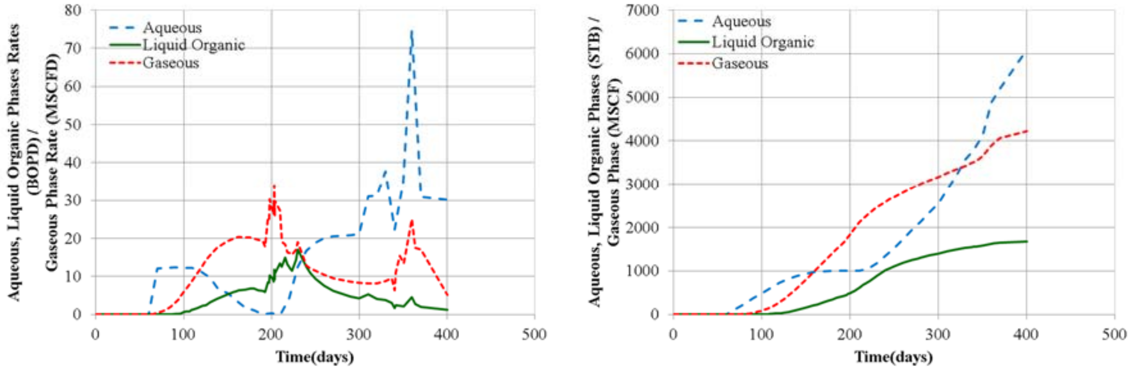

Fig. 8 Production rates and cumulative productions of phases: standard case (Shell ICP)

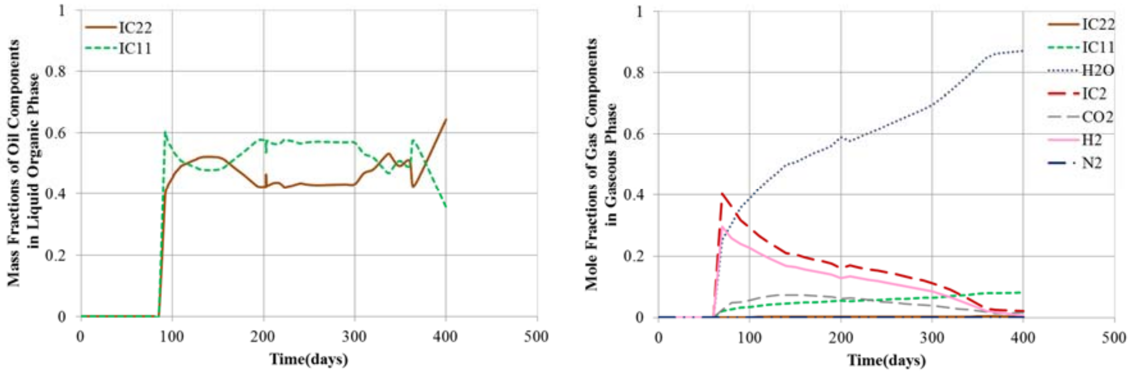

(a) Mass fractions of oil components in liquid organic phase

(b) Mole fractions of gas components in gaseous phase

Fig. 9 Fractions of components in produced fluid: standard case (Shell ICP)

The reservoir profiles of kerogen mass fraction, pressure, temperature, and phase saturations are shown in Fig. 10 - Fig. 15. Almost whole kerogen decomposes in the hexagon at 330 days. Pressure profiles at the matrix shows the higher pressure in the hexagon due to the occurrence of the fluids from the kerogen decomposition, but the pressure at the fracture profiles show different appearance, because it mostly depends on the fluid flow in the fracture. Temperature profiles of the matrix and fracture domains are analogous. In the profiles of the phase saturations, we observe that the aqueous phase replaces the liquid organic phase and gaseous phase as production proceeds.

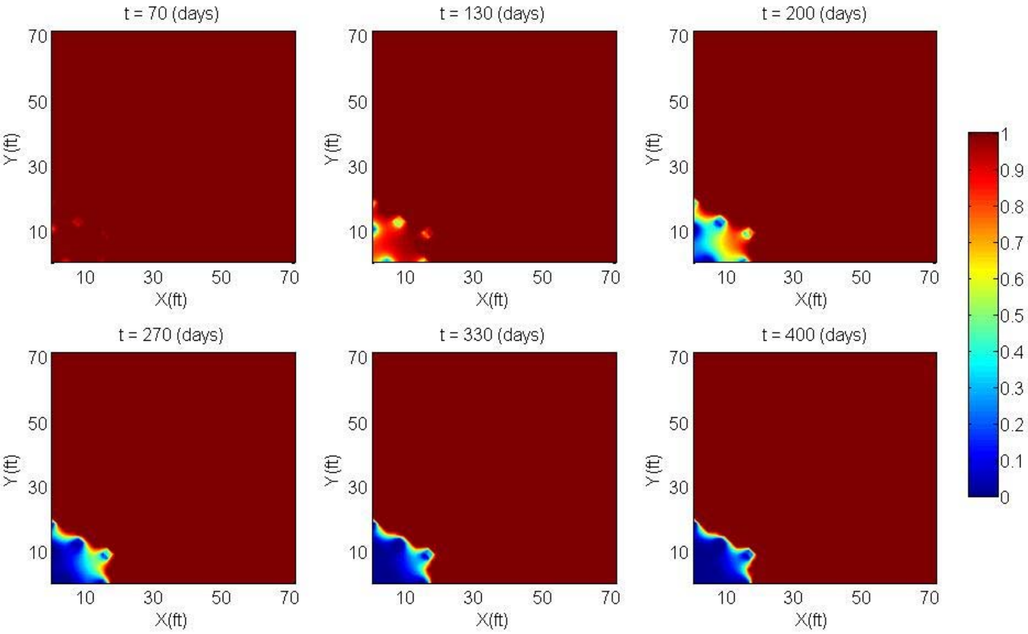

Fig. 10 Profiles of kerogen mass fraction: standard case (Shell ICP)

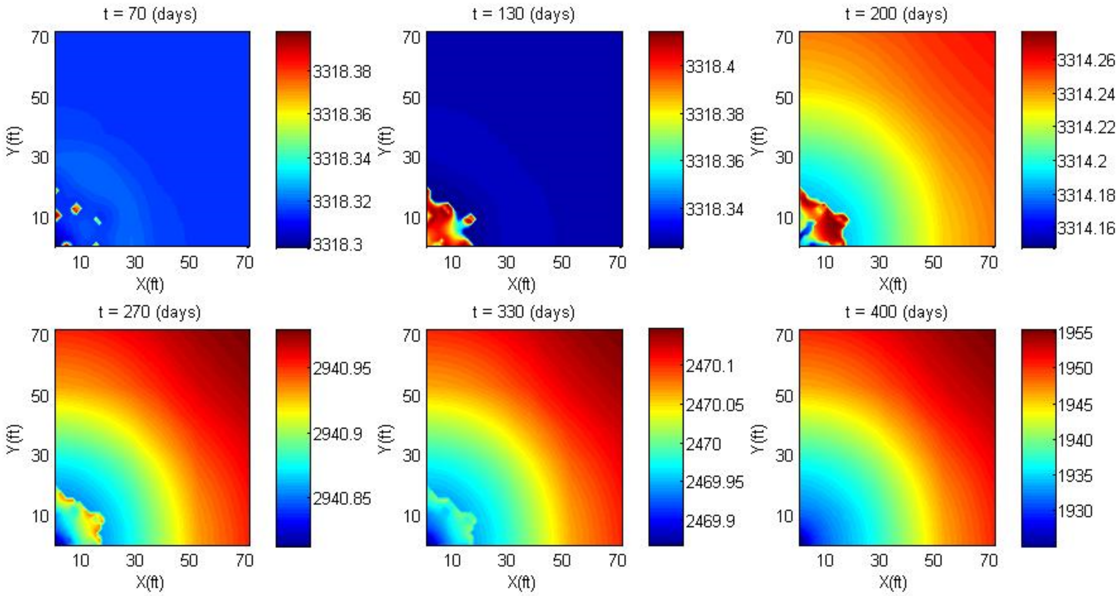

(a) Profiles of pressure at the matrix domain

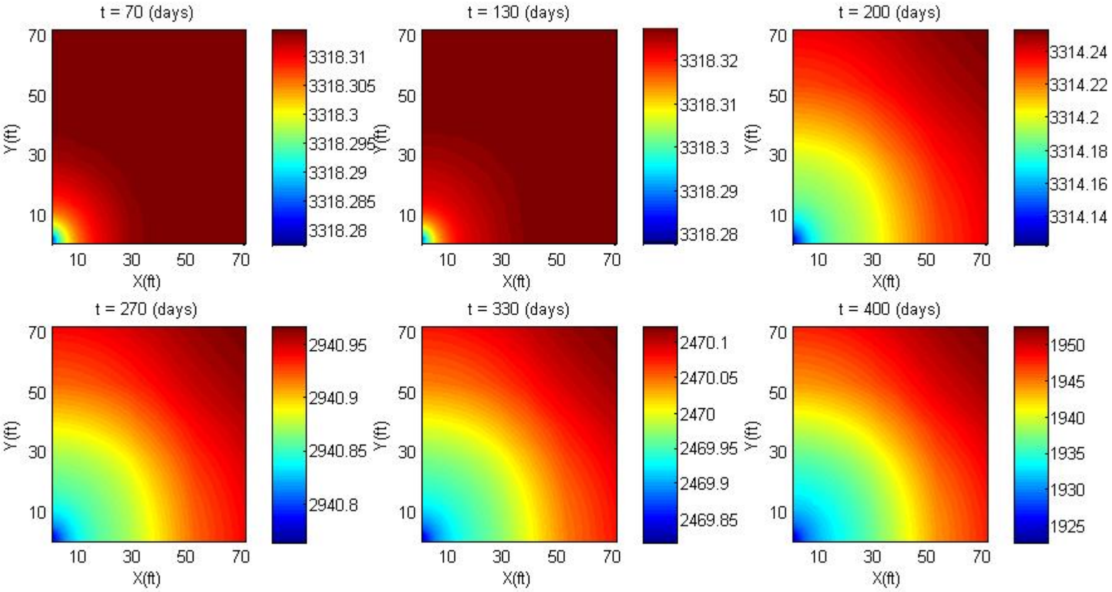

(b) Profiles of pressure at the fracture domain

Fig. 11 Profiles of pressure: standard case (Shell ICP)

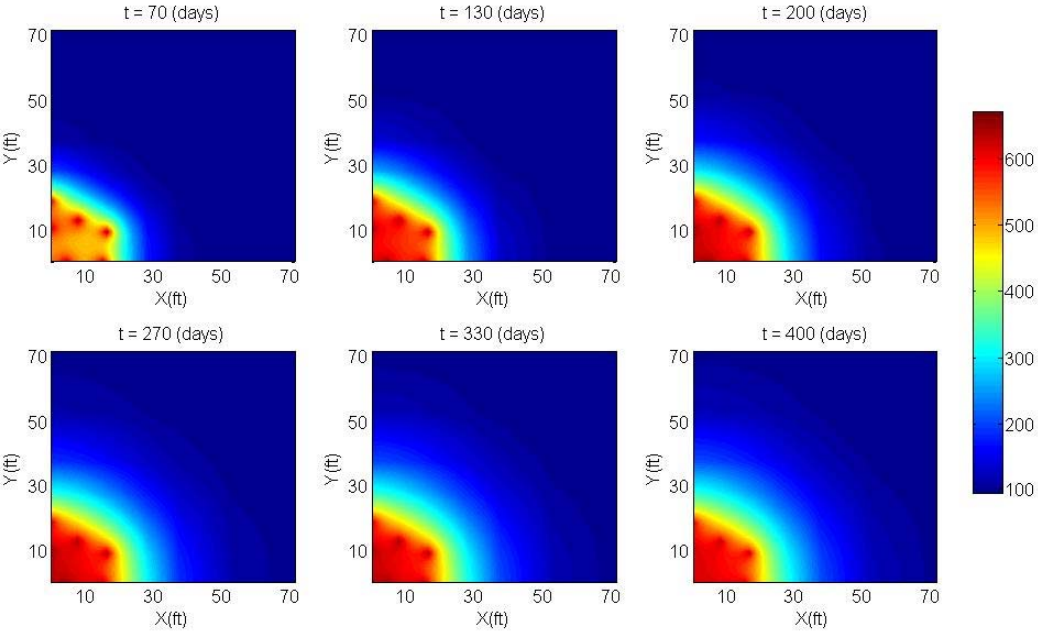

(a) Profiles of temperature at the matrix domain

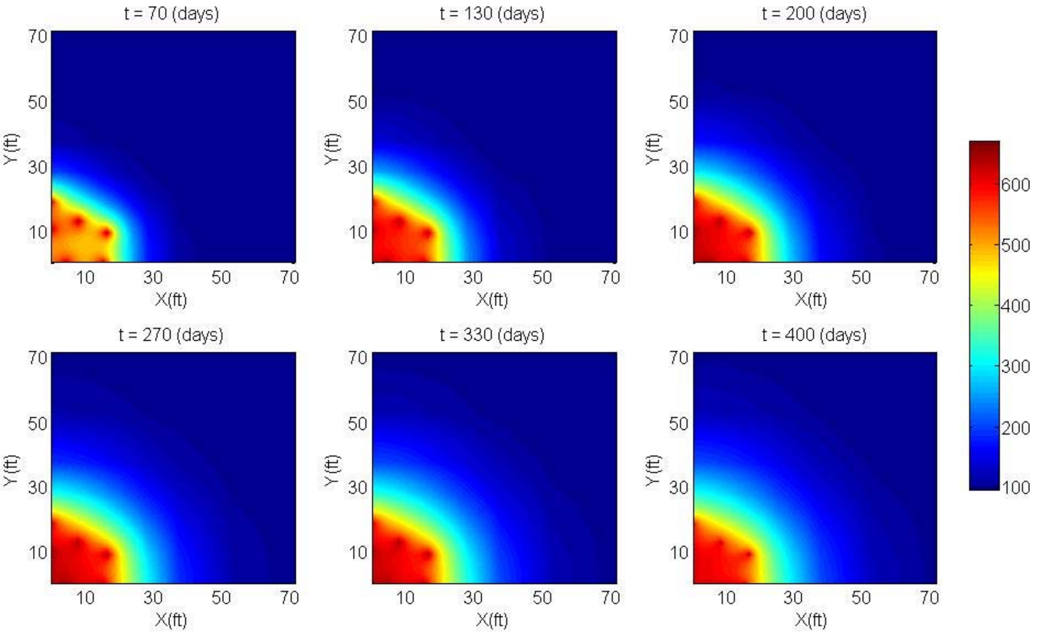

(b) Profiles of temperature at the fracture domain

Fig. 12 Profiles of temperature: standard case (Shell ICP)

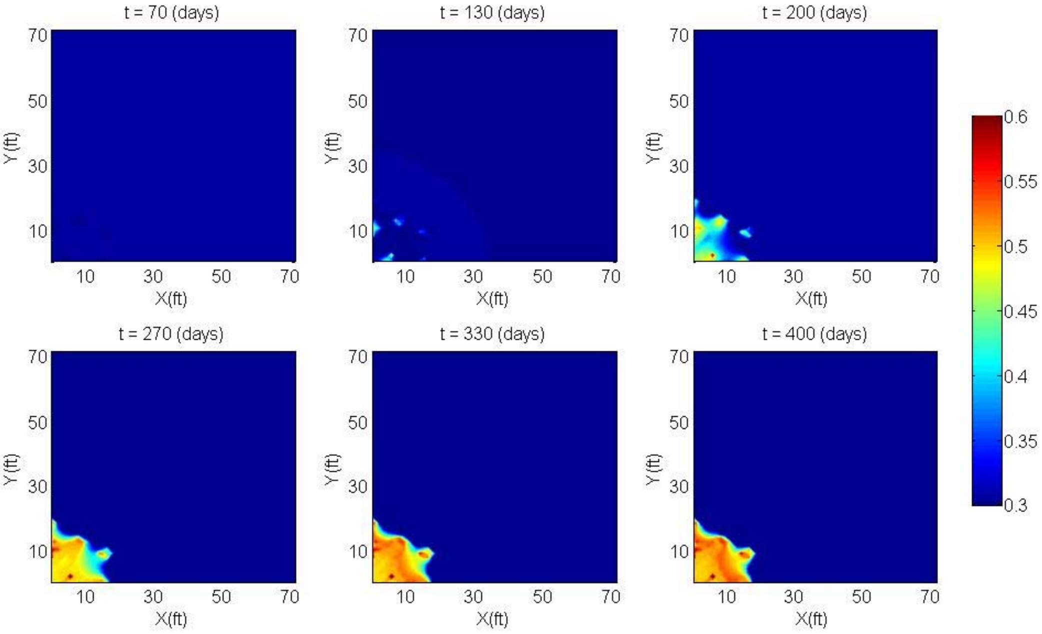

(a) Profiles of aqueous phase saturation at the matrix domain

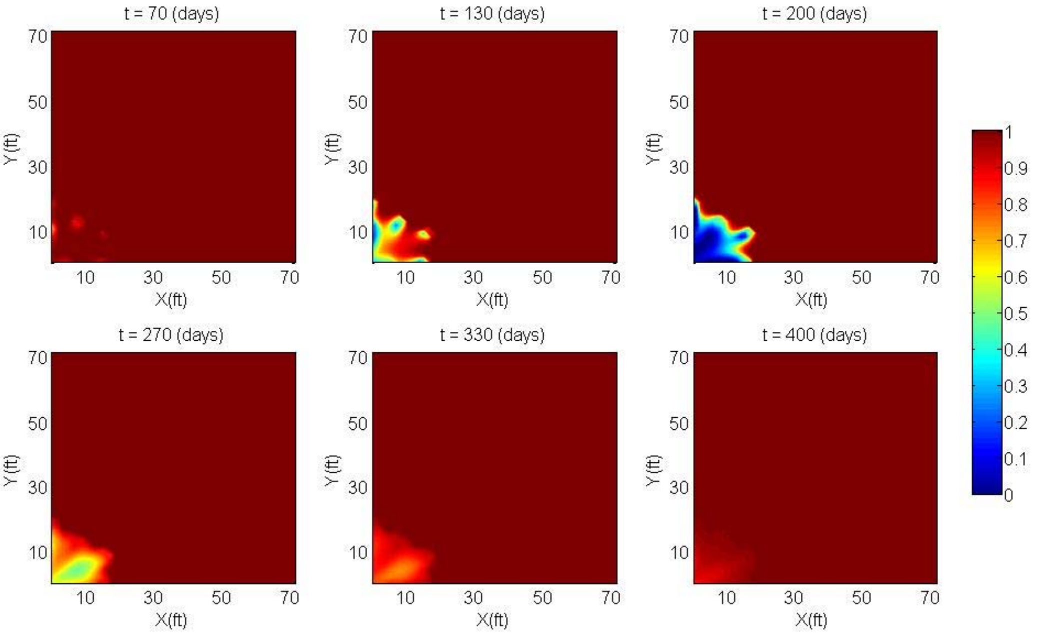

(b) Profiles of aqueous phase saturation at the fracture domain

Fig. 13 Profiles of aqueous phase saturation: standard case (Shell ICP)

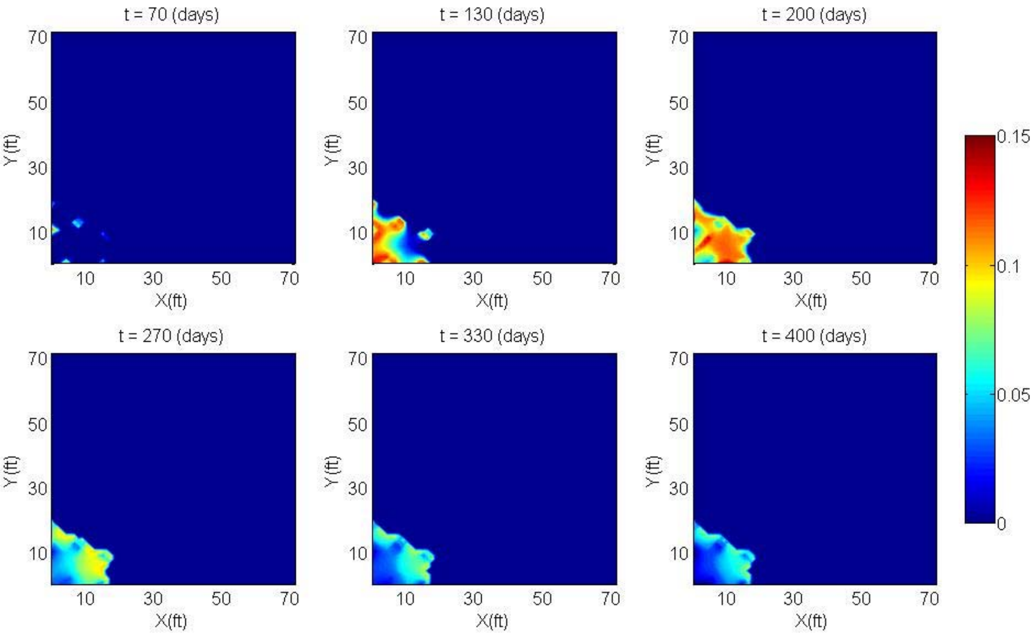

(a) Profiles of liquid organic phase saturation at the matrix domain

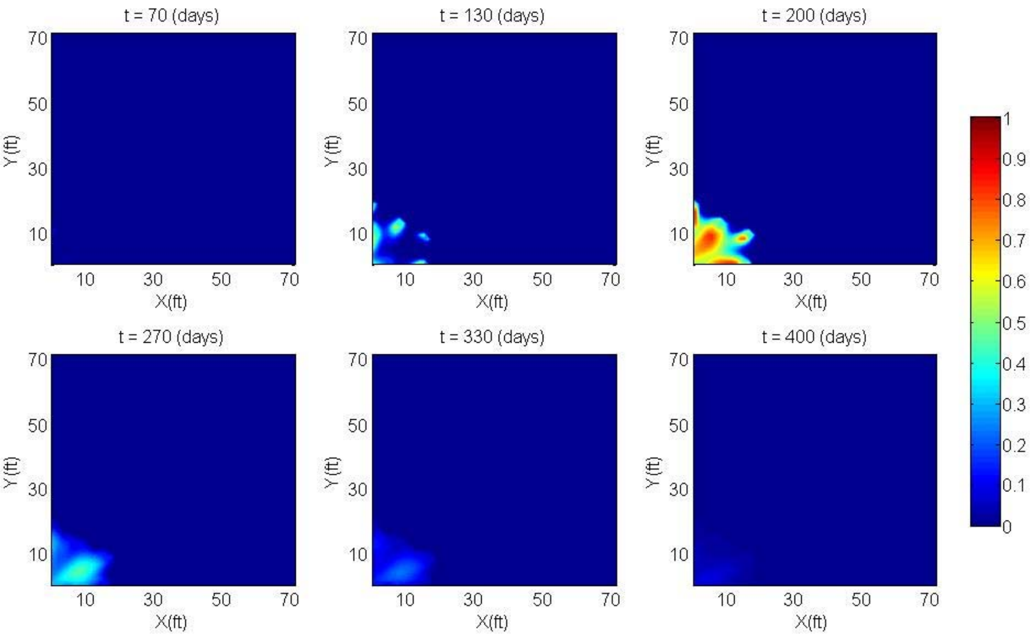

(b) Profiles of liquid organic phase saturation at the fracture domain

Fig. 14 Profiles of liquid organic phase saturation: standard case (Shell ICP)

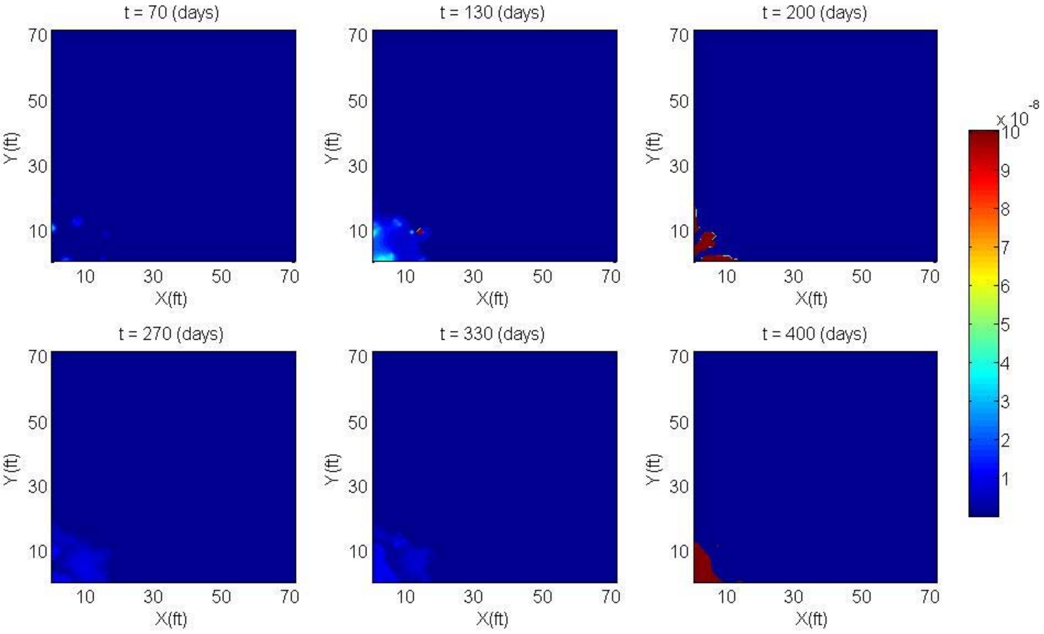

(a) Profiles of gaseous phase saturation at the matrix domain

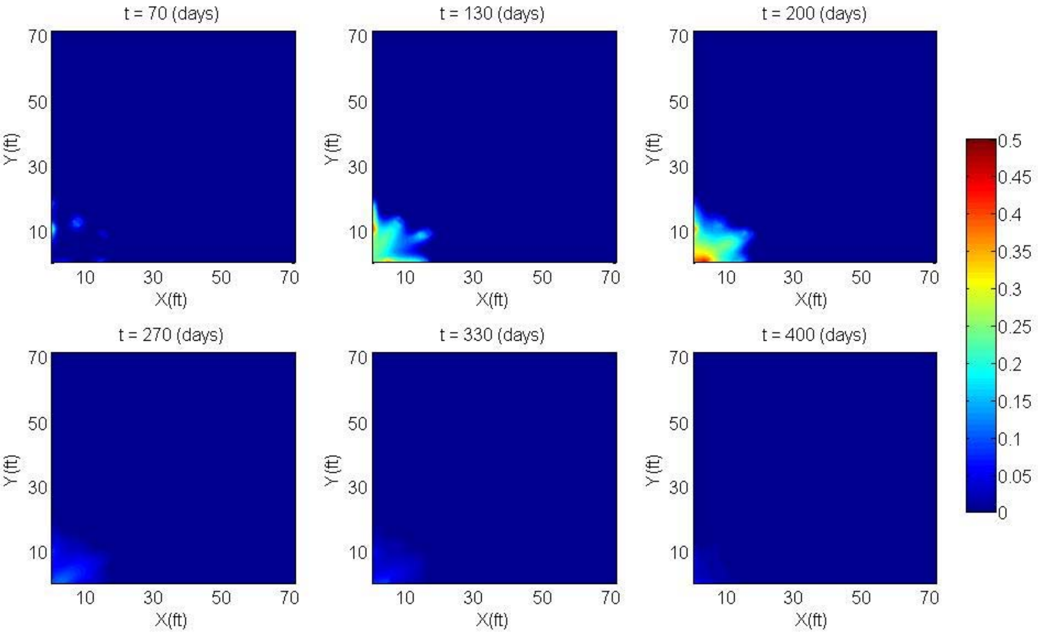

(b) Profiles of gaseous phase saturation at the fracture domain

Fig. 15 Profiles of gaseous phase saturation: standard case (Shell ICP)

4.2 Case 1: absence of pre-existing fracture network

We simulate the case of non-fractured reservoir, in order to examine the effect of pre-existing fracture network. Formation matrix properties are the same to the standard case. In-situ upgrading and production proceed for 360 days, and the simulation results are shown in Fig. 16 – Fig. 25. The fluids are produced with the variable flowing bottomhole pressure as shown in Fig. 16. The kerogen mass in place versus time is provided in Fig. 16.

In Fig. 17, we observe that the liquid organic phase production shows different behavior from the field data, and has the less cumulative production than the field production data. We find the higher remaining liquid organic phase saturation after the procedure in Fig. 24. Gaseous phase production is higher than that of standard case, due to the lower effective permeability of aqueous phase and liquid organic phase than standard case (fractured reservoir). The simulation results are summarized in Table 15.

Table 15 Summary of the simulation results: validation case1 (Shell ICP)

Parameters	Values	Parameters	Values
Duration (days)	360	Aqueous production (STB)	673
Remaining kerogen (%)	0.42	GOR (MSCF/STB)	8.16
Liquid organic production (STB)	735	HC gas production (MSCF)	1,419
Gaseous production (MSCF)	6,000	Produced HC (BOE)	985

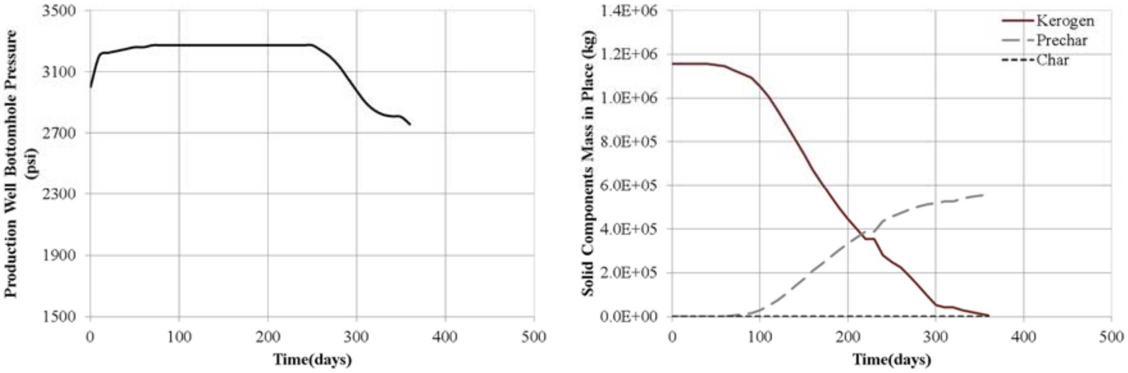

(a) Flowing bottomhole pressure (b) Kerogen mass in place

Fig. 16 Flowing bottomhole pressure and kerogen mass in place: validation case 1 (Shell ICP)

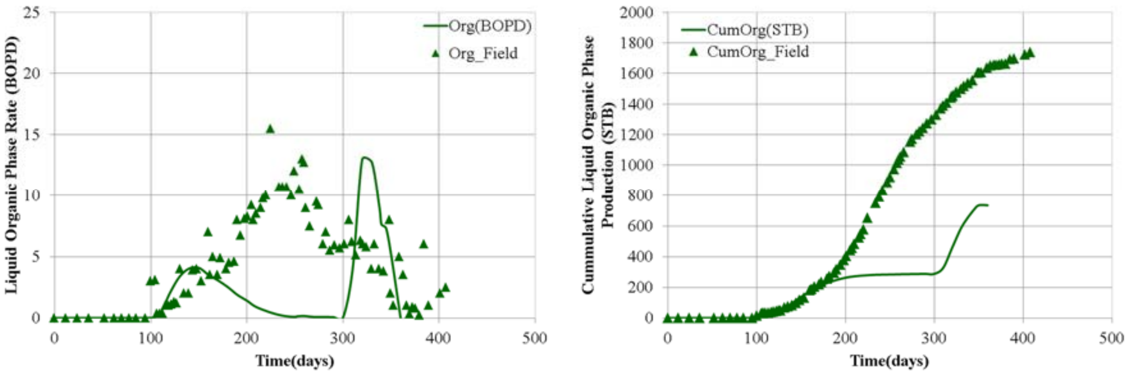

Fig. 17 Production rate and cumulative production of liquid organic phase: validation case 1 (Shell ICP)

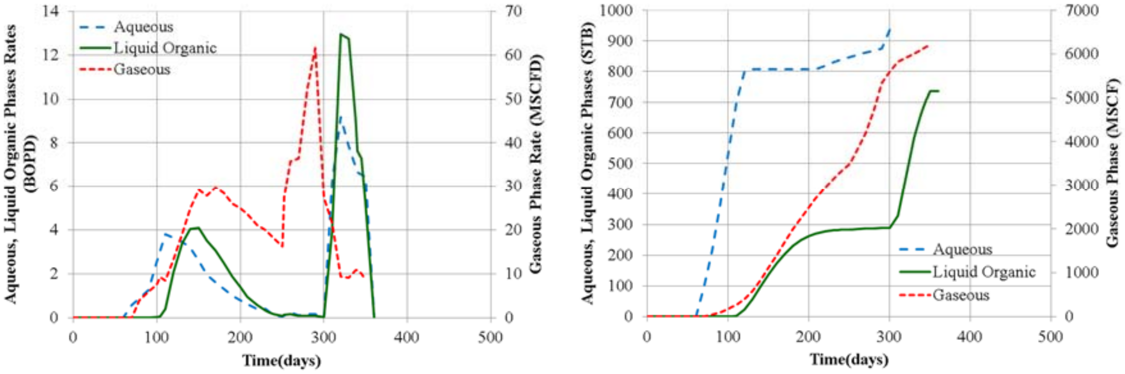

Fig. 18 Production rates and cumulative productions of phases: validation case 1 (Shell ICP)

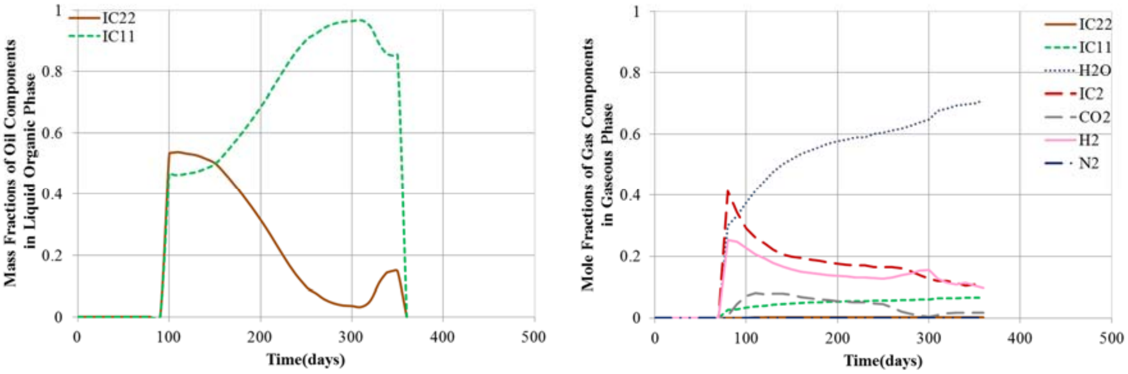

(a) Mass fractions of oil components in liquid organic phase

(b) Mole fractions of gas components in gaseous phase

Fig. 19 Fractions of components in produced fluid: validation case 1 (Shell ICP)

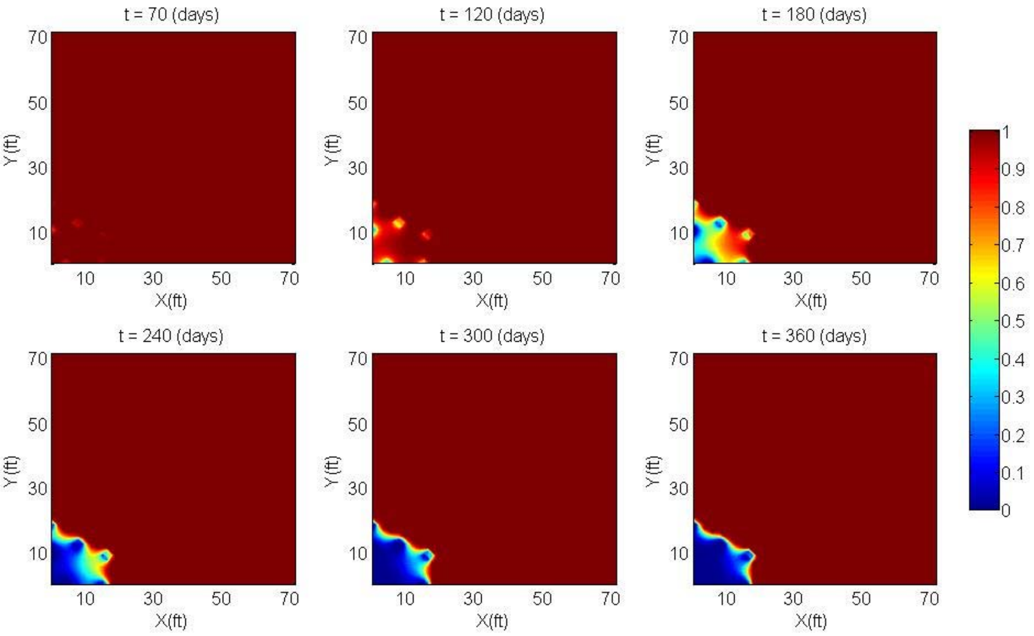

Fig. 20 Profiles of kerogen mass fraction: validation case 1 (Shell ICP)

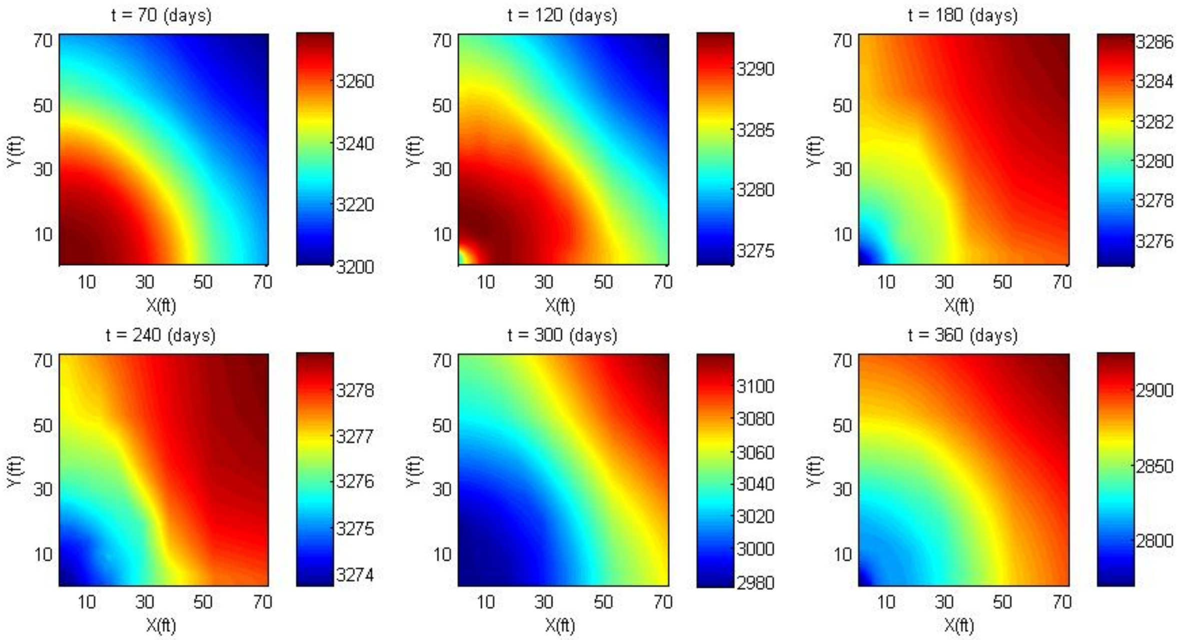

Fig. 21 Profiles of pressure: validation case 1 (Shell ICP)

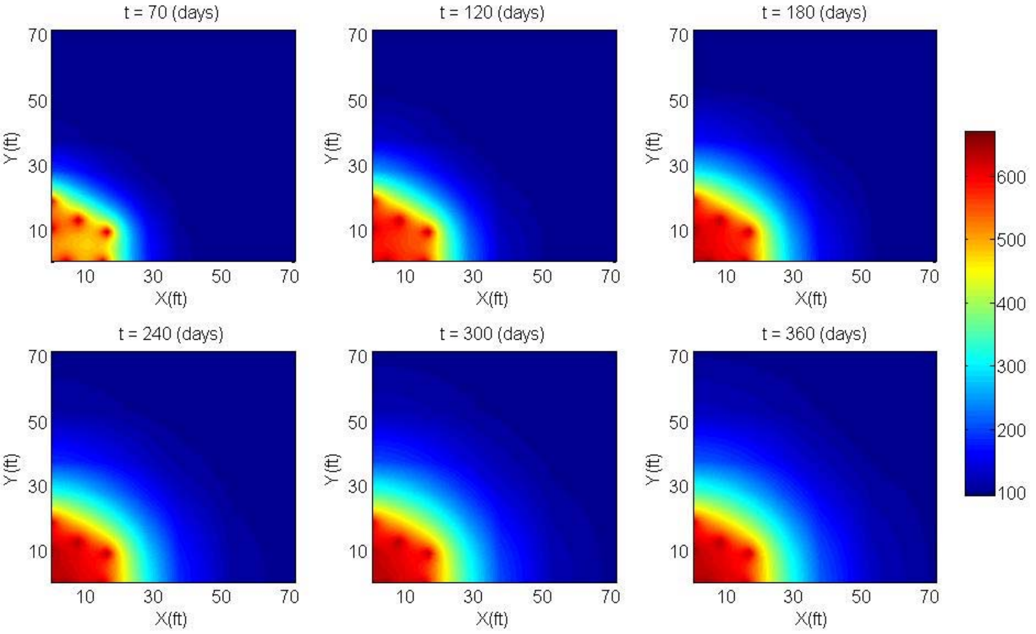

Fig. 22 Profiles of temperature: validation case 1 (Shell ICP)

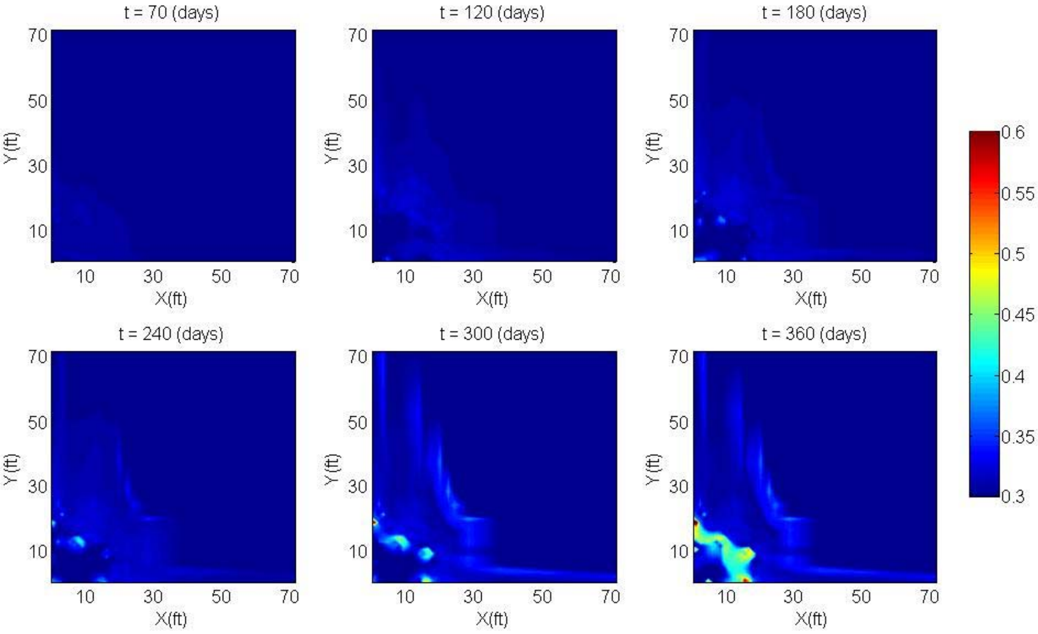

Fig. 23 Profiles of aqueous phase saturation: validation case 1 (Shell ICP)

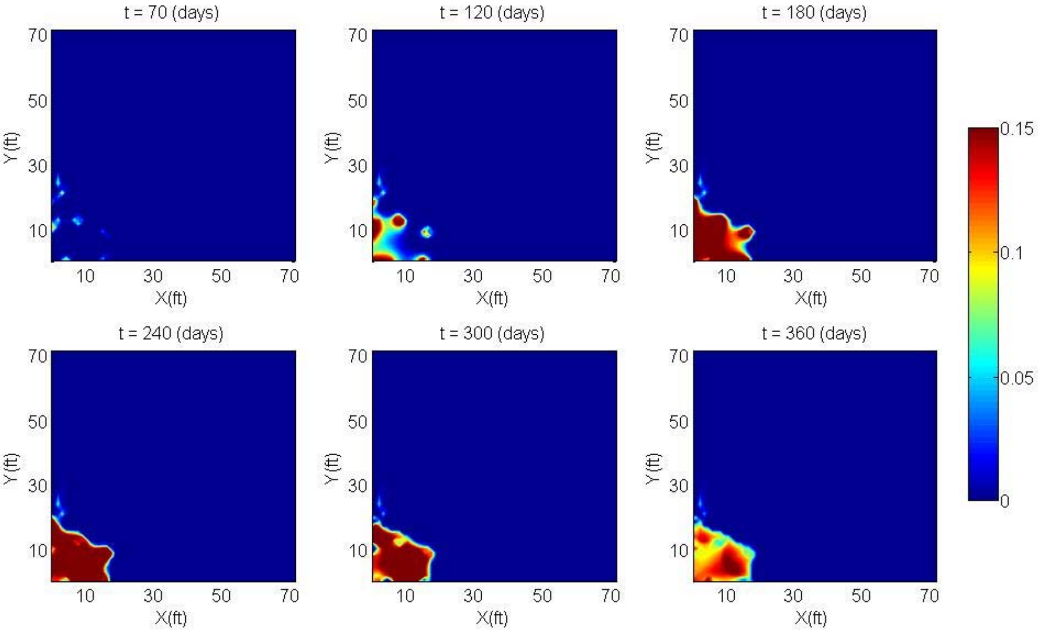

Fig. 24 Profiles of liquid organic phase saturation: validation case 1 (Shell ICP)

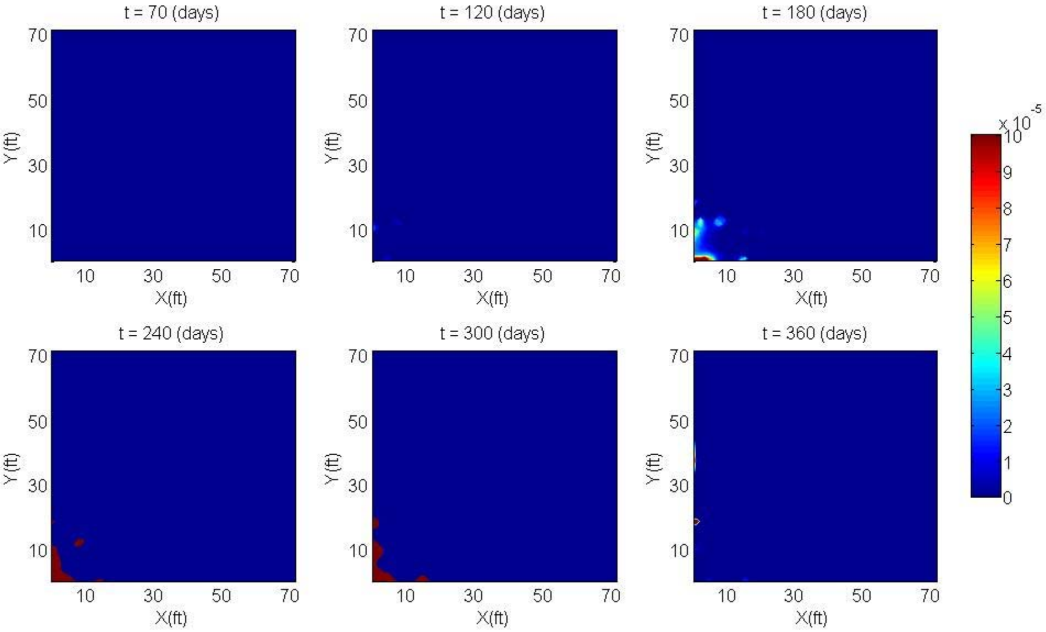

Fig. 25 Profiles of gaseous phase saturation: validation case 1 (Shell ICP)

4.3 Case 2: oil shale grade

We performed the sensitivity analyses of the oil shale grades by using low oil shale grade (15 gal/ton) and high oil shale grade (35 gal/ton). Matrix permeability is computed by using the regression from the data of Table 1. We expect that the oil shale grade and corresponding organic matter content affects the flowing ability of the fluids from the matrix to the fracture domain as well as the total amount of the hydrocarbon production.

4.3.1 Low oil shale grade

In this case, the model has the different organic matter content, porosity and matrix permeability as well as the oil shale grade as listed in Table 16. The organic matter content is computed by substituting the oil shale grade into the Eq. (2.5), and the formation porosity is computed from the organic matter contents and initial saturations. Permeability of the rock is computed from the regression formula drawn from the Table 1. The in-situ upgrading and the production process proceeds for 400 days, by using the variable flowing bottomhole pressure as provided in Fig. 26. The simulation results are shown in Fig. 27 – Fig. 31. We find that the recoverable amount of liquid organic phase is lower than the field data. The simulation results are summarized in Table 17.

Table 16 Porosity and matrix permeability of the formation: validation case 2-1 (Shell ICP)

Reservoir properties	Values
Oil shale grade (gal/ton)	15
Organic matter contents (volume fraction)	0.195
Porosity	0.28
Formation matrix permeability k_x and k_z (md)	22, 11

Table 17 Summary of the simulation results: validation case 2-1 (Shell ICP)

Parameters	Values	Parameters	Values
Duration (days)	400	Aqueous production (STB)	3,170
Remaining kerogen (%)	0.1	GOR (MSCF/STB)	5.22
Liquid organic production (STB)	720	HC gas production (MSCF)	511
Gaseous production (MSCF)	3,760	Produced HC (BOE)	810

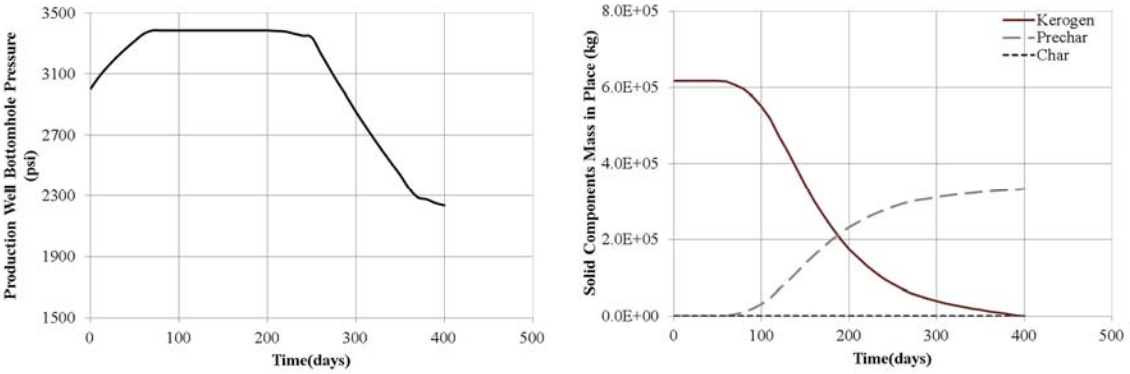

(a) Flowing bottomhole pressure (b) Kerogen mass in place

Fig. 26 Flowing bottomhole pressure and kerogen mass in place: validation case 2-1 (Shell ICP)

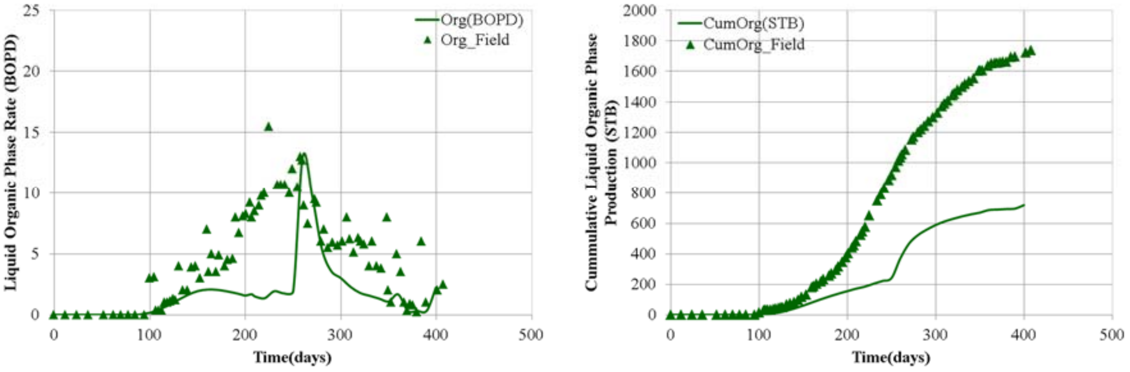

Fig. 27 Production rate and cumulative production of liquid organic phase: validation case 2-1 (Shell ICP)

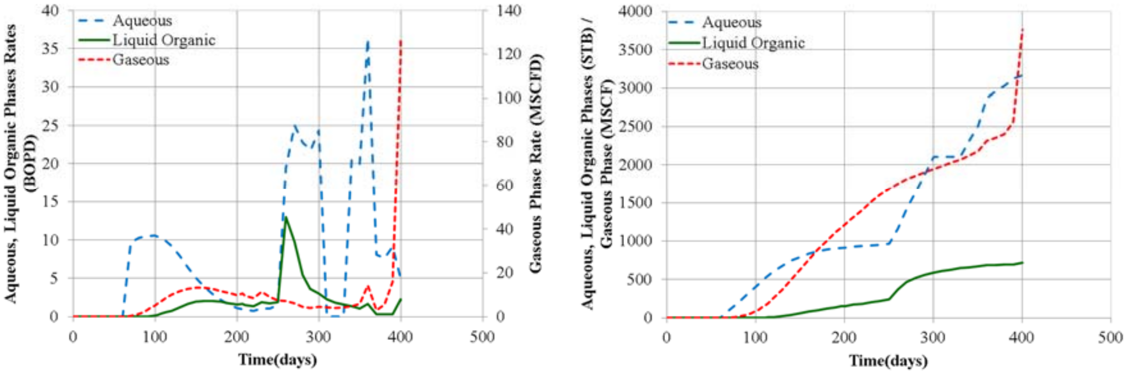

Fig. 28 Production rates and cumulative productions of phases: validation case 2-1 (Shell ICP)

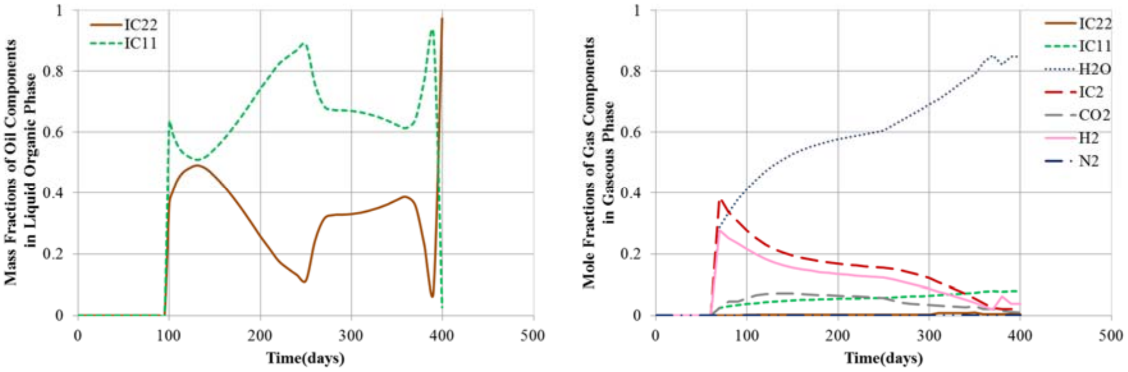

(a) Mass fractions of oil components in liquid organic phase

(b) Mole fractions of gas components in gaseous phase

Fig. 29 Fractions of components in produced fluid: validation case 2-1 (Shell ICP)

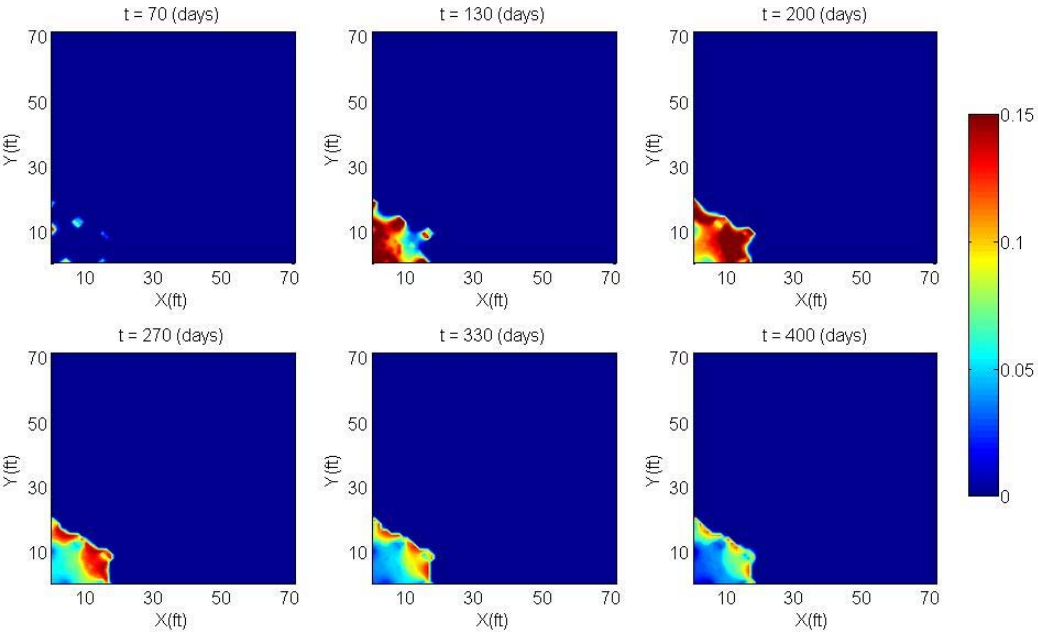

(a) Profiles of liquid organic phase saturation at the matrix domain

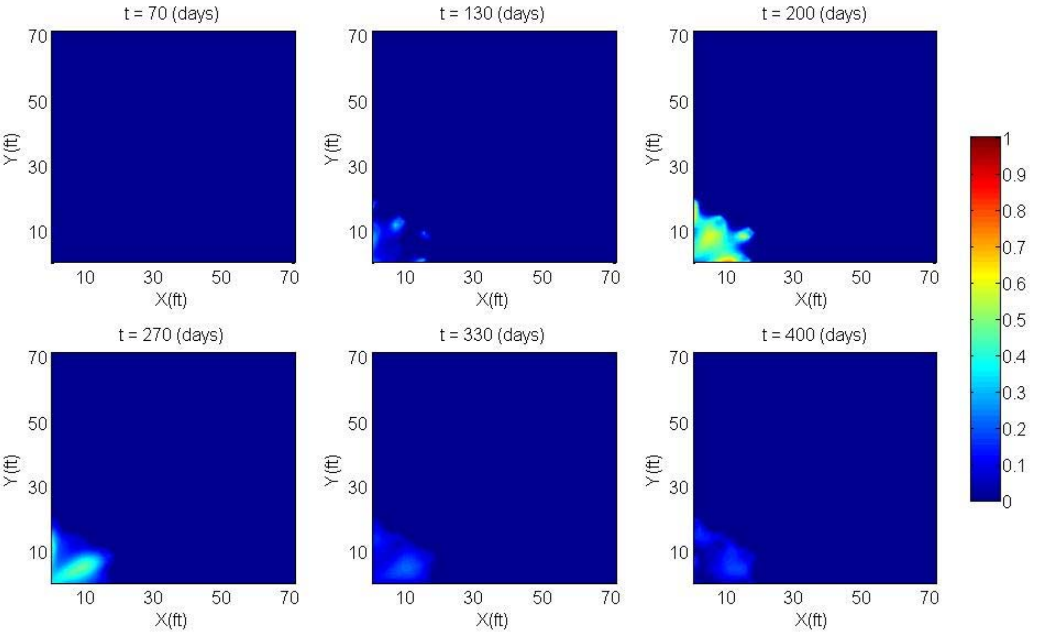

(b) Profiles of liquid organic phase saturation at the fracture domain

Fig. 30 Profiles of liquid organic phase saturation: validation case 2-1 (Shell ICP)

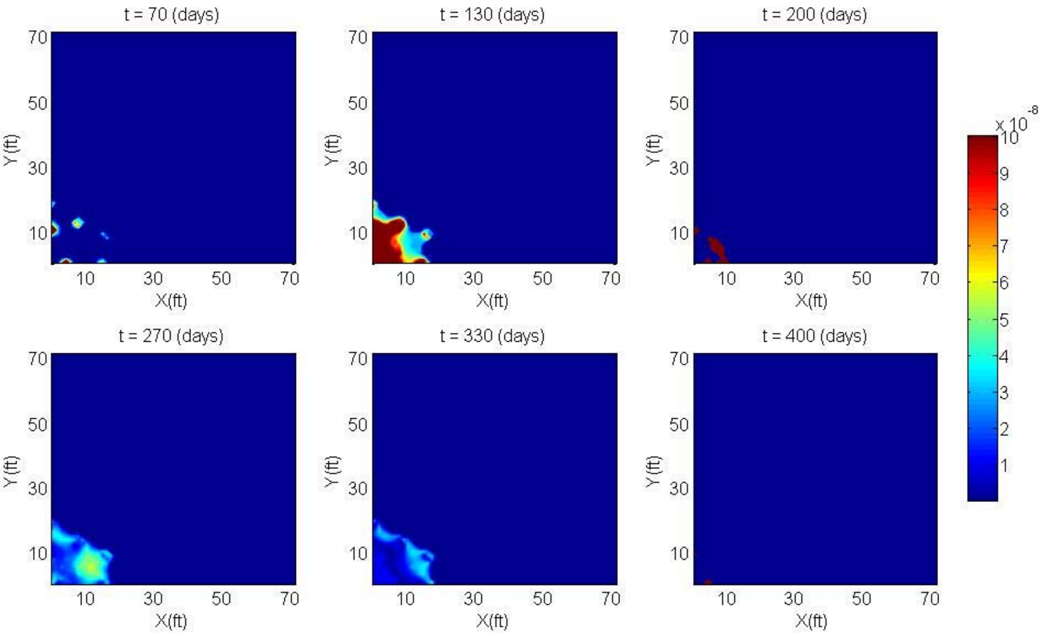

(a) Profiles of gaseous phase saturation at the matrix domain

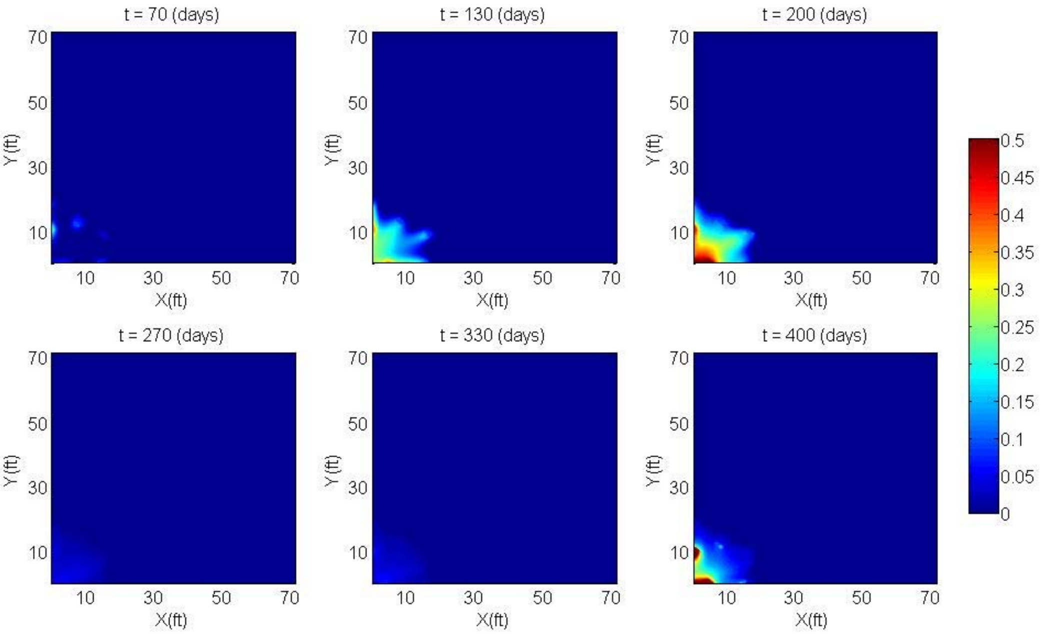

(b) Profiles of gaseous phase saturation at the fracture domain

Fig. 31 Profiles of gaseous phase saturation: validation case 2-1 (Shell ICP)

4.3.2 High oil shale grade

In this case, we use the oil shale grade of 35 gal/ton. The organic matter content is computed by substituting the oil shale grade into the Eq. (2.5), and the formation porosity is computed from the organic matter contents and initial saturations. Permeability of the rock is computed from the regression formula drawn from the Table 1. The higher organic matter content makes higher porosity and matrix permeability than standard case as listed in Table 18. We expect that the faster hydrocarbon production as well as larger amount of production than the standard case. The simulation results are shown in Fig. 32 – Fig. 36. The production proceeds for 380 days by using variable flowing bottomhole pressure as shown in Fig. 32. In Fig. 33, we observe that the production of liquid organic phase shows the higher values than field production data. In the profiles of liquid organic phase saturation, we find the higher saturations than the standard case. The simulation results are summarized in Table 19.

Table 18 Porosity and matrix permeability of the formation: validation case 2-2 (Shell ICP)

Reservoir properties	Values
Oil shale grade (gal/ton)	35
Organic matter contents (volume fraction)	0.393
Porosity	0.56
Formation matrix permeability k_x and k_z (md)	288, 144

Table 19 Summary of the simulation results: case 2-2 (Shell ICP)

Parameters	Values	Parameters	Values
Duration (days)	380	Aqueous production (STB)	7,625
Remaining kerogen (%)	5.0e-3	GOR (MSCF/STB)	1.66
Liquid organic production (STB)	2,916	HC gas production (MSCF)	1,082
Gas. production (MSCF)	4,842	Produced HC (BOE)	3,108

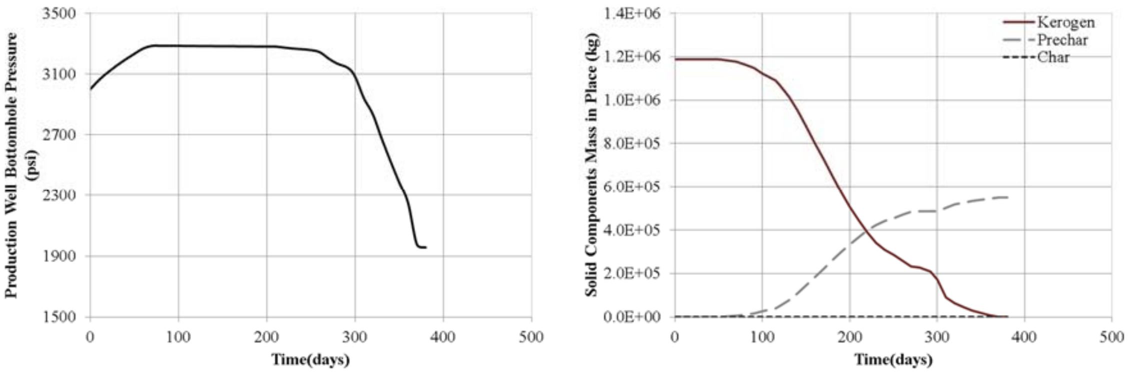

(a) Flowing bottomhole pressure (b) Kerogen mass in place

Fig. 32 Flowing bottomhole pressure and kerogen mass in place: validation case 2-2 (Shell ICP)

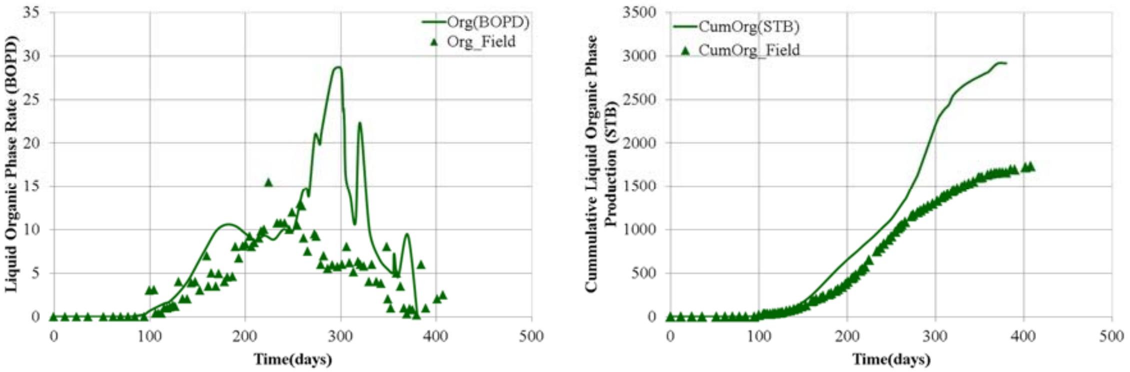

Fig. 33 Production rate and cumulative production of liquid organic phase: validation case 2-2 (Shell ICP)

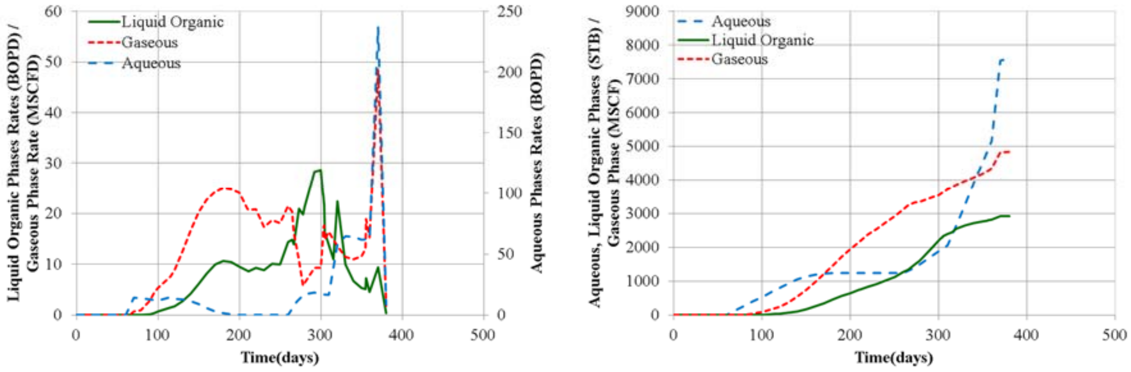

Fig. 34 Production rates and cumulative productions of phases: validation case 2-2 (Shell ICP)

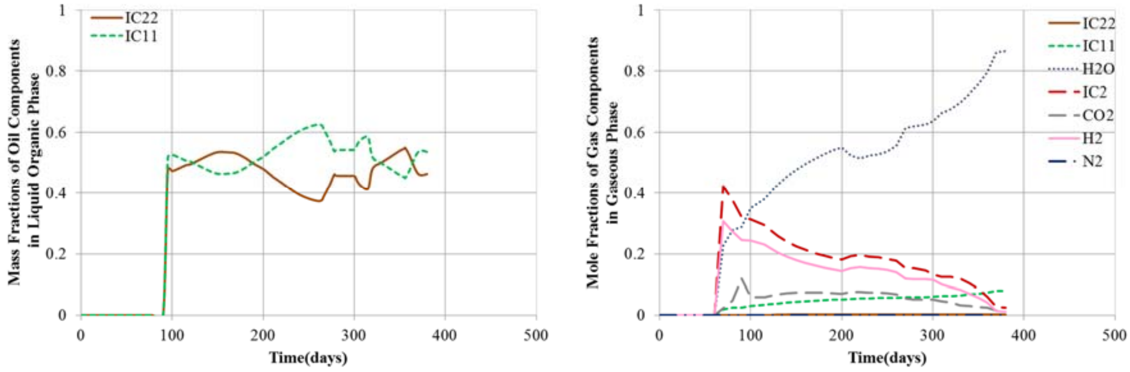

(a) Mass fractions of oil components in liquid organic phase

(b) Mole fractions of gas components in gaseous phase

Fig. 35 Fractions of components in produced fluid: validation case 2-2 (Shell ICP)

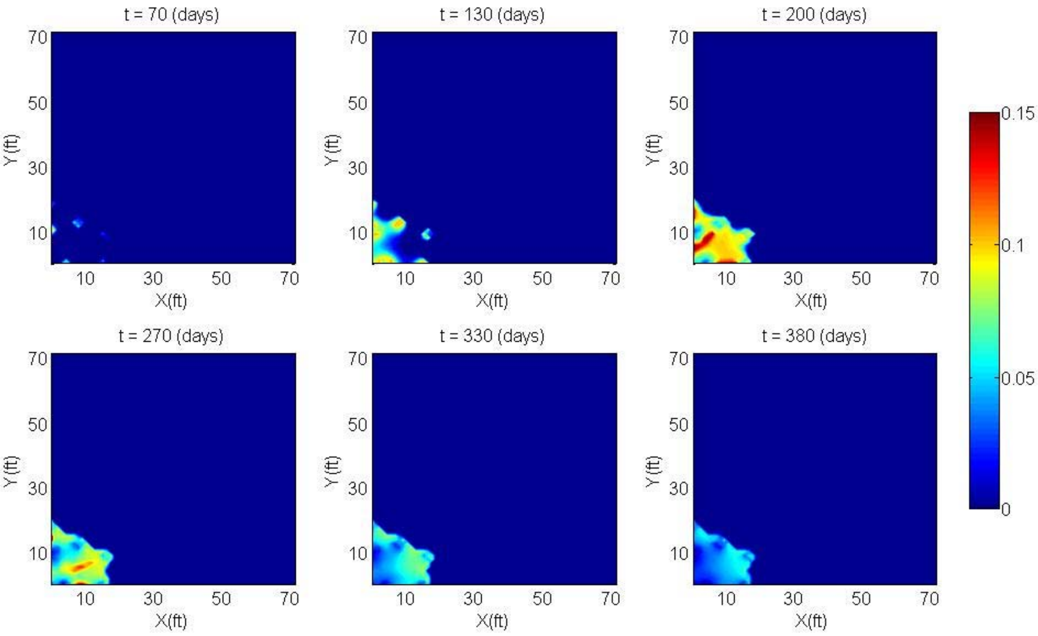

(a) Profiles of liquid organic phase saturation at the matrix domain

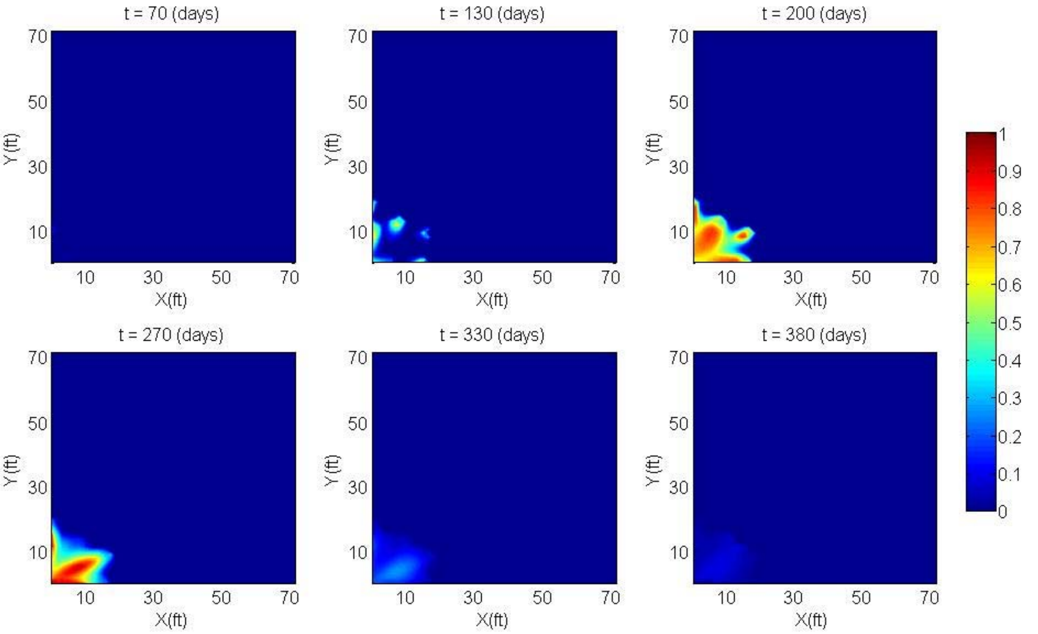

(b) Profiles of liquid organic phase saturation at the fracture domain

Fig. 36 Profiles of liquid organic phase saturation: validation case 2-2 (Shell ICP)

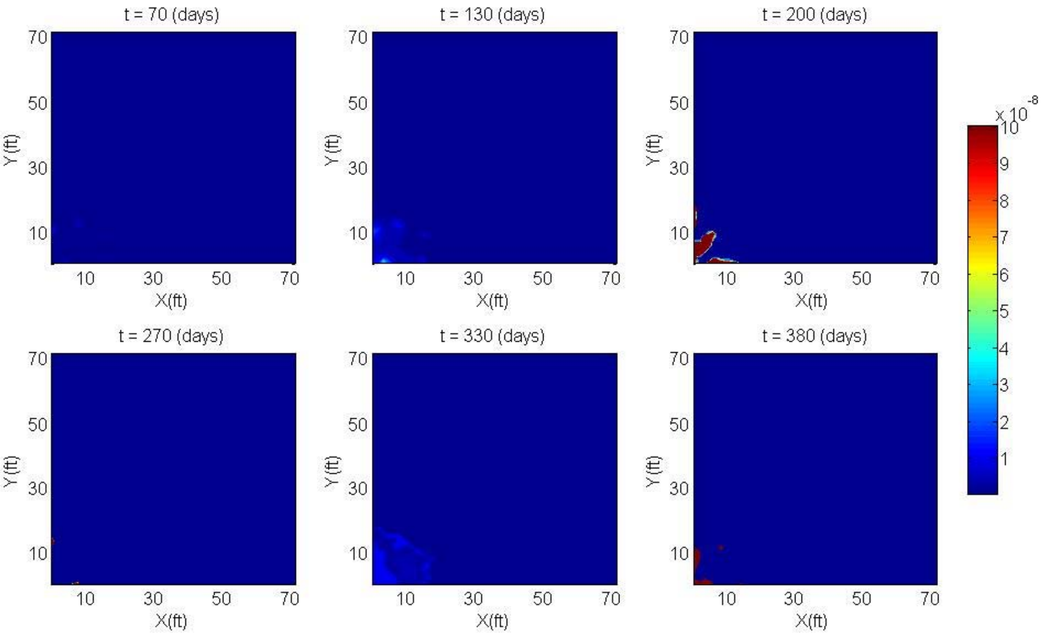

(a) Profiles of gaseous phase saturation at the matrix domain

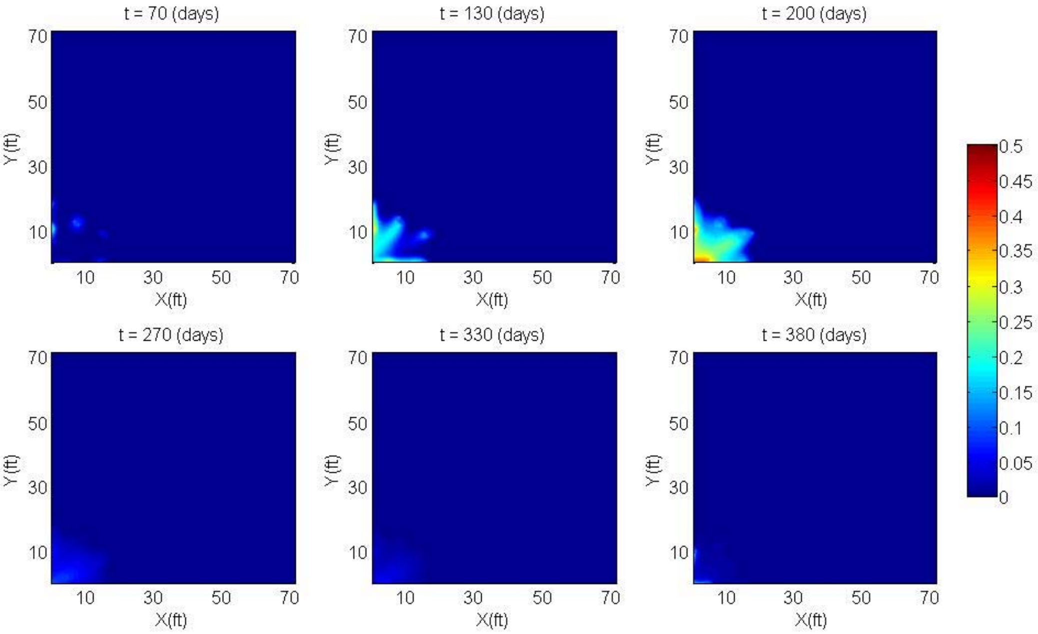

(b) Profiles of gaseous phase saturation at the fracture domain

Fig. 37 Profiles of gaseous phase saturation: validation case 2-2 (Shell ICP)

4.4 Case 3: permeability of pre-existing fracture network

In the case 3, we examine the effect of the fracture network permeability. We use a low fracture permeability of 80 md, and high fracture permeability of 300 md, respectively. We expect that the fracture permeability will affect the time necessary for the in-situ upgrading and production.

4.4.1 Low fracture permeability

In this 80 md-permeability of fracture case, the in-situ upgrading and production proceeds for 400 days, by using the variable flowing bottomhole pressure as shown in Fig. 38. The simulation results are provided in Fig. 38 – Fig. 41, and they are summarized in Table 20. We find the smaller liquid organic phase production than field production data. Lower fracture permeability than standard case causes the cracking of more liquid organic phase into gaseous and solid products before it reaches the production well.

Table 20 Summary of the simulation results: validation case 3-1 (Shell ICP)

Parameters	Values	Parameters	Values
Duration (days)	400	Aqueous production (STB)	9,130
Remaining kerogen (%)	0.23	GOR (MSCF/STB)	3.22
Liquid organic production (STB)	1,420	HC gas production (MSCF)	821
Gaseous production (MSCF)	4,600	Produced HC (BOE)	1,566

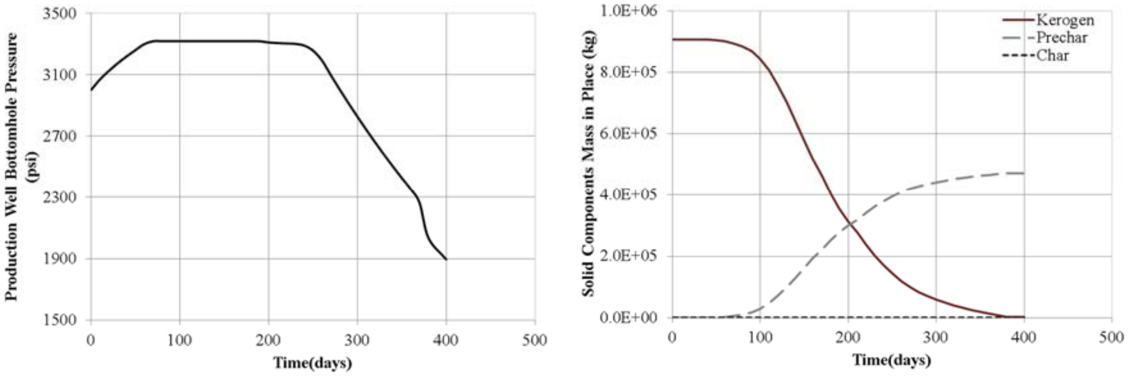

(a) Flowing bottomhole pressure (b) Kerogen mass in place

Fig. 38 Flowing bottomhole pressure and kerogen mass in place: validation case 3-1 (Shell ICP)

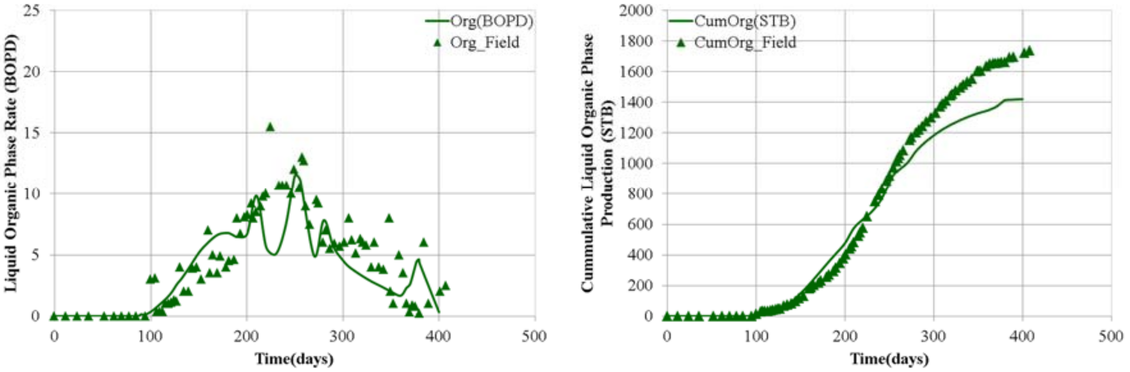

Fig. 39 Production rate and cumulative production of liquid organic phase: validation case 3-1 (Shell ICP)

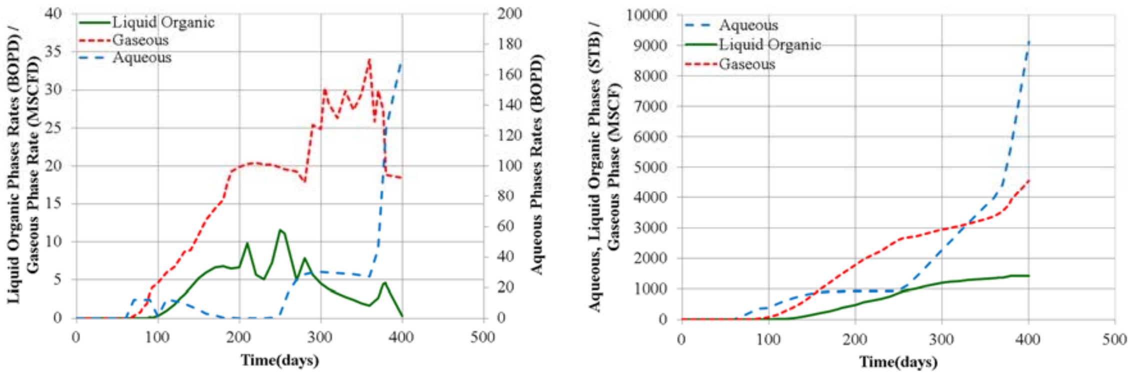

Fig. 40 Production rates and cumulative productions of phases: validation case 3-1 (Shell ICP)

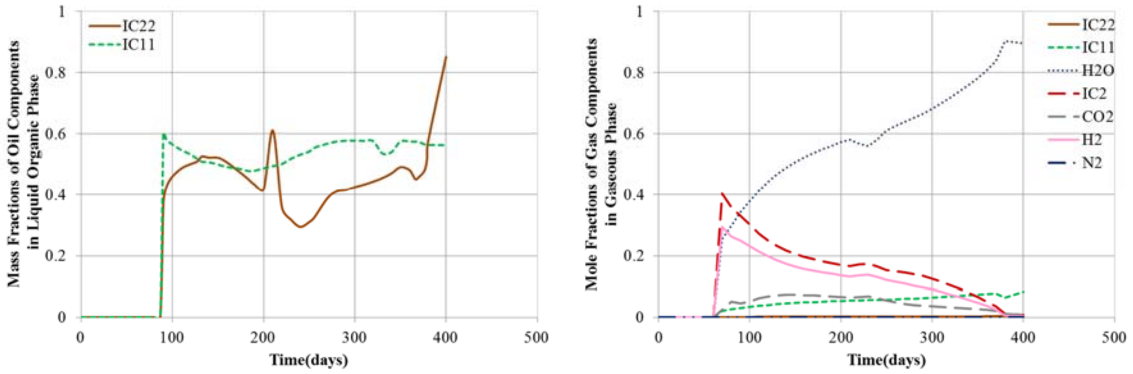

(a) Mass fractions of oil components in liquid organic phase

(b) Mole fractions of gas components in gaseous phase

Fig. 41 Fractions of components in produced fluid: validation case 3-1 (Shell ICP)

4.4.2 High fracture permeability

In this 300 md-permeability of the fracture network case, the in-situ upgrading and the production continues for 335 days, by using the variable flowing bottomhole pressure as shown in Fig. 42. The simulation results are provided in Fig. 42 – Fig. 45, and they are summarized in Table 21. The hydrocarbon is produced faster than the field production data. The remaining kerogen after the production is 11.72 %, which is caused from the shorter duration of the in-situ upgrading and production.

Table 21 Summary of the simulation results: validation case 3-2 (Shell ICP)

Parameters	Values	Parameters	Values
Duration (days)	335	Aqueous production (STB)	6,450
Remaining kerogen (%)	11.72	GOR (MSCF/STB)	2.62
Liquid organic production (STB)	1,740	HC gas production (MSCF)	848
Gaseous production (MSCF)	4,550	Produced HC (BOE)	1,889

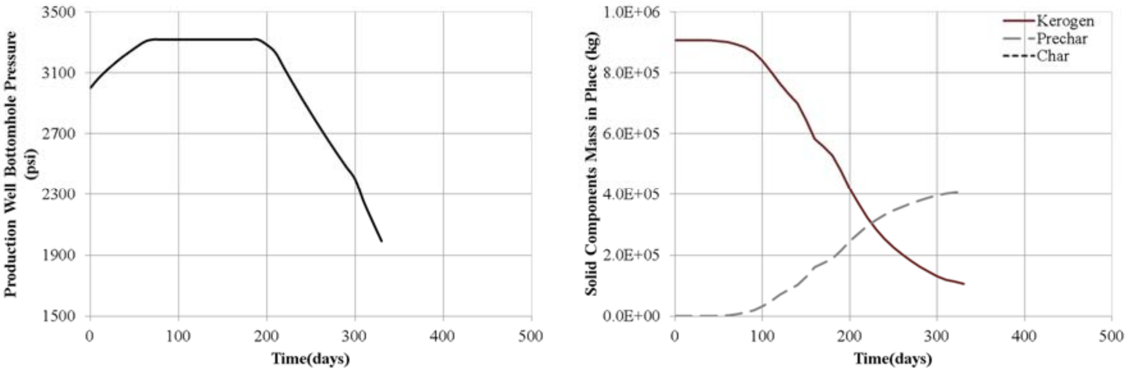

(a) Flowing bottomhole pressure (b) Kerogen mass in place

Fig. 42 Flowing bottomhole pressure and kerogen mass in place: validation case 3-2 (Shell ICP)

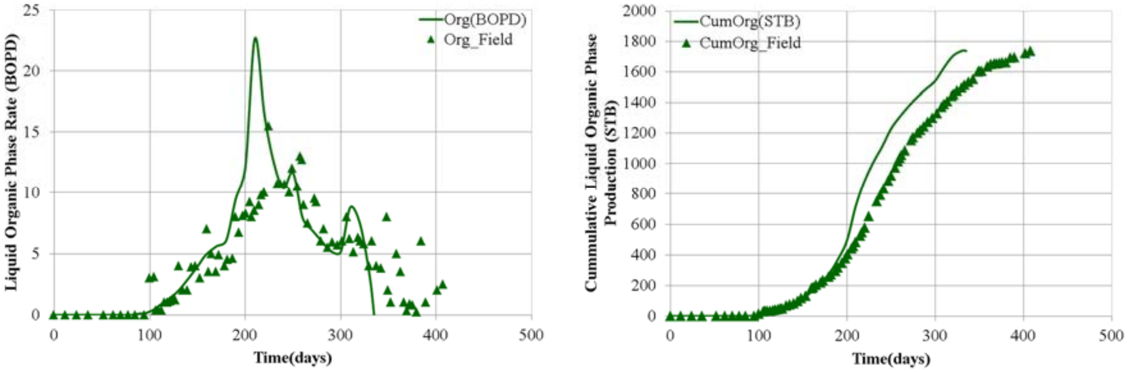

Fig. 43 Production rate and cumulative production of liquid organic phase: validation case 3-2 (Shell ICP)

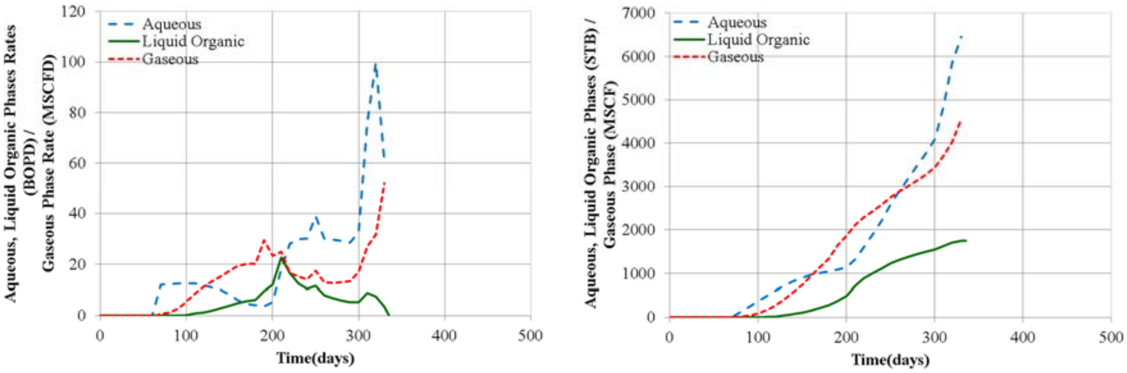

Fig. 44 Production rates and cumulative productions of phases: validation case 3-2 (Shell ICP)

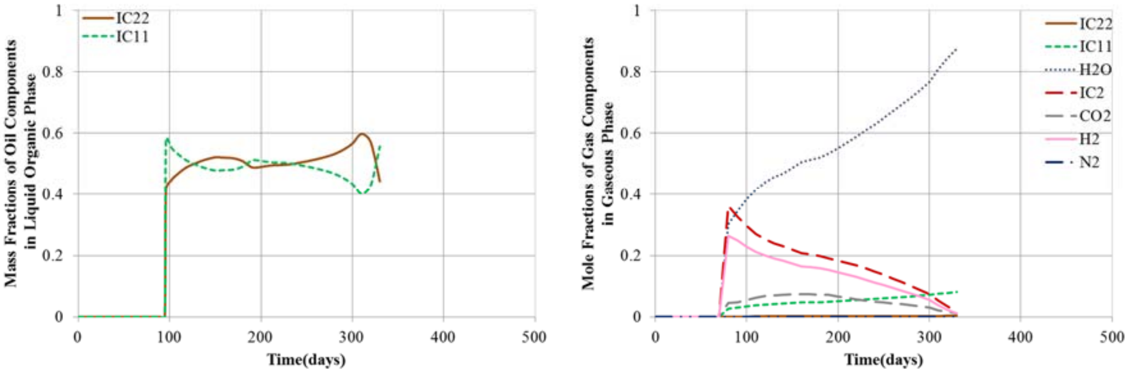

(a) Mass fractions of oil components in liquid organic phase

(b) Mole fractions of gas components in gaseous phase

Fig. 45 Fractions of components in produced fluid: validation case 3-2 (Shell ICP)

4.5. Case 4: thermal conductivity of formation

In the case 4, we examine the effect of the thermal conductivity of the formation on the production. We use the Eq. (2.2) for the low thermal conductivity case, and 3 W/m-K for the high thermal conductivity, respectively.

4.5.1 Low thermal conductivity

In this low thermal conductivity case, the simulation continues for 410 days, by using the variable flowing bottomhole pressure as shown in Fig. 46. The simulation results are provided in Fig. 46 – Fig. 51, and they are summarized in Table 22. The decomposition of kerogen occurs from later time than standard case, and it leads to the lower hydrocarbon production than the field production data. It is confirmed from the profiles of the temperature and kerogen mass fraction.

Table 22 Summary of the simulation results: validation case 4-1 (Shell ICP)

Parameters	Values	Parameters	Values
Duration (days)	410	Aqueous production (STB)	2,630
Remaining kerogen (%)	9.87	GOR (MSCF/STB)	2.60
Liquid organic production (STB)	1,144	HC gas production (MSCF)	748
Gaseous production (MSCF)	2,972	Produced HC (BOE)	1,276

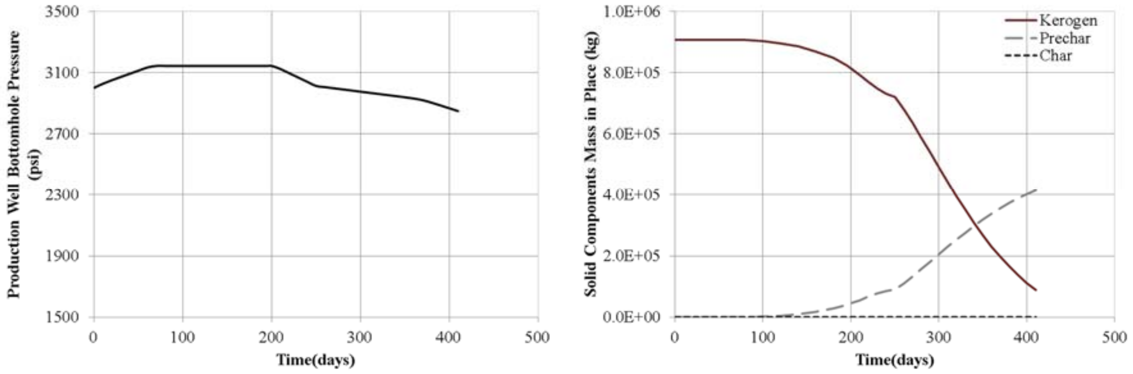

(a) Flowing bottomhole pressure (b) Kerogen mass in place

Fig. 46 Flowing bottomhole pressure and kerogen mass in place: validation case 4-1 (Shell ICP)

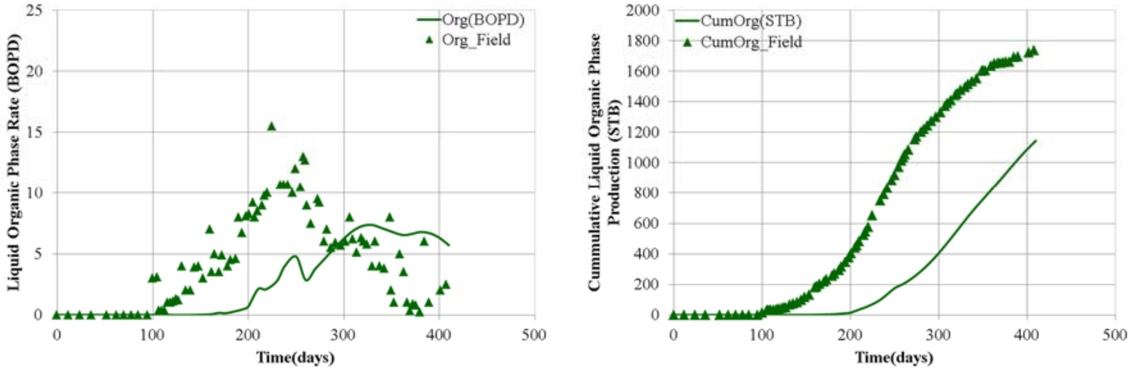

Fig. 47 Production rate and cumulative production of liquid organic phase: validation case 4-1 (Shell ICP)

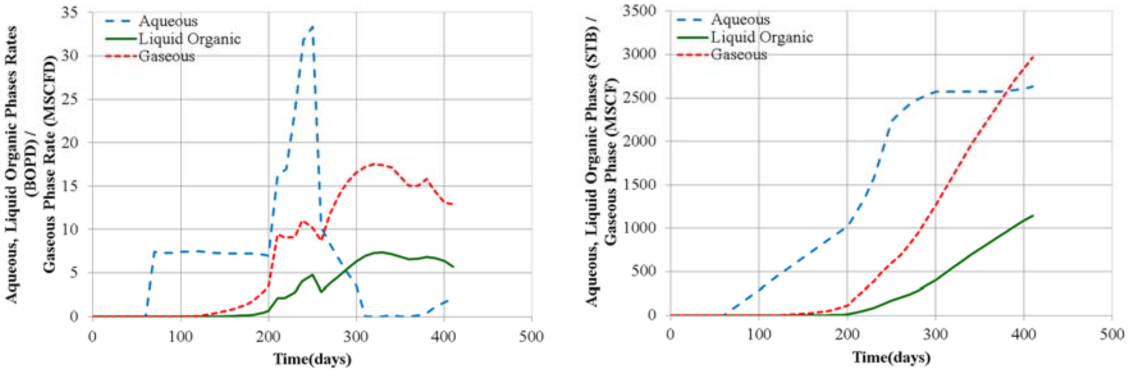

Fig. 48 Production rates and cumulative productions of phases: validation case 4-1 (Shell ICP)

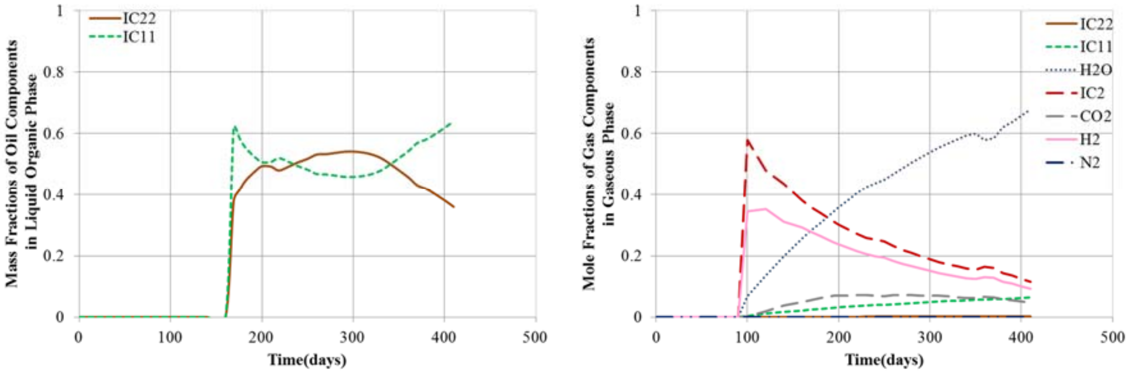

(a) Mass fractions of oil components in liquid organic phase

(b) Mole fractions of gas components in gaseous phase

Fig. 49 Fractions of components in produced fluid: validation case 4-1 (Shell ICP)

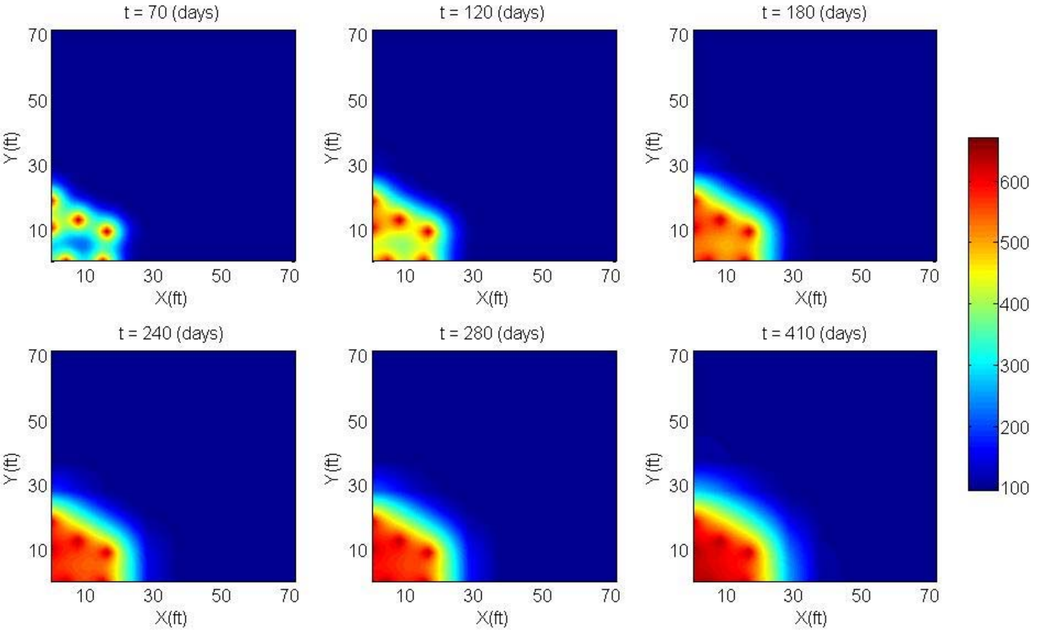

Fig. 50 Profiles of temperature at the matrix domain: validation case 4-1 (Shell ICP)

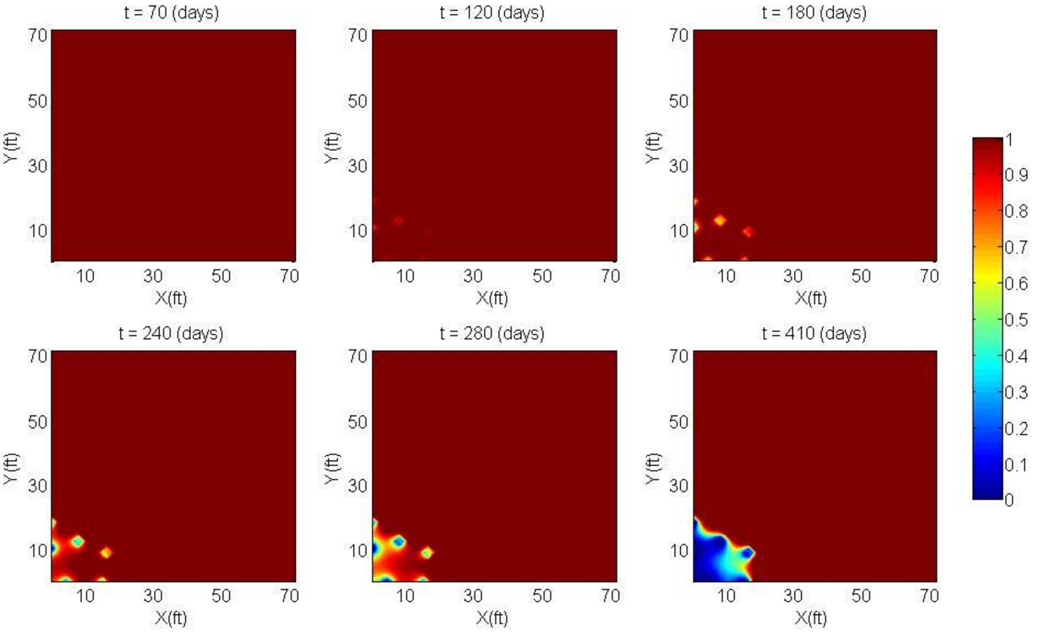

Fig. 51 Profiles of kerogen mass fraction: validation case 4-1 (Shell ICP)

4.5.2 High thermal conductivity

In this 3.0 W/m-K-thermal conductivity of the formation case, the simulation continues for 310 days, by using the variable flowing bottomhole pressure as shown in Fig. 52. The simulation results are provided in Fig. 52 – Fig. 57, and they are summarized in Table 23. The production of the hydrocarbon should resume faster than the standard case and the low thermal conductivity case, in order to avoid the excessive cracking of liquid organic phase into gaseous phase and solid products. We observe the smaller liquid organic phase production than field production data, due to the cracking of the liquid organic phase in the wider area than the standard case.

Table 23 Summary of the simulation results: validation case 4-2 (Shell ICP)

Parameters	Values	Parameters	Values
Duration (days)	310	Aqueous production (STB)	11,960
Remaining kerogen (%)	0.03	GOR (MSCF/STB)	3.24
Liquid organic production (STB)	1,430	HC gas production (MSCF)	853
Gaseous production (MSCF)	4,624	Produced HC (BOE)	1,578

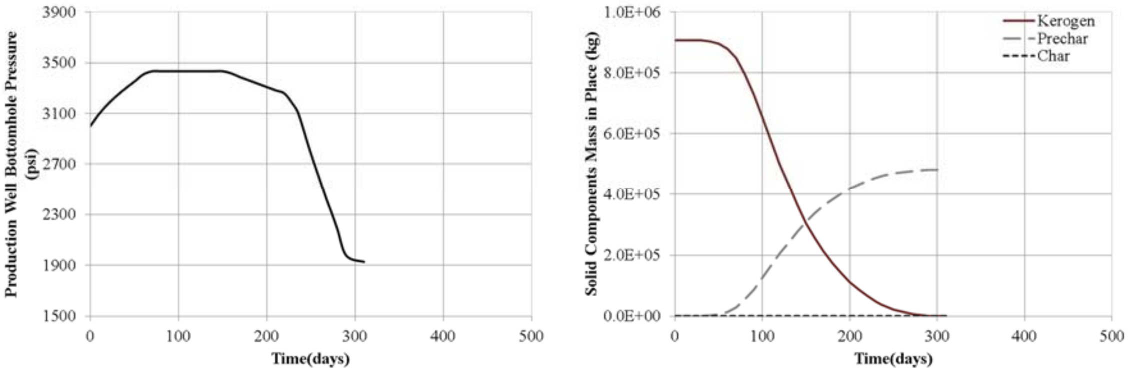

(a) Flowing bottomhole pressure

(b) Kerogen mass in place

Fig. 52 Flowing bottomhole pressure and kerogen mass in place: validation case 4-2 (Shell ICP)

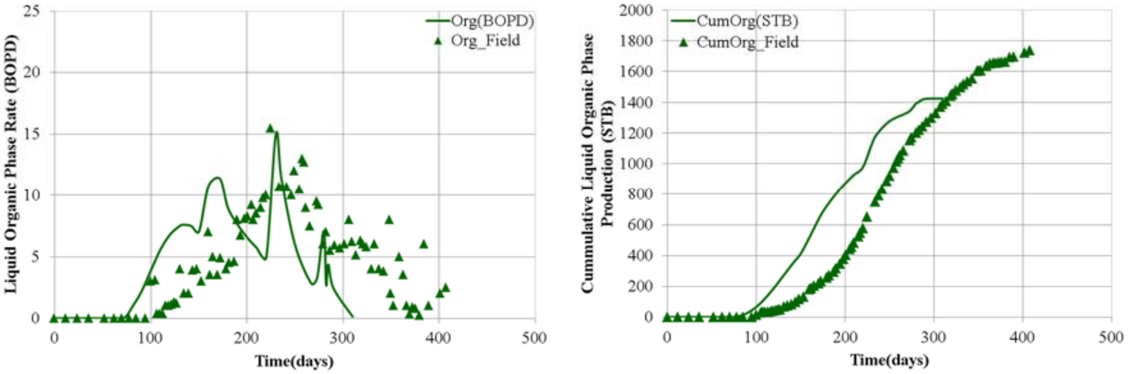

Fig. 53 Production rate and cumulative production of liquid organic phase: validation case 4-2 (Shell ICP)

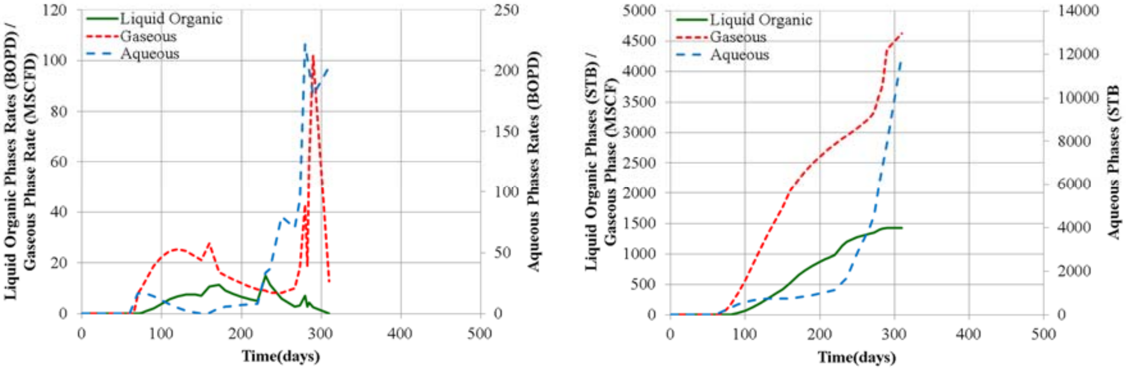

Fig. 54 Production rates and cumulative productions of phases: validation case 4-2 (Shell ICP)

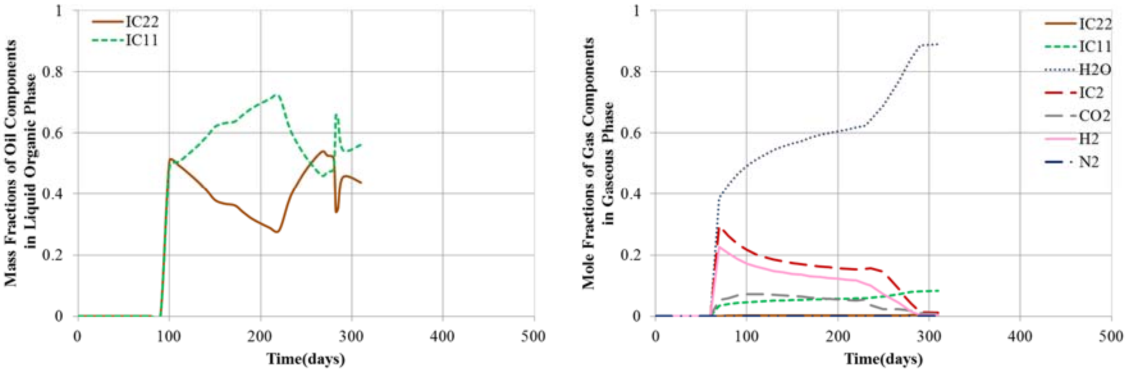

(a) Mass fractions of oil components in liquid organic phase

(b) Mole fractions of gas components in gaseous phase

Fig. 55 Fractions of components in produced fluid: validation case 4-2 (Shell ICP)

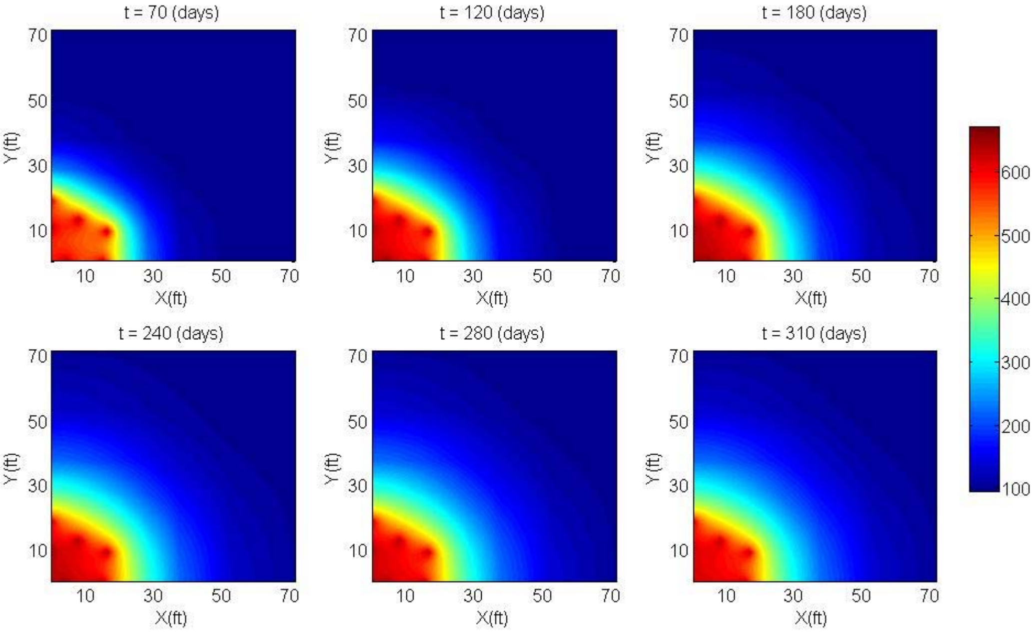

Fig. 56 Profiles of temperature at the matrix domain: validation case 4-2 (Shell ICP)

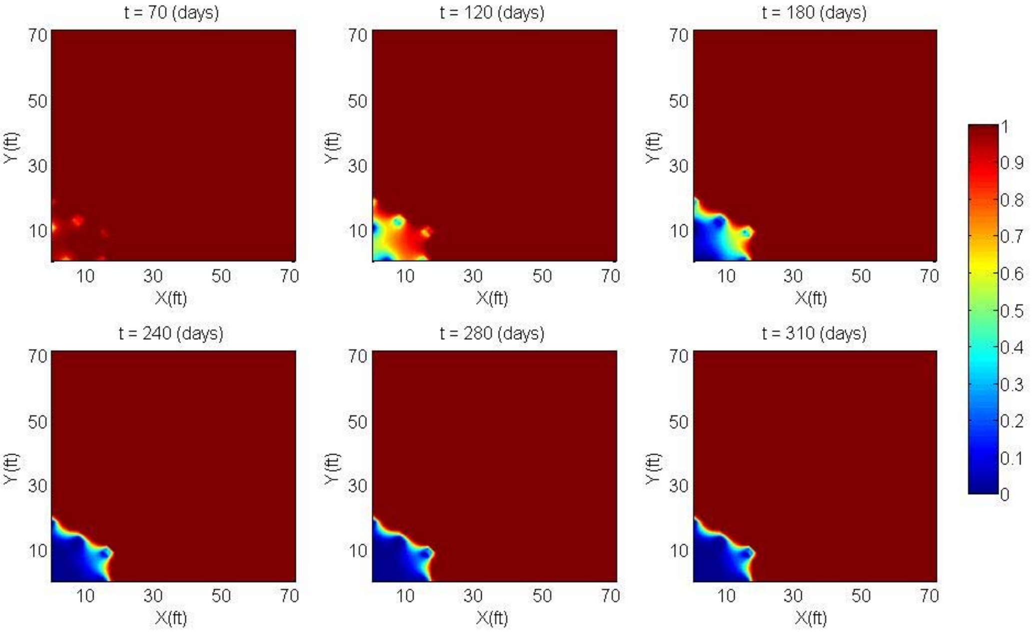

Fig. 57 Profiles of kerogen mass fraction: validation case 4-2 (Shell ICP)

4.6 Chapter summary

In this chapter, we validated the developed simulator by reproducing the filed production data of Shell ICP process. We conducted the sensitivity analyses related to the presence or absence of the fracture network, oil shale grade (organic matter content), fracture network permeability, and the formation thermal conductivity. The validated model has an oil shale grade of 25 gal/ton, fracture permeability of 150 md, and formation thermal conductivity of 150 W/m-K.

We find the following conclusions in this chapter.

1. Absence of the fracture network results the more gaseous phase production and the less liquid phases (aqueous phase and liquid organic phase) production.
2. Oil shale grade affects the amount of remaining liquid organic phase in the matrix domain as well as the amount of recoverable hydrocarbons. This is caused from that the oil shale grade and corresponding organic matter content affect the matrix porosity and permeability.
3. Permeability of the fracture domain has the effect on the amount of the cracked liquid organic phase as well as the time necessary for production and the amount of recoverable hydrocarbon production.
4. Thermal conductivity of the formation affects the speed of the kerogen decomposition and the amount of the cracked liquid organic phases. Higher thermal conductivity doesn't lead to the greater hydrocarbon production, by cracking of the more liquid organic phase.

CHAPTER V

CASE STUDY

In this chapter, we study the diverse application cases of in-situ upgrading process, by using the validated reservoir model obtained from CHATER IV. This study includes Shell ICP as a pattern, ExxonMobil Electrofrac, and TAMU Steamfrac processes. We define and analyze the significant effects of the factors for each process, and evaluate and compare the energy efficiency of each case. It allows us the to find out the most effective heating and production strategy for each case.

5.1 Shell ICP process

Shell ICP process can be utilized as a set of the multiple hexagonal patterns as illustrated in Fig. 58. We simulate a quarter of one pattern by using the 2D model with 14*17 grid blocks. The model has 14*17-ft^2 area with 113 ft-height. The outer grey part in the simulation geometry in Fig. 58 consists of inactive cells, which is not accounted in the computation. We conducted the various simulation runs with 6 cases, by using different heater temperatures and process durations.

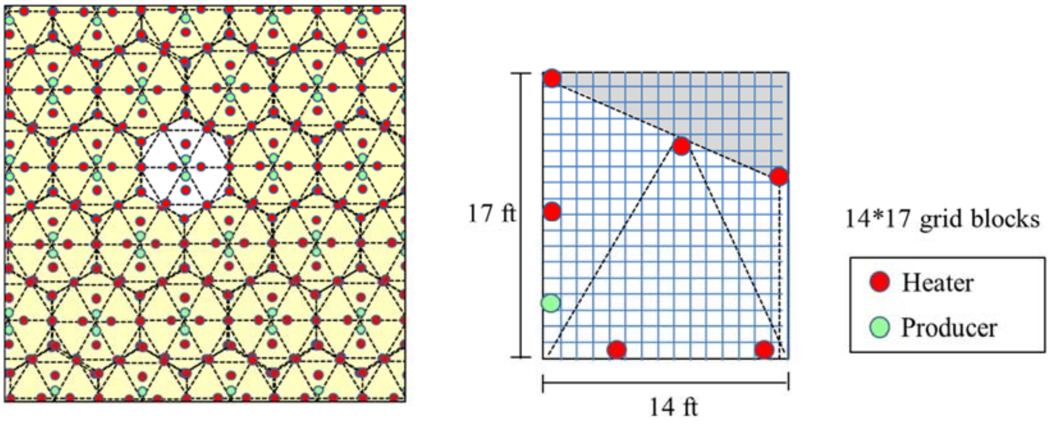

Fig. 58 Configuration and simulation geometry of Shell ICP in a pattern

5.1.1 Case 1: heater temperature of 650 °F

In this case, we implement the in-situ upgrading and production as the same manner as the validation case in CHAPTER IV. We use a temperature of the vertical heaters of 650 °F, and continue the production during 320 days, by using the variable flowing bottomhole pressure as shown in Fig. 59. The simulation results are shown in Fig. 59 – Fig. 65, and they are summarized in Fig. 24. The results are computed in one pattern. Formation temperature in the pattern evenly reaches 650 °F at 150 days, and the whole kerogen decomposes at 200 days. In this simulation run, the time of heating and production is significantly longer than the time necessary for the kerogen decomposition in the pattern, and it results in the small amount of the recoverable hydrocarbons due to the excessive cracking. This is observed at the saturation profiles of liquid organic phase in Fig. 65.

By summing up the heat flux in the every grid block of the reservoir, we could get the energy input of 741 BOE introduced from the heaters to the reservoir. Here, the thermal energy was converted into the chemical energy by using the conversion factor of 1.706e-10 J/BOE. In Fig. 62, we can find the cumulative energy input, energy output and energy efficiency. The energy efficiency at the process completion is 51.6 %. The maximum energy efficiency is 54 % during the process, and it approaches at 170 days.

Table 24 Summary of the simulation results: application case 1 (Shell ICP)

Parameters	Values	Parameters	Values
Duration (days)	320	GOR (MSCF/STB)	12.9
Remaining kerogen (%)	0	HC gas production (MSCF)	883
Liquid organic production (STB)	263	Produced HC (BOE)	419
Gaseous production (MSCF)	3,386	Energy input (BOE)	741
Aqueous production (STB)	937	Energy efficiency (%)	51.6

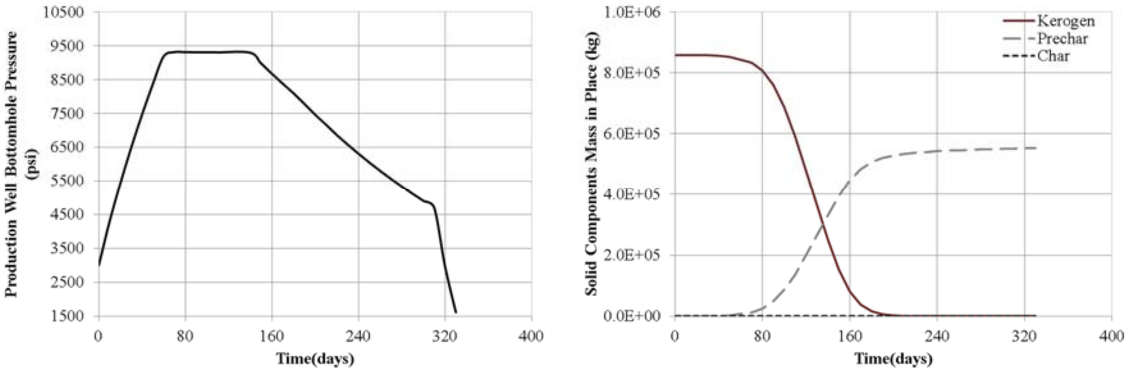

(a) Flowing bottomhole pressure (b) Kerogen mass in place

Fig. 59 Flowing bottomhole pressure and kerogen mass in place: application case 1 (Shell ICP)

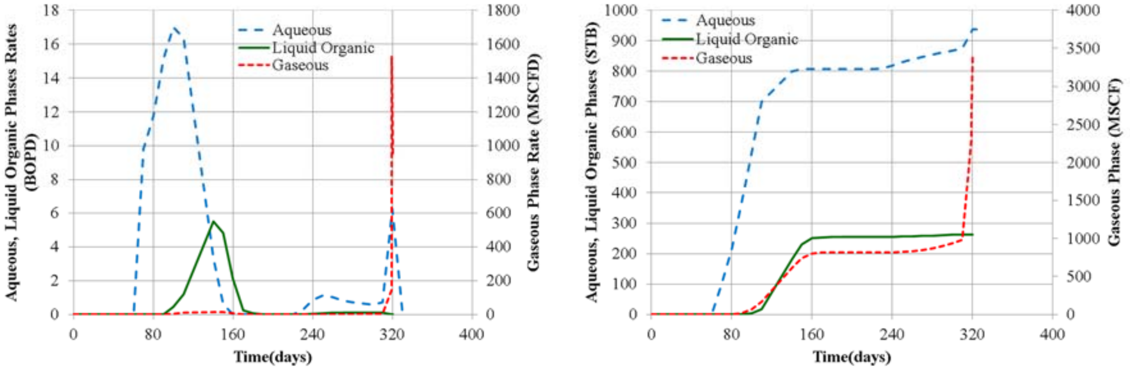

Fig. 60 Production rates and cumulative productions of phases: application case 1 (Shell ICP)

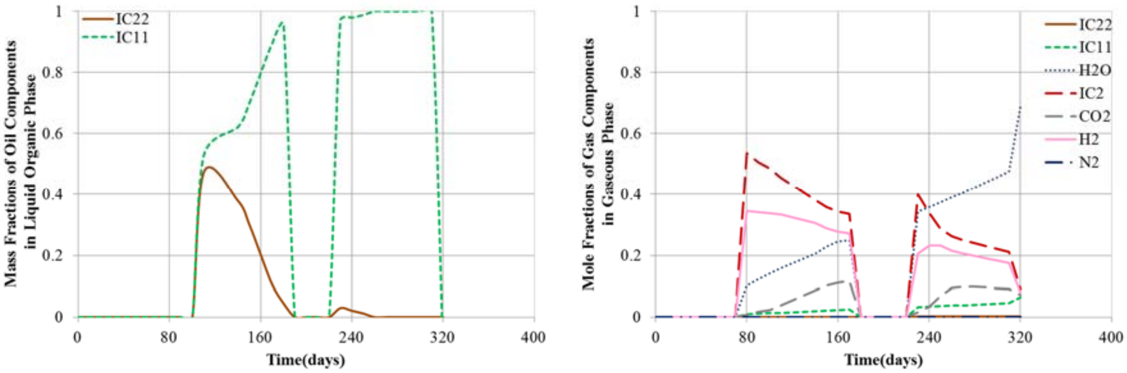

(a) Mass fractions of oil components in liquid organic phase

(b) Mole fractions of gas components in gaseous phase

Fig. 61 Fractions of components in produced fluid: application case 1 (Shell ICP)

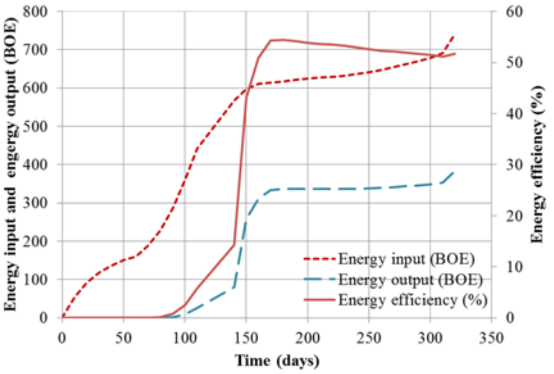

Fig. 62 Energy input, energy output and energy efficiency: application case 1 (Shell ICP)

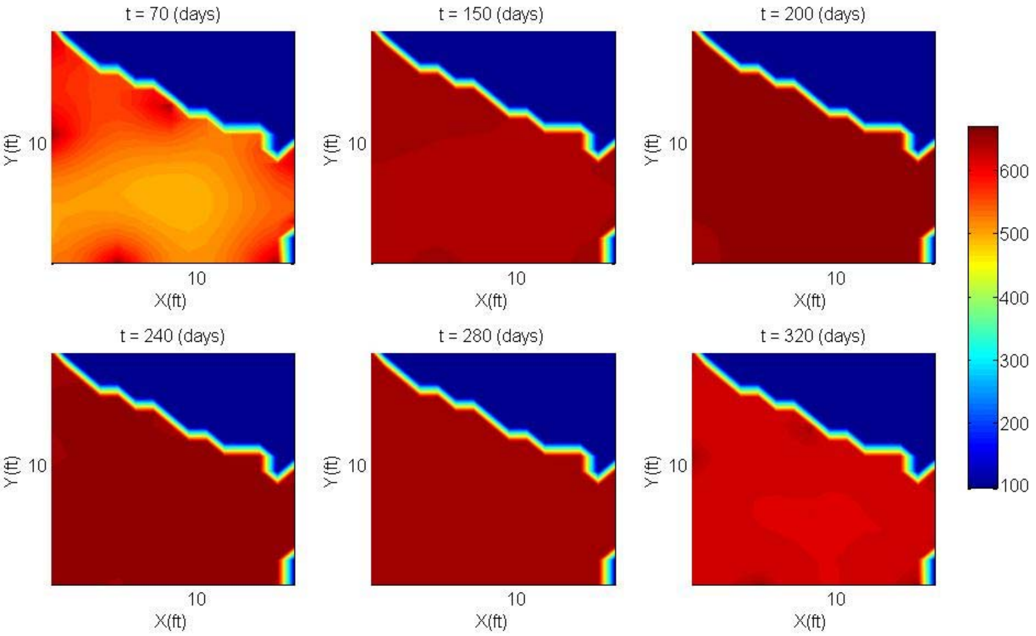

Fig. 63 Profiles of temperature at the matrix: application case 1 (Shell ICP)

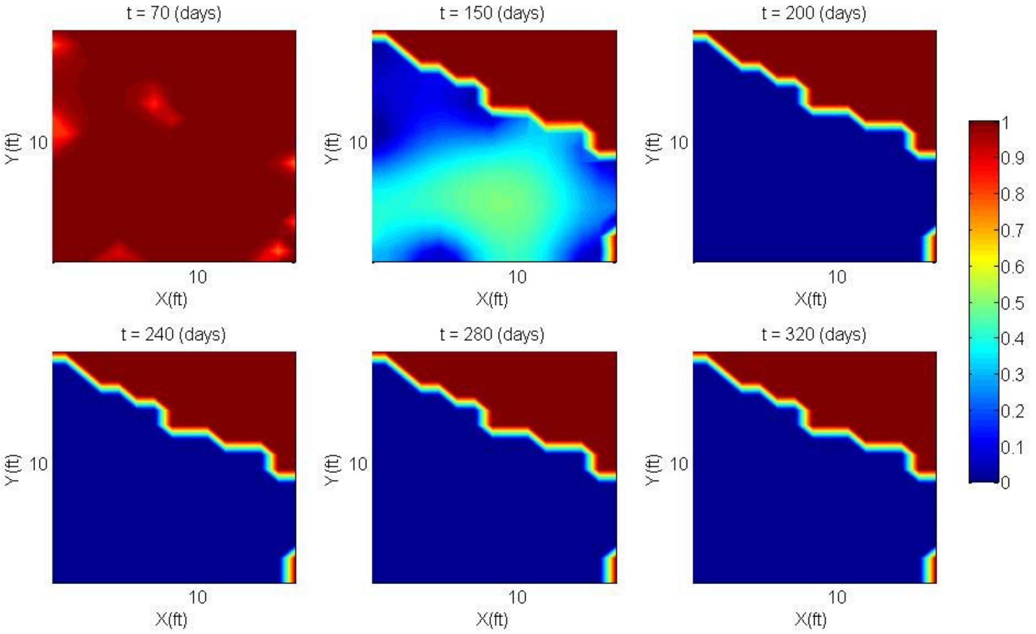

Fig. 64 Profiles of kerogen mass fraction: application case 1 (Shell ICP)

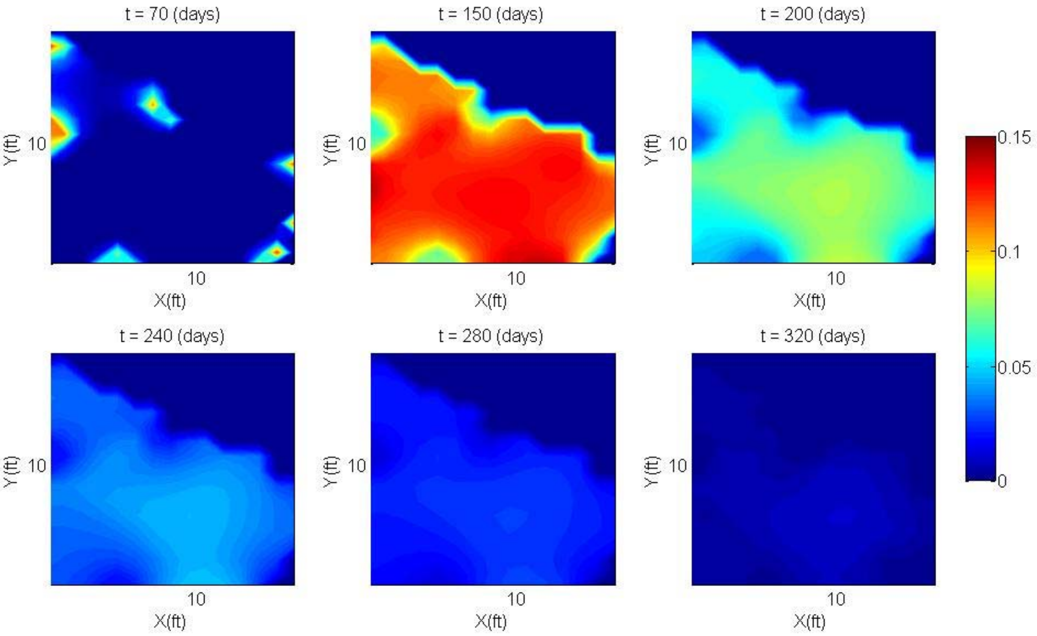

(a) Profiles of liquid organic phase saturation at the matrix domain

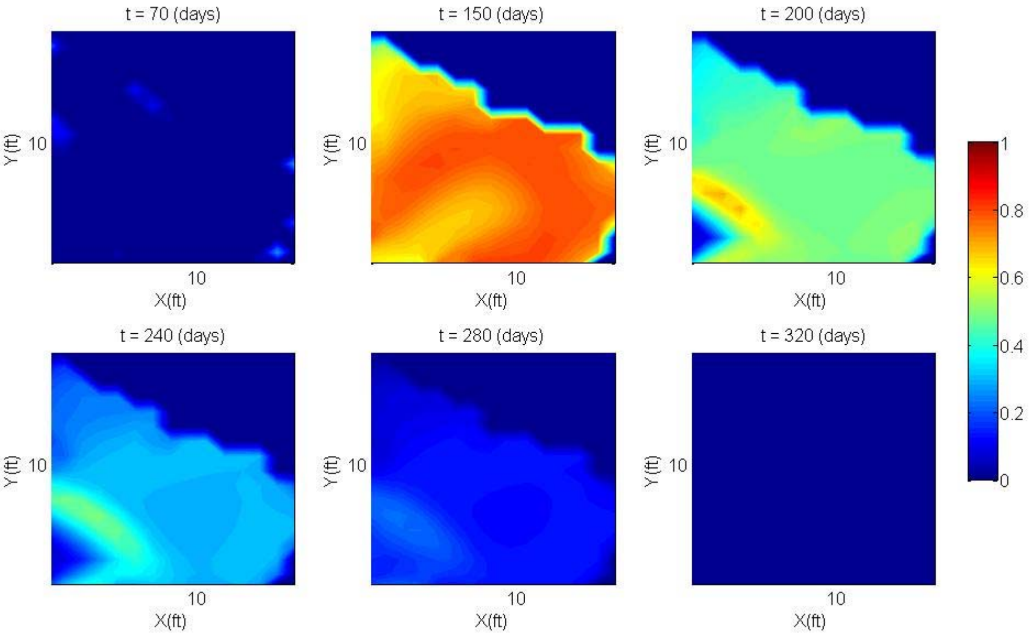

(b) Profiles of liquid organic phase saturation at the fracture domain

Fig. 65 Profiles of liquid organic phase saturation: application case 1 (Shell ICP)

5.1.2 Case 2: heater temperature of 650 °F, shorter production period than case 1

In order to avoid the excessive cracking of liquid organic phase, we conduct the simulation case of short time period. The heater temperature is 650 °F as the same as the case 1, but the in-situ upgrading and production time is 164 days, by using the variable flowing bottomhole pressure as shown in Fig. 66. The simulation results are provided in Fig. 66 – Fig. 69, and they are summarized in Table 25. The results are computed in one pattern.

The total produced hydrocarbon is 802 BOE, and the energy input is 1,350 BOE, and it leads the energy efficiency of 59.3 %. The amount of the hydrocarbon production is greater than the case 1, but the higher energy input makes insignificant increase of energy efficiency. The withdrawal of larger amount of hydrocarbon fluid necessitates the higher energy input for maintaining the heater temperature.

Table 25 Summary of the simulation results: application case 2 (Shell ICP)

Parameters	Values	Parameters	Values
Duration (days)	164	GOR (MSCF/STB)	7.48
Remaining kerogen (%)	14.36	HC gas production (MSCF)	637
Liquid organic production (STB)	689	Produced HC (BOE)	802
Gaseous production (MSCF)	5,154	Energy input (BOE)	1,350
Aqueous production (STB)	1,304	Energy efficiency (%)	59.3

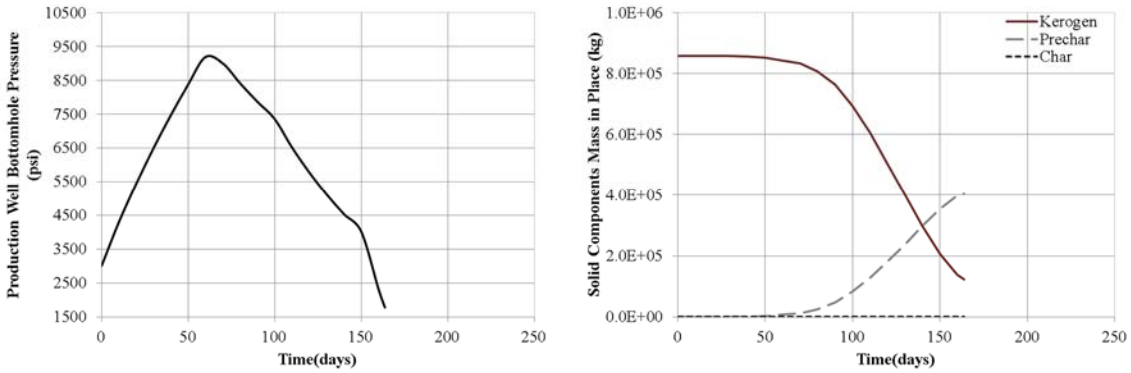

(a) Flowing bottomhole pressure

(b) Kerogen mass in place

Fig. 66 Flowing bottomhole pressure and kerogen mass in place: application case 2 (Shell ICP)

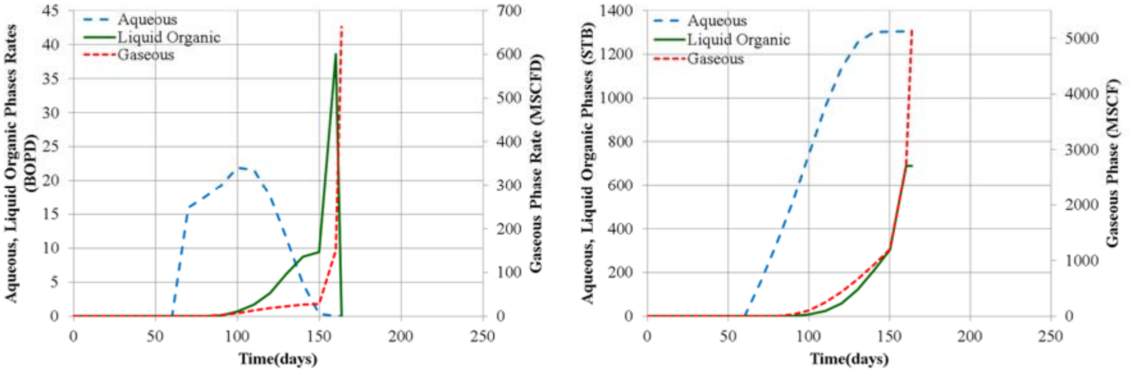

Fig. 67 Production rates and cumulative productions of phases: application case 2 (Shell ICP)

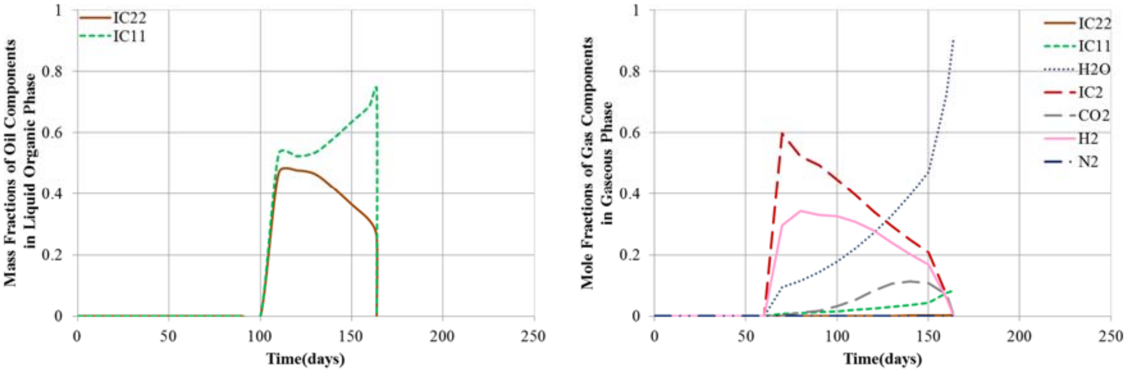

(a) Mass fractions of oil components in liquid organic phase

(b) Mole fractions of gas components in gaseous phase

Fig. 68 Fractions of components in produced fluid: application case 2 (Shell ICP)

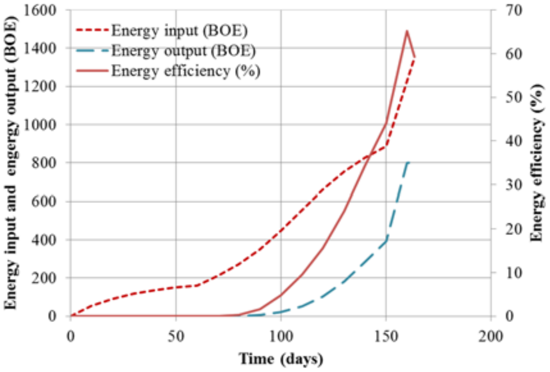

Fig. 69 Energy input, energy output and energy efficiency: application case 2 (Shell ICP)

5.1.3 Case 3: heater temperature of 635 °F

In the case 3, we conducted the simulation by using the lower heater temperature of 635 °F, in order to decrease the amount of cracked liquid organic phase, and to extend the time for enough kerogen decomposition. We simulate the 240 days of the heating and production, by using variable flowing bottomhole pressure as shown in Fig. 70. The simulation results are provided in Fig. 70 – Fig. 73, and they are summarized in Table 26. The results are computed in one pattern.

The lower heater temperature allows the longer time for kerogen decomposition while avoiding excessive cracking of liquid organic phase. This leads the greater hydrocarbon production and higher energy efficiency. The energy efficiency after the process is 87.7 %.

Table 26 Summary of the simulation: application 3 (Shell ICP)

Parameters	Values	Parameters	Values
Duration (days)	240	GOR (MSCF/STB)	8.01
Remaining kerogen (%)	1.26	HC gas production (MSCF)	668
Liquid organic production (STB)	786	Produced HC (BOE)	904
Gaseous production (MSCF)	6,304	Energy input (BOE)	1,032
Aqueous production (STB)	957	Energy efficiency (%)	87.7

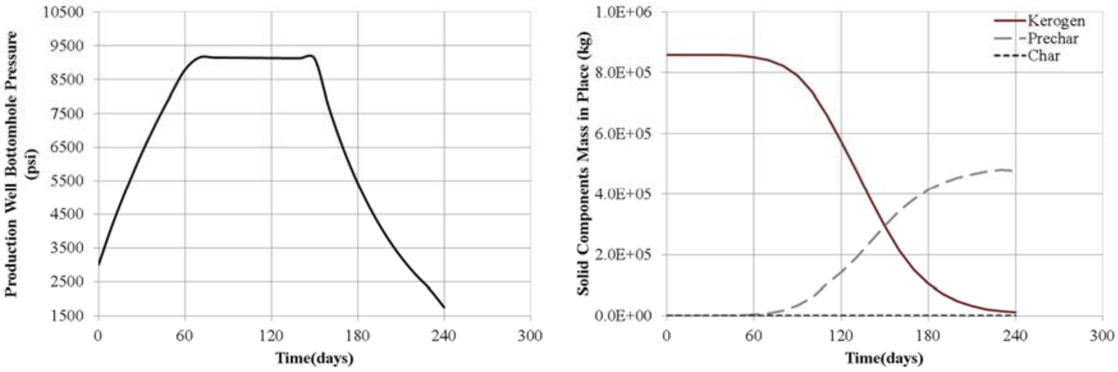

(a) Flowing bottomhole pressure (b) Kerogen mass in place

Fig. 70 Flowing bottomhole pressure and kerogen mass in place: application case 3 (Shell ICP)

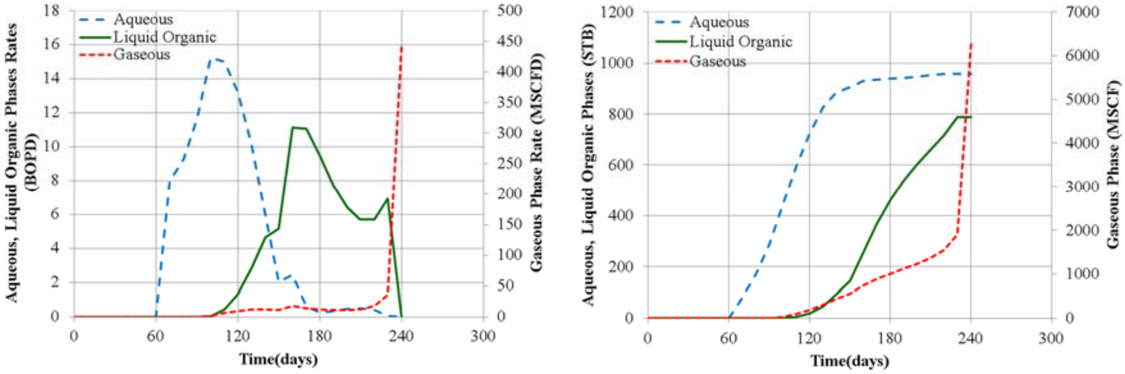

Fig. 71 Production rates and cumulative productions of phases: application case 3

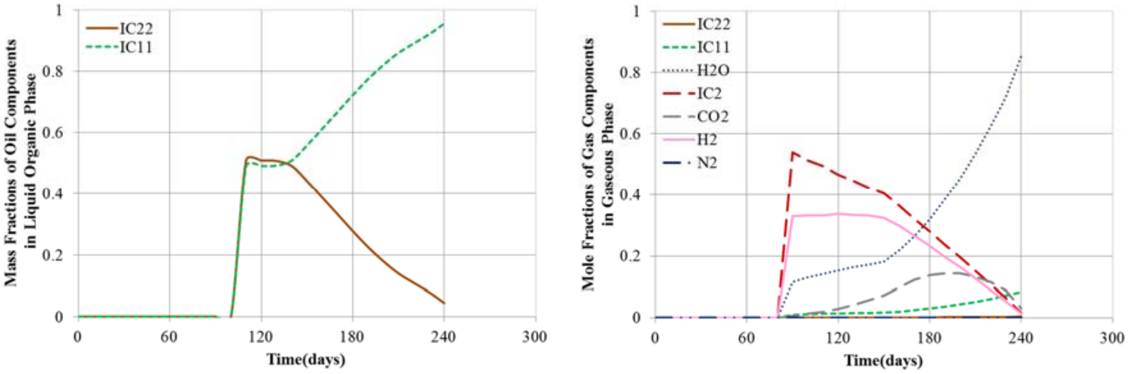

(a) Mass fractions of oil components in liquid organic phase

(b) Mole fractions of gas components in gaseous phase

Fig. 72 Fractions of components in produced fluid: application case 3 (Shell ICP)

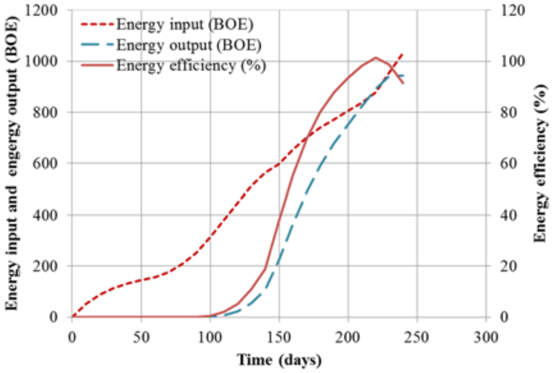

Fig. 73 Energy input, energy output and energy efficiency: application case 3 (Shell ICP)

5.1.4 Case 4: heater temperature of 625 °F

In the case 4, we conducted the simulation by using the lower heater temperature of 625 °F. We simulate the 240 days of the heating and production, by using variable flowing bottomhole pressure as shown in Fig. 74. The simulation results are provided in Fig. 74 – Fig. 77, and they are summarized in Table 27. The results are computed in one pattern.

The lower heater temperature allows the longer time for kerogen decomposition while avoiding excessive cracking of liquid organic phase. This leads the greater hydrocarbon production and higher energy efficiency. The energy efficiency after the process is 106 %, and it means the higher energy withdrawal than the energy input.

Table 27 Summary of the simulation: application case 4 (Shell ICP)

Parameters	Values	Parameters	Values
Duration (days)	240	GOR (MSCF/STB)	4.57
Remaining kerogen (%)	4.10	HC gas production (MSCF)	652
Liquid organic production (STB)	942	Produced HC (BOE)	1,057
Gaseous production (MSCF)	4,310	Energy input (BOE)	993
Aqueous production (STB)	976	Energy efficiency (%)	106

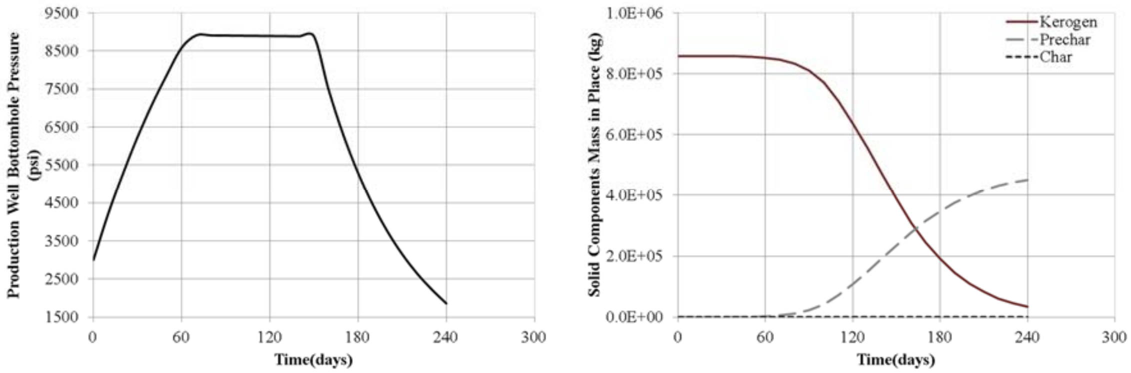

(a) Flowing bottomhole pressure (b) Kerogen mass in place

Fig. 74 Flowing bottomhole pressure and kerogen mass in place: application case 4 (Shell ICP)

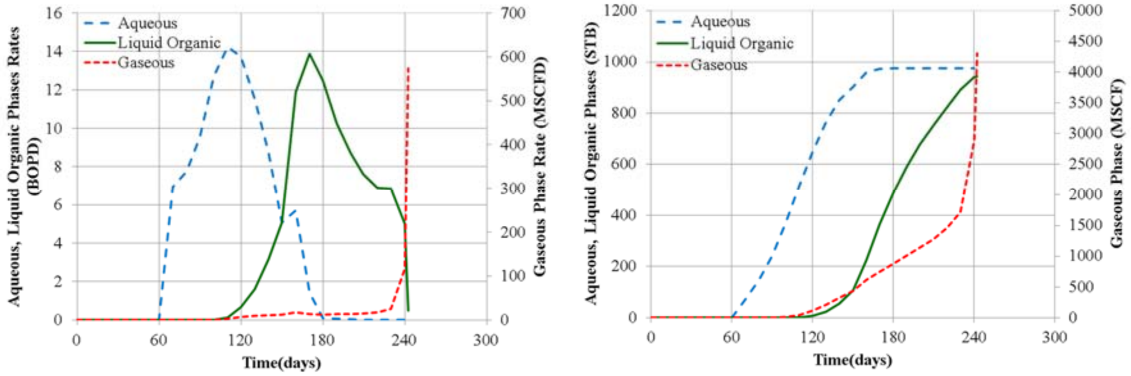

Fig. 75 Production rates and cumulative productions of phases: application case 4

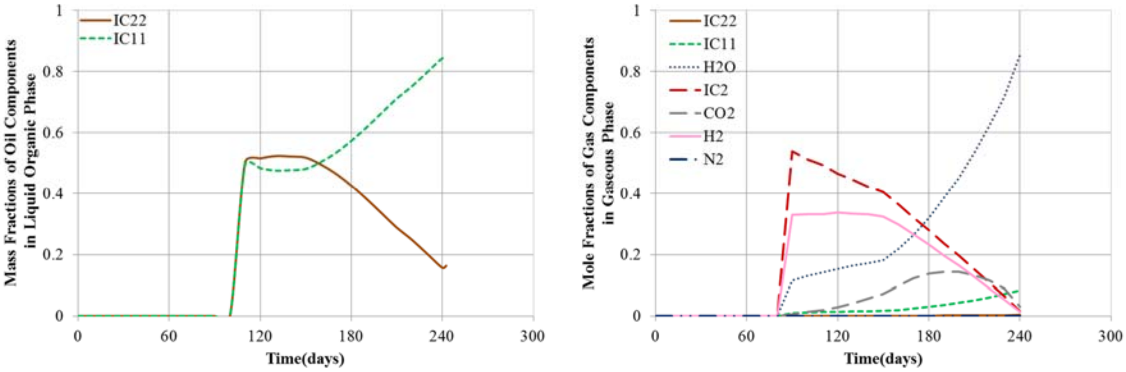

(a) Mass fractions of oil components in liquid organic phase

(b) Mole fractions of gas components in gaseous phase

Fig. 76 Fractions of components in produced fluid: application case 4 (Shell ICP)

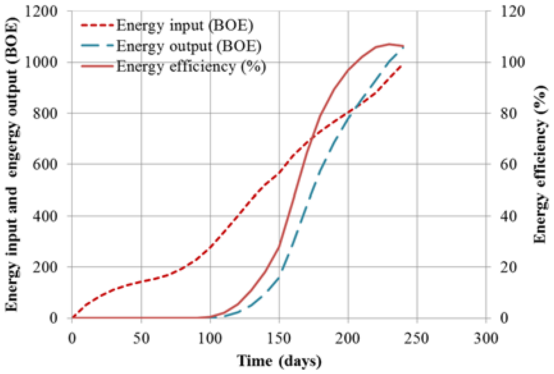

Fig. 77 Energy input, energy output and energy efficiency: application case 4 (Shell ICP)

5.1.5 Case 5: heater temperature of 620 °F

In the case 5, we tried the lower heater temperature of 620 °F. We simulate the 340 days of the heating and production, by using variable flowing bottomhole pressure as shown in Fig. 78. The simulation results are provided in Fig. 78 – Fig. 81, and they are summarized in Table 28. The results are computed in one pattern.

The lower heater temperature allows the longer time for kerogen decomposition while avoiding excessive cracking of liquid organic phase. This leads the greater hydrocarbon production and higher energy efficiency. The energy efficiency after the process is 103 %.

Table 28 Summary of the simulation results: application 4 (Shell ICP)

Parameters	Values	Parameters	Values
Duration (days)	340	GOR (MSCF/STB)	3.69
Remaining kerogen (%)	0.55	HC gas production (MSCF)	713
Liquid organic production (STB)	951	Produced HC (BOE)	1,077
Gaseous production (MSCF)	3,507	Energy input (BOE)	1,041
Aqueous production (STB)	950	Energy efficiency (%)	103

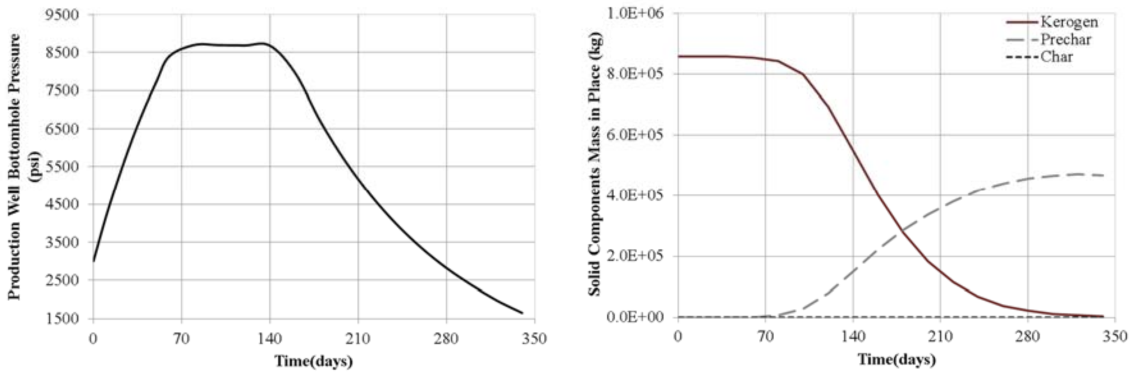

(a) Flowing bottomhole pressure (b) Kerogen mass in place

Fig. 78 Flowing bottomhole pressure and kerogen mass in place: application case 5 (Shell ICP)

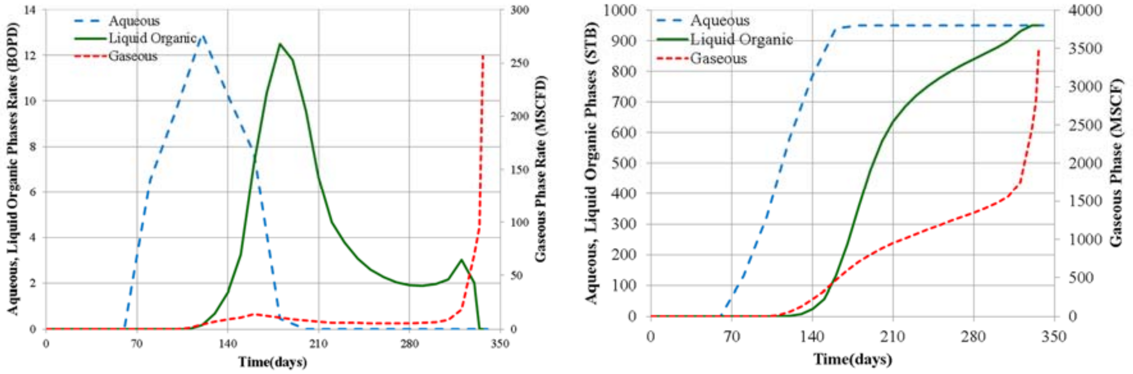

Fig. 79 Production rates and cumulative productions of phases: application case 5

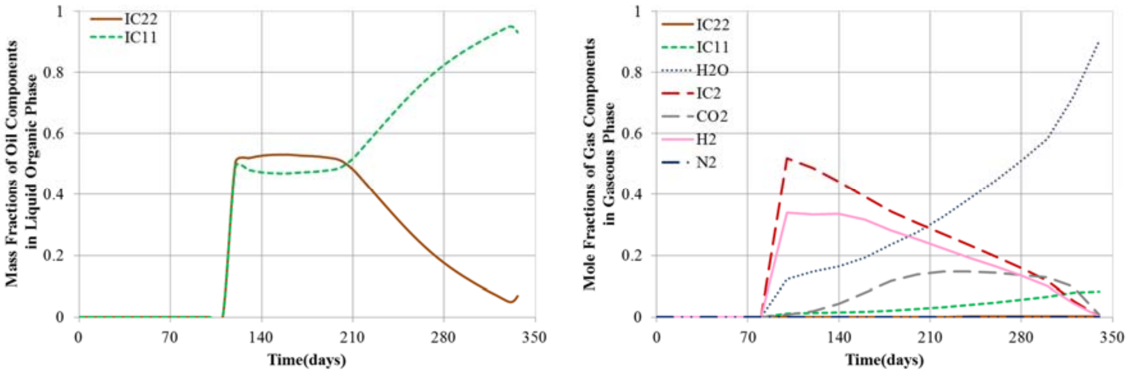

(a) Mass fractions of oil components in liquid organic phase

(b) Mole fractions of gas components in gaseous phase

Fig. 80 Fractions of components in produced fluid: application case 5 (Shell ICP)

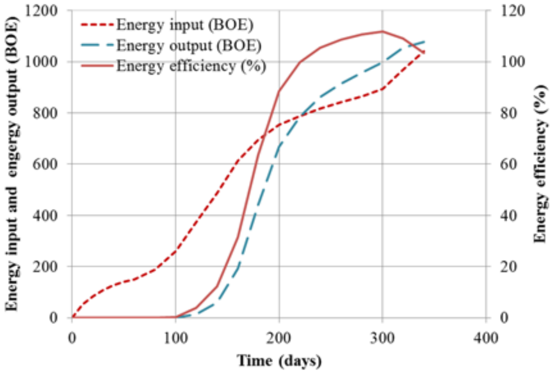

Fig. 81 Energy input, energy output and energy efficiency: application case 5 (Shell ICP)

5.1.6 Case 6: heater temperature of 610 °F

In the case 5, we tried the lower heater temperature of 610 °F. We simulate the 340 days of the heating and production, by using variable flowing bottomhole pressure as shown in Fig. 82. The simulation results are provided in Fig. 82 – Fig. 91, and they are summarized in Table 29. The results are computed in one pattern.

The lower heater temperature allows the longer time for kerogen decomposition while avoiding excessive cracking of liquid organic phase. This leads the greater hydrocarbon production and higher energy efficiency. The energy efficiency after the process is 144 %.

Table 29 Summary of the simulation results: application case 6 (Shell ICP)

Parameters	Values	Parameters	Values
Duration (days)	340	GOR (MSCF/STB)	2.03
Remaining kerogen (%)	2.66	HC gas production (MSCF)	693
Liquid organic production (STB)	1,415	Produced HC (BOE)	1,542
Gaseous production (MSCF)	2,871	Energy input (BOE)	1,071
Aqueous production (STB)	1,050	Energy efficiency (%)	144

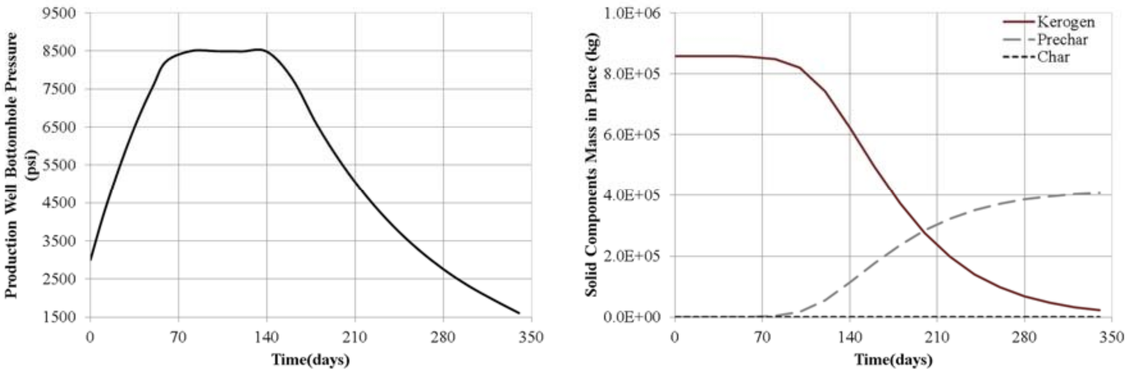

(a) Flowing bottomhole pressure

(b) Kerogen mass in place

Fig. 82 Flowing bottomhole pressure and kerogen mass in place: application case 6 (Shell ICP)

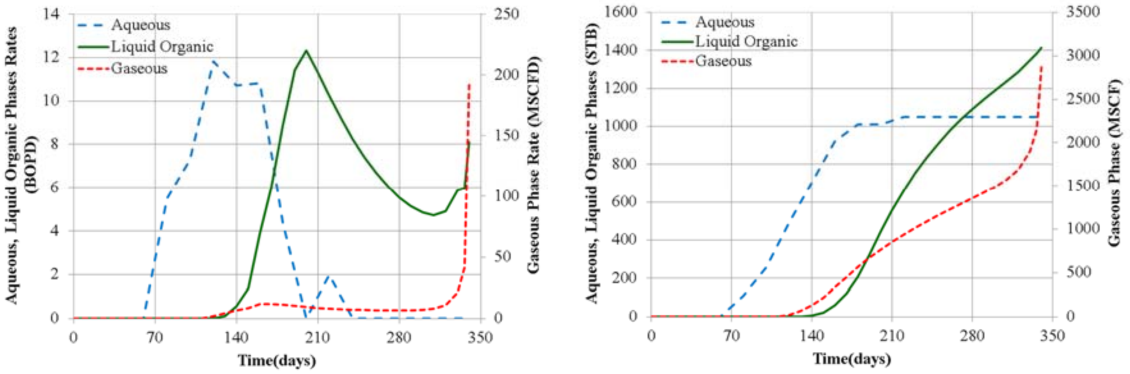

Fig. 83 Production rates and cumulative productions of phases: application case 6 (Shell ICP)

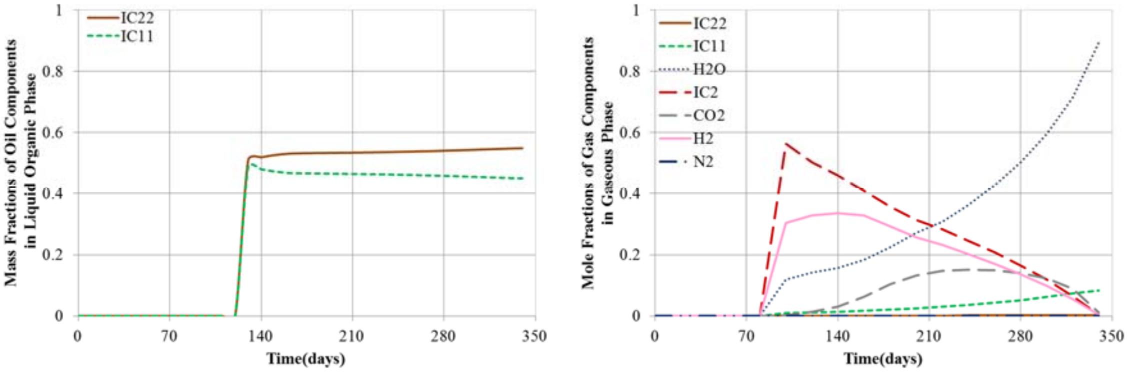

(a) Mass fractions of oil components in liquid organic phase

(b) Mole fractions of gas components in gaseous phase

Fig. 84 Fractions of components in produced fluid: application case 6 (Shell ICP)

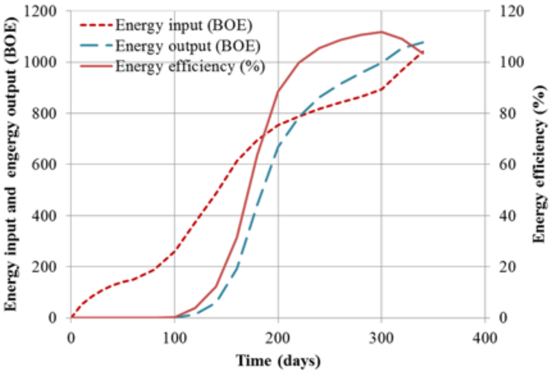

Fig. 85 Energy input, energy output and energy efficiency: application case 6 (Shell ICP)

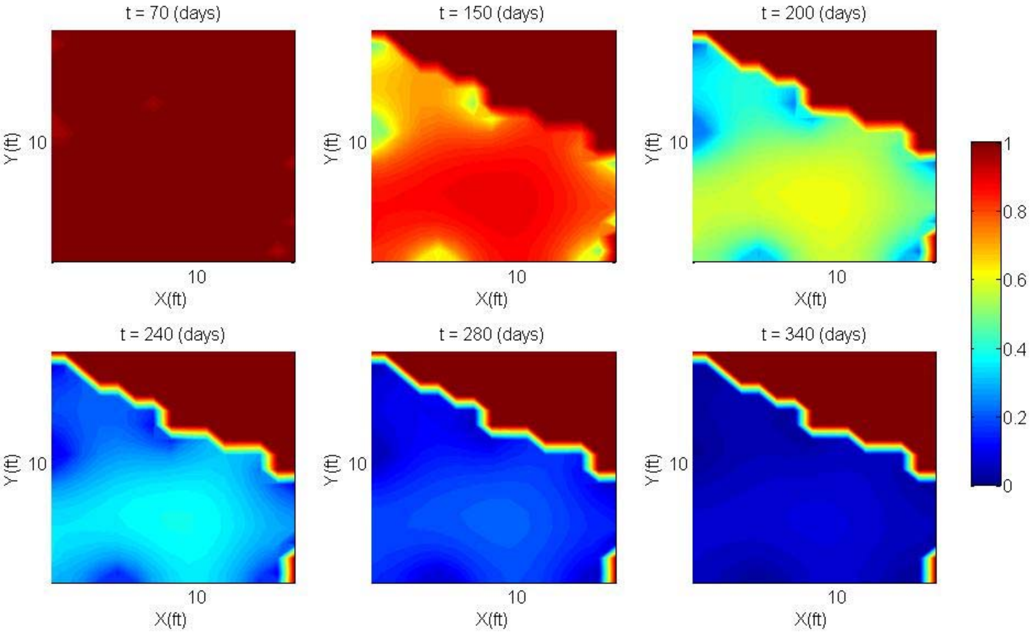

Fig. 86 Profiles of kerogen mass fraction: application case 6 (Shell ICP)

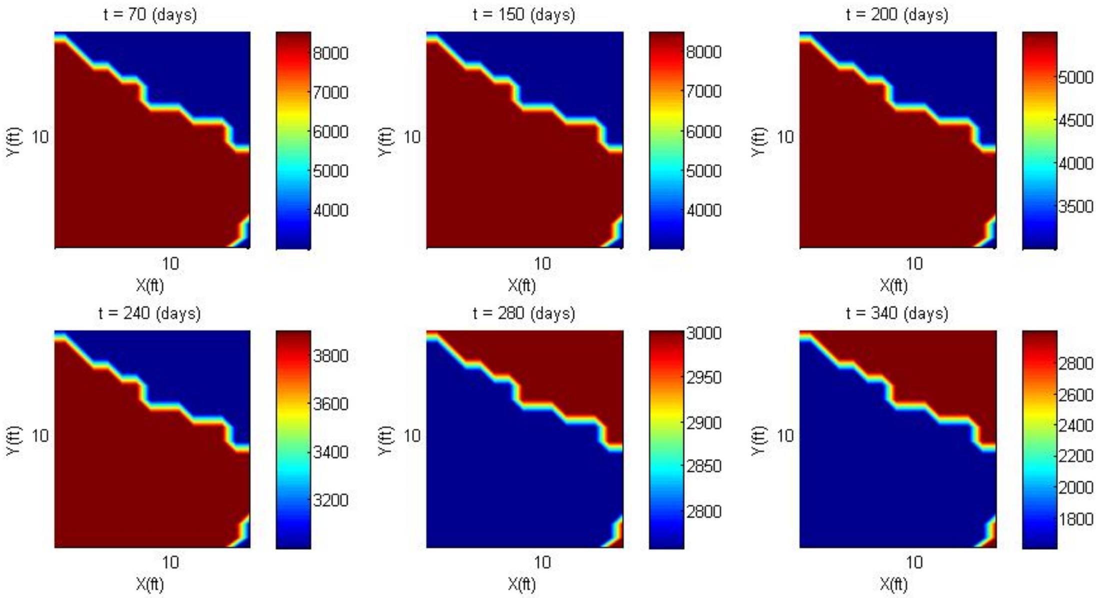

(a) Profiles of pressure at the matrix domain

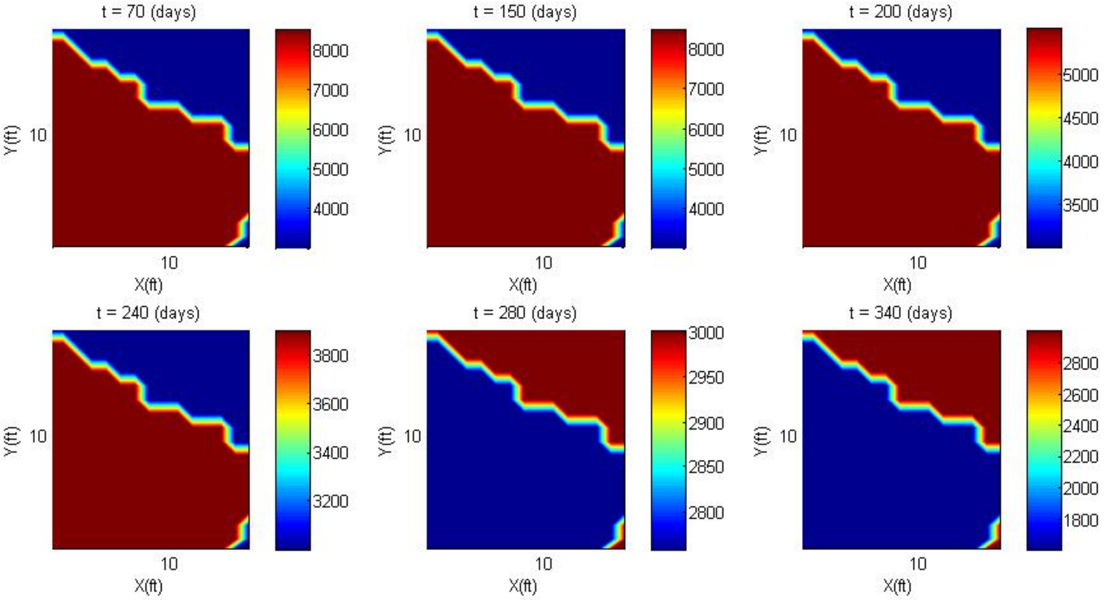

(b) Profiles of pressure at the fracture domain

Fig. 87 Profiles of pressure: application case6 (Shell ICP)

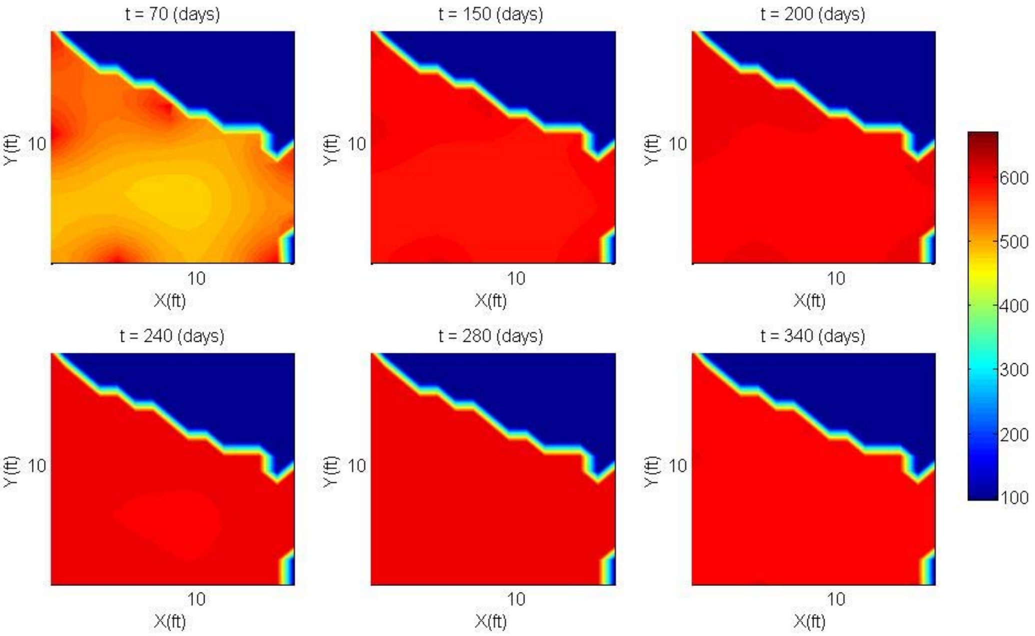

(a) Profiles of temperature at the matrix domain

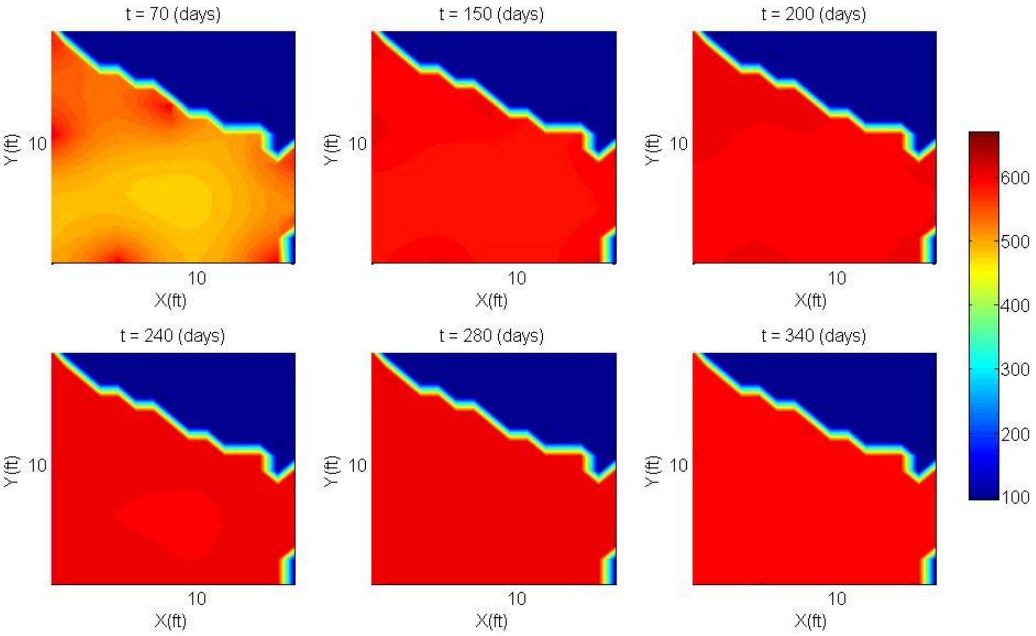

(b) Profiles of temperature at the fracture domain

Fig. 88 Profiles of temperature: application case6 (Shell ICP)

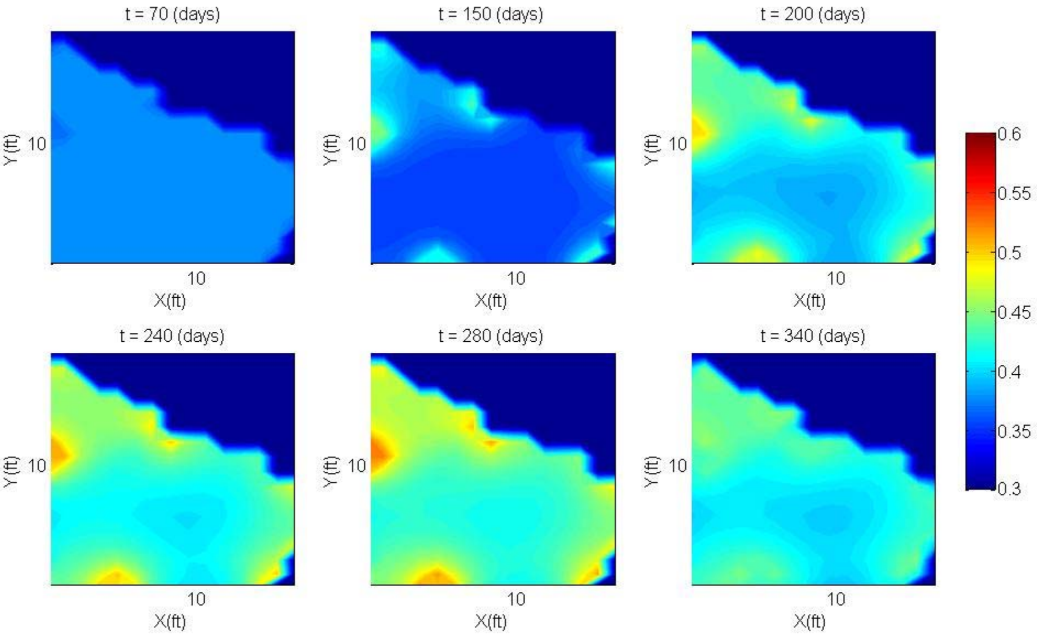

(a) Profiles of aqueous phase saturation at the matrix domain

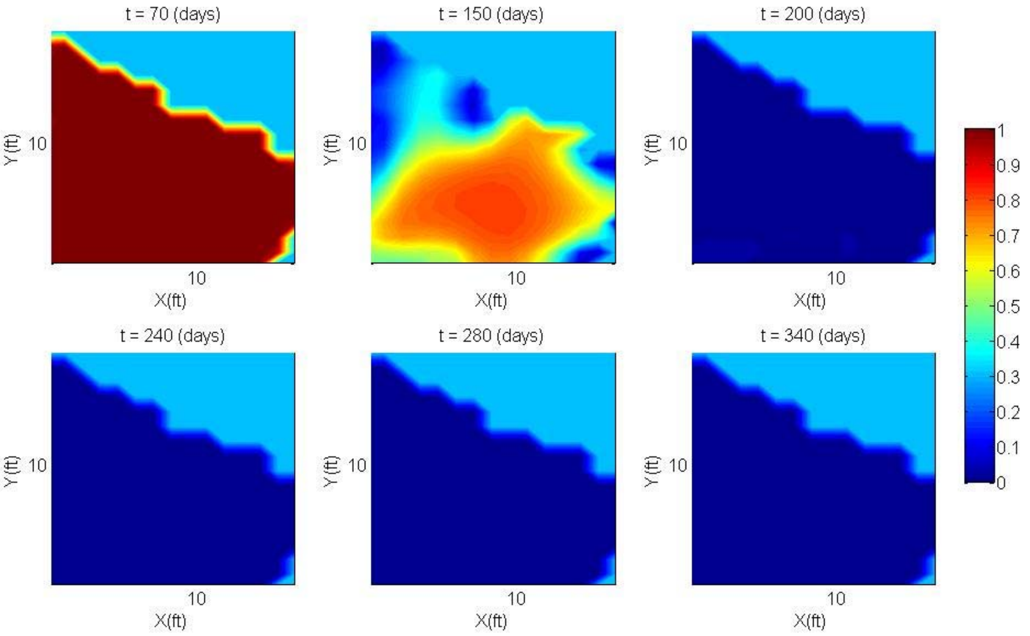

(b) Profiles of aqueous phase saturation at the fracture domain

Fig. 89 Profiles of aqueous phase saturation: application case6 (Shell ICP)

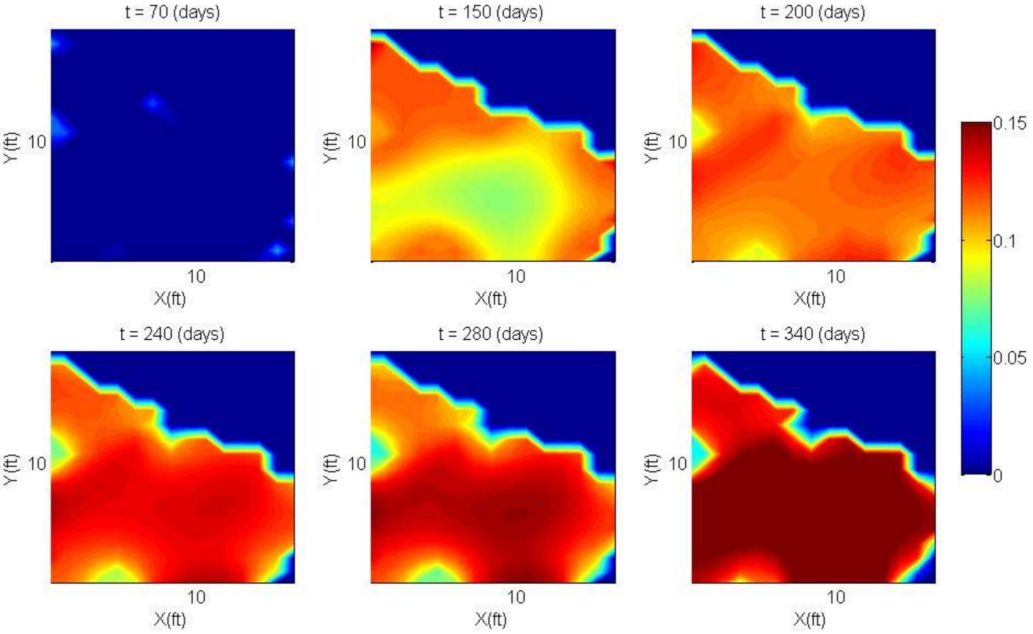

(a) Profiles of liquid organic phase saturation at the matrix domain

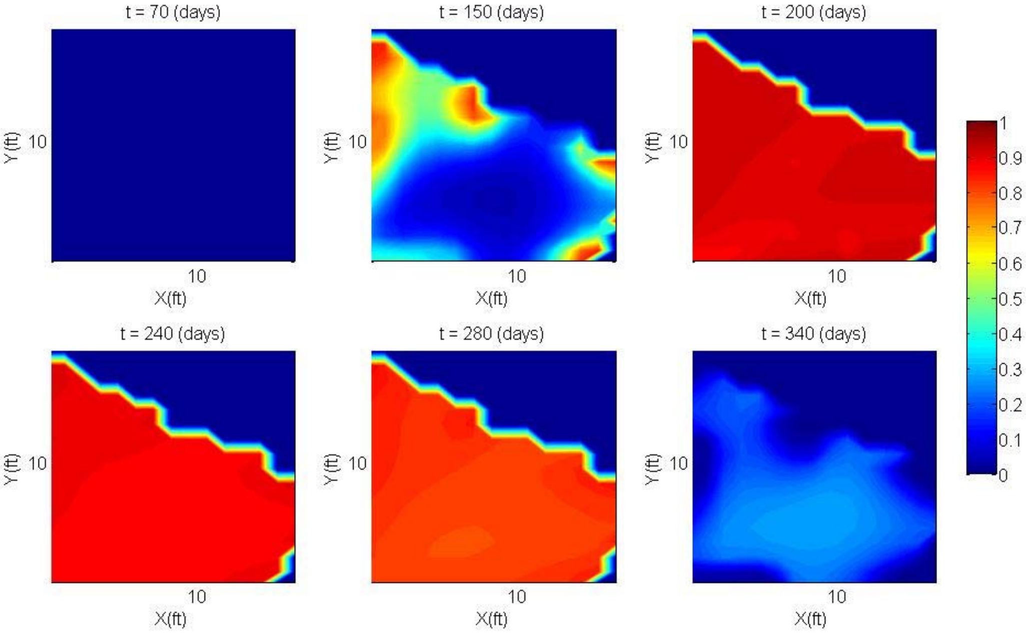

(b) Profiles of liquid organic phase saturation at the fracture domain

Fig. 90 Profiles of liquid organic phase saturation: application case6 (Shell ICP)

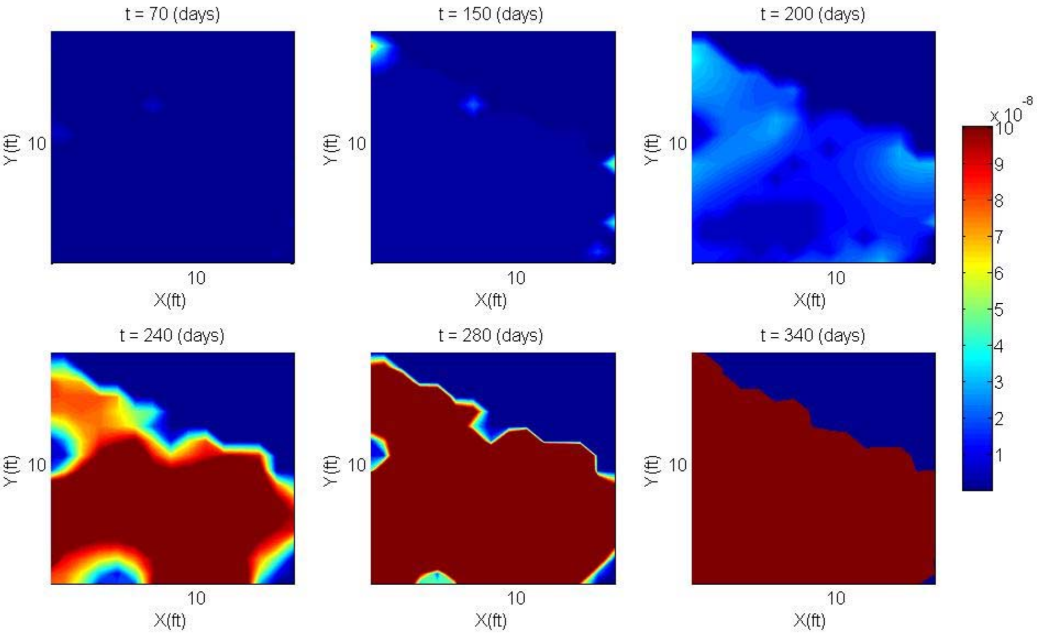

(a) Profiles of gaseous phase saturation at the matrix domain

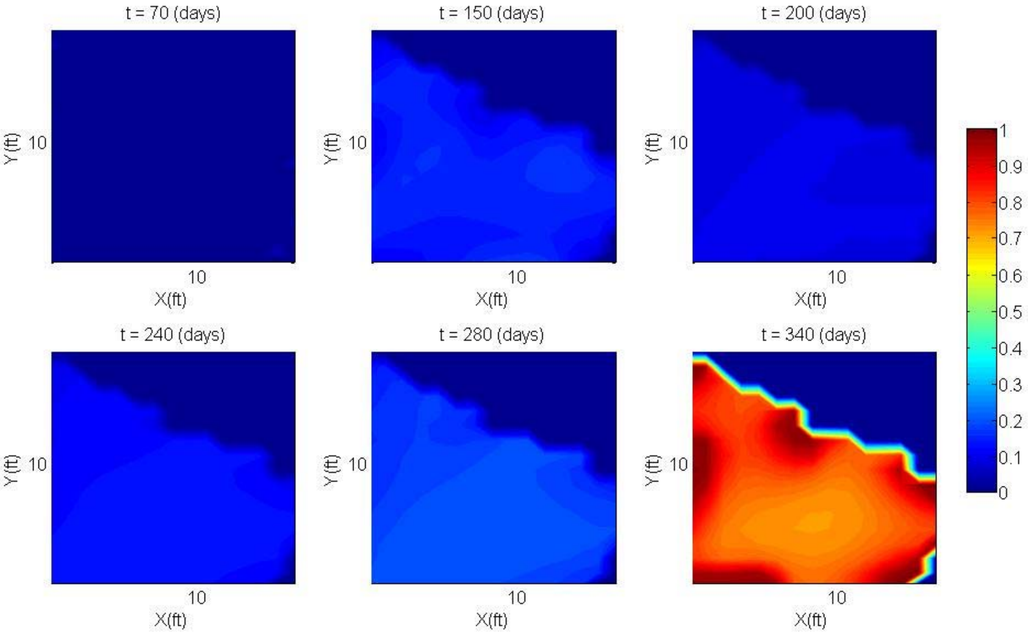

(b) Profiles of gaseous phase saturation at the fracture domain

Fig. 91 Profiles of gaseous phase saturation: application case6 (Shell ICP)

5.2 ExxonMobil Electrofrac process

ExxonMobil Electrofrac process entails electrical conduction to heat the oil shales. It creates a longitudinal fracture in a horizontal well, and propped it with a material that conducts electricity as shown in Fig. 92. The fluids are produced from the four vertical wells located aside from a fracture. This process can utilize a multilateral well with each branch containing a longitudinal fracture as shown in Fig. 93. Fracture height, fracture width, and fracture spacing are 80 ft, 80 ft, and 40 ft, respectively. In this process, we conduct the simulations of multilateral well case. We simulate an eighth of a single fracture by using a 3D model of 7*5*13 grid blocks as shown in Fig. 94.

We expect that the electrical conductivity of the proppant has a significant effect on the process efficiency. In this regard, we conduct the sensitivity analyses of the proppant electrical conductivity. The electrical conductivity can be related by using Wiedemann–Franz law as provided in Eq. (5.1) (Jones and March 1973).

$$\frac{K}{\sigma} = LT \tag{5.1}$$

Here, K is the thermal conductivity in W/m-K, σ is the electrical conductivity in Ω^{-1}-m^{-1}, L is the Lorenz number (2.44e-8 W-Ω/K^2), and T is the temperature in Kelvin. We can compute the equivalent thermal conductivity to the electrical conductivity by substituting the various σ and horizontal well temperature (650 °F) into the Eq. (5.1).

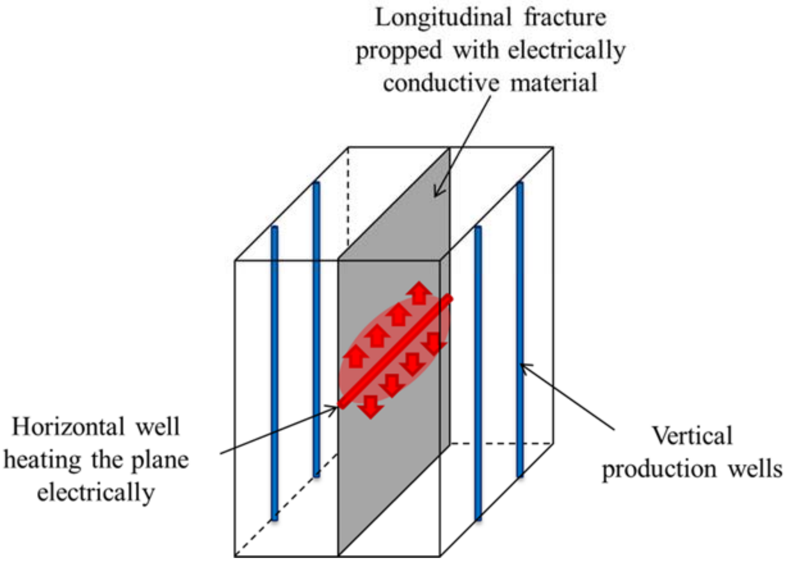

Fig. 92 Concept of the ExxonMobil Electrofrac

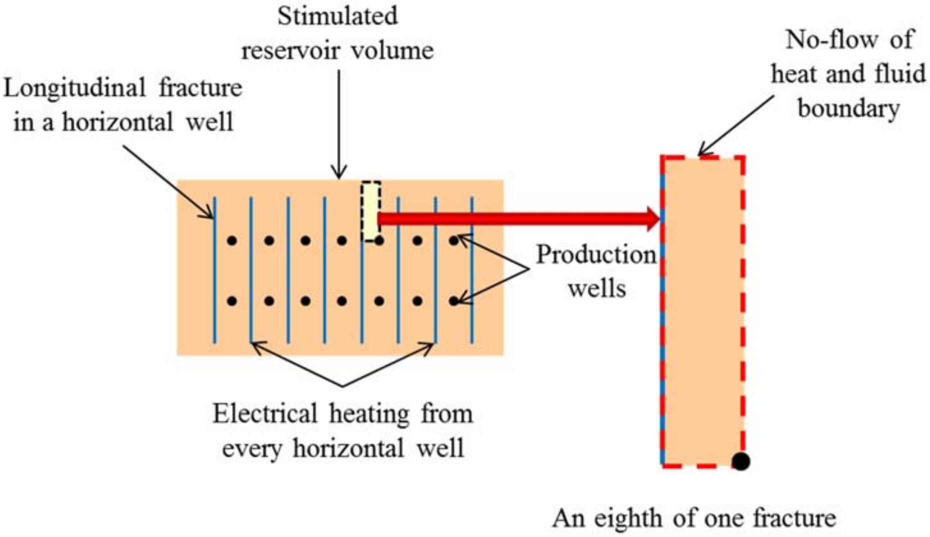

Fig. 93 Configuration of the reservoir model in the ExxonMobil Elecrofrac case

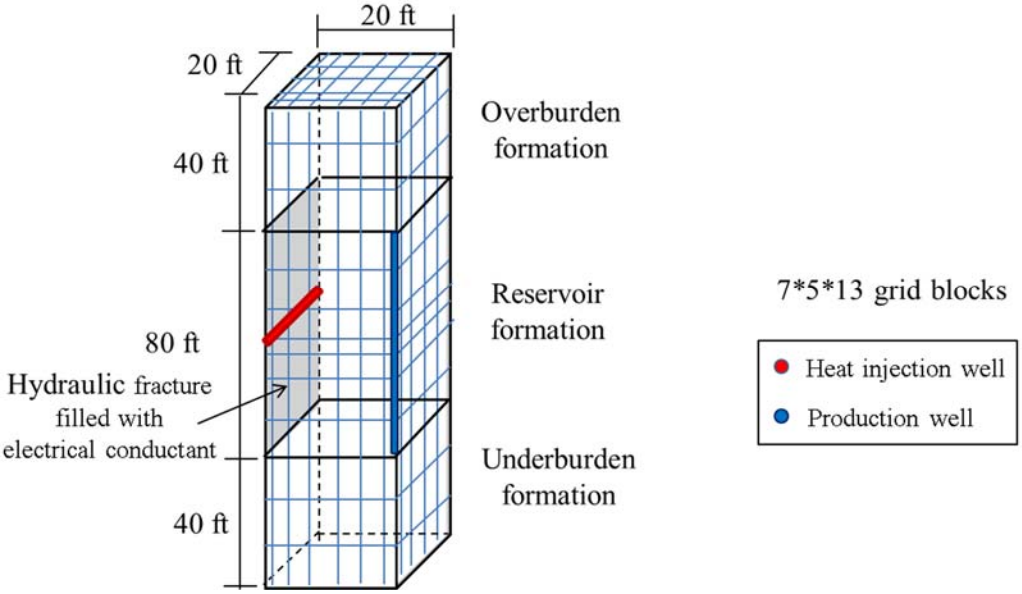

Fig. 94 Simulation geometry for the ExxonMobil Elecrofrac case

5.2.1 Case 1: proppant electrical conductivity of 2.055E5 Ω^{-1}-m^{-1}

In this case, we use the proppant electrical conductivity of 2.055E5 $\Omega^{-1}m^{-1}$. The equivalent thermal conductivity is 3.1 W/m-K. We implement the in-situ upgrading and production with the injection well temperature of 650 °F. The heating and production continues until 7 years, by using the variable flowing bottomhole pressure at the top of the producer. The simulation results are shown in the Fig. 95 – Fig. 100Fig. 102, and they are summarized in Table 30. The results are computed in one fracture.

Only the kerogen at the middle of the reservoir near to the hydraulic fracture decomposes, as shown in Fig. 99. It is resulted from that the temperature of the hydraulic fracture doesn't approach to an evenly high temperature as illustrated in the Fig. 100. The energy efficiency at 7 years is 8.59 %.

Table 30 Summary of the simulation results: case 1 (ExxonMobil Electrofrac)

Parameters	Values	Parameters	Values
Duration (years)	7	GOR (MSCF/STB)	0.82
Remaining kerogen (%)	97.4	HC gas production (MSCF)	85
Liquid organic production (STB)	114	Produced HC (BOE)	129
Gaseous production (MSCF)	93.5	Energy input (BOE)	1,504
Aqueous production (STB)	1.85E4	Energy efficiency (%)	8.59

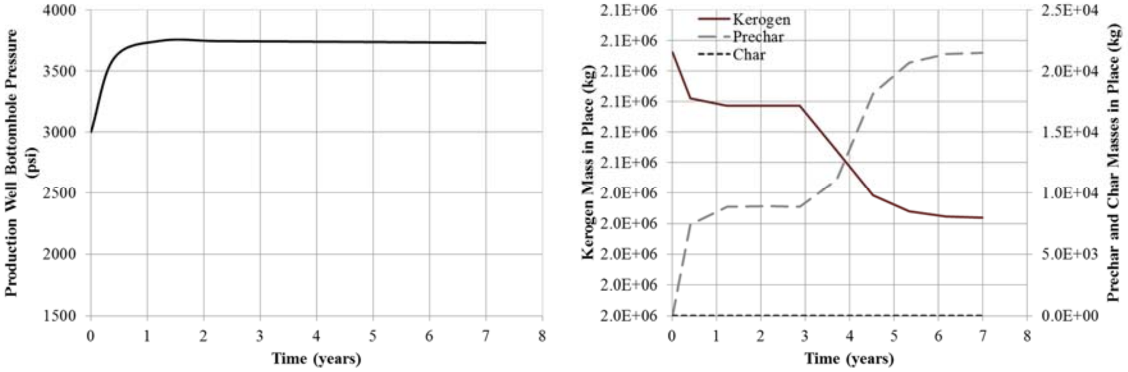

(a) Flowing bottomhole pressure (b) Kerogen mass in place

Fig. 95 Flowing bottomhole pressure and kerogen mass in place: case 1 (ExxonMobil Electrofrac)

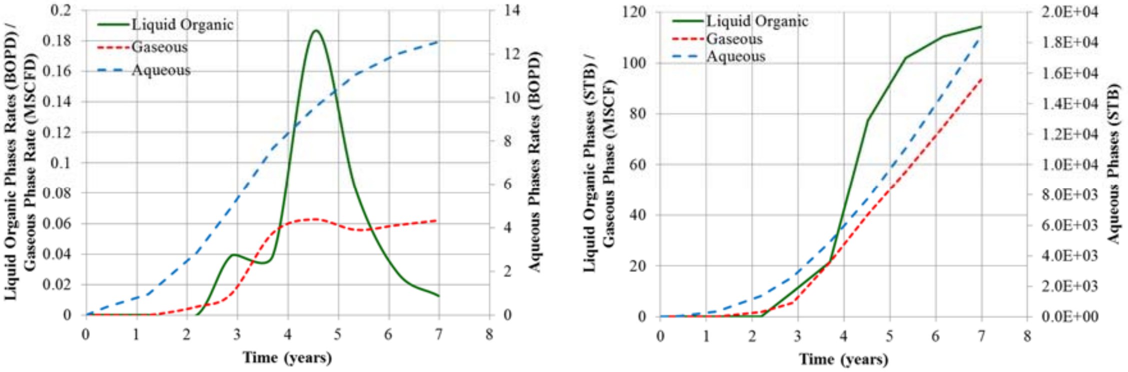

Fig. 96 Production rates and cumulative productions of phases: case 1 (ExxonMobil Electrofrac)

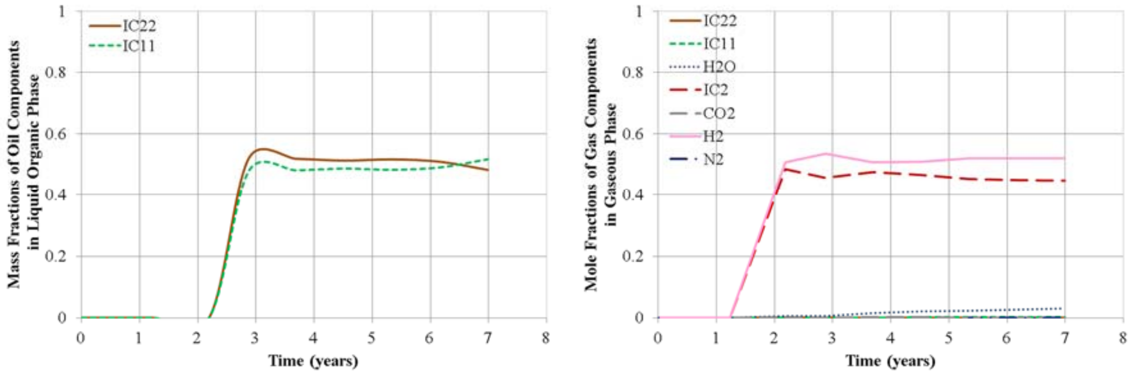

(a) Mass fractions of oil components in liquid organic phase

(b) Mole fractions of gas components in gaseous phase

Fig. 97 Fractions of components in produced fluid: case 1 (ExxonMobil Electrofrac)

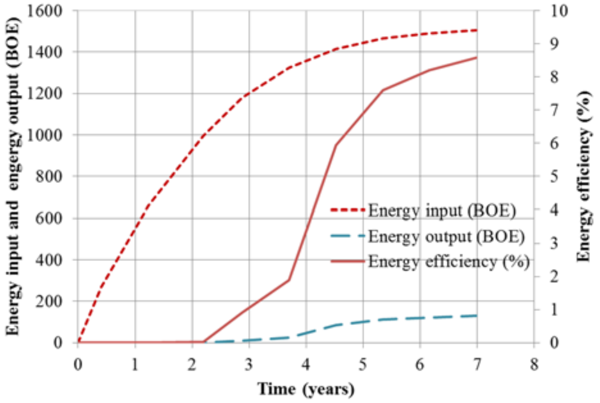

Fig. 98 Energy input, energy output and energy efficiency: case 1 (ExxonMobil Electrofrac)

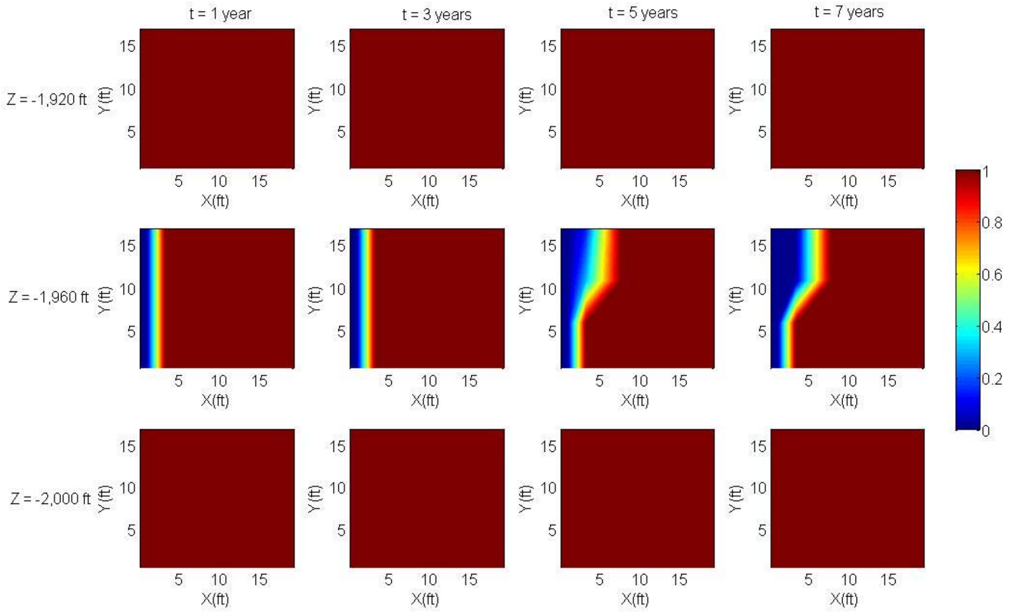

Fig. 99 Profiles of kerogen mass fraction: case 1 (ExxonMobil Electrofrac)

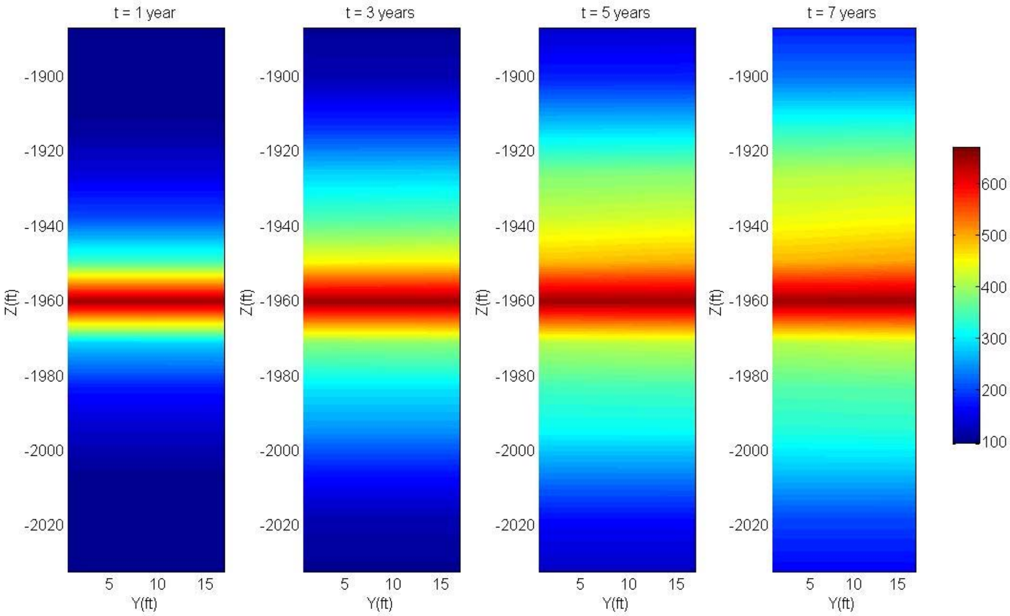

Fig. 100 Temperature profiles at the overburden, hydraulic fracture and underburden formation: case 1 (ExxonMobil Electrofrac)

5.2.2 Case 2: proppant electrical conductivity of 3.315E6 Ω^{-1}-m^{-1}

In this case, we use the proppant electrical conductivity of 3.315E6 $\Omega^{-1}m^{-1}$. The equivalent thermal conductivity is 50 W/m-K. We implement the in-situ upgrading and production with the injection well temperature of 650 °F. The heating and production continues until 7 years, by using the variable flowing bottomhole pressure at the top of the producer. The simulation results are shown in the Fig. 101 – Fig. 106, and they are summarized in Table 31. The results are computed in one fracture.

The kerogen at the middle of the reservoir near to the hydraulic fracture and the kerogen at the top of the reservoir decompose, but the kerogen at the bottom of the reservoir doesn't decompose as shown in Fig. 105. The temperature at the hydraulic fracture is higher than case 1 as shown in Fig. 106. The energy efficiency at 7 years is 15.8 %.

Table 31 Summary of the simulation results: case 2 (ExxonMobil Electrofrac)

Parameters	Values	Parameters	Values
Duration (years)	7	GOR (MSCF/STB)	1.61
Remaining kerogen (%)	97.0	HC gas production (MSCF)	284
Liquid organic production (STB)	181	Produced HC (BOE)	232
Gaseous production (MSCF)	292	Energy input (BOE)	1,464
Aqueous production (STB)	3.14E4	Energy efficiency (%)	15.8

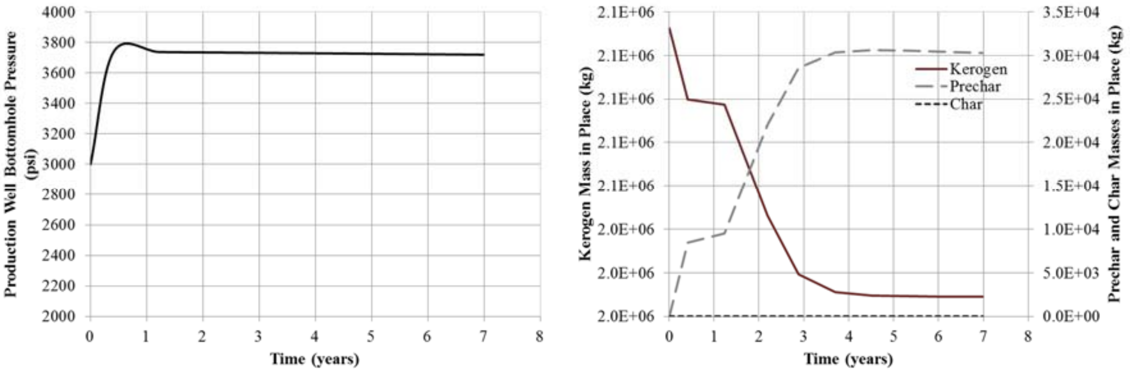

(a) Flowing bottomhole pressure (b) Kerogen mass in place

Fig. 101 Flowing bottomhole pressure and kerogen mass in place: case 2 (ExxonMobil Electrofrac)

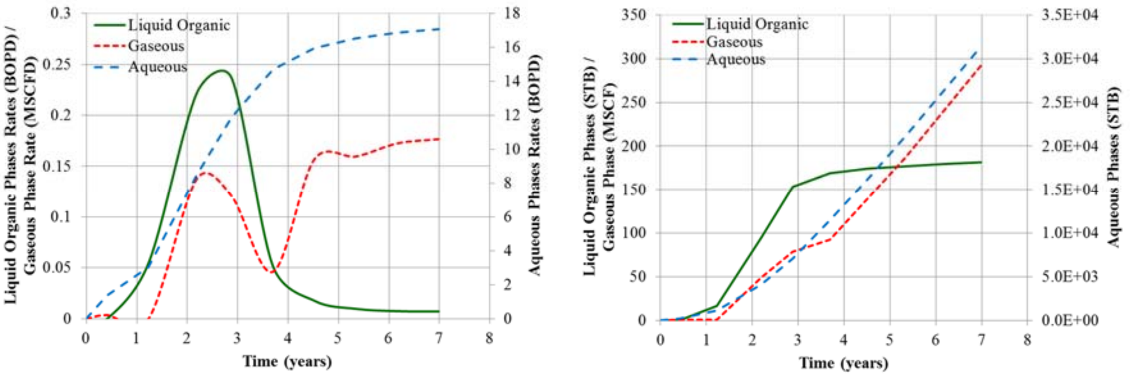

Fig. 102 Production rates and cumulative productions of phases: case 2 (ExxonMobil Electrofrac)

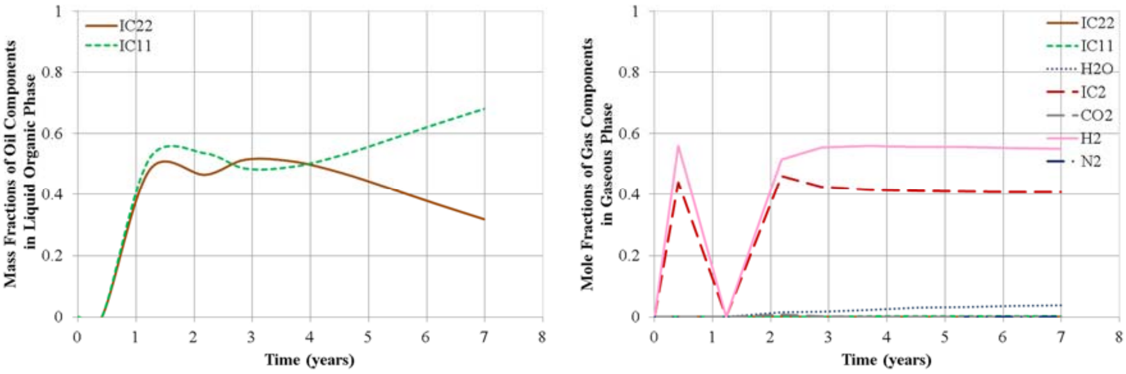

(a) Mass fractions of oil components in liquid organic phase

(b) Mole fractions of gas components in gaseous phase

Fig. 103 Fractions of components in produced fluid: case 2 (ExxonMobil Electrofrac)

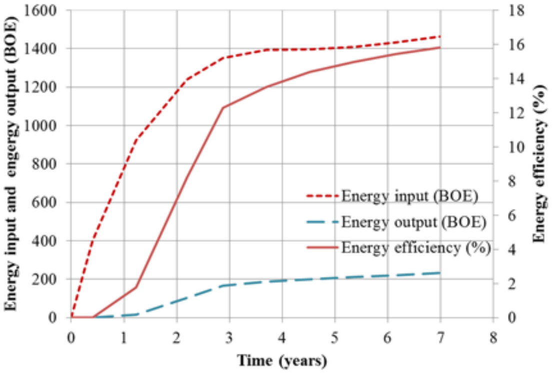

Fig. 104 Energy input, energy output and energy efficiency: case2 (ExxonMobil Electrofrac)

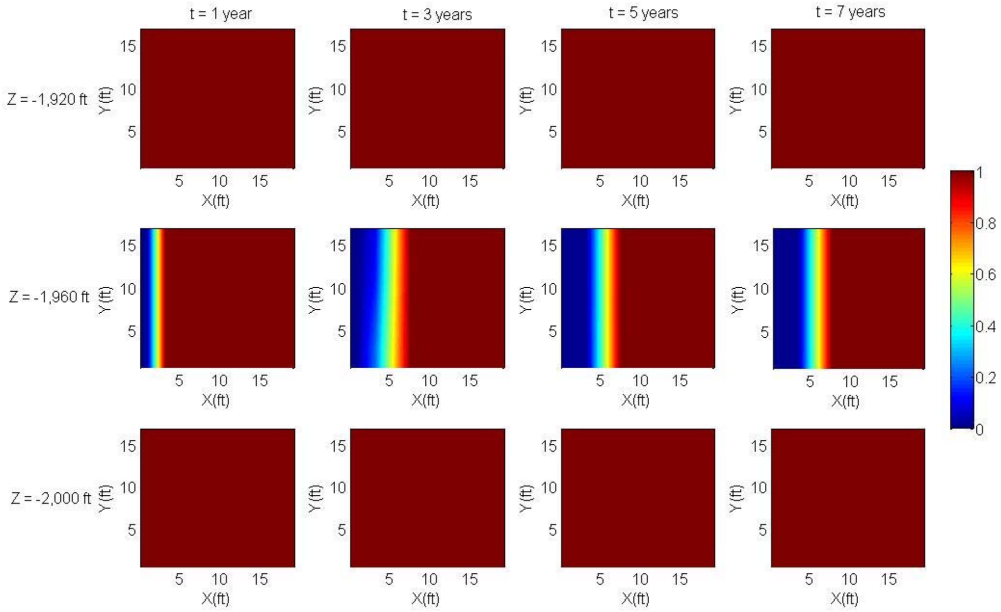

Fig. 105 Profiles of kerogen mass fraction: case 2 (ExxonMobil Electrofrac)

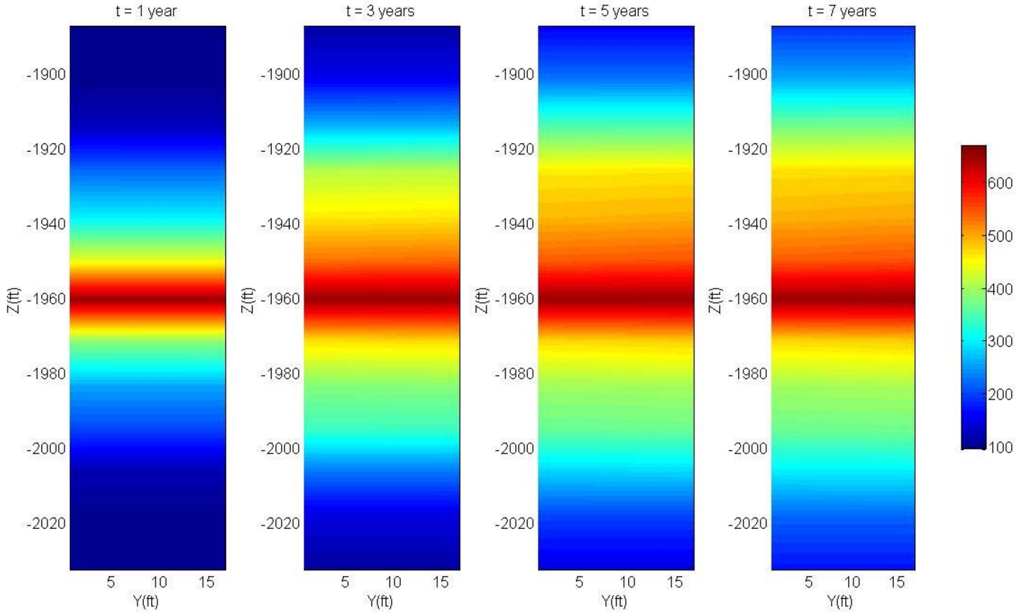

Fig. 106 Temperature profiles at the overburden, hydraulic fracture and underburden formation: case 2 (ExxonMobil Electrofrac)

5.2.3 Case 3: proppant electrical conductivity of 9.945E6 Ω^{-1}-m^{-1}

In this case, we use the proppant electrical conductivity of 9.945E6 $\Omega^{-1}m^{-1}$. The equivalent thermal conductivity is 150 W/m-K. We implement the in-situ upgrading and production with the injection well temperature of 650 °F. The heating and production continues until 7 years, by using the variable flowing bottomhole pressure at the top of the producer. The simulation results are shown in the Fig. 107 – Fig. 112 , and they are summarized in Table 32. The results are computed in one fracture.

The profiles of the remaining kerogen are shown in Fig. 111. The whole kerogen at the top of the reservoir decomposes, and the kerogen at the middle and bottom of the reservoir decompose from the region near to the hydraulic fracture. The temperature at the hydraulic fracture is much higher than case 1 and 2 as shown in Fig. 112. The energy efficiency approaches the maximum value, 34.6 %, at 4 years. The energy efficiency at 7 years is 33.6 %.

Table 32 Summary of the simulation results: case 3 (ExxonMobil Electrofrac)

Parameters	Values	Parameters	Values
Duration (years)	7	GOR (MSCF/STB)	2.13
Remaining kerogen (%)	93.6	HC gas production (MSCF)	583
Liquid organic production (STB)	321	Produced HC (BOE)	401
Gaseous production (MSCF)	685	Energy input (BOE)	1,192
Aqueous production (STB)	4.02E4	Energy efficiency (%)	33.6

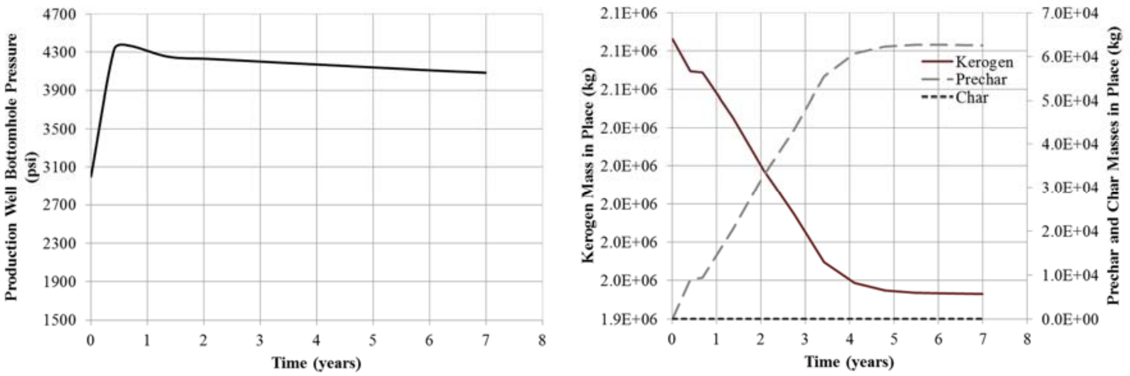

(a) Flowing bottomhole pressure (b) Kerogen mass in place

Fig. 107 Flowing bottomhole pressure and kerogen mass in place: case 3 (ExxonMobil Electrofrac)

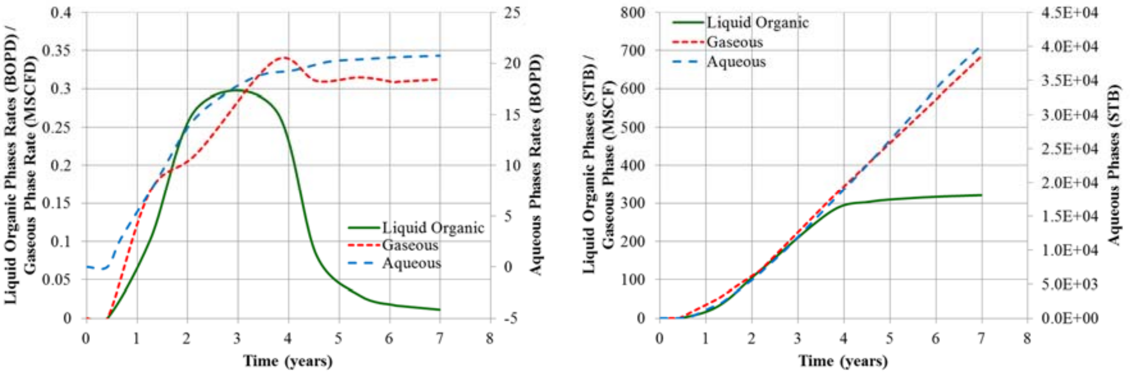

Fig. 108 Production rates and cumulative productions of phases: case 3 (ExxonMobil Electrofrac)

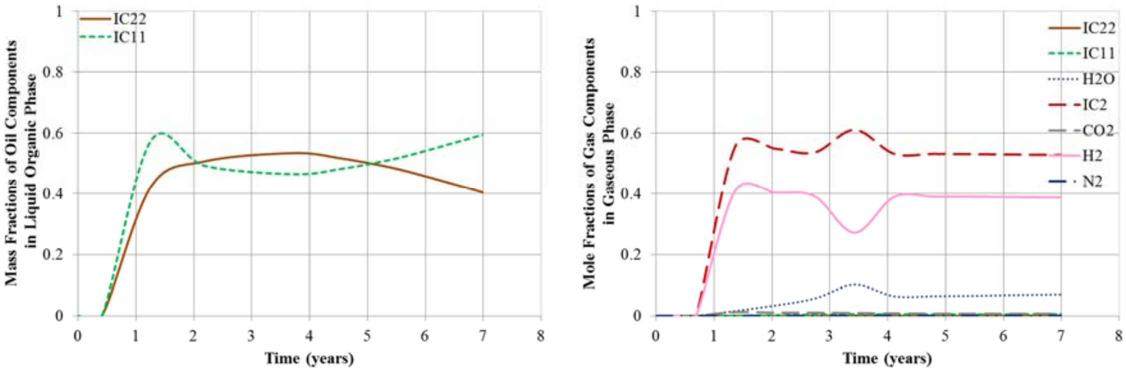

(a) Mass fractions of oil components in liquid organic phase

(b) Mole fractions of gas components in gaseous phase

Fig. 109 Fractions of components in produced fluid: case 3 (ExxonMobil Electrofrac)

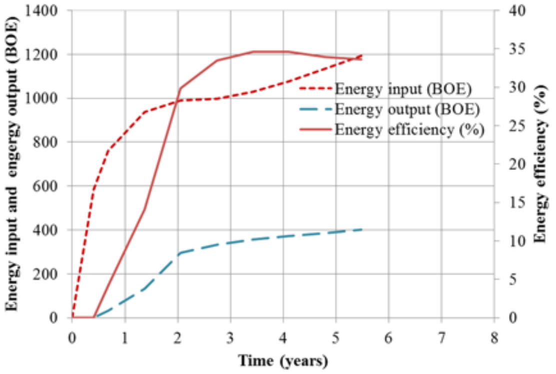

Fig. 110 Energy input, energy output and energy efficiency: case3 (ExxonMobil Electrofrac)

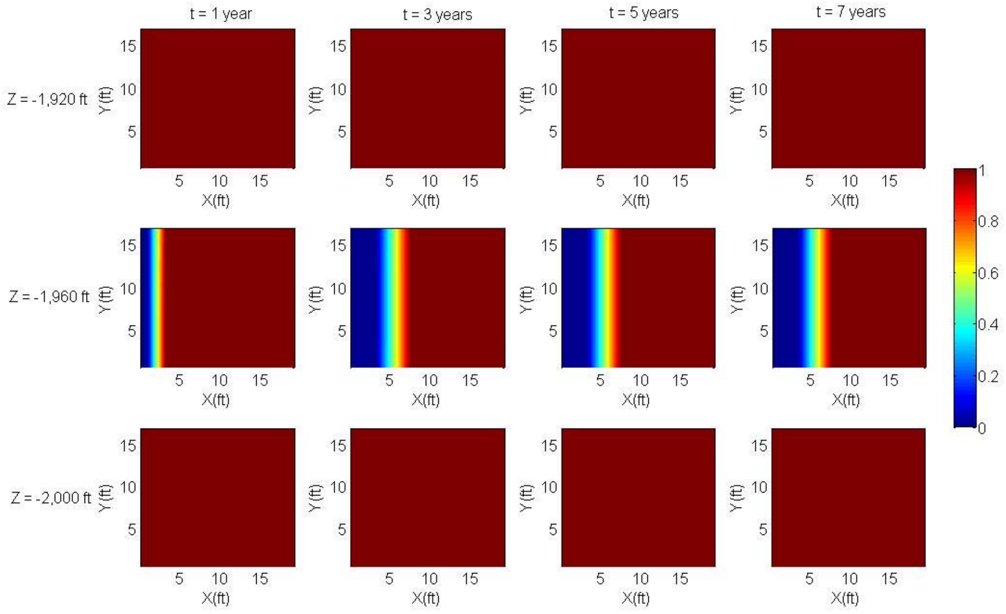

Fig. 111 Profiles of kerogen mass fraction: case 3 (ExxonMobil Electrofrac)

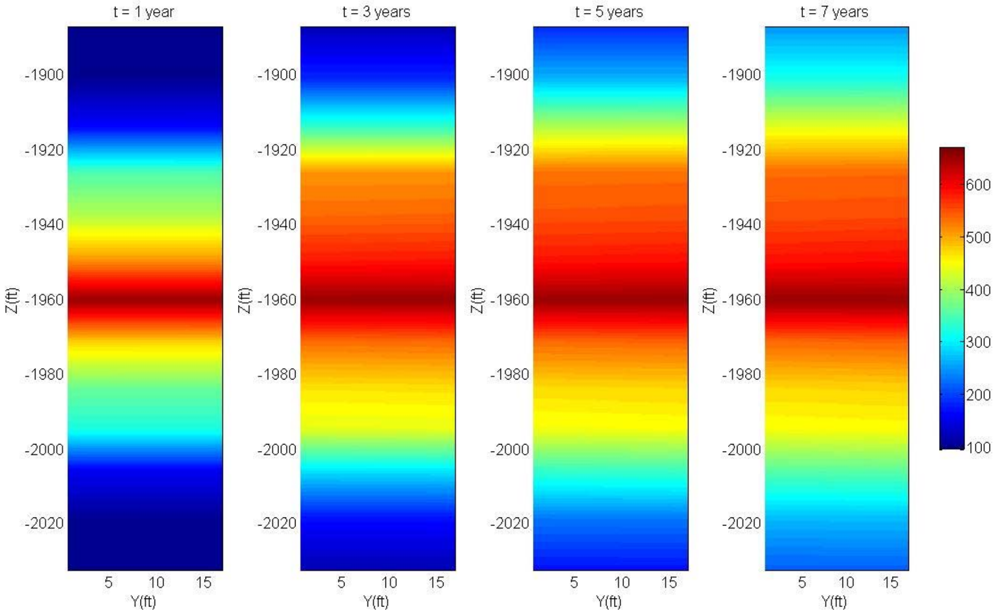

Fig. 112 Temperature profiles at the overburden, hydraulic fracture and underburden formation: case 3 (ExxonMobil Electrofrac)

5.2.4 Case 4: proppant electrical conductivity of 1.989E7 Ω^{-1}-m^{-1}

In this case, we use the proppant electrical conductivity of 1.989E7 Ω^{-1}m^{-1}. The equivalent thermal conductivity is 300 W/m-K. We implement the in-situ upgrading and production with the injection well temperature of 650 °F. The heating and production continues until 7 years, by using the variable flowing bottomhole pressure at the top of the producer. The simulation results are shown in the Fig. 113 – Fig. 123, and they are summarized in Table 33. The results are computed in one fracture.

The profiles of the remaining kerogen are shown in Fig. 117. The whole kerogen at the top of the reservoir decomposes, and the kerogen at the middle and bottom of the reservoir decompose from the region near to the hydraulic fracture. The temperature at the hydraulic fracture is much higher than the previous cases as shown in Fig. 118. The energy efficiency approaches the maximum value, 77.9 %, at 5 years. The energy efficiency at 7 years is 74.1 %.

In this case, we find that the kerogen remains at the middle to the bottom parts of the reservoir even with very high thermal conductivity of the injection material and the evenly high temperature at the hydraulic fracture. This is because heat rises, and we penetrate the top of the producer to avoid the excessive aqueous phase production.

Table 33 Summary of the simulation results: case 5 (ExxonMobil Electrofrac)

Parameters	Values	Parameters	Values
Duration (years)	7	GOR (MSCF/STB)	0.85
Remaining kerogen (%)	83.0	HC gas production (MSCF)	756
Liquid organic production (STB)	1,111	Produced HC (BOE)	1,244
Gaseous production (MSCF)	948	Energy input (BOE)	1,678
Aqueous production (STB)	4.78E4	Energy efficiency (%)	74.1

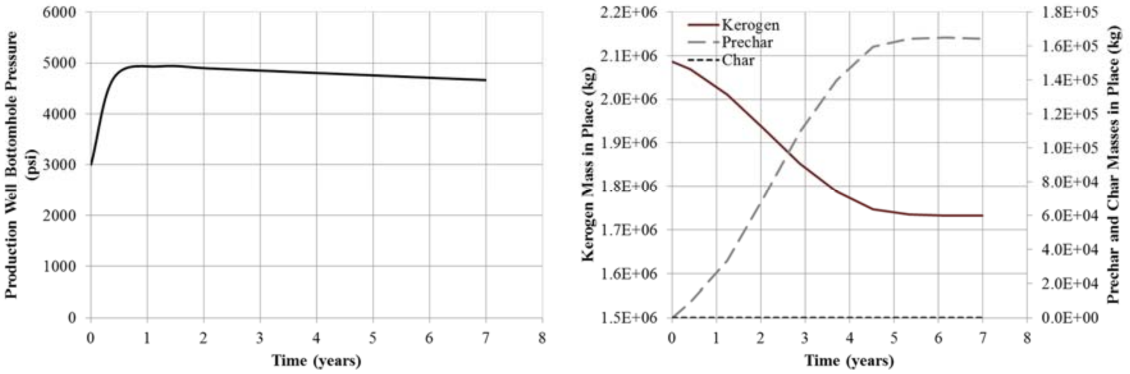

(a) Flowing bottomhole pressure (b) Kerogen mass in place

Fig. 113 Flowing bottomhole pressure and kerogen mass in place: case 5 (ExxonMobil Electrofrac)

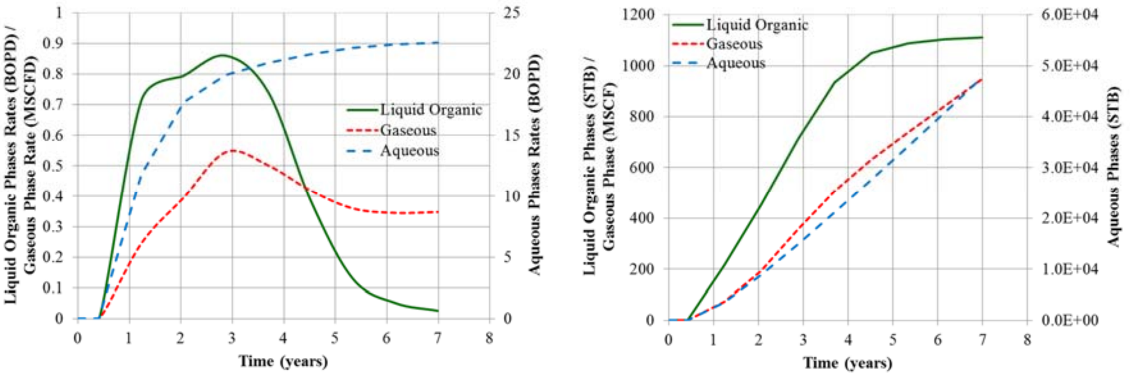

Fig. 114 Production rates and cumulative productions of phases: case 5 (ExxonMobil Electrofrac)

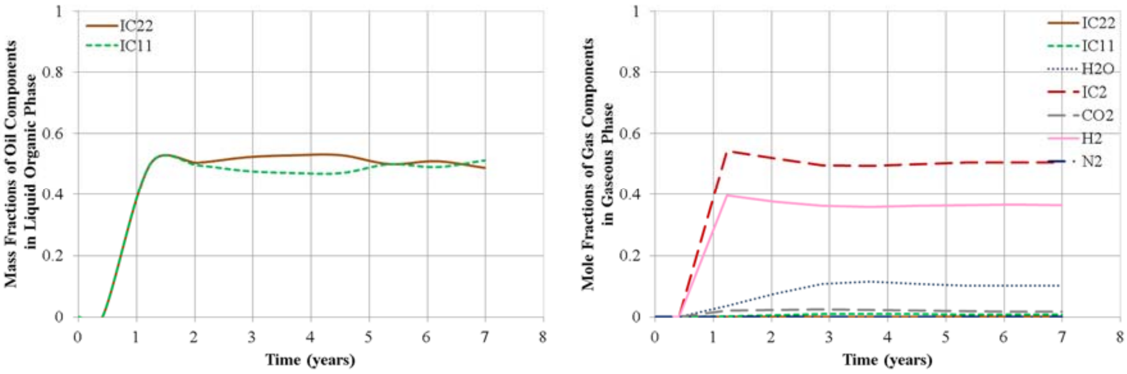

(a) Mass fractions of oil components in liquid organic phase

(b) Mole fractions of gas components in gaseous phase

Fig. 115 Fractions of components in produced fluid: case 5 (ExxonMobil Electrofrac)

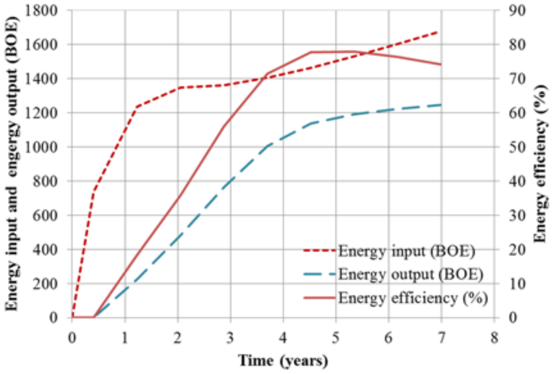

Fig. 116 Energy input, energy output and energy efficiency: case 5 (ExxonMobil Electrofrac)

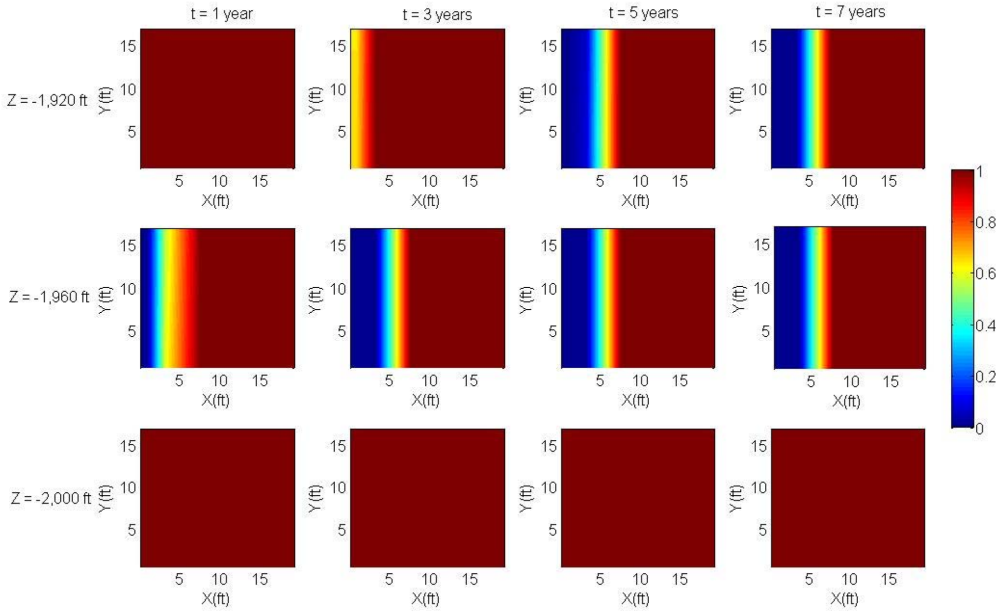

Fig. 117 Profiles of kerogen mass fraction: case 5 (ExxonMobil Electrofrac)

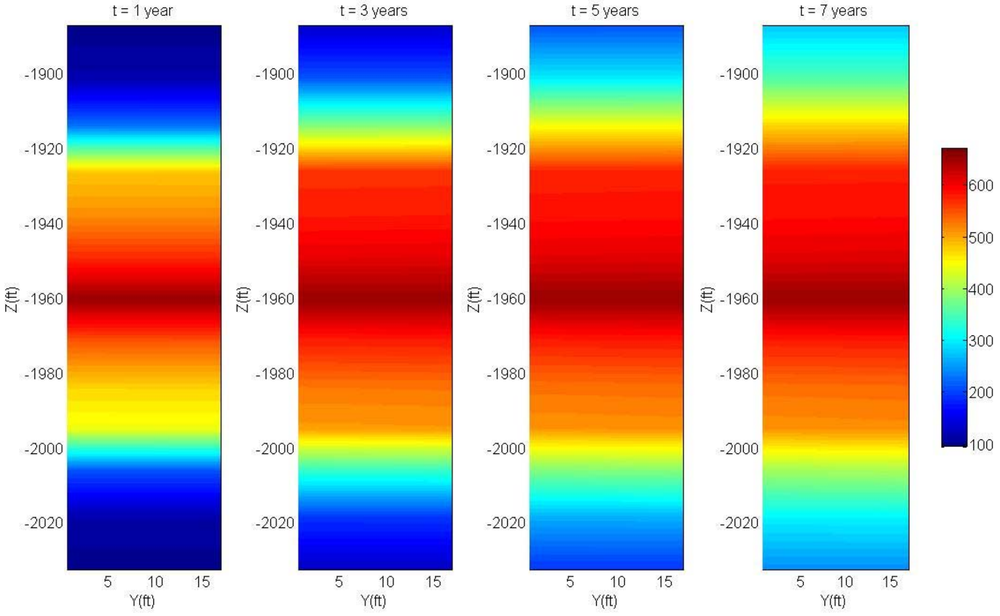

Fig. 118 Temperature profiles at the overburden, hydraulic fracture and underburden formation: case 5 (ExxonMobil Electrofrac)

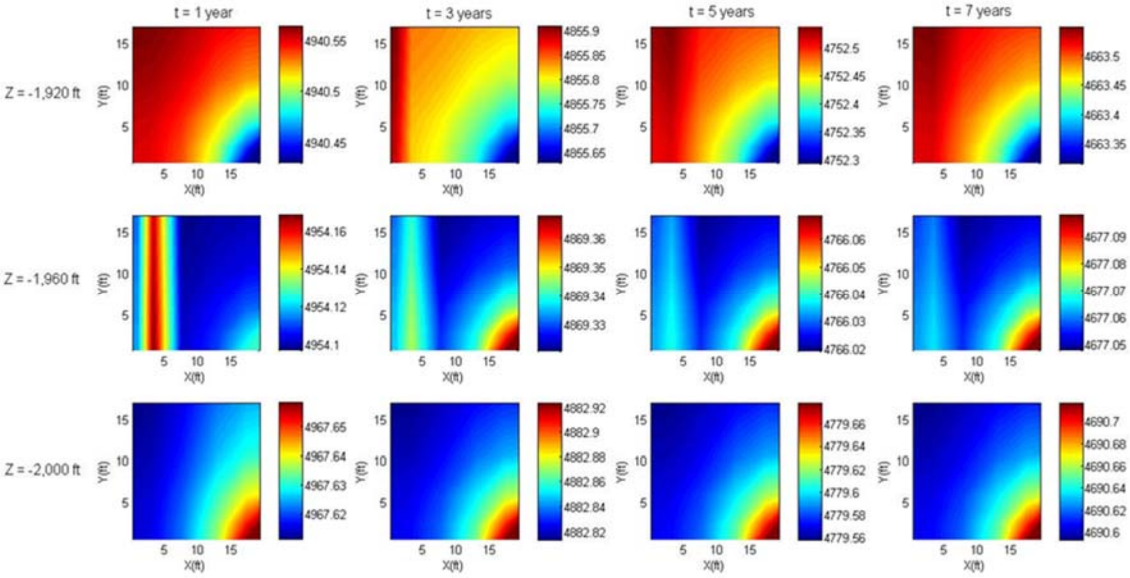

(a) Profiles of pressure at the matrix domain

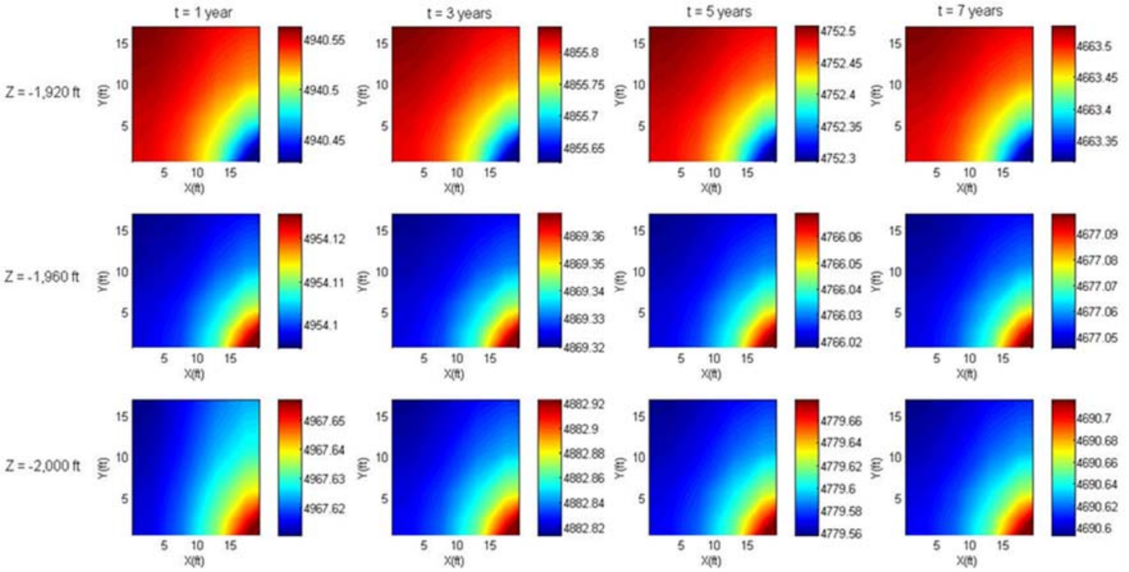

(b) Profiles of pressure at the fracture domain

Fig. 119 Profiles of pressure: case 5 (ExxonMobil Electrofrac)

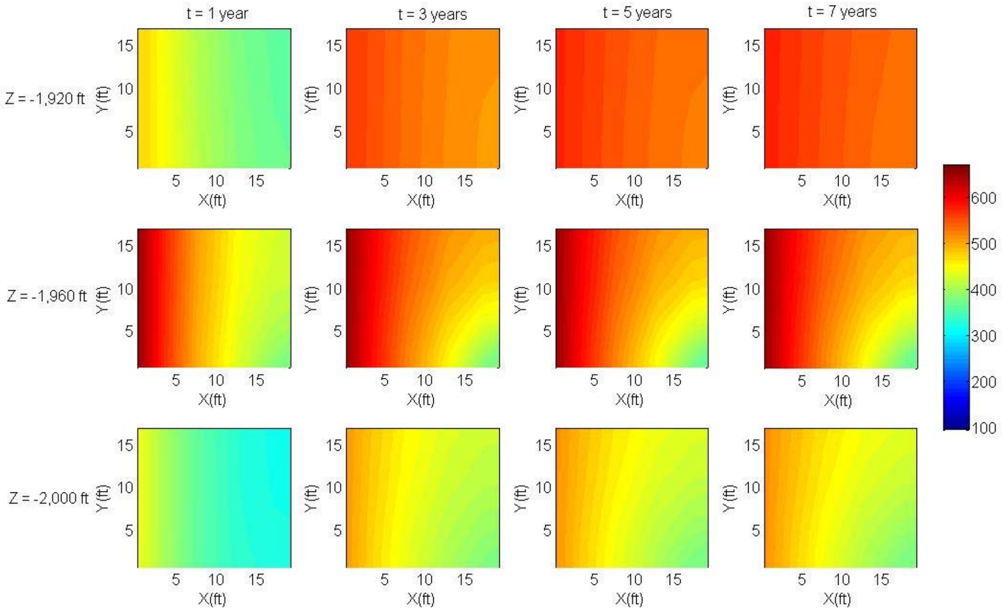

(a) Profiles of temperature at the matrix domain

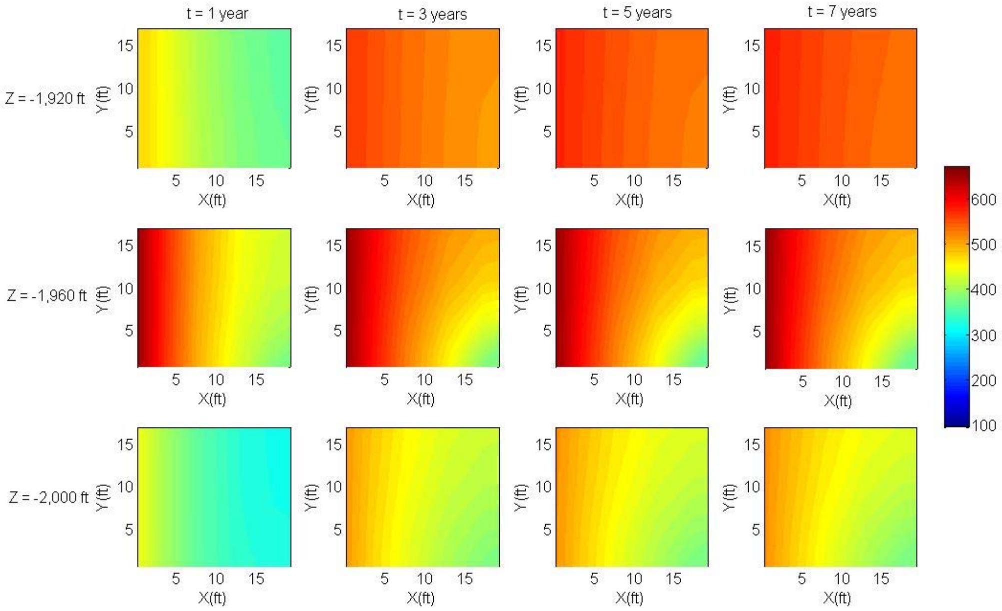

(b) Profiles of temperature at the fracture domain

Fig. 120 Profiles of temperature: case 5 (ExxonMobil Electrofrac)

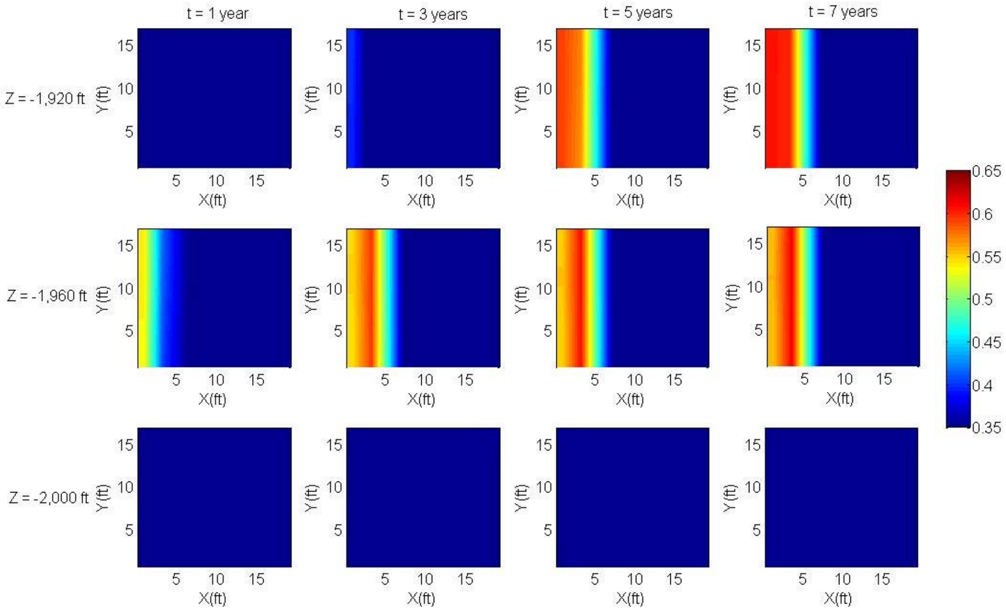

(a) Profiles of aqueous phase saturation at the matrix domain

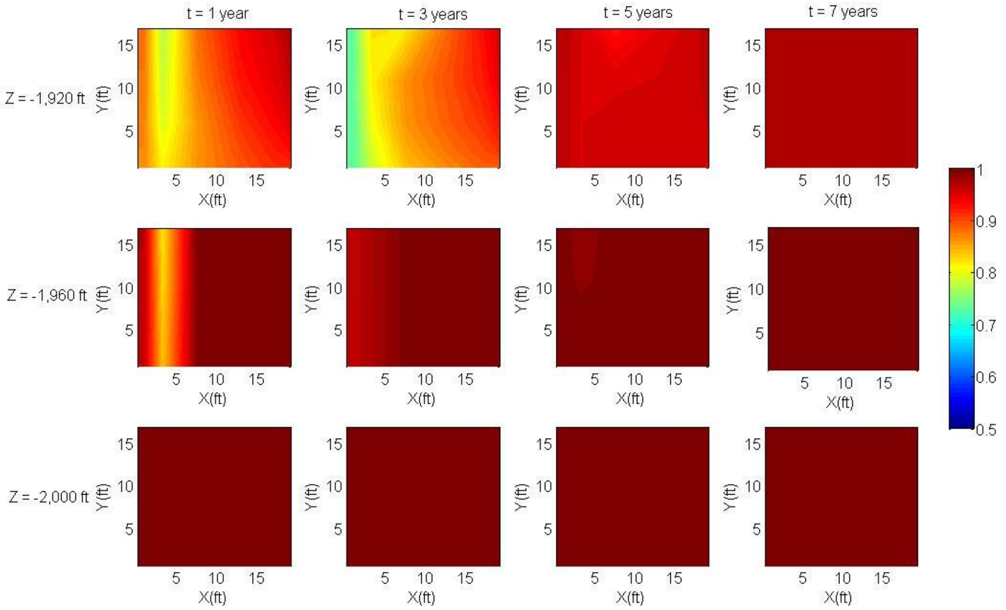

(b) Profiles of aqueous phase saturation at the fracture domain

Fig. 121 Profiles of aqueous phase saturation: case 5 (ExxonMobil Electrofrac)

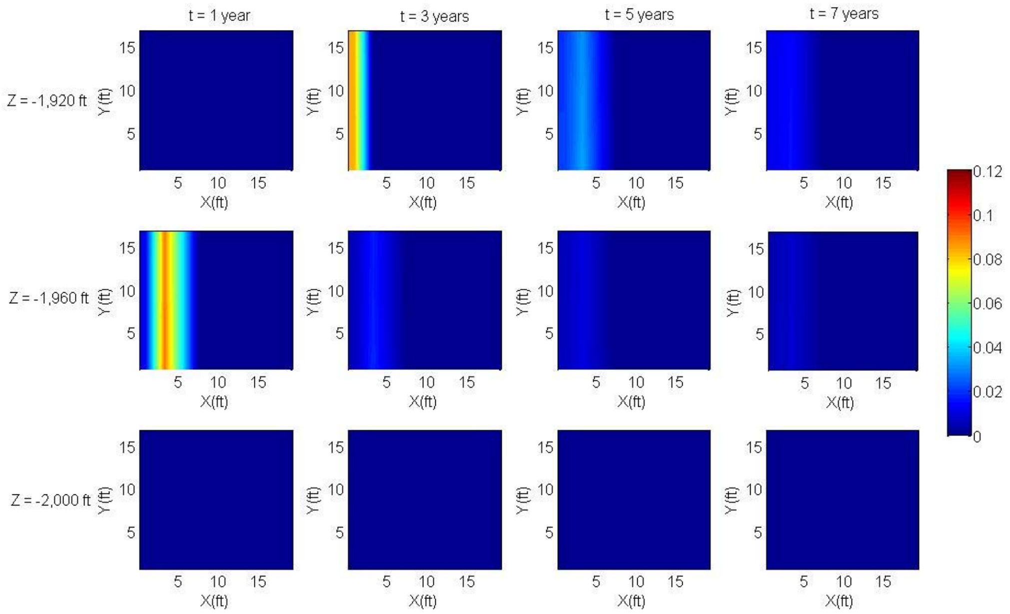

(a) Profiles of liquid organic phase saturation at the matrix domain

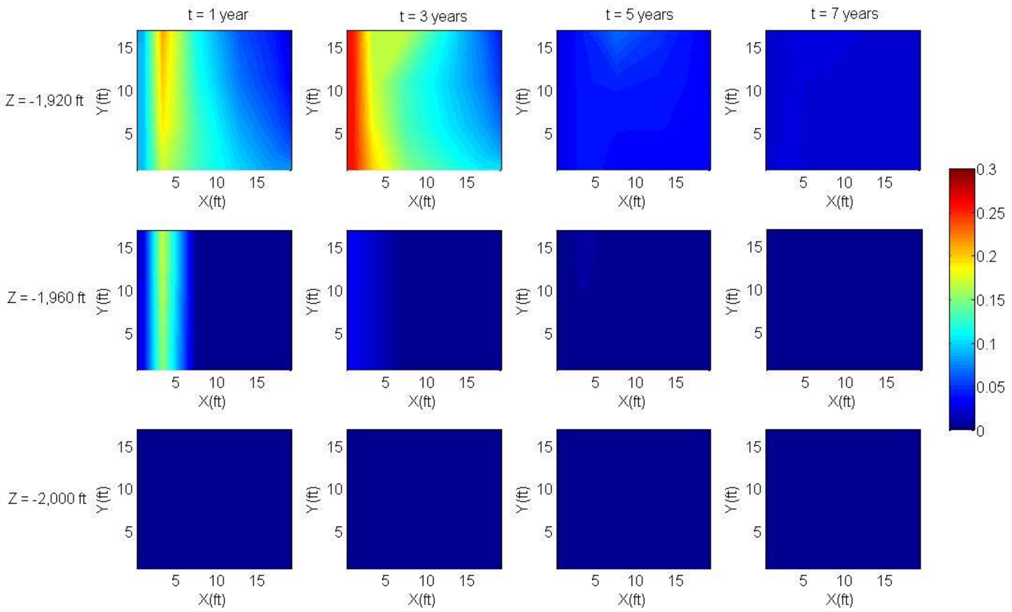

(b) Profiles of liquid organic phase saturation at the fracture domain

Fig. 122 Profiles of liquid organic phase saturation: case 5 (ExxonMobil Electrofrac)

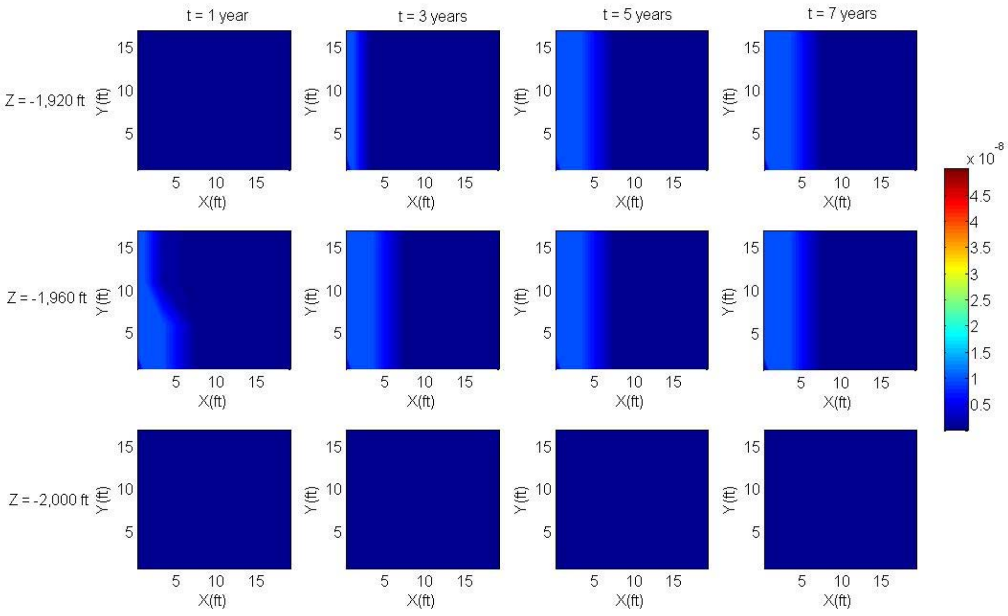

(a) Profiles of gaseous phase saturation at the matrix domain

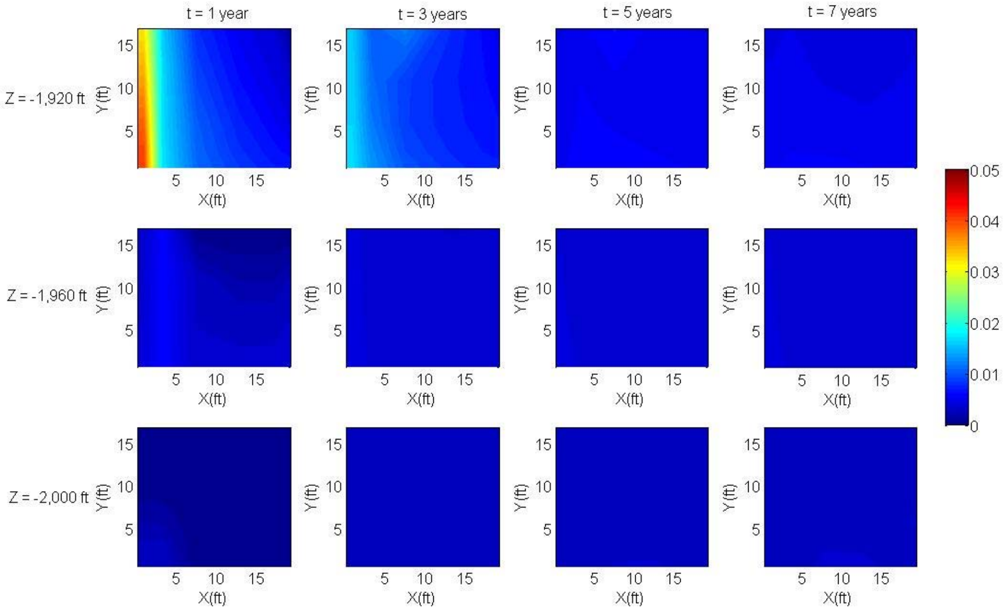

(b) Profiles of gaseous phase saturation at the fracture domain

Fig. 123 Profiles of gaseous phase saturation: case 5 (ExxonMobil Electrofrac)

5.3 TAMU Steamfrac process

TAMU Steamfrac process entails the steam injection into the horizontal wells with multiple transverse hydraulic fractures. It is proposed with the expectation of the effective heating by convection as well as conduction. We study the effect of steam injection strategy on the process efficiency. The simulation cases include the huff-and-puff methods with diverse number of wells (one, two, and three), and the case of continuous injection and production.

5.3.1 Case 1: huff-and-puff method by using one well

We consider the reservoir model as shown in Fig. 124. Fracture height, fracture width, and fracture spacing are 80 ft, 80 ft, and 40 ft, respectively. We consider one well for both of injection and production. We simulate a quarter of the single fracture unit. We use a 3D model of 7*8*13 grid blocks as shown in Fig. 125. We repeat the following stages of huff-and-puff method. The simulation continued for 900 days. The injection rate is figured out from the maximum allowable pressure of the formation.

(1) Inject steam (enthalpy of 1.5E6 J/kg and rate of 0.4 kg/s per one fracture unit) for 1 day.
(2) Rest for 1 day.
(3) Produce fluid (rate of 0.4 kg/s per one fracture unit) for 1 day.

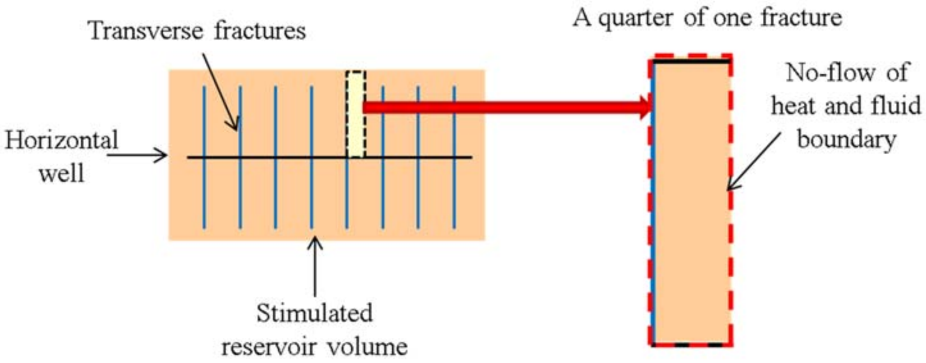

Fig. 124 Configuration of the reservoir model in case 1 (TAMU Steamfrac)

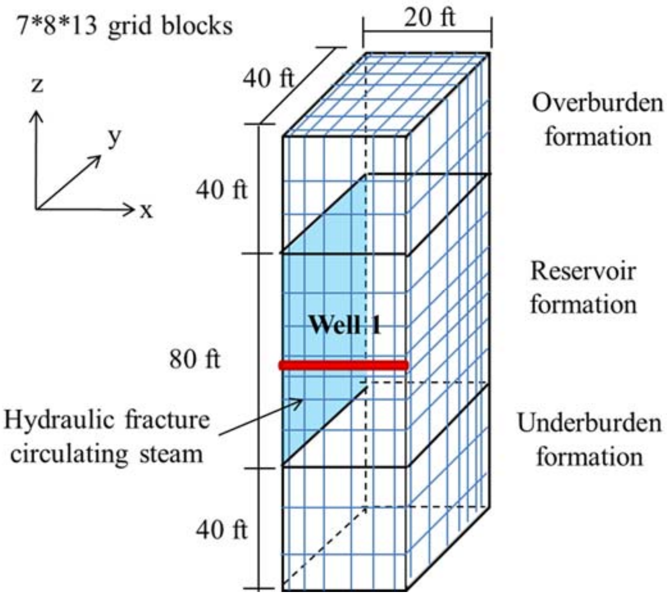

Fig. 125 Simulation model in case 1 (TAMU Steamfrac)

The results of the 900 days of huff-and-puff method are provided in the Fig. 126 – Fig. 128. The results are computed in one fracture. We only produced 23 STB of liquid organic phase per one fracture, and this case turns out to be less efficient. In the Fig. 128, we can see that the formation temperature is almost evenly increasing, but the temperature doesn’t reach a sufficiently high temperature for the kerogen decomposition in a wide area. The simulation results are summarized in Table 34. The Steam Oil Ratio (SOR) is 4.450E5 (kg/STB).

Table 34 Summary of the simulation results: case 1 (TAMU Steamfrac)

Parameters	Values	Parameters	Values
Duration (days)	900	HC gas production (MSCF)	0.17
Remaining kerogen (%)	99.78	Produced HC (BOE)	23.33
Liquid organic production (STB)	23.30	Energy input (BOE)	2,653
Gaseous production (MSCF)	0.66	Energy efficiency (%)	8.79e-3
Aqueous production (STB)	6.52E4	SOR (kg/STB)	4.450E5
GOR (MSCF/STB)	2.85e-2		

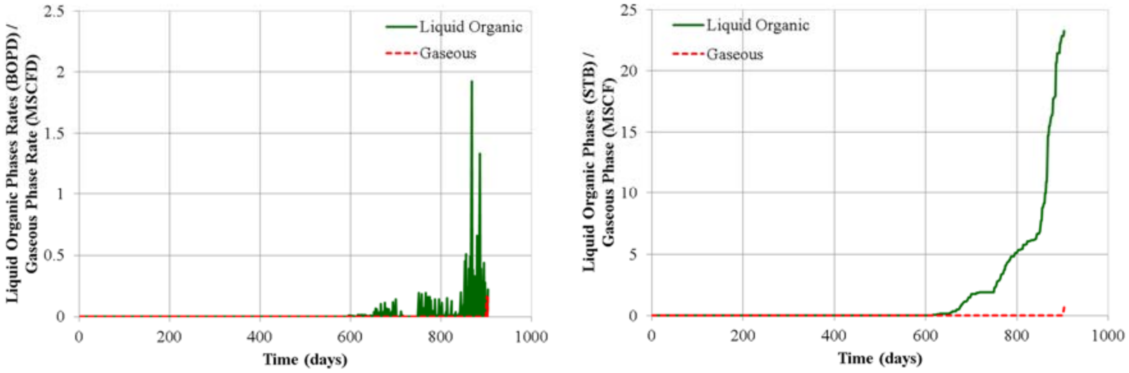

Fig. 126 Production rates and cumulative productions of phases: case 1 (TAMU Steamfrac)

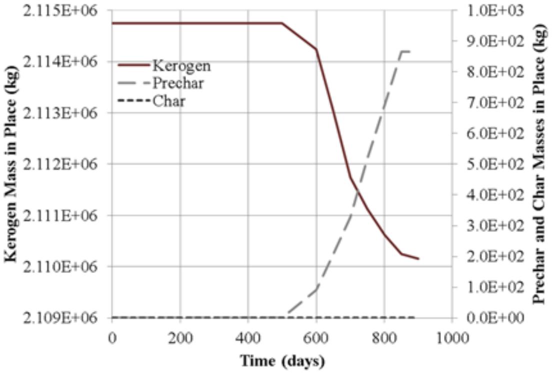

Fig. 127 Solid products mass in place: case 1 (TAMU Steamfrac)

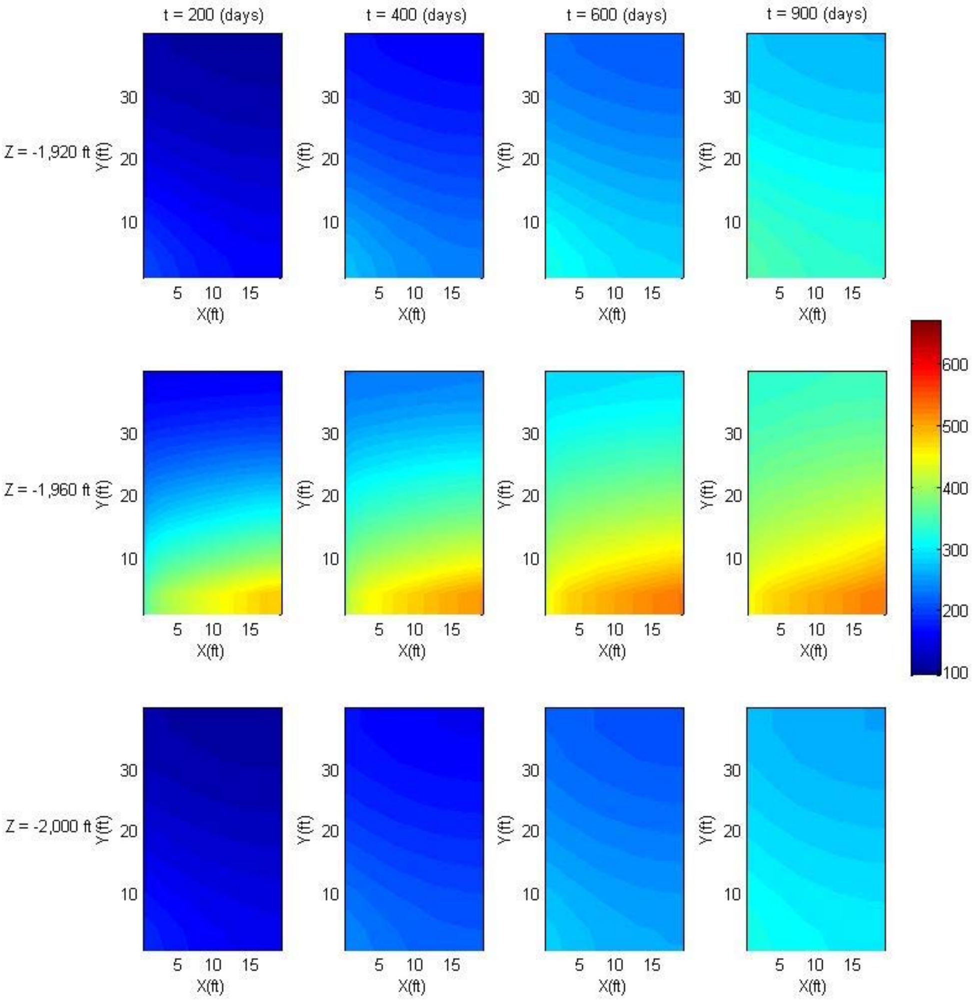

Fig. 128 Profiles of temperature at matrix domain: case 1 (TAMU Steamfrac)

5.3.2 Case 2: huff-and-puff method by using two wells

We consider the reservoir model as shown in Fig. 129. Fracture height, fracture width, and fracture spacing are 80 ft, 80 ft, and 40 ft, respectively. We consider two wells for injection and production. One is at the middle and center of the reservoir, and the other is at the bottom and center of the reservoir. We simulate a quarter of the single fracture unit as the previous case. We use a 3D model of 7*8*13 grid blocks as shown in Fig. 130. We repeat the following stages of huff-and-puff method. The simulation continued for 330 days.

1. Inject steam into well 1 (enthalpy of 1.5E6 J/kg and rate of 0.4 kg/s per one fracture unit) for 1 day.
2. Rest for 1 day.
3. Produce from well 2 (rate of 0.4 kg/s per one fracture unit) for 1 day.

After two weeks of cycling, we switch the well, and repeat as follows.

4. Inject steam into well 2 (enthalpy of 1.5E6 J/kg and rate of 0.4 kg/s per one fracture unit) for 1 day.
5. Rest for 1 day.
6. Produce from well 1 (rate of 0.4 kg/s per one fracture unit) for 1 day.

After two-weeks of cycling, we switch the well, and repeat from (1).

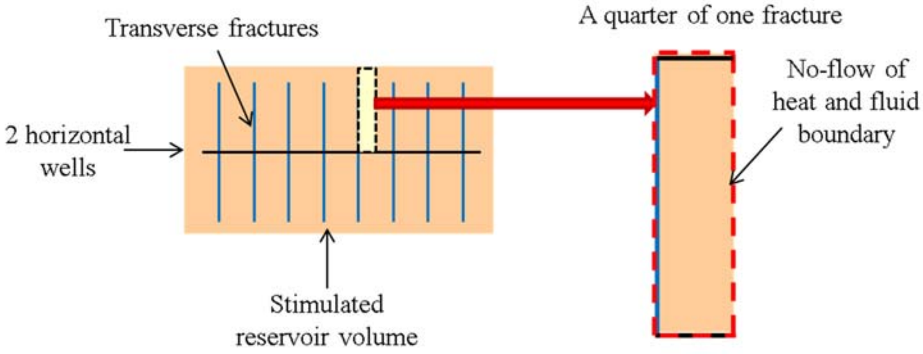

Fig. 129 Configuration of the reservoir model in case 2 (TAMU Steamfrac)

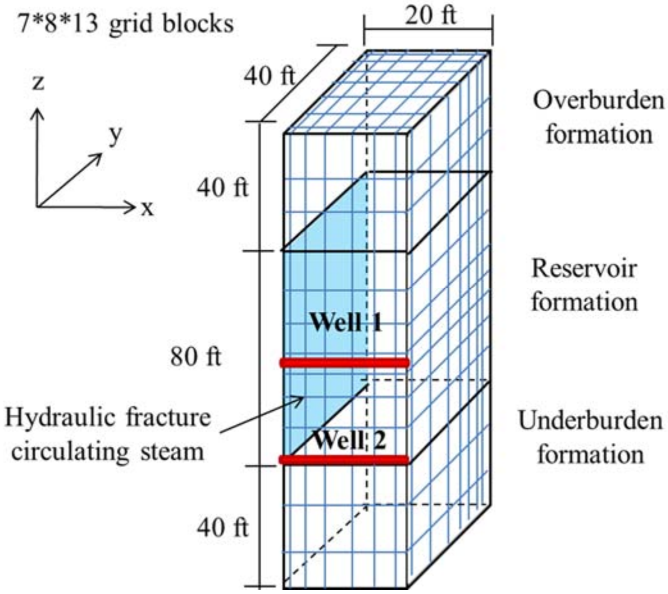

Fig. 130 Simulation model in case 2 (TAMU Steamfrac)

The results of the 330 days of huff-and-puff method are provided in the Fig. 131 – Fig. 133. The results are computed in one fracture. We only produced 4.8 STB of liquid organic phase per one fracture, and this case turns out to be less efficient. In the Fig. 133, we can see that the formation temperature is increasing in a wide area, but the temperature doesn't reach a sufficiently high temperature for the large amount of kerogen decomposition. The simulation results are summarized in Table 35. The SOR is 7.920E5 (kg/STB).

Table 35 Summary of the simulation results: case 2 (TAMU Steamfrac)

Parameters	Values	Parameters	Values
Duration (days)	330	HC gas production (MSCF)	6.18e-3
Remaining kerogen (%)	99.88	Produced HC (BOE)	4.80
Liquid organic production (STB)	4.80	Energy input (BOE)	973
Gaseous production (MSCF)	0.02	Energy efficiency (%)	7.94e-3
Aqueous production (STB)	2.39E4	SOR (kg/STB)	7.920E5
GOR (MSCF/STB)	5.15e-3		

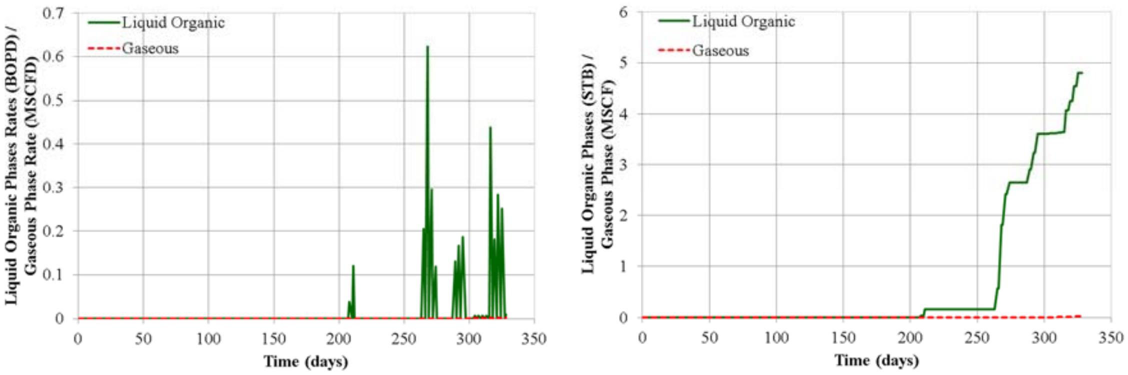

Fig. 131 Production rates and cumulative productions of phases: case 2 (TAMU Steamfrac)

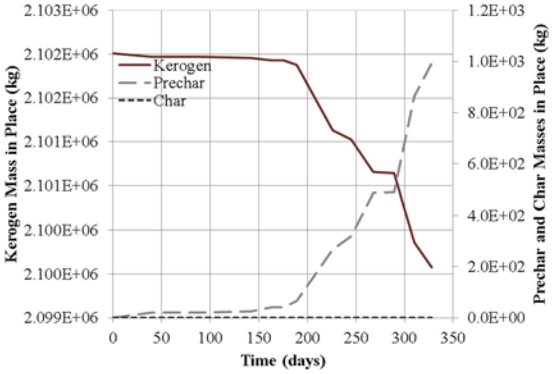

Fig. 132 Solid products mass in place: case 1 (TAMU Steamfrac)

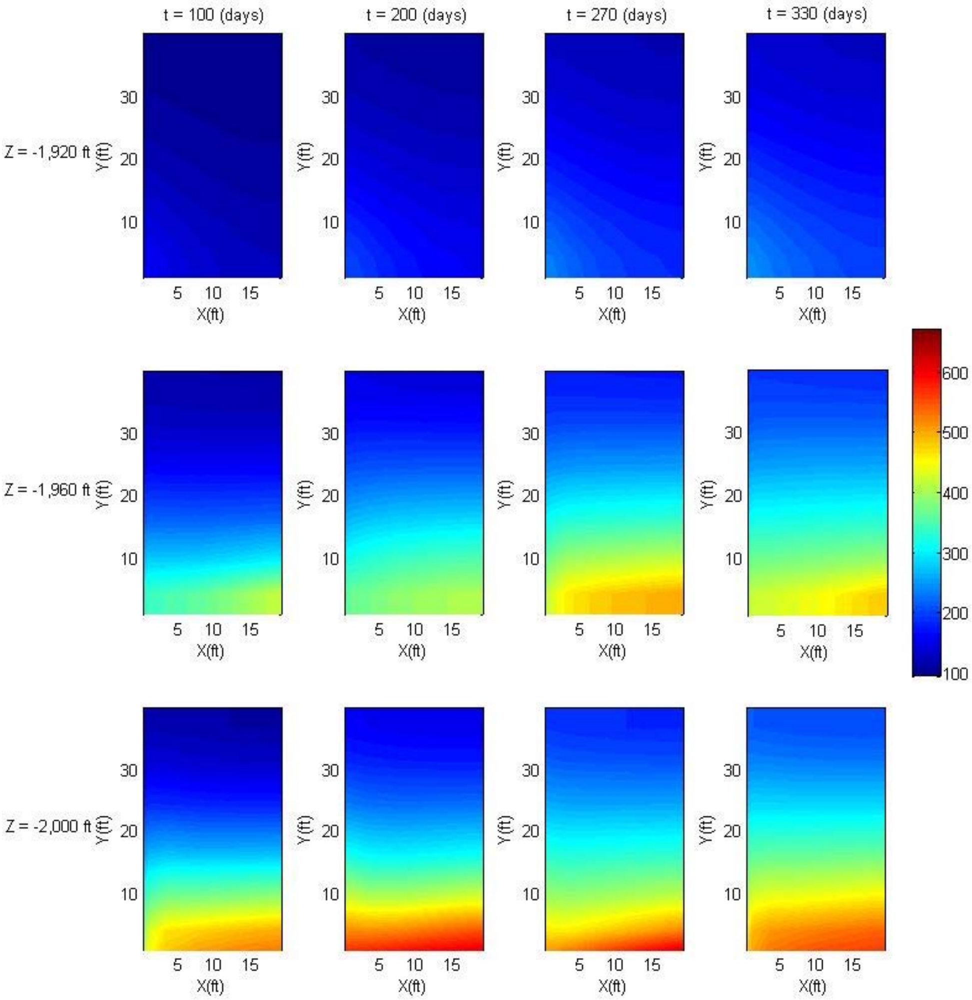

Fig. 133 Profiles of temperature at matrix domain: case 2(TAMU Steamfrac)

5.3.3 Case 3: huff-and-puff method by using three wells

We consider the reservoir model as shown in Fig. 134. Fracture height, fracture width, and fracture spacing are 80 ft, 80 ft, and 40 ft, respectively. We consider three wells for injection and production. One is at the middle and center of the reservoir, and the others are at the bottom and corners of the reservoir. We simulate a quarter of the single fracture unit as the previous case. We use a 3D model of 7*8*13 grid blocks as shown in Fig. 135. We repeat the following stages of huff-and-puff method. The simulation continued for 370 days.

(1) Inject steam into well 1 (enthalpy of 1.5E6 J/kg and rate of 0.4 kg/s per one fracture unit) for 1 day.
(2) Rest for 1 day.
(3) Produce from two well 2 (rate of 0.2 kg/s from each well per one fracture unit) for 1 day.

After two weeks of cycling, we switch the well, and repeat as follows.

(4) Inject steam into two well 2 (enthalpy of 1.5E6 J/kg and rate of 0.2 kg/s for each well per one fracture unit) for 1 day.
(5) Rest for 1 day.
(6) Produce from well 1 (rate of 0.4 kg/s per one fracture unit) for 1 day.

After two-weeks of cycling, we switch the well, and repeat from (1).

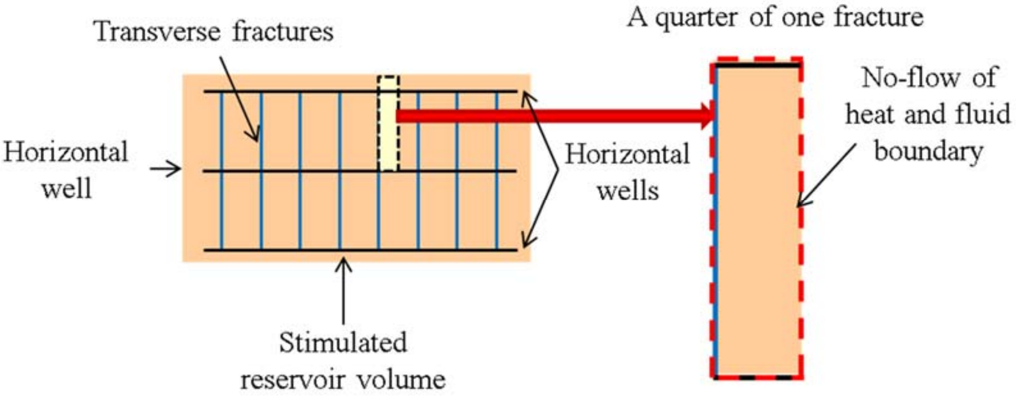

Fig. 134 Configuration of the reservoir model in case 3 (TAMU Steamfrac)

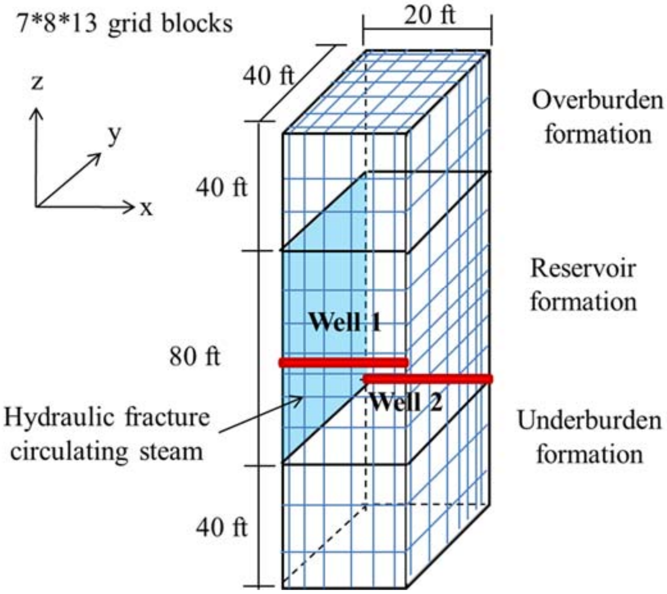

Fig. 135 Simulation model in case 3 (TAMU Steamfrac)

The results of the 370 days of huff-and-puff method are provided in the Fig. 136 – Fig. 138. The results are computed in one fracture. We only produced 4.86 STB of liquid organic phase per one fracture, and this case turns out to be less efficient. In the Fig. 138, we can see that the formation temperature is increasing in a wide area, but the temperature doesn't reach a sufficiently high temperature for the large amount of kerogen decomposition. The simulation results are summarized in Table 36. The SOR is 8.747E5 (kg/STB).

Table 36 Summary of the simulation runs: case 3 (TAMU Steamfrac)

Parameters	Values	Parameters	Values
Duration (days)	370	HC gas production (MSCF)	2.23e-3
Remaining kerogen (%)	99.80	Produced HC (BOE)	4.86
Liquid organic production (STB)	4.86	Energy input (BOE)	1,088
Gaseous production (MSCF)	0.01	Energy efficiency (%)	4.47e-3
Aqueous production (STB)	2.67E4	SOR (kg/STB)	8.747E5
GOR (MSCF/STB)	1.88e-3		

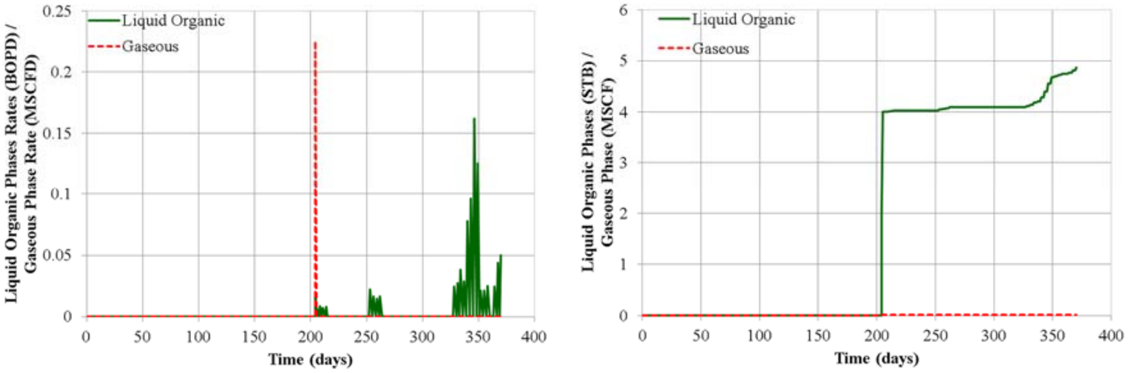

Fig. 136 Production rates and cumulative productions of phases: case 3 (TAMU Steamfrac)

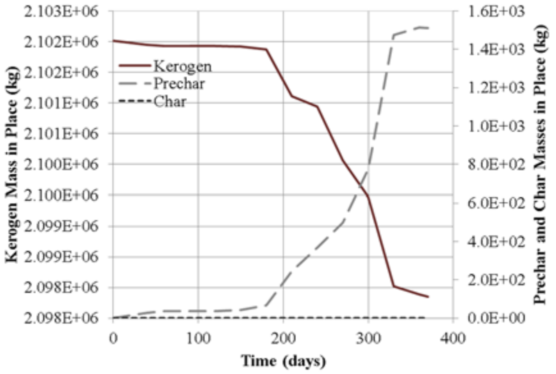

Fig. 137 Solid products mass in place: case 3 (TAMU Steamfrac)

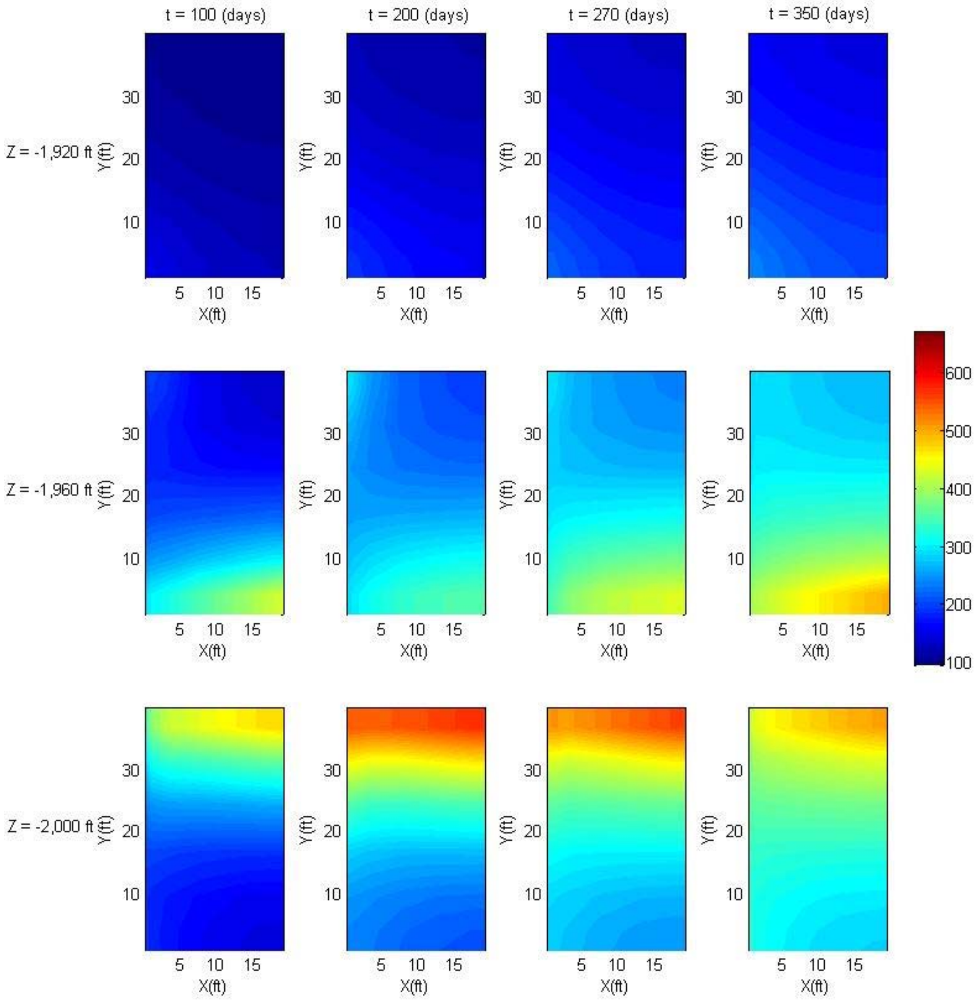

Fig. 138 Profiles of temperature at matrix domain: case 3 (TAMU Steamfrac)

5.3.4 Case 4: continuous injection and production by using three wells

In order to achieve more hydrocarbon production than huff-and-puff methods, we conducted case 4 by using continuous injection and production. As the same reservoir configuration and the simulation model geometry to the case 3, we simulate the case of continuous injection production with three wells. We repeat following stages.

(1) Inject steam into well 1 (enthalpy of 1.5E6 J/kg and rate of 0.4 kg/s per one fracture unit), and produce the fluid from the two well 2 with a constant flowing bottomhole pressure.
(2) After a sufficiently long time (50 days – 100 days), change the wells, and inject steam into two well 2 (enthalpy of 1.5E6 J/kg and rate of 0.2 kg/s for each well per one fracture unit), and produce fluid from well 1 with a constant flowing bottomhole pressure.

The simulation results are shown in Fig. 139 – Fig. 153, and they are summarized in Table 37. The results are computed in one fracture. It shows that this case is more efficient than the previous cases of huff-and-puff methods, but the upper part of the reservoir is not sufficiently heated, and kerogen doesn’t decompose in this region. The energy efficiency approaches the maximum value, 68.6 %, at 510 days. The remaining kerogen is 42.9 %, and the SOR is 1,896 (kg/STB).

Table 37 Summary of the simulation results: case 4 (TAMU Steamfrac)

Parameters	Values	Parameters	Values
Duration (years)	2	HC gas production (MSCF)	610
Remaining kerogen (%)	42.9	Produced HC (BOE)	3,115
Liquid organic production (STB)	3,007	Energy input (BOE)	5,762
Gaseous production (MSCF)	754	Energy efficiency (%)	54.1
Aqueous production (STB)	1.34E5	SOR (kg/STB)	1,896
GOR (MSCF/STB)	0.25		

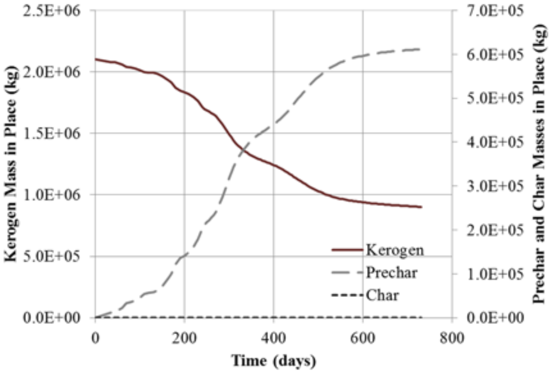

Fig. 139 Solid products mass in place: case 4 (TAMU Steamfrac)

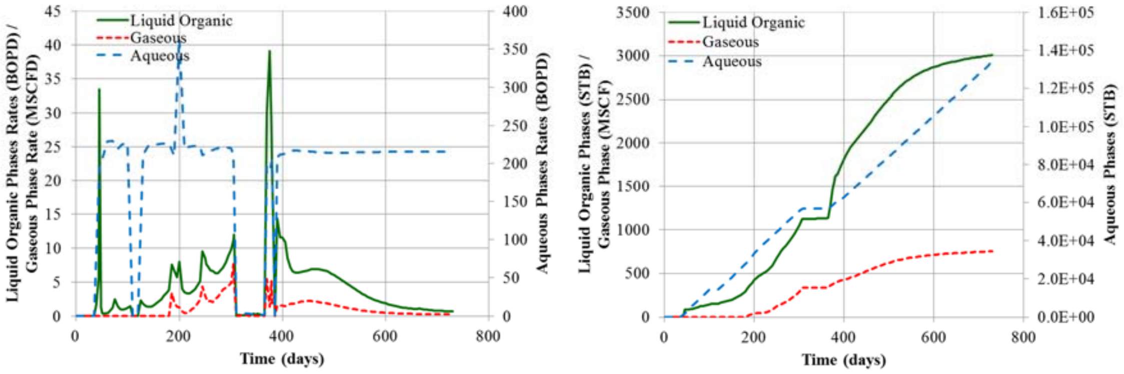

Fig. 140 Production rates and cumulative productions of phases: case 4 (TAMU Steamfrac)

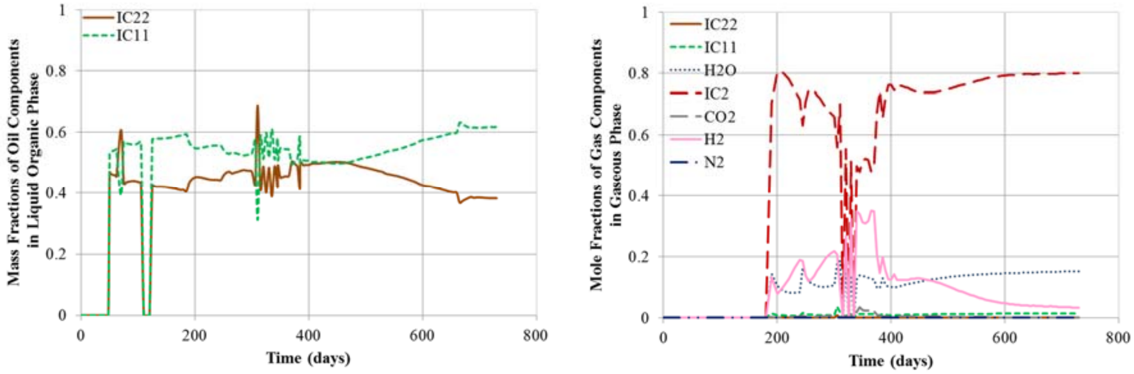

(a) Mass fractions of oil components in liquid organic phase

(b) Mole fractions of gas components in gaseous phase

Fig. 141 Fractions of components in produced fluid: case 4 (TAMU Steamfrac)

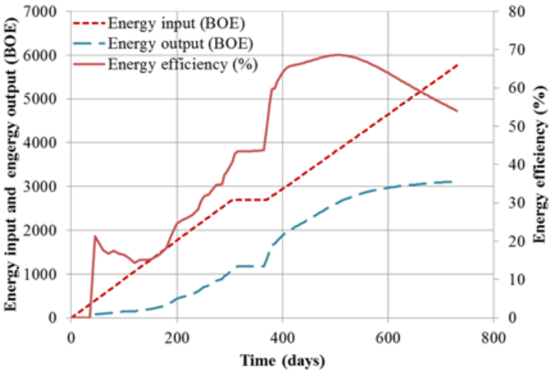

Fig. 142 Energy input, energy output and energy efficiency: case 4 (TAMU Steamfrac)

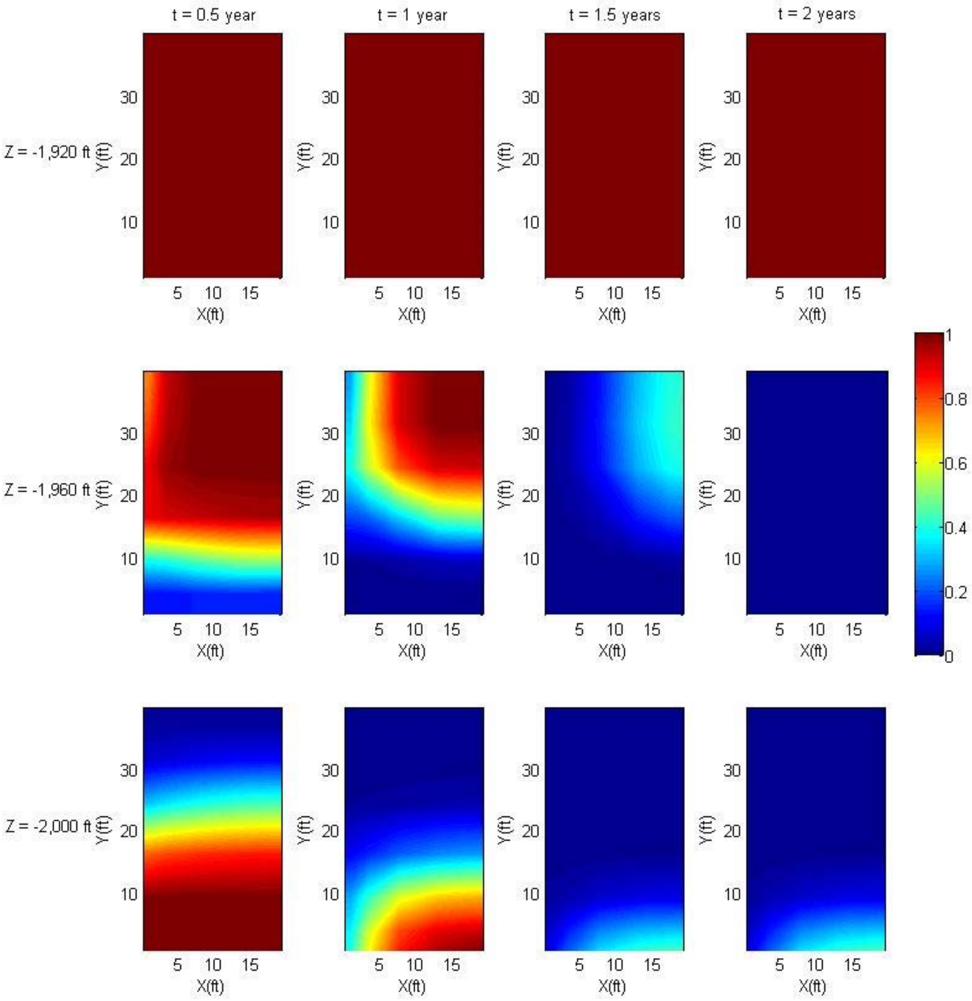

Fig. 143 Profiles of kerogen mass fraction: case 4 (TAMU Steamfrac)

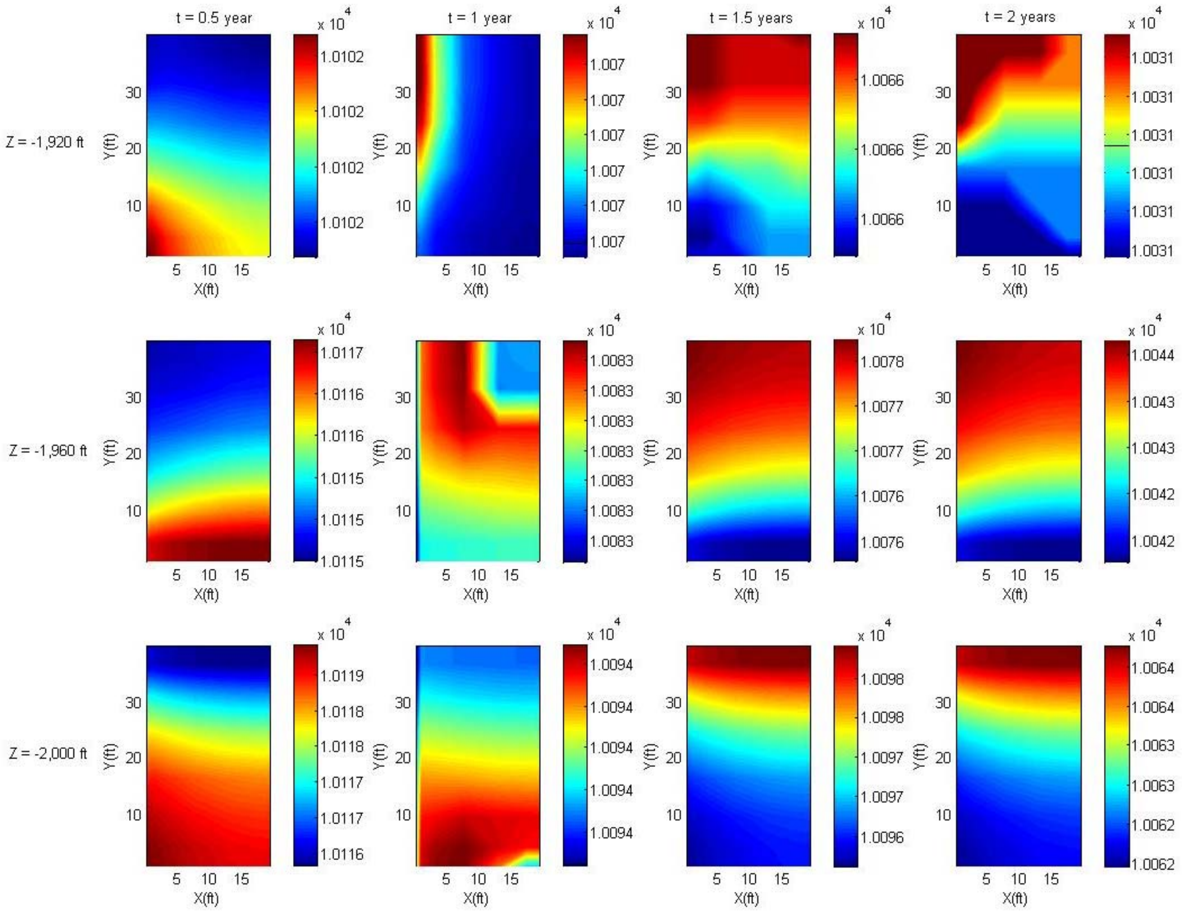

Fig. 144 Profiles of pressure at matrix domain: case 4 (TAMU Steamfrac)

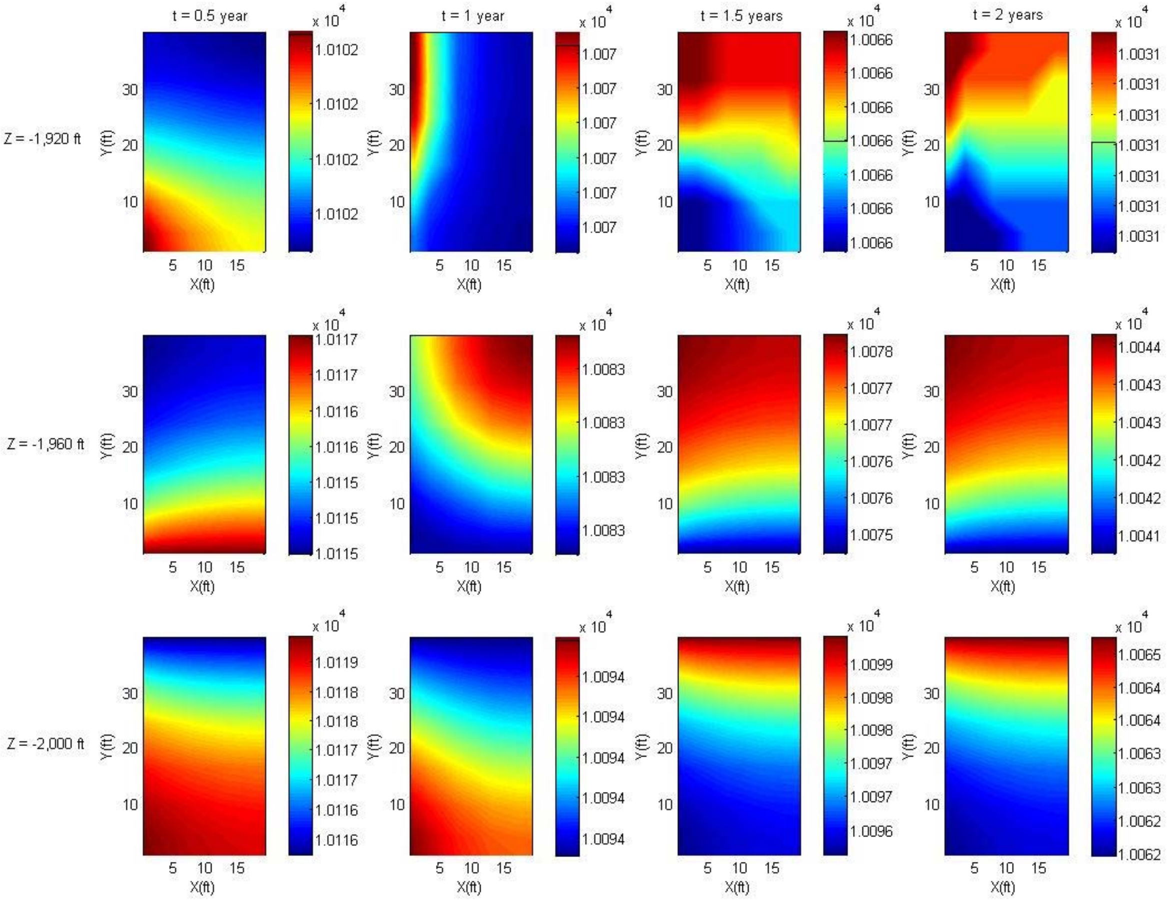

Fig. 145 Profiles of pressure at fracture domain: case 4 (TAMU Steamfrac)

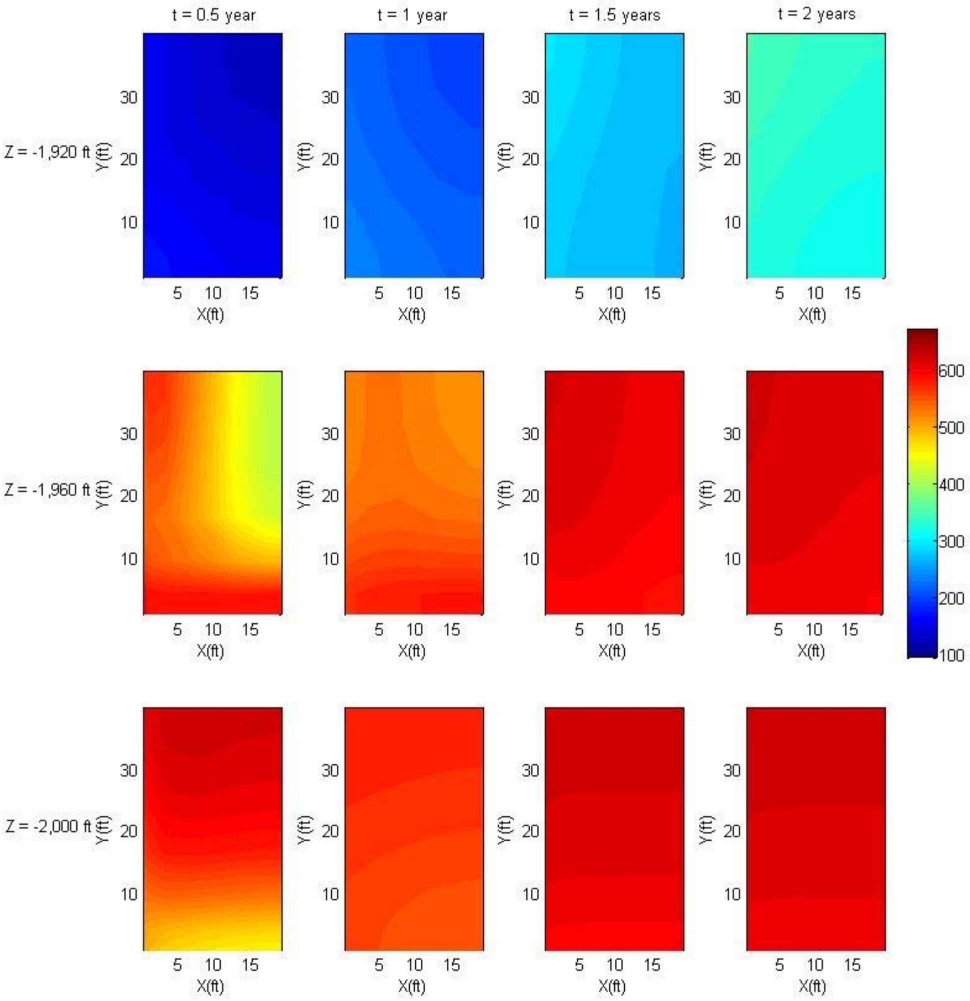

Fig. 146 Profiles of temperature at matrix domain: case 4 (TAMU Steamfrac)

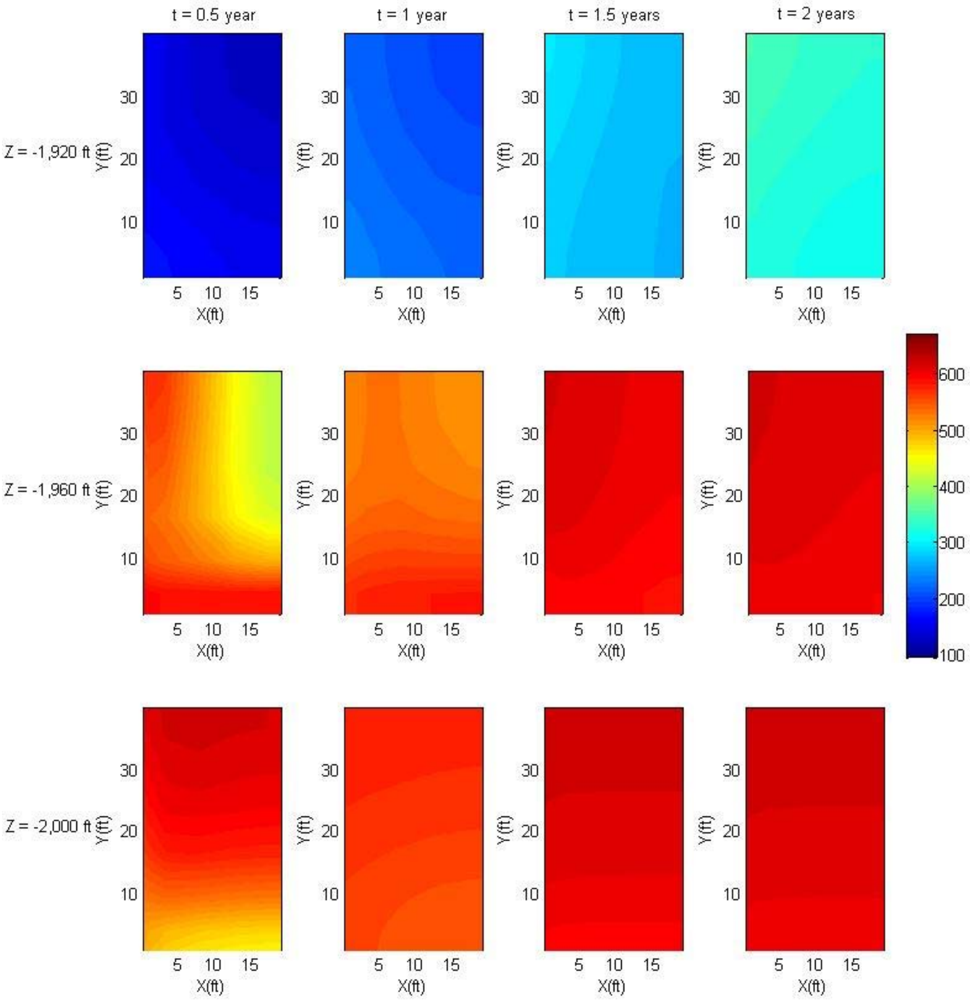

Fig. 147 Profiles of temperature at fracture domain: case 4 (TAMU Steamfrac)

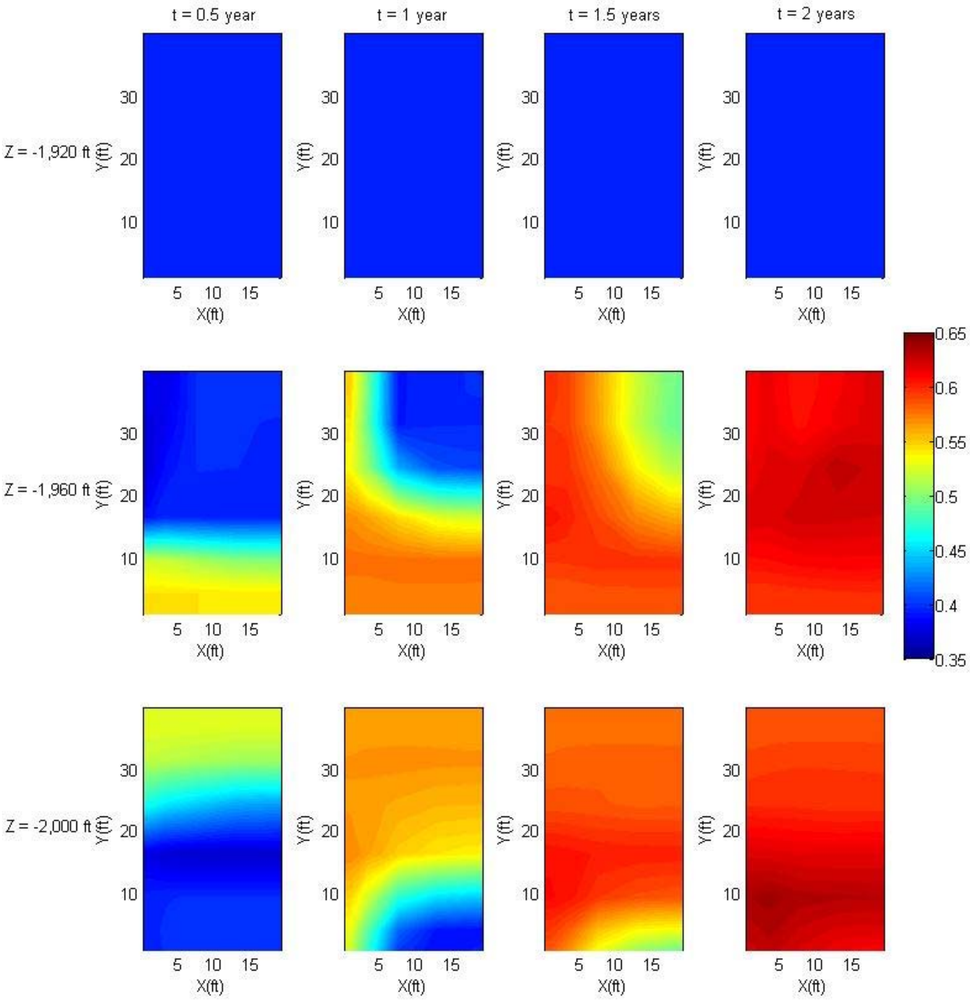

Fig. 148 Profiles of aqueous phase saturation at matrix domain: case 4 (TAMU Steamfrac)

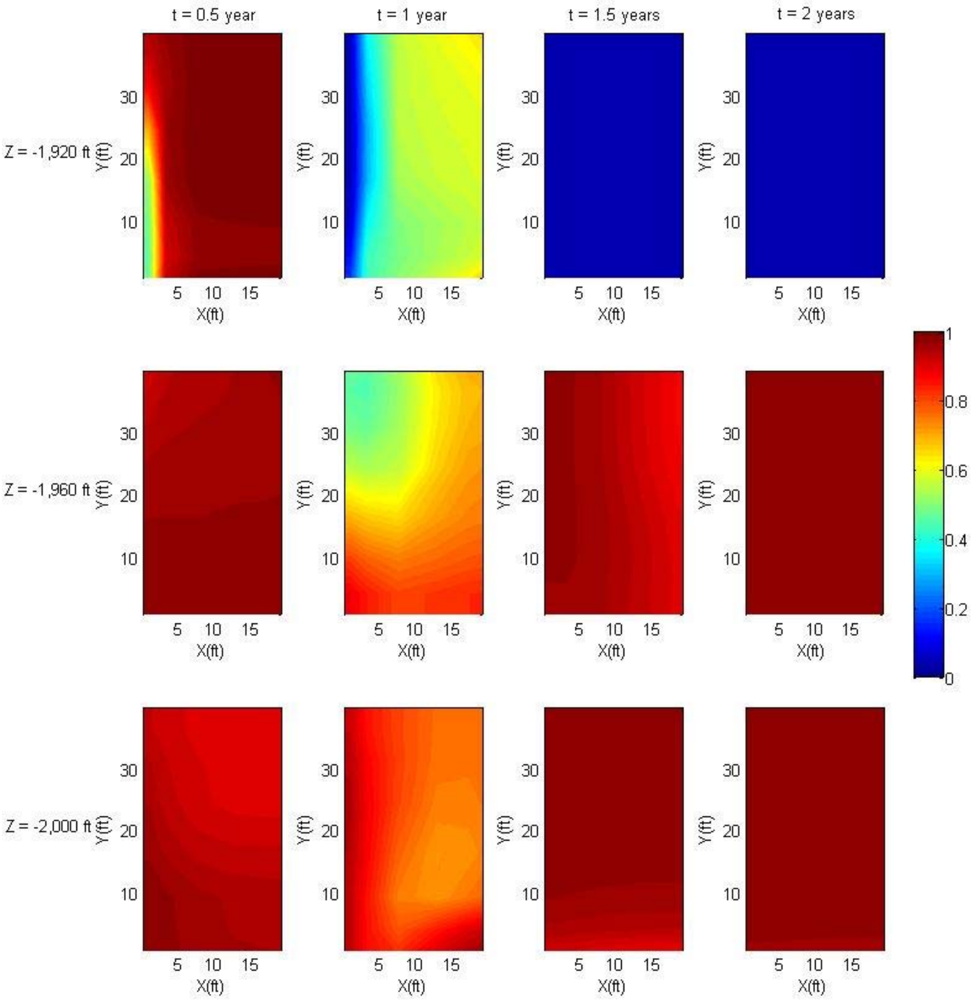

Fig. 149 Profiles of aqueous phase saturation at fracture domain: case 4 (TAMU Steamfrac)

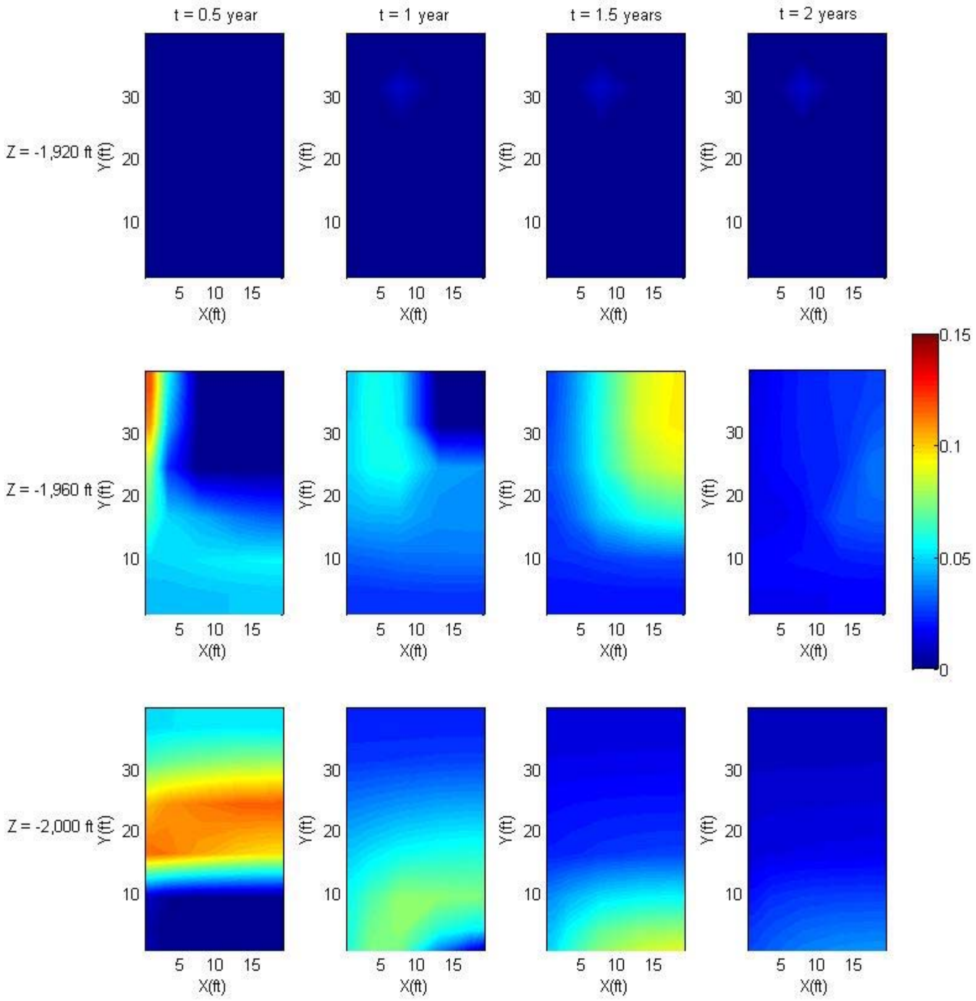

Fig. 150 Profiles of liquid organic phase saturation at matrix domain: case 4 (TAMU Steamfrac)

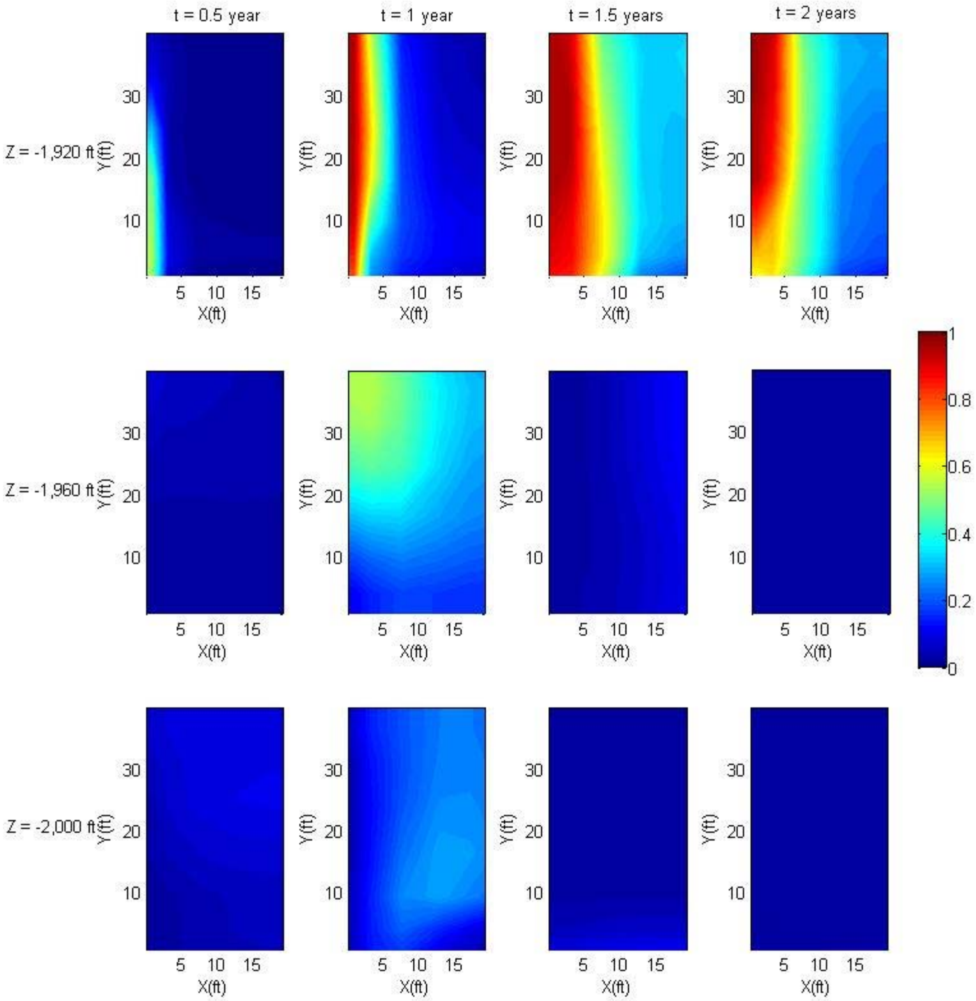

Fig. 151 Profiles of liquid organic phase saturation at fracture domain: case 4 (TAMU Steamfrac)

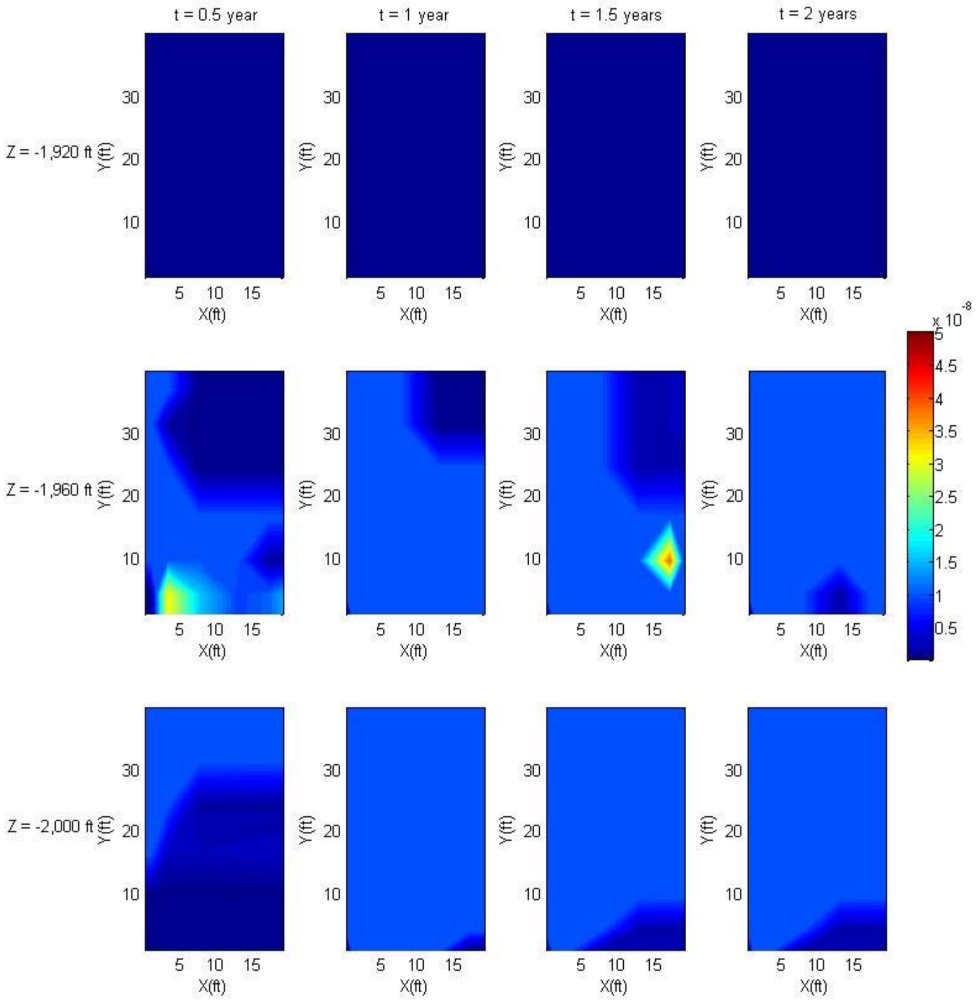

Fig. 152 Profiles of gaseous phase saturation at matrix domain: case 4 (TAMU Steamfrac)

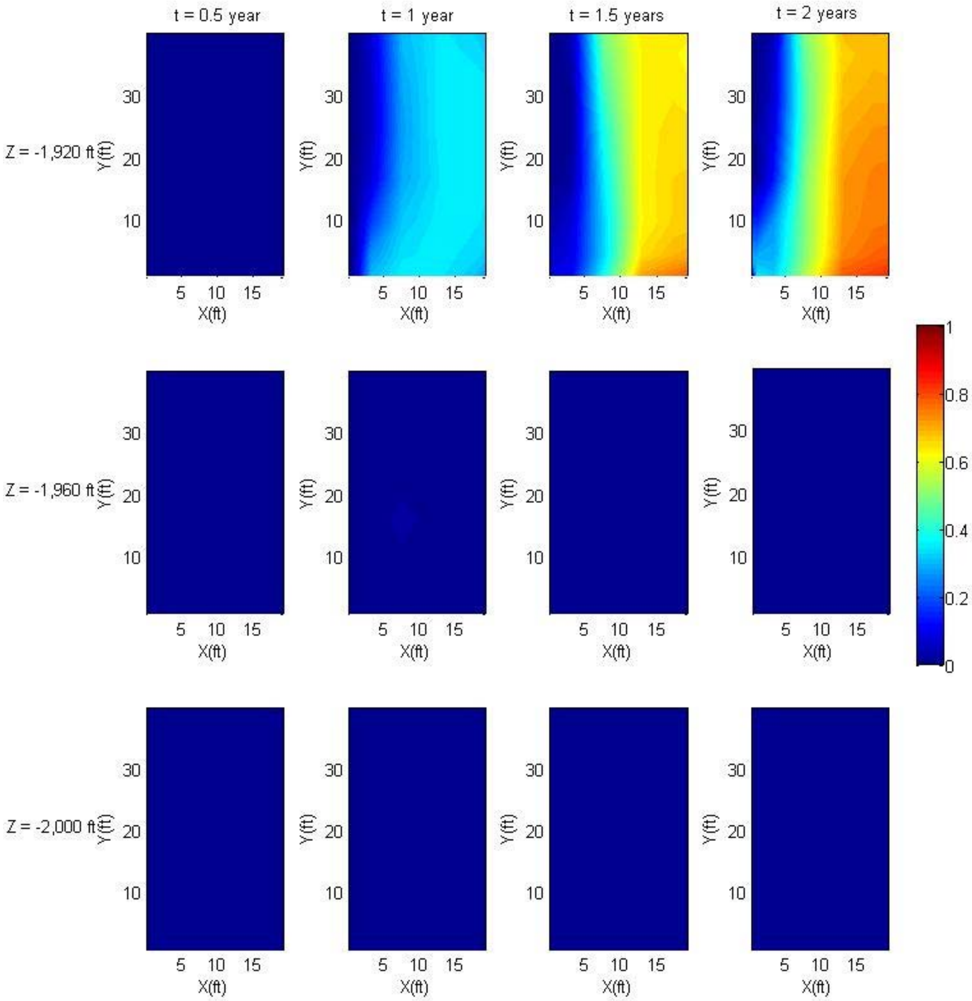

Fig. 153 Profiles of gaseous phase saturation at fracture domain: case 4 (TAMU Steamfrac)

5.4 Economics evaluation

We evaluate the economics of each process by computing NPV. The NPV model is described by using Eq. (5.2) as follows (Balen et al. 1988, Jukes et al. 2012).

$$NPV = \sum_{n=1}^{N} \frac{R_n}{(1+i)^n} - I \tag{5.2}$$

Here, NPV is the net present value, R_n is the annual revenue from the production, i is the discount rate, N is the total number of years, and I is the initial investment. R_n is described by using Eq. (5.3) as follows.

$$R_n = \left[\Delta Q_{o,n} \cdot P_o + \Delta Q_{G,n} \cdot P_G\right] \cdot (1 - f_r) \cdot (1 - f_t) \cdot (1 - f_o) \tag{5.3}$$

Here, $\Delta Q_{o,n}$ and $\Delta Q_{G,n}$ are the cumulative liquid organic phase production and gaseous phase production during the n-th year, and P_o and P_G are the prices of liquid organic phase (\$/STB) and gaseous phase (\$/MSCF), respectively. f_r, f_t, and f_o are the royalty, tax, and operating cost in fractions, respectively. Each process of in-situ upgrading has the different initial investment (I) and operating cost (f_o) from each other as listed in Table 38. The assumed costs for the items in Table 38 are listed in Table 39.

Based on this, we compute the NPV of the best scenarios for the Shell ICP, ExxonMobil Electrofrac and TAMU Steamfrac, which have the highest energy efficiency. In order to compare the NPV of them, we will use the same total reservoir volume for them. The volume of one pattern for Shell ICP and one single fracture unit for ExxonMobil Electrofrac and TAMU Steamfrac are as follows.

$$V_{Shell} = 88{,}580 \quad ft^3$$

$$V_{Exxon} = 256{,}000 \quad ft^3$$

$$V_{TAMU} = 256{,}000 \quad ft^3$$

Here, 289 patterns of Shell ICP and 100 hydraulic fractures of ExxonMobil Electrofrac and Shell ICP have almost the same volume, 2.56E7 *ft*^{3}. We compute the NPV for each case with this volume.

Table 38 Items of expenses for the in-situ upgrading processes

Processes	Items of the expenses	
Shell ICP	Capex	Drilling of the multiple vertical wells (c_{dvw}) Completion of the vertical wells (c_{cvw})
	Opex	Heating the vertical wells (c_{ht})
Exxon's Electrofrac	Capex	Drilling of the multiple horizontal wells and vertical wells (c_{dvw}, c_{dhw}) Completion of the wells (c_{cvw}, c_{chw}) Fracturing treatment (c_{fr}) Injection of the conductive material (c_{icm})
	Opex	Heating of the horizontal wells (c_{ht})
TAMU Steamfrac	Capex	Drilling of the horizontal wells (c_{dhw}) Completion of the horizontal wells (c_{chw}) Fracturing treatment (c_{fr})
	Opex	Steam injection (c_{ist})

Table 39 Cost of the items

Items	Cost	Items	Cost
c_{dvw} ($/ft)	45	c_{ist} ($/kg)	5.5e-3
c_{cvw} ($/ft)	75	f_r (%)	10
c_{dhw} ($/ft)	90	f_t (%)	30
c_{chw} ($/ft)	150	i (%)	10
c_{ht} ($/BOE)	0.4135	P_o ($/STB)	100
c_{fr} ($/#)	7,300	P_G ($/MSCF)	6.5
c_{icm} ($/kg)	22		

5.4.1 Shell ICP case 6

In the case of Shell ICP, there exist 2 producers and 16 heaters in one pattern. We consider 289 patterns for 340 days of process. We get following values by substituting the number of wells, and duration of the production.

$$\begin{aligned} I &= n_{vw} \cdot d_{vw} \cdot c_{dvw} + n_{pw} \cdot d_{cvw} \cdot c_{cvw} \\ &= (289 \cdot 18) \cdot 2{,}056.5\,(ft) \cdot 45\ (\$/ft) + (289 \cdot 2) \cdot 113\,(ft) \cdot 75\,(\$/ft) = \$4.863E8 \end{aligned}$$

$$F_o = c_{ht} \cdot energy\ input = 289 \cdot 0.4135(\$/BOE) \cdot 1{,}071(BOE) = \$1.280E5$$

$$\begin{aligned} R_{340\,d} &= 289 \cdot [1{,}415\,(STB) \cdot 100\,(\$/STB) + 693\,(MSCF) \cdot 6.5\,(\$/MSCF)] \cdot \\ &\quad (1-0.1) \cdot (1-0.3) \cdot (1-2.631e^{-4}) = \$2.658E7 \end{aligned}$$

$$NPV = -\$4.618E8$$

Here, n_{vw}, n_{pw}, d_{vw}, d_{cvw}, and F_o are the number of the vertical wells, the number of the production wells, the depth of the vertical wells, the distance of the completion in the vertical wells, and the operating cost in \$, respectively.

5.4.2 ExxonMobil Electrofrac case 4

In the case ExxonMobil Electrofrac, there exist 1 horizontal well and 2 vertical wells in a single fracture unit. We consider 100 hydraulic fractures for 7 years of process. We get following values by substituting the number of wells and hydraulic fractures, and duration of the production.

$$\begin{aligned} I &= n_{vw} \cdot d_{vw} \cdot c_{dvw} + n_{pw} \cdot d_{cvw} \cdot c_{cvw} + n_{hw} \cdot L_{hw} \cdot c_{dhw} + n_{hf} \cdot c_{fr} + c_{icm} \cdot m_{icm} \\ &= (100 \cdot 2) \cdot 2{,}080\,(ft) \cdot 45\ (\$/ft) + (100 \cdot 2) \cdot 12\,(ft) \cdot 75\,(\$/ft) + \\ &\quad 100 \cdot (80)(ft) \cdot 90\,(\$/ft) + 100 \cdot 7{,}300\,(\$/\#) + 100 \cdot 22(\$/kg) \cdot 1.189E4(kg) \\ &= \$4.651E7 \end{aligned}$$

$$F_o = c_{ht} \cdot energy\ input = 100 \cdot 0.4135(\$/BOE) \cdot 1{,}678(BOE) = \$6.939E4$$

$$\begin{aligned} R_1 &= 100 \cdot [215(STB) \cdot 100\,(\$/STB) + 64.8(MSCF) \cdot 6.5\,(\$/MSCF)] \cdot \\ &\quad (1-0.1) \cdot (1-0.3) \cdot (1-1.490e^{-3}) = \$1.379E6 \end{aligned}$$

$$R_2 = 100 \cdot [238\,(STB) \cdot 100\,(\$/STB) + 97.6\,(MSCF) \cdot 6.5\,(\$/MSCF)] \cdot (1-0.1) \cdot (1-0.3) \cdot (1-1.490e^{-3}) = \$1.537E6$$

$$R_3 = 100 \cdot [258\,(STB) \cdot 100\,(\$/STB) + 127\,(MSCF) \cdot 6.5\,(\$/MSCF)] \cdot (1-0.1) \cdot (1-0.3) \cdot (1-1.490e^{-3}) = \$1.675E6$$

$$R_4 = 100 \cdot [222\,(STB) \cdot 100\,(\$/STB) + 116\,(MSCF) \cdot 6.5\,(\$/MSCF)] \cdot (1-0.1) \cdot (1-0.3) \cdot (1-1.490e^{-3}) = \$1.444E6$$

$$R_5 = 100 \cdot [157\,(STB) \cdot 100\,(\$/STB) + 184\,(MSCF) \cdot 6.5\,(\$/MSCF)] \cdot (1-0.1) \cdot (1-0.3) \cdot (1-1.490e^{-3}) = \$1.063E6$$

$$R_6 = 100 \cdot [11\,(STB) \cdot 100\,(\$/STB) + 83\,(MSCF) \cdot 6.5\,(\$/MSCF)] \cdot (1-0.1) \cdot (1-0.3) \cdot (1-1.490e^{-3}) = \$1.031E5$$

$$R_7 = 100 \cdot [10\,(STB) \cdot 100\,(\$/STB) + 82.5\,(MSCF) \cdot 6.5\,(\$/MSCF)] \cdot (1-0.1) \cdot (1-0.3) \cdot (1-1.490e^{-3}) = \$9.663E4$$

$$NPV = -\$4.170E7$$

5.4.3 TAMU Steamfrac case 4

In the case of TAMU Steamfrac, there exist 3 horizontal wells in a single fracture unit. We consider 100 hydraulic fractures for 2 years of process. We get following values by substituting the numbers of wells and hydraulic fractures, and duration of the production.

$$\begin{aligned} I &= n_{hw} \cdot L_{hw} \cdot c_{dhw} + n_{pw} \cdot L_{chw} \cdot c_{chw} + n_{hf} \cdot c_{fr} \\ &= 3 \cdot (100 \cdot 40)(ft) \cdot 90(\$/ft) + 3 \cdot (100 \cdot 40)(ft) \cdot 150(\$/ft) + 100 \cdot 7{,}300(\$/\#) \\ &= \$3.610E6 \end{aligned}$$

$$F_o = c_{ist} \cdot steam\ \ injection = 100 \cdot 5.5e^{-3}\,(\$/kg) \cdot 2.281E7\,(kg) = \$1.255E7$$

$$R_1 = 100 \cdot [1{,}133(STB) \cdot 100\,(\$/STB) + 276\,(MSCF) \cdot 6.5\,(\$/MSCF)] \cdot (1-0.1) \cdot (1-0.3) \cdot (1-0.7765) = \$1.620E6$$

$$R_2 = 100 \cdot [1{,}874\,(STB) \cdot 100\,(\$/STB) + 334\,(MSCF) \cdot 6.5\,(\$/MSCF)] \cdot (1-0.1) \cdot (1-0.3) \cdot (1-0.7765) = \$2.669E6$$

$$NPV = \$5.317E5$$

In summary, we have the following Capex, Opex and NPV for each process as shown in Table 40. Shell ICP has the highest Capex, and lowest NPV. ExxonMobil Electrofrac has the lowest Opex. TAMU Steamfrac has the lowest Capex due to the less number of wells, but it has the highest Opex due to the steam injection. Only TAMU Steamfrac leads to the surplus of the process.

Table 40 Costs and NPV for each process

Processes	Capex ($)	Opex ($)	NPV ($)
Shell ICP	4.863E8	1.280E5	-4.618E8
ExxonMobil Electrofrac	4.651E7	6.939E4	-4.170E7
TAMU Steamfrac	3.610E6	1.255E7	5.317E5

5.5 Chapter summary

In this chapter, we studied the diverse processes in-situ upgrading - Shell ICP, ExxonMobil Electrofrac and TAMU Steamfrac. The process efficiency and the amount of recoverable hydrocarbons for each process are analyzed under diverse conditions. Shell ICP, ExxonMobil Electrofrac, and TAMU Steamfrac are significantly affected by the heater temperature, the thermal conductivity of the injection material, and the steam injection strategy (huff-and-puff with 1, 2, or 3 wells, and continuous injection and production), respectively.

We find the following conclusions in this chapter.

1. In Shell ICP, heater temperature has a significant effect on the amount of the recoverable hydrocarbon and energy efficiency, and the higher temperature doesn't guarantee the more production, because the high temperature of heater accelerates the cracking of liquid organic phase. The best case (heater temperature of 610 °F) has the energy efficiency of 144 %.
2. In ExxonMobil Electrofrac, electrical conductivity of the proppant significantly affects the amount of recoverable hydrocarbon and energy efficiency. Also, there exists dead zone for kerogen decomposition (lower part of the reservoir), because we penetrate the top of the producer to avoid the excessive production of aqueous phase. The best case (proppant electrical conductivity of 1.989E7 $\Omega^{-1}m^{-1}$) has the energy efficiency of 74.1 %.
3. In TAMU Steamfrac case, the strategy of steam injection greatly affects the energy efficiency and productivity. Huff-and-puff methods turned out to be less efficient, because they didn't allow the enough amount of heat introduced to the reservoir. The continuous injection and production promotes the faster heating and simultaneous production of generated hydrocarbons. The best case (continuous injection and production by using three wells) has the energy efficiency of 54.1 %.

4. Computation of NPV by considering large reservoir (volume of 2.56E7 ft^3) shows that Shell ICP and ExxonMobil Electrofrac have deficit. Shell ICP and ExxonMobil Electrofrac have the huge Capex than TAMU Steamfrac due to the large number of wells. TAMU Steamfrac has the highest Opex due to the continuous steam injection, but it has the highest and positive NPV.

CHAPTER VI

CONCLUSIONS

Oil shales are the promising energy resource, but the commercial production of them has not been achieved due to the technical challenges. In this dissertation, we determine and examine the factors affecting the successful hydrocarbon production from the oil shales. This is done by utilizing the fully implicit capability of the simulation of kerogen pyrolysis for the oil shale in-situ upgrading, which is developed in this research.

In the simulator development, we includes all known physics and chemistry of the systems we are interested in, and accurately accounts for the phase equilibria and phase transition thermodynamics. It solves 11 mass and energy balance equations per element simultaneously, and provides a powerful tool for the simulation of the kerogen pyrolysis in the oil shales and evaluation of the diverse processes of the in-situ upgrading.

The simulator was successfully validated by matching the production data of Shell ICP process, and we intensively studied the effect of the reservoir parameters on the production behavior. They include the presence of the naturally fractured zone, oil shale grade (organic matter content) of the oil shales, permeability of the fracture network, and the thermal conductivity of the formation. These series of sensitivity analyses provide the idea on the successful hydrocarbon production from the oil shales under the various reservoir environments as well as the realistic model of the oil shale formation (validated model).

In the case study, we conducted the diverse simulations of the in-situ upgrading processes including Shell ICP, ExxonMobil Electrofrac and TAMU Steamfrac. We defined the factors significantly affecting the efficiency of each process, and examined their effect on the productivity and the energy efficiency. These works provide the guidelines for the successful hydrocarbon production from the oil shales by expecting the optimal strategy of each process. By computing the NPV for the same reservoir size, we find that the TAMU Steamfrac is favorable, since it has the highest and positive NPV.

REFERENCES

Balen, R.M., Mens, H., and Economides, M.J. 1988. Applications of the Net Present Value (Npv) in the Optimization of Hydraulic Fractures. In *SPE Eastern Regional Meeting*: Society of Petroleum Engineers.ISBN 1555635741.

Biglarbigi, K., Crawford, P., Carolus, M. et al. 2010. Rethinking World Oil-Shale Resource Estimates. In *SPE Annual Technical Conference and Exhibition*.

Biglarbigi, K., Dammer, A., Cusimano, J. et al. 2007. Potential for Oil Shale Development in the United States. In *SPE Annual Technical Conference and Exhibition*.

Braun, R.L. 1981. Mathematical Modeling of Modified in Situ and Aboveground Oil Shakle Retorting. *Lawrence Livermore National Laboratory* **46**.

Braun, R.L. and Burnham, A.K. 1990. Mathematical Model of Oil Generation, Degradation, and Expulsion. *Energy & Fuels* **4** (2): 132-146.

Brooks, R.H. and Corey, A.T. 1964. Hydraulic Properties of Porous Media, Hydrology Papers, No. 3, Colorado State University, Ft. *Collins, Colo*.

Chang, C.-H. and Zhao, X. 1990. A New Generalized Equation for Predicting Volumes of Compressed Liquids. *Fluid Phase Equilibria* **58** (3): 231-238.

Chung, T.H., Ajlan, M., Lee, L.L. et al. 1988. Generalized Multiparameter Correlation for Nonpolar and Polar Fluid Transport Properties. *Industrial & engineering chemistry research* **27** (4): 671-679.

Chung, T.H., Lee, L.L., and Starling, K.E. 1984. Applications of Kinetic Gas Theories and Multiparameter Correlation for Prediction of Dilute Gas Viscosity and Thermal Conductivity. *Industrial & Engineering Chemistry Fundamentals* **23** (1): 8-13.

Corey, A.T. 1954. The Interrelation between Gas and Oil Relative Permeabilities. *Producers Monthly* **19** (1): 38-41.

Crawford, P., Biglarbigi, K., Dammer, A. et al. 2008. Advances in World Oil-Shale Production Technologies. In *SPE Annual Technical Conference and Exhibition*.

Dyni, J.R. 2006. *Geology and Resources of Some World Oil-Shale Deposits*: US Department of The Interior, US Geological Survey. Original edition. ISBN.

Eseme, E., Urai, J.L., Krooss, B.M. et al. 2007. Review of Mechanical Properties of Oil Shales: Implications for Exploitation and Basin Modelling. *Oil Shale* **24** (2): 159-174.

Fan, Y., Durlofsky, L., and Tchelepi, H. 2010. Numerical Simulation of the in-Situ Upgrading of Oil Shale. *SPE Journal* **15** (2): 368-381.

Fowler, T. and Vinegar, H. 2009. Oil Shale Icp-Colorado Field Pilots. In *SPE Western Regional Meeting*.

Ghosh, A., Chapman, W.G., and French, R.N. 2003. Gas Solubility in Hydrocarbons—a Saft-Based Approach. *Fluid Phase Equilibria* **209** (2): 229-243.

Hazra, K., Lee, K., Ehlig-Economides, C. et al. 2013. Comparison of Heating Methods for in-Situ Oil Shale Extraction. In *IOR 2013-From Fundamental Science to Deployment*.ISBN 2214-4609.

Jones, W. and March, N.H. 1973. *Theoretical Solid State Physics: Perfect Lattices in Equilibrium*: Courier Dover Publications. Original edition. ISBN 0486650154.

Jukes, R.H., Mcintosh, C.J., Amorer, G.J. et al. 2012. Npv-Based Design for Coal Seam Reservoirs. In *SPE Canadian Unconventional Resources Conference*: Society of Petroleum Engineers.ISBN 1613992475.

Kahl, W.R. 1999. Numerical Simulation of Primary Petroleum Migration, Massachusetts Institute of Technology.

Kay, W. 1936. Density of Hydrocarbon Gases and Vapors at High Temperature and Pressure. *Ind. Eng. Chem* **28** (9): 1014-1019.

Kyle, B. 1999. Chemical and Process Thermodynamics. In: Prentice Hall PTR (Upper Saddle River, NJ). 0130812447.

Lee, S., Speight, J.G., and Loyalka, S.K. 2007. *Handbook of Alternative Fuel Technologies*: crc Press. Original edition. ISBN 142001451X.

Logvinyuk, V., Makarenkov, V., Malyshev, V. et al. 1970. Solubility of Gases in Petroleum Products. *Chemistry and Technology of Fuels and Oils* **6** (5): 353-355.

Lorenz, J.C. 2003. Fracture Systems in the Piceance Basin: Overview and Comparison with Fractures in the San Juan and Green River Basins.

Lucas, K. 1981. Die Druckabhängigkeit Der Viskosität Von Flüssigkeiten–Eine Einfache Abschätzung. *Chemie Ingenieur Technik* **53** (12): 959-960.

Meyer, C.A., McClintock, R., and Silvestri, G. 1993. *Asme Steam Tables: Thermodynamic and Transport Properties of Steam: Comprising Tables and Charts for Steam and Water, Calculated Using the 1967 Ifc Formulation for Industrial Use, in Conformity with the 1963 International Skeleton Tables, as Adopted by the Sixth International Conference on the Properties of Steam*: American Society of Mechanical Engineers. Original edition. ISBN 0791806324.

Moridis, G. 2008. Tough+ Hydrate V1. 0 User's Manual: A Code for the Simulation of System Behavior in Hydrate-Bearing Geologic Media.

Mualem, Y. 1976. A New Model for Predicting the Hydraulic Conductivity of Unsaturated Porous Media. *Water Resources Research* **12** (3): 513-522.

Olgaard, D.L., Otten, G.A., Phillips, T.C. et al. 2009. Exxonmobil’s Electrofrac Process for in Situ Oil Shale Conversion. In *PDF). AAAPG Annual Convention. San Antonio: American Association of Petroleum Geologists. http://www. nevtahoilsands. com/pdf/Oil-Shale-and-Tar-Sands-Company-Profiles. pdf. Retrieved*:04-12.

Parker, J., Lenhard, R., and Kuppusamy, T. 1987. A Parametric Model for Constitutive Properties Governing Multiphase Flow in Porous Media. *Water Resources Research* **23** (4): 618-624.

Pedley, J.B. 1994. *Thermochemical Data and Structures of Organic Compounds*: CRC Press. Original edition. ISBN 1883400015.

Peng, D.-Y. and Robinson, D.B. 1976. A New Two-Constant Equation of State. *Industrial & Engineering Chemistry Fundamentals* **15** (1): 59-64.

Poling, B.E., Prausnitz, J.M., John Paul, O.C. et al. 2001. *The Properties of Gases and Liquids*: McGraw-Hill New York. Original edition. ISBN.

Prats, M. and O'Brien, S. 1975. The Thermal Conductivity and Diffusivity of Green River Oil Shales. *Journal of Petroleum Technology* **27** (1): 97-106.

Pruess, K., Moridis, G., and Oldenburg, C. 1999. *Tough2 User's Guide, Version 2.0*: Lawrence Berkeley National Laboratory Berkeley. Original edition. ISBN.

Ragland, K., Aerts, D., and Baker, A. 1991. Properties of Wood for Combustion Analysis. *Bioresource technology* **37** (2): 161-168.

Riazi, M. and Roomi, Y. 2007. A Method to Predict Solubility of Hydrogen in Hydrocarbons and Their Mixtures. *Chemical Engineering Science* **62** (23): 6649-6658.

Riedel, L. 1954. Liquid Density in the Saturated State. Extension of the Theorem of Corresponding States Ii. *Chem.-Ing.-Tech* **26**: 259-264.

Shen, C. 2009. Reservoir Simulation Study of an in-Situ Conversion Pilot of Green-River Oil Shale. In *SPE Rocky Mountain Petroleum Technology Conference*.

Stone, H. 1970. Probability Model for Estimating Three-Phase Relative Permeability. *Journal of Petroleum Technology* **22** (02): 214-218.

Tables-Hydrocarbons, T.T. 1996. Thermodynamics Research Center. *Texas A&M University System: College Station, TX, extant*.

Teja, A. and Rice, P. 1981. Generalized Corresponding States Method for the Viscosities of Liquid Mixtures. *Industrial & Engineering Chemistry Fundamentals* **20** (1): 77-81.

Thoram, S. and Ehlig-Economides, C. 2011. Heat Transfer Applications for the Stimulated Reservoir Volume (Srv). In *SPE Annual Technical Conference and Exhibition*.

Van Genuchten, M.T. 1980. A Closed-Form Equation for Predicting the Hydraulic Conductivity of Unsaturated Soils. *Soil Science Society of America Journal* **44** (5): 892-898.

Vernik, L. and Nur, A. 1992. Ultrasonic Velocity and Anisotropy of Hydrocarbon Source Rocks. *Geophysics* **57** (5): 727-735.

Vinegar, H. 2006. Shell's in-Situ Conversion Process. In *26th Oil Shale Symposium, Golden, Colorado, October 16*, 18:2006.

Wellington, S.L., Berchenko, I.E., De Rouffignac, E.P. et al. 2005. In Situ Thermal Processing of an Oil Shale Formation to Produce a Desired Product. In: Google Patents.

Yaws, C. Yaws' Handbook of Thermodynamic and Physical Properties of Chemical Compounds, Knovel, 2003. *Online version available at: http://www. knovel. com/knovel2/Toc. jsp.*